Hybrid Numerical-Experimental Testing of Active and Semi-Active Suspensions

Eamcharoenying, Pooh

Award date:
2015

Awarding institution:
University of Bath

UNIVERSITY OF BATH

Hybrid Numerical-Experimental Testing of Active and Semi-Active Suspensions

Pooh Eamcharoenying
A thesis submitted for the degree of Doctor of Philosophy
University of Bath
Department of Mechanical Engineering
April 2015

Abstract

This thesis details the development of an experimental test rig to measure the performance of semi-active and active vehicle suspensions. Due to the variety of suspension components, configurations and vehicle types that might adopt active suspensions a hybrid numerical-experimental test rig were developed using simulation and a range of mechanical and microprocessor hardware. Using Model-in-the-Loop and Hardware-in-the-Loop systems representing the suspension allows for flexibility in the testing of various suspension components. Similarly a model-in-the-loop system representing the vehicle structure was developed to investigate flexible systems such as those found in an aircraft. This allows the dynamic interaction between the structural flexible vibration modes and the suspension to be established.

Actuator tracking errors are crucial to the accuracy and stability of model-in-the-loop systems. Friction was shown to be a major source of tracking error for the suspension model-in-the-loop actuator and this led to the development of a novel force controlled friction compensator which resulted in a 37% improvement of the test rig accuracy and a reduction of peak force error by approximately 50%. Another source of tracking error which directly effects system stability is system delays caused by actuator, sensor, computational and filter lags. The effect of these delays upon the accuracy and stability of the test rig is analysed and discussed. Finally, passive, semi-active and active skyhook quarter car experiments were conducted and verified using the hybrid test rig. The results show that characteristics of passive, semi-active and active suspensions, and their dynamic interaction with a flexible vehicle structure can be successfully replicated using the test rig.

Acknowledgements

I would like to thank my supervisors Andy Hillis and Jos Darling for all their guidance and support throughout the project. Many thanks to Pejman Iravani who had to endure with me since the undergraduate days and without him this research would not have begun in the first place. Thanks to Alan Jefferis for the technical assistance in the construction of the test rig. The completion of the thesis would certainly have been more difficult without the help of colleague Jawaad Bhatti. I would like to thank him for wise insights, practical assistance as most of all friendship. Thanks to my colleagues Zuhayr Rymansaib, Zhenyu Du, Nick Hockings and Jack Gan for all the good times we had in the lab.

Finally, I would like to thank my family whose support means the world to me. Special mentions to my sister Namnueng Eamcharoenying, my brother Napon Eamcharoenying and my partner Pimchanok Thavipoke. Most of all I reserve special gratitude for my father and mother, Suthichai and Chantarat Eamcharoenying. It is their support and encouragement that enabled me to begin this journey and kept me going through the difficult moments. This thesis is dedicated to all of you.

Contents

Abstract **1**

Acknowledgements **2**

1. Introduction **7**

1.1 Background 7

1.2 Thesis Objectives 8

1.3 Outline 8

2. Vehicle Suspension - A Background **10**

2.1 Introduction 10

2.2 Types of Suspension 11

2.3 Passive Suspension 12

2.4 Active Suspension 14

2.5 Semi-Active Suspension 16

2.6 Springs 18

2.7 Dampers 18

2.7.1 Hydraulic Shock Absorbers 18

2.7.2 Variable Orifice Hydraulic Shock Absorber 18

2.7.3 Electrorheological and Magnetorheological Shock Absorber 20

2.8 Active Suspension Actuators 23

2.8.1 Hydraulic Actuators 23

2.8.2 Electromagnetic Actuators 24

2.9 Variable Stiffness Suspensions 25

2.10 Suspension Control 30

2.10.1 Skyhook Control and Variants 30

2.10.2 Optimal Control 31

2.10.3 Preview Control 32

2.10.4 Non-Linear Control 34

2.11 Hybrid Numerical-Experimental Testing 37

2.11.1 Background 37

2.11.2 Previous Applications 39

2.11.3 Delay Compensation 42

2.11.4 Performance Evaluation 44

2.12 Conclusions 44

3. Suspension Test Rig 46
3.1 Motivation for Rig Design 46
3.2 Test Rig Concept Design 46
3.3 Test Rig Mechanical Design 49
3.4 Test Rig Sensors and Signal Processing 52
3.5 Dynamic Similitude Testing 53
3.6 Rig Performance Validation 57
3.7 Conclusions 65
4. Friction Compensation 66
4.1 Introduction 66
4.2 Experimental Rig 68
4.3 Controller Structure 69
4.4 Friction Compensation for Deterministic Systems 70
4.5 Friction Compensation for Non-Deterministic Systems 73
4.5.1 Zero Velocity Crossing Estimation 73
4.5.2 Force Spike Detection 74
4.6 Experimental Results 76
4.6 Two Step Compensation 80
4.7 Conclusions 84
5. Test Rig Control Loop Analysis 85
5.1 Single Mass Model 85
5.1.1 Single Mass Model 85
5.1.2 Single Mass System - Suspension MIL Model 86
5.1.3 Single Mass System – Vehicle Structure MIL Model 87
5.1.4 Equivalence of Suspension MIL and Sprung Mass Position MIL 88
5.1.5 Critical Time Delay of Single Mass MIL System 89
5.1.6 Critical Time Delay of Double MIL 91
5.2 Single Mass Model Parameters Variation 93
5.2.1 Variation of Time Constant 93
5.2.2 Variation of Natural Frequency 95
5.2.3 Variation of Damping Ratio 98
5.2.4 Conclusion 102
5.3 Two Mass Model 103
5.3.1 State Space Quarter Car Model 103

5.3.2 MIL Suspension Model 104
5.3.3 MIL vehicle structure Model 105
5.3.4 Combined Suspension MIL and Vehicle structure MIL 106
5.3.5 Stability of Suspension MIL 107
5.3.6 Stability of Vehicle structure MIL 107
5.4 Quarter Car MIL Suspension Parameters Variation 110
5.5 Quarter Car MIL Vehicle Structure Parameters Variation 112
5.6 Quarter Car Combined MIL vehicle structure and MIL Suspension Parameters Variation 114
5.7 Conclusion 115
6. Quarter Car Experimental Validation 116
6.1 Test System Description 116
6.1.1 Overall System 116
6.1.2 Electric Actuator Controller 117
6.1.3 Hydraulic Actuator Controller 120
6.1.3 Tyre Stiffness Identification 122
6.1.3 Rail Guide Friction Identification 123
6.2 Real-Time Control Stability 124
6.3 Real-Time Test – Point Mass 130
6.3.1 Passive Drop Test - No Ground Disturbance 130
6.3.2 Passive Drop Test with 1.6Hz Pseudo Random Road 137
6.3.3 Passive Drop Test with 10Hz Pseudo Random Road 141
6.4 Conclusion 146
7. Active and Flexible Structure Testing 147
7.1 Active and Semi-Active Point Mass 147
7.1.1 Semi-Active Skyhook 147
7.1.2 Fully Active 149
7.1.3 Comparison of Passive, Semi-Active and Active 152
7.2 Real Time Test - Flexible Structure Sprung Mass Test 154
7.2.1 Flexible Beam Structure 154
7.2.2 Passive Test 157
7.2.2 Semi-Active Test 159
7.2.3 Active Test 162
7.2.4 Comparison of Passive and Active Suspension Performance 164
7.3 Conclusion 166

8. Conclusion and Future Work 167
8.1 Conclusion 167
8.2 Future Work 168
References 171
Appendix A 182
Appendix A1 – Quarter Car MIL Suspension Parameters Variation Analysis 182
Appendix A1.1 Variation of Time Constant 182
Appendix A1.2 Variation of Sprung Mass Natural Frequency 185
Appendix A1.3 Variation of Sprung Mass Damping Coefficient 190
Appendix A1.4 Variation of Tyre Stiffness 193
Appendix A1.5 Variation of Wheel Mass 194
Appendix A2 – Quarter Car MIL Vehicle Structure Parameters Variation 196
Appendix A2.1 Variation of Time Delay 196
Appendix A2.2 Variation of Sprung Mass Natural Frequency 197
Appendix A2.3 Variation of Sprung Mass Damping Ratio 201
Appendix A2.4 Variation of Tyre Stiffness 203
Appendix A2.5 Variation of Wheel Mass 205
Appendix A3 – Quarter Car Combined MIL Vehicle Structure and MIL Suspension Parameters Variation 208
Appendix A3.1 Variation of Time Delay 208
Appendix A3.2 Variation of Sprung Mass Natural Frequency 209
Appendix A3.3 Variation of Sprung Mass Damping Ratio 213
Appendix A3.4 Variation of Tyre Stiffness 215
Appendix A3.5 Variation of Wheel Mass 216
Appendix B 218
Appendix B1 – Validation of Semi-Active Skyhook Test 218
Appendix B2 – Validation of Active Skyhook Test 222
Appendix B3 – Validation of Passive Flexible Cross Structure Test 226
Appendix B4 – Validation of Semi-Active Flexible Cross Structure Test 231
Appendix B5 – Validation of Active Flexible Cross Structure Test 236

1. Introduction

1.1 Background

Active and semi-active suspension has been an area studied by many researchers dating back to the 1970's [1, 2]. Due to the multi-disciplinary nature of active suspension systems, demanding integration of mechanical, electrical and computer systems, it has attracted interest from researchers in the fields of automotive, control, fluid power, electrical motors and even artificial intelligence. Recent advances in computational power, speed and cost, alongside the development of better actuators and sensors, have led to an acceleration in the speed with which active and semi-active suspension systems are becoming viable alternatives to passive suspensions [3]. Generally speaking, active and semi-active suspension systems either control suspension forces directly or through a variable mechanism such that better vehicle handling and comfort is achieved when compared to the passive alternative.

There is a substantial variety in the types of active and semi-active suspensions that have been investigated. Typically active suspensions can be implemented using hydraulic or electrical actuators with sufficient force and bandwidth. Semi-active suspensions operate by varying a damper's pressure/flow characteristic and associated damping coefficient; typical means to achieve this are electro-hydraulic systems, or more recently using smart electro and magnetorheological fluids. There are also various types of passive springs, dampers and tyres that can be employed. Furthermore there are different suspension configurations such as having a spring in series with an actuator or a configuration that enables variable stiffness. Active suspension control implementation is highly dependent on the choice of actuators and their dynamics, the aim being to ensure that the performance is close to the ideal control strategy with no actuator delay. The broad range of technologies and configurations that can be employed for a vehicle suspension suggests that a rig that can readily test different suspension types would be very beneficial for rapid design processes [4].

In addition to the different suspension types, there are also various vehicle structures, some of which may be flexible such as aircraft. It would also be beneficial in terms of speeding up the design process if the vehicle structure could be implemented through a numerical model and physical forces imposed via an actuator forming part of the test rig loop. This would overcome the limitations of a static mass typical of a quarter car test rig and allow full vehicle testing without the need of real vehicle prototyping. By including a numerical model of the vehicle structure, the suspension's interaction with the vehicle body structural vibration can be studied experimentally.

Testing techniques which combine real test pieces interacting dynamically with numerical models whose outputs are tracked by an actuator are known as hybrid numerical-experimental testing. The essential characteristic of hybrid testing is that it combines the dynamic interaction between real test components and a numerical simulation model in real time. This is possible through the use of sensor readings as an input into the numerical model, and an actuator which tracks the desired output of the numerical model. This way the test piece and the numerical model interact physically through the actuator as a force producing element.

Hybrid testing has been studied extensively for structural engineering applications due to the difficulty and costs of testing large structures at real scale. More specifically hybrid testing has been termed 'substructuring' by some structural engineering researchers [4]. Outside of structural engineering and common in suspension applications, hybrid experiments have also been referred to as 'hardware in the loop' (HIL) testing [5]. This refers to experiments where hardware of interest, normally the component to be actively controlled, forms the test piece while the rest of the system is numerically modelled. 'Model in the loop' (MIL) refers to systems that track a numerical model output using an actuator, within an experimental test loop [6]. With this definition of HIL and MIL systems, all hybrid experimental systems such as substructured test rigs, MIL test rigs or HIL test rigs must comprise of both an HIL and a MIL element.

1.2 Thesis Objectives

The aim of this thesis is to build a hybrid numerical-experimental suspension test rig capable of:

1. Testing different suspension unit components and control algorithms.
2. Testing different vehicle structures with flexible modes of vibration.

The motivation behind this goal is associated with the variety of active and semi-active suspension configurations and vehicle structures. The suitability and viability of suspension systems is highly dependent on the type of vehicle, the ride and the cost requirements. The researcher is interested in experimentally testing the trade-off between different types of suspension. This is very difficult as various actuators and smart dampers are required for experimental comparison. It is hoped that by developing a MIL suspension, suspension components and systems can be tested to a reasonable degree of accuracy. On top of the MIL suspension, a MIL vehicle structure is incorporated so that the test rig can account for vehicle structural dynamics which interact with the suspension system. This allows full vehicle testing without needing the actual vehicle and is especially beneficial to large vehicles with substantial structural flexibility such as an aircraft.

If successful this would serve as an important simulation/experimental tool in the earlier stages of suspension system design. This challenge presents an opportunity to study the application of hybrid numerical-experimental methods in the simulation of automotive suspensions [4].

1.3 Outline

The structure of the thesis, after the introduction in Chapter 1, is summarized here. Chapter 2 presents background literature concerning various types of passive, semi-active and active suspensions. The benefits of each method are discussed along with their physical implementation and control algorithm. In Chapter 3 background literature on experimental rig building is discussed with particular focus on hybrid numerical-experimental methods, along with the actual rig design proposed for this study. In Chapter 4 friction is identified as a source of rig inaccuracy as it interferes with the force tracking of the MIL suspension actuator. Friction compensation methods are reviewed in the section and a novel friction compensation approach is proposed and tested experimentally. Chapter 5 contains an analysis of the test rig performance for various testing conditions. Chapter 6 presents validation of quarter car experimental results which indicate the rig performance in terms

of accuracy and stability by comparison with the ideal emulated system. In Chapter 7 experiments are conducted using a flexible sprung mass structure for passive, semi-active and active suspensions. The results are anlaysed and shown that the hybrid numerical-experimental test rig is capable of capturing the characteristics of semi-active and active suspensions. Conclusions and discussion on the direction of future work in presented in Chapter 8.

2. Vehicle Suspension - A Background

2.1 Introduction

A vehicle suspension is a system of components which supports the weight of the vehicle and provides a suitable ground clearance. In addition to structural support the two main objectives of suspensions is to isolate the vehicle body from road undulations and to maintain contact between the road and tyres. Typically, a vehicle suspension system consists of springs, dampers and possibly actuators. Suspensions also transmit lateral and longitudinal forces from the tyre to the vehicle body during manoeuvres such as cornering, acceleration and deceleration.

The wheel and axle unit is referred to as the unsprung mass and consists of components whose weight are not supported by the suspension such as the wheel, tyre, brake components and parts of drive shafts and steering linkages. The vehicle body is referred to as the sprung mass which consists of all the vehicle components whose weight is supported by the suspension such as the vehicle frame, engine and passengers.

The two primary suspension objectives of sprung mass vibration isolation and the minimisation of tyre load fluctuations present conflicting objectives. Sprung mass vibration isolation is generally considered to be a measure of ride comfort while contact between the tyre and road, a measure of handling performance [7]. By maintaining an appropriate contact force between the tyre and road this ensures that there is sufficient traction for acceleration, braking and cornering.

The ride and handling characteristics of the vehicle are dependent on the tyre characteristics, unsprung mass, suspension components characteristics and also the configuration of the suspension geometry. It is common in vehicle suspension literature to approximate the suspension system using a quarter car model, as shown in Figure 2.1. Here the geometry of the suspension is considered as a two degree of freedom model with strictly vertical motion, although in reality there may be other degrees of freedom which typically involve small displacements and are considered negligible.

Vibrations caused by the irregularity of the road profile are transmitted through the tyre, wheel and suspension to the vehicle body. The vehicle suspension produces a force which acts in the opposite directions on the vehicle sprung and unsprung mass. This means that sprung mass vibration isolation and tyre ground contact force minimisation represent conflicting demands which can only be theoretically overcome if the sprung and unsprung mass were equal in inertia and vibrating completely in phase. Unfortunately this is not the case as the sprung and unsprung masses are different by at least an order of magnitude and the two modes of vibration, in phase and out of phase, occur at different frequencies. Furthermore the resulting vibration is neither completely in phase nor out of phase but is a combination of the two vibration modes. The significance of this is that there exists an optimal trajectory whereby improvements in comfort or handling could not be improved upon without a trade-off between the two.

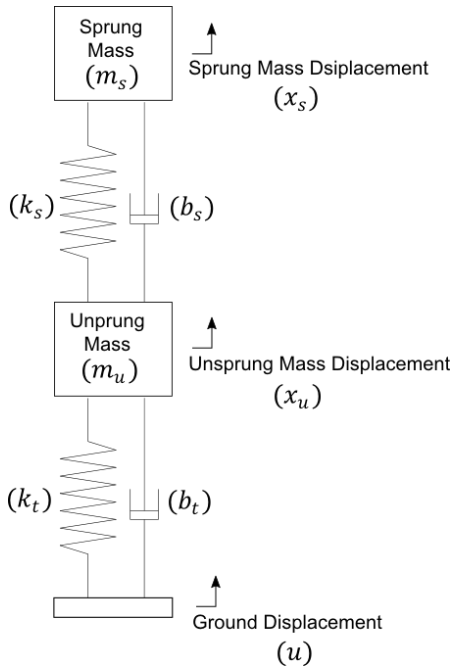

Figure 2.1 – Quarter car Model.

2.2 Types of Suspension

The relatively recent development of suspension systems with control capability has led to the categorisation of suspension systems generally in terms of passive, semi-active and active suspensions. Passive suspensions are the traditional type of vehicle suspension consisting of passive springs and dampers whose characteristics are fixed. A conventional passive suspension system has the ability to store energy via a spring and to dissipate it via a damper. For passive suspensions, good ride comfort requires a soft suspension, while good handling and high load carrying capacity requires a stiff suspension. Passive suspensions are therefore off-line tuned to attain a level of compromise between the conflicting requirements depending on the desired application.

Active and semi-active suspensions can overcome the constraints of a passive suspension by varying the force generation properties of the suspension. The suspension force is normally controlled in response to feedback of the vehicle states such as sprung mass velocity or suspension deflection. This allows the suspension to be controlled to achieve the desired compromise between various performance trade-offs as a direct response to actual vibrations caused by the road irregularity.

Semi-active suspensions have dampers with a variable damping coefficient which can be altered on-line in real-time [8]. Typically the variable damper is controlled externally by a command signal; how the variable damping is achieved depends on the type of semi-active damper that is utilised. Semi-active systems generally have low power consumption and are safe in the case of semi-active damper failure which simply results into a passive suspension system. Semi-active dampers cannot input energy into the suspension system but can vary the energy dissipation characteristics of the suspension.

Active suspensions use an actuator to input energy into the suspension system meaning that the vehicle can be lifted [3]. This enables force control of the suspension system allowing greater performance and control over the body and wheel motion such that the conflicting requirements of ride and handling are better managed than with semi-active suspensions. The inevitable drawbacks of the active systems are associated with the higher weight, size, power consumption and failure modes.

Within each type of suspension architecture whether passive, semi-active or active there are numerous types of suspension components that can be utilised. These include various types of passive springs, passive dampers, semi-active dampers, and active actuators.

2.3 Passive Suspension

The performance of the passive suspensions is often studied using the quarter car model as depicted in Figure 2.1. Quarter car models have been shown to represent vehicle suspensions with good accuracy and its simplicity allows useful analytical insights into the performance and limitations of suspensions [3]. Generally, the tyre damping is taken to be zero as tyre damping in vehicles is very low and has negligible effect [3]. A passive suspension has two natural modes of vibration since it has two degree of freedoms. The lower frequency mode associated with in-phase vibration between the sprung and unsprung mass is referred to as the body hop mode. The higher frequency mode associated with out of phase vibration is referred to as the wheel hop mode. The wheel hop frequency will always be greater than the body hop frequency as the unsprung mass is connected to two springs on either side, resulting in a combination of stiffness, while the sprung mass sees two springs in series with a reduced effective stiffness. In addition, the body mass is generally an order of magnitude higher than the wheel mass.

Figure 2.2 illustrates the effect of suspension damping on the sprung mass and the tyre deflection frequency response. As damping is increased sprung mass vibration isolation at the sprung mass natural frequency improves at the expense of worse performance between the body and wheel hop frequency and also beyond the tyre hop natural frequency. Suspension damping cannot supress the sprung mass vibration at the tyre hop frequency due to the two masses vibrating out of phase. In terms of tyre deflection, higher damping reduces both natural frequency peaks, but worsens the performance in the range between the natural frequencies. For frequencies beyond the wheel hop, damping has relatively little effect of the tyre deflection frequency response.

Figure 2.3 shows the normalised dimensionless root mean square (RMS) of the sprung mass acceleration and suspension travel across the frequency range. The plot reveals a number of trade-offs that occur in a passive suspension. There is a trade-off between sprung mass vibration isolation and suspension travel. This is shown by an increase in suspension stiffness leading to a reduction of suspension travel but an increase in sprung mass vibration. Another trade-off is the increase of suspension damping up to the minimum point on the curve; here there is a trade-off between sprung mass acceleration, suspension travel and also tyre deflection. Beyond the minimum point increases in damping worsens both passenger comfort and suspension travel.

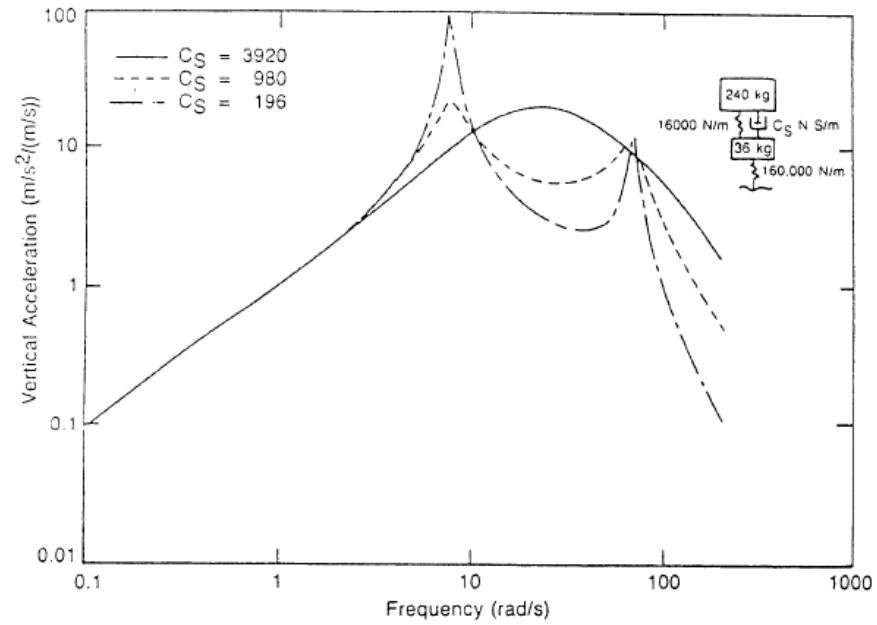

a. Vertical acceleration response

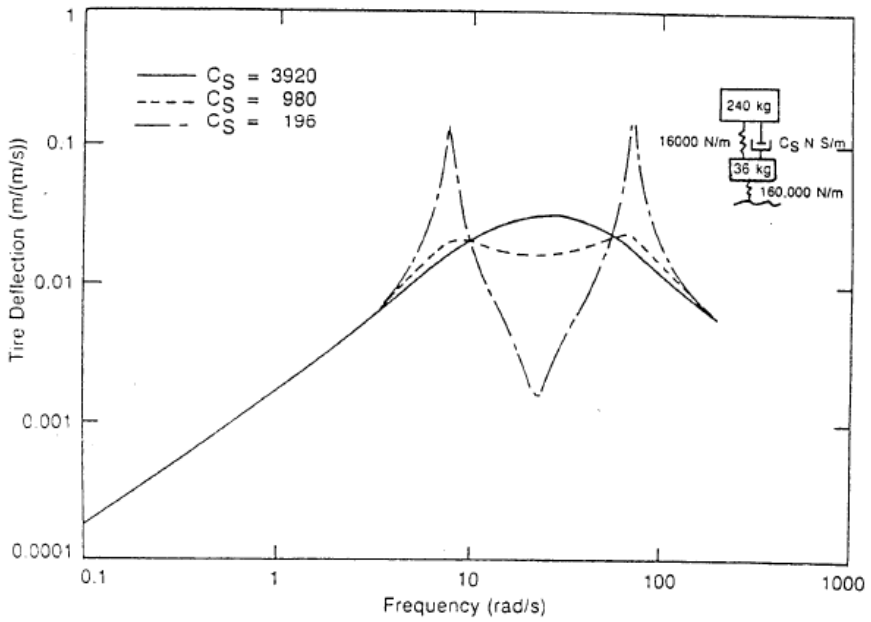

b. Tire deflection response

Figure 2.2 – Effect of damping on sprung mass acceleration and tyre deflection frequency response [9].

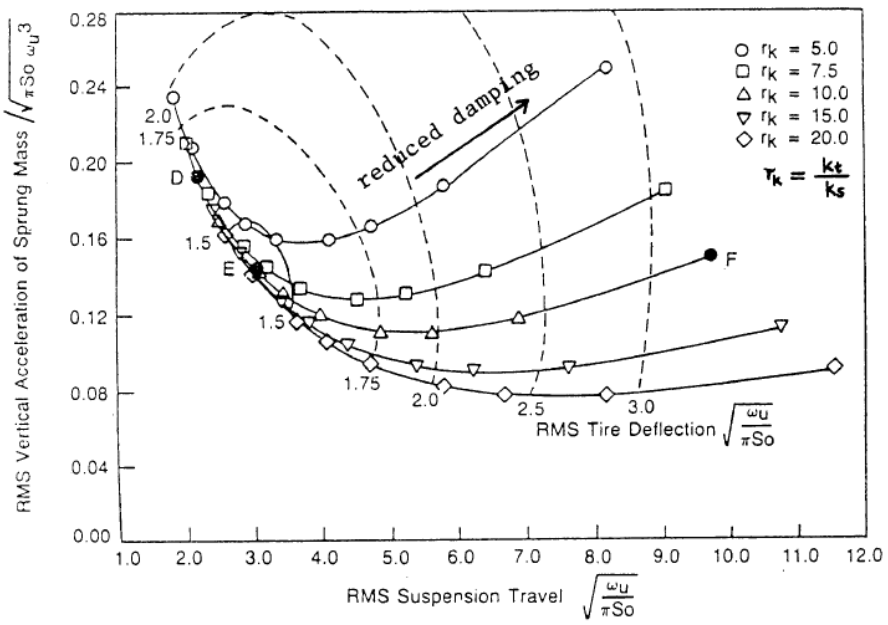

Figure 2.3 – Effect of varying suspension stiffness and damping [9].

2.4 Active Suspension

In active suspensions, the limitations of the passive suspensions can theoretically be overcome by inputting energy into the suspension system. This is achieved by adding an active actuator to the suspension which allows force generation independent of suspension motion. The actuator is controlled to deliver a force determined by the suspension control strategy. Depending on the control objective and sensor measurements available, the suspension force can be a function of system states such as sprung mass velocity or suspension displacement. A mechanical diagram of an active suspension is shown in Figure 2.4.

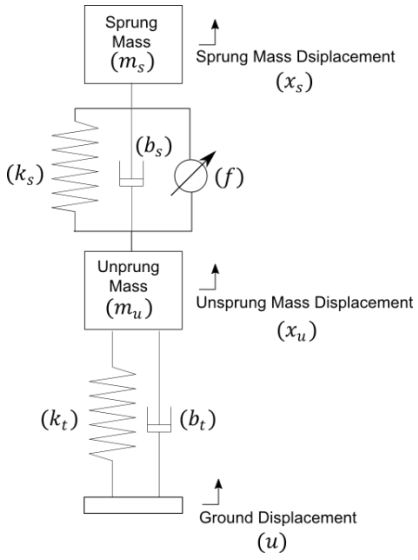

Figure 2.4 – Active quarter car suspension.

Although active suspensions can overcome the trade-off between sprung and unsprung mass vibration isolation when compared to the passive suspensions, this is not possible at the wheel hop frequency. At the wheel hop frequency the masses vibrate out of phase, meaning that the suspension force may only supress vibration of either the sprung or unsprung mass. This can be demonstrated by the equation of the quarter car model, given by the summation of sprung mass and unsprung mass equations of motion,

$$m_s\ddot{x}_s + m_u\ddot{x}_u + k_t(x_u - u) = 0 \tag{2.1}$$

Here m_s is the sprung mass, m_u the unsprung mass, x_s is the sprung mass displacement, x_u the unsprung mass displacement, k_u and b_u are the suspension stiffness and damping, k_t and b_t are the tyre stiffness and damping. By taking the Laplace transform of the equation of motion, the magnitude gain of the sprung mass acceleration to ground disturbance velocity reveals an invariant point,

$$\frac{\ddot{x}_s(j\omega_u)}{\dot{u}(j\omega_u)} = \frac{\sqrt{m_u k_t}}{m_s} \tag{2.2}$$

The invariant point occurs at the wheel hop frequency, ω_u, where,

$$\omega_u = \sqrt{\frac{k_t}{m_u}} \tag{2.3}$$

This invariant point is independent of any suspension force and only exists for the case where there is no tyre damping force [10]. Nevertheless the invariant point demonstrates the inability of any suspension force to effectively reduce sprung mass vibration at the wheel hop frequency region. Figure 4.5 shows the frequency response of an example automobile active suspension compared to a passive suspension. It can be seen from the plot that sprung mass vibration isolation is unachievable at the wheel hop frequency. Other control strategies which aim to reduce the unsprung mass vibration, such as groundhook control, can reduce the wheel vibration at wheel hop frequency [11].

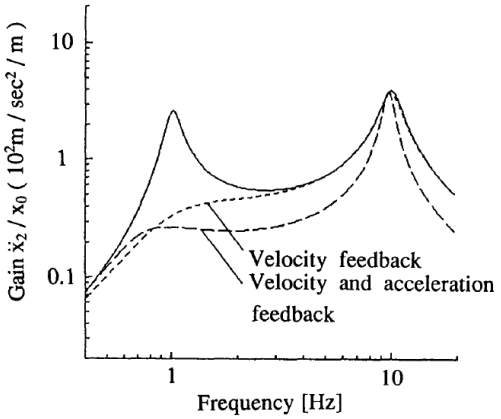

Figure 2.5 – Sprung mass vibration comparison for active and passive suspension [10].

In addition to vibration isolation capabilities, active suspensions allow vehicle attitude correction during manoeuvres such as accelerating, braking and cornering. Active suspensions also allow the dynamic control of ride height in configurations where a spring is used in series with a hydraulic actuator.

The various types of active suspensions may be categorised according to their frequency bandwidth. These are often separated into “fully active suspension” and “slow active suspension” [12], with frequencies of above and lower than 8Hz respectively [13]. Suspensions with the capability of changing ride height but unable to actively isolate vibration are termed load levellers. These may employ actuators and have been historically achieved using pneumatic and hydro pneumatic levellers [12].

2.5 Semi-Active Suspension

The concept of semi-active suspension systems was first introduced by Karnopp and Crosby in the early 1970s, using the well-known skyhook control algorithm and variable dampers [2]. Semi-active systems are unable to input energy into the suspension system. They vary the characteristics of the passive components, normally the damping coefficient but sometimes through the variation of the spring stiffness. Semi-active damper systems only change the force/velocity characteristics of the damper and affect the energy dissipation characteristics of the suspension relative to its motion. This is achieved by supplying a small amount of energy to operate a mechanism that adjusts the level of damping, the adjustments normally occurs at relatively high frequencies [12].

Suspension control strategies evolve around determining the desired suspension force based upon the conflicting suspension requirements; these strategies are directly applicable to active suspensions. Due to its energy dissipation property, semi-active dampers can only produce the desired control force when the suspension motion allows. This means that semi-active control algorithms switch to minimal damping when the damper force is acting in the opposite direction to the desired control force. Many studies have demonstrated using analytical methods how semi-active dampers compare with their passive counterpart in terms of vibration isolation [9, 8]. Furthermore studies have shown that semi-active systems can achieve nearly the same performance as fully active systems, but with much lower cost and a complexity similar to that of passive suspensions [12, 8]. The energy dissipation nature of dampers ensures that stability problems that can occur with active suspensions are not possible in semi-active systems.

Variable damping mechanisms are normally separated into two types, those that act in two states (on/off) and those that are continuously variable. Figure 2.6 shows the mechanical equivalent diagram of a semi-active variable damping suspension. A review of semi-active suspension research can be found in [8, 10, 12]. Figure 2.7 shows the typical frequency response plot of a semi-active suspension applying skyhook control compared with passive suspension. The plot shows that the semi-active suspension is able to achieve the best aspects of a lightly damped and highly damped suspension in terms of sprung mass vibration isolation, overcoming the trade-off characterised by passive suspensions.

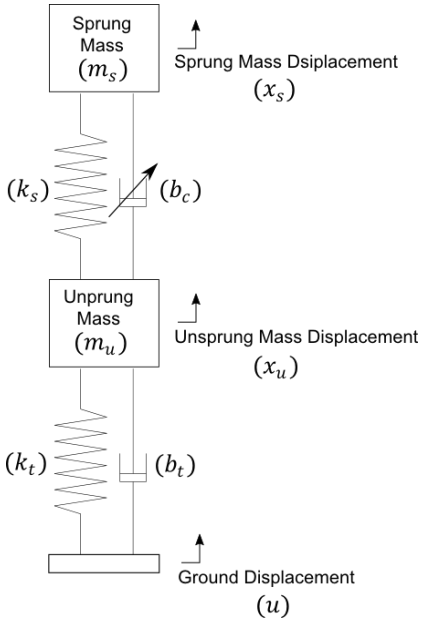

Figure 2.6 – Mechanical diagram of variable damping semi-active suspension.

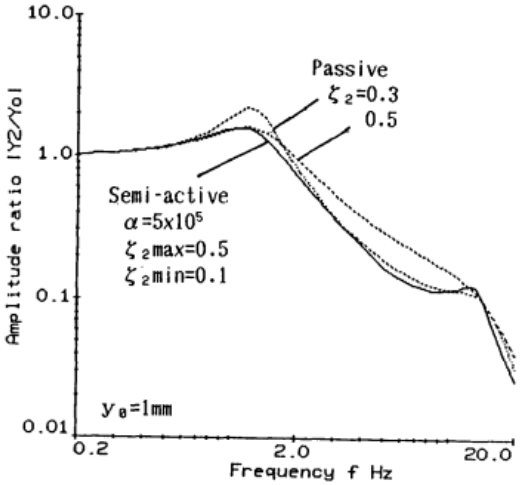

Figure 2.7 – Performance of semi-active skyhook suspension compared to hard and soft damping [10].

2.6 Springs

The choice of a suspension spring depends on many factors that the designer has to take into account such as weight, suspension travel, load variation and space envelope. The typical types of springs employed on vehicles are coil springs, leaf springs, torsion bars and gas springs.

Generally the force/displacement characteristics of coil springs are approximated as linear if they exhibit a uniform coil. However coil springs could be designed such that they exhibit non-linear behaviour. This can be achieved by varying along the length of the spring, the coil diameter, spring diameter and the spring pitch. Examples of non-linear coil springs are conical springs which are cone shaped [14]. Leaf springs are well known to be non-linear due to the nature of beam bending, contact between the spring leaves and hysteresis due to friction effects [15]. Torsion springs exhibit a non-linear behaviour in vehicle suspensions due to the translation of torque which varies linearly with rotational angle into force in the vertical direction. Gas springs are also non-linear due to the thermodynamic properties of gas compression and expansion. The characteristic of each spring will vary depending on the type of spring and the details in their design.

2.7 Dampers

Dampers are the mechanical devices responsible for energy dissipation in suspension systems. Most vehicle dampers operate using turbulent orifice flow where the pressure drop is associated with the resisting shear force caused by squeezing fluid through a small gap. Dampers normally use mineral oil but more recently smart fluid dampers, which allow the control of damping forces such as electrorheological and magnetorheological dampers have, been studied extensively for semi-active suspension application. Other unusual types of dampers for vehicles include those that are based on dry friction; these employ variable damping since fixed frictional dampers have poor performance [16].

2.7.1 Hydraulic Shock Absorbers

Most vehicle dampers are passive hydraulic shock absorbers. Normally these consist of a cylinder, rod and piston containing a Belleville washer valve. The restriction of fluid flow through the piston valve creates a resisting shear force between fluid layers, which is commonly modelled to be proportional to velocity. Two common designs of commercial shock absorbers are the monotube and twin-tube shock absorbers [17].

2.7.2 Variable Orifice Hydraulic Shock Absorber

As traditional suspensions already utilise hydraulic dampers, minor modification of these systems can be achieved relatively simply. The variable orifices can either be integrated in the damper cylinder piston or in an external bypass, which often is constructed in the form of a ring channel. The orifice adjustment is often achieved using an electric motor or by means of electromagnetic valves [18].

The majority of early studies focused on a simple form of on-off control using solenoid valves, where damping was varied between two states of high and low damping [19]. Like active systems, on-off semi-active dampers are classed as high or low bandwidth. Usually in slow bandwidth systems the damper rate is set high to optimize vehicle control and handling during cornering, and set to a soft setting when subjected to road disturbances. Commercial application of such slow semi-active on-off hydraulic systems is reported to have been implemented in certain models of Mercedes and Opel cars, the semi-active dampers are provided by Bilstein and Delco respectively [17]. Koni, a manufacturer of dampers, have a product fitted with on-off variable damping, termed FSD (Frequency Selective Damping). The system selects between low or high damping depending on the objective of comfort or handling [20].

One of the earlier experimental studies of high bandwidth semi-active dampers showed that chatter is a real problem, exhibited by rapid switching between on-off damping states, controlled as a function of the instantaneous dynamic state of the system [21]. This chatter is undesirable due to possible damage to the control valve caused by the fluctuating high frequency acceleration. They proposed a control based solution which reduced chatter and achieved an acceptable but limited suspension performance at high frequency. Experimental investigations by Nell and Steyn used a relatively unsophisticated damper by creating a bypass for a control valve [22]. Highly non-linear valve dynamics were reported to be a function of damper velocity and direction of state switching. Even with these issues the damper showed good vibration isolation performance on a single degree of freedom test rig with a time delay ranging from 42.2 - 61.1 ms.

More complex forms of continuously variable damping rate have also been extensively studied. Experiments using a continuously variable damper controlled by an internal valve in a Hardware-in-the-Loop (HIL) test rig showed that the performances of on-off and continuously variable systems are comparable [23]. However the on-off condition was able to use less suspension working space but at the expense of larger body accelerations. Comparable performance between on-off and continuously variable damping was also illustrated experimentally using hydraulic shock absorbers [24] and more recently through numerical simulation [19]. Test results on the continuously variable damper showed 21 percent improvement in the dynamic tyre force and a 28 percent reduction in body acceleration when using full state feedback and 13 and 22 percent when using a modified skyhook scheme [23]. A limitation of experiments was that although the HIL test was conducted for a heavy truck, their damper was for a typical car, and the issue was resolved by scaling up the damping force [23].

Extensive testing of a variable damper specifically for a heavy vehicle was undertaken by Kitching, Cole and Cebon [25]. A prototype variable damper was constructed and the damping rate was controlled by a proportional spool valve. HIL test results showed that the main benefits with the Modified Skyhook Damper controlled semi-active damper were achieved mainly at the low frequency body hop mode. The semi-active damper reduced the RMS body accelerations by 12.3 percent, 10.2 percent, and 5.2 percent for the motorway, principal and minor roads respectively. The variable damper was capable of delivering forces of up to 18 kN and successfully dealt with instantaneous velocities approaching 1 ms^{-1} and generated a continuously variable damping coefficient in the range 2 $kNsm^{-1}$ to 150 $kNsm^{-1}$. Control of the spool position of the proportional valve was found to be susceptible to the pulsating oil flow forces generated by the excited damper. A simple compensation strategy which demanded a solenoid current approximately proportional to

the absolute oil flow rate through the valve significantly reduced this undesirable effect. Closed-loop control of the damper force was realized using a linear PID force feedback strategy. A time delay of 25 ms was measured in the damper when responding to a 10 kN transient in the demanded force. A non-linear damper model, which included valve dynamics and effects due to oil compressibility, provided an accurate representation of the prototype damper for frequencies up to 15 Hz.

A considerable number of semi-active dampers have been found in commercial automobiles. The Continuous-Damper-Control (CDC) system from Sachs is one of the commercial state of the art variable damper systems [18]. The damper contains a proportional valve and has continuously variable switching times between 11 and 40 ms depending on the piston's direction and velocity, and also on the direction of the switching. According to [17], Sachs CDC are found in BMW series 7, VW Phaeton, VW Toureg, Audi A8, Lancia Thesis and Porsche Cayenne. Bilstein is another manufacturer of semi-active dampers of both continuously variable and on-off types. Their systems have been adopted in the Porsche 959 street model, Corvette ZR1 and Ferrari [17]. Another manufacturer of semi-active dampers is Tenneco Automotive, their suspension is reported to be capable of approximately 10 ms delay which would allow effective control of both the wheel and body hop. These suspensions have been found in the Audi A6, Volvo S60R, V70R and the S80 [17].

Semi-active damping experiments have also been applied to aircraft landing gear. A semi-active landing gear drop test employing high speed servo-vales was conducted by replacing a standard oleo pneumatic landing gear with a cylinder and a single acting jack [26]. Two hydraulic accumulators were used, one to restore the characteristics of the original landing gear and another to drive the servo-valve which regulated the orifice area. The servo-valve used was a commercial MOOG unit (Mod.D760), with four channels and a bandwidth of 40 Hz. The system was used as a low cost alternative for testing of the working principles of the device. The work confirmed the effectiveness of semi-active control of the shock-absorber in the reduction of strut load at landing and confirmed the result of simulations.

2.7.3 Electrorheological and Magnetorheological Shock Absorber

Developments of electrorheological (ER) fluids [27] and magnetorheological (MR) fluids [28] began independently in the 1940s. Both are kinds of smart fluid, made by mixing fine colloidal suspensions of polarizable particles into a liquid with low viscosity. The particles form into chain-like fibrous structures in the presence of a high electric field or a magnetic field as illustrated in Figure 2.8. The effect of the chainlike structure is to increase the fluid resistance to flow through shear stress such that the fluid develops a yield stress which has to be overcome to induce fluid flow [29]. The suspension can be liquefied nearly instantaneously by removal of the electric field or the magnetic field. The ability ER and MR fluids to rapidly alter flow resistance make them an attractive candidate for the application of mechanical dampers.

Research in ER and MR fluids were scant after the initial discovery until a resurgence of interest beginning in the early 1990s when MR fluids were 're-discovered' [29, 30]. Although substantial progress was made in the development of ER fluids, engineering devices based upon ER fluids remained in prototype and commercialization was never achieved [29]. However, MR fluids achieved a significant commercial application in 2002 when MR dampers were incorporated in Cadillac Seville STS automobiles [29].

The reason behind the commercial success of MR dampers when compared to ER dampers is the differing properties of the two fluids. The main advantages of MR fluids over ER fluids are that, MR fluids have higher yield stress than ER fluids, require a lower voltage power supply, and have a broader operating temperature range [31]. Table 2.1 shows a comparison of the properties of ER and MR fluids.

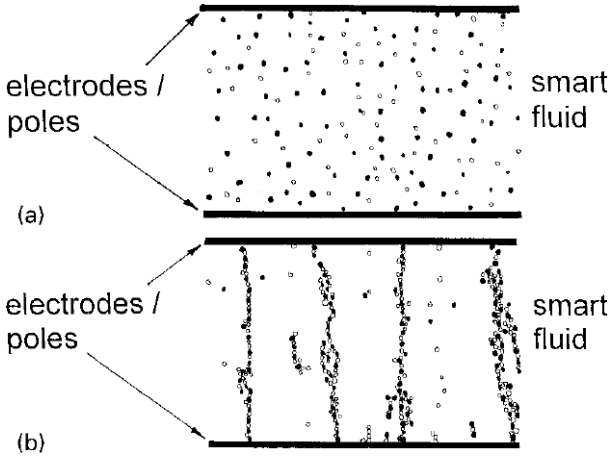

Figure 2.8 – Structure of smart fluid. a) no field applied b) significant field applied [29]

Property	MR suspension	ER fluid
Maximum yield stress	50–100 kPa	2–5 kPa
Maximum field	~250 kA/m	~250 kV/m
Apparent plastic viscosity	0.1–10 Pa s	0.1–1.0 Pa s
Operable temp. range	−40 to 150 °C	−10 to 90 °C
Density	3–4 g/cm^3	1–2 g/cm^3
η/τ_0^2	10^{-11} to 10^{-10} s/Pa	10^{-8} to 10^{-7} s/Pa
Maximum energy density	0.1 J/cm^3	0.001 J/cm^3
Power supply (typical)	2–50 V; 1–2 A	2000–5000 V; 1–0 mA

Table 2.1 – Comparison between MR and ER fluids [32].

The rheological property of MR fluids depend on many factors, among them are the concentration and density of the particles, particle size, particle shape and the choice of carrier fluid [31]. The major criteria for selecting the particle material for MR dampers are high magnetic saturation and low coercivity such that highest damping forces and most rapid demagnetization is achieved. An investigation into MR fluids showed that contaminants in the MR fluid, although important, are not critical to the damper's performance [30]. In the absence of a field, both ER and MR fluids have similar viscosity and are a function of the carrier oil, suspension agents and particle loading. Particle settling is shown to occur at very slow rates for MR fluids [33], furthermore this is not a major concern for automobile suspensions where there is constant mixing of fluid particles while in operation. One barrier to the widespread adoption of MR fluids and dampers is the problem of in-use thickening as reported by Carlson [34].

Another difficulty in the implementation of the control of smart fluid dampers lies in their significantly non-linear nature [35]. MR and ER fluids behave in a similar manner and share common mechanical models [29]. MR fluids are shown to have hysteresis in terms of force-movement and force-velocity relationships [29]. The yield stress nature of MR fluids can be described using a Bingham plastic model but this does not capture the dynamics of the hysteresis effects.

In order to fully capture the characteristics of the MR damper numerous models have been developed. Spencer et al. proposed a modified Bouc–Wen model to describe the MR damper behavior [36]. This model which involves as many as 14 parameters can accurately capture both the force–displacement and the force–velocity hysteresis loops. Kamath and Wereley developed an augmented six-parameter model to accurately describe both the force–displacement and the force–velocity hysteresis cycles [37]. This was constructed using a non-linear combination of linear mechanisms. Li et al. also proposed a non-linear viscoelastic–plastic model to describe the dynamic behaviours of the MR damper with good results under sinusoidal excitation [38]. Choi et al. proposed and compared a polynomial based model against the Buoc Wen model with experimental results showing the model's superior performance in open loop control [39].

The Lord Corporation is a commercial producer of MR fluids and MR dampers. Many academic researchers have based their experiments on MR dampers supplied by Lord Corporation. The product bulletin of Lord Corporation claims that their damper response time is less than 60 ms for a 180 kN MR damper [40]. The MagneRide^{TM} system, now part of Beijing West Industries, Ltd., incorporates MR fluid supplied by Lord Corporation and has been fitted into vehicles such as the Audi TT, Audi R8, Buick Lucerne, Ferrari 599GTB and Holden HSV Commodore [41]. The MagneRide^{TM} system was initially developed by Delphi Corporation which includes implementation in the 2002 Cadillac Seville STS [42]. Here Delphi claims that the MR fluid has a response time within 1 ms. Although MR fluids have very fast response times within 1ms, the real response time of MR dampers are dominated by the inductance of the electromagnets and the impedance output of the driving electronics resulting in response times ranging from 20ms to 200ms depending on operating conditions [42].

MR dampers have been suggested for many applications where large damping forces are required. Other than automotive applications, the MR damper has been suggested for civil engineering applications [43, 44]. The MR damper has also been proposed for aerospace application [45]. Currently the principal handicap of such fluids and the barrier to their widespread commercial acceptance in many areas is still their relatively high cost, difficulty in control due to non-linearity and hysteresis, durability and fluid thickening after extensive usage.

2.8 Active Suspension Actuators

Active suspension systems can be divided into two types according to their bandwidth. Suspensions with high bandwidth can react to higher frequency components of the road disturbance and thus offer higher performance. However, this usually results in an increase in power consumption and computational effort, and requires high broadband actuators. The main obstacle for commercialisation of such systems is the significant power requirement and fast response, which for hydraulic systems requires costly precision manufacturing. In addition, the sensitivity to contamination suffered by electrohydraulic valves often renders such technology inappropriate for road going cars. In order to reduce the cost and power of active suspensions, practical designs generally function as a low-bandwidth system that requires peak powers of the order of 4 kW for road vehicle applications. Lower bandwidth systems are effective with regards to lower frequency disturbances around the body hop frequency but cannot react swiftly to high frequency components.

2.8.1 Hydraulic Actuators

The most obvious means of actuation first explored by engineers in the field was through hydraulic actuation. Hydraulic systems are a mature technology and are readily available commercially. In a fully active design, a hydraulic active suspension system may be realized simply by replacing the passive hydraulic damper with a hydraulic actuator. In a partially active system the passive damper remains and a hydraulic actuator can be placed in series with the passive spring. The biggest advantages of hydraulic systems are their high force to weight ratio when compared to their electromagnetic equivalent. Due to technology maturity, the design processes are simpler and off the shelf components and proven electrohydraulic control systems are readily available [46]. Hydraulic systems are also highly reliable as proven in various fields, especially those requiring high power.

Very sophisticated and high bandwidth hydraulic systems are more difficult to implement because rapid dynamic response is hard to achieve due to pressure losses, flexible hoses and valve dynamics [46]. The non-linear nature of hydraulic actuators and the coupling between cylinder pressures and vehicle dynamics make active control difficult, hence, many active hydraulic suspensions found in literature have limited bandwidths of 2-4 Hz [47]. In durability test applications hydraulic actuators have been shown to achieve bandwidths of over 50 Hz although the control goal was displacement as opposed to force control, suggesting that for hydraulic actuators “force tracking” is difficult [47]. Due to the demanding requirement of active suspensions, hydraulic systems have been reported to be expensive and high in energy consumption [48].

Two hydraulic suspension systems have been successfully implemented and are currently available on a commercial level in the automotive field. Only one system is an active suspension in the traditional sense - a partially active system called Active Body System developed by Mercedes [18]. Subsequent work reported that the Mercedes Active Body Control (ABC) suspension system uses low-bandwidth hydraulic actuators with a peak power consumption of 4 kW and controlled using the skyhook algorithm [49, 50]. Here a hydraulic actuator is applied in series with a spring and the active system is capable of correcting low frequency vehicle attitudes of pitch and roll up to 2 Hz, and isolation of road induced vibrations up to 6 Hz. The BMW dynamic drive system incorporates a

rotational hydraulically actuated active anti-roll bar which operates in conjunction with semi-active dampers [18].

Another well-known implementation is the Lotus active suspension developed in the 1980s for use in their Formula 1 racing cars [51]. Despite the sporting success the active suspension enjoyed, when Lotus patented the technology and tried to develop a commercially viable version of the active suspension they were unsuccessful. This was due primarily to the difficulty of producing low cost, high performance electrohydraulic valves. Another promising system is the suspension developed by the Visteon Corp, which uses hydraulic struts and a positive displacement pump/motor unit with power regeneration capabilities and frequency domain control [50].

In the aviation field, the active suspension concept was tested by NASA in the late 90s [52]. The landing gear of the A-6 Intruder aircraft was modified by drilling holes in the upper and lower chamber and connecting high and low pressure reservoirs so that fluid could enter or exit the chambers. Two electro hydraulic servo valves with frequency responses approaching 100 Hz were used to control the flow. Test results showed a fourfold fuselage vibration reduction. Despite the performance gains, the system required a high maximum flow rate of 1.6 litres/s resulting in large accumulators and hydraulic pumps. Problems of high friction levels were noted by the researchers as the main hindrance to performance improvement and they commented that a major redesign of the landing gear was likely to be required.

2.8.2 Electromagnetic Actuators

Electromagnetic systems have a number of advantages over a hydraulic alternatives. These include higher bandwidth of the actuator, higher controllability both in terms of force and displacement and the absence of fluids and therefore leakages [46]. Unlike hydraulic systems, the power consumption of the system is discontinuous and a current is supplied to the motor only when a force is required. Also, the forces produced by an electric motor are identical in both compression and extension. Traditional motors must translate rotation into linear motion using ball screws or other mechanisms, and also normally involve gearing to increase the torque output. This motion conversion would normally introduce complications such as non-linearities associated with backlash and increased weight. The development of electric motors has rapidly advanced, helped by improvements in electronics, leading to increasingly powerful and efficient linear motors with precise control of motion and force, packaged in a small unit and eliminating the need for rotational motion translation [48].

Despite the many benefits of electromagnetic systems, many challenges remain in the delivery of commercially viable suspensions. The biggest issue is the relatively low power to weight ratio of electromagnetic systems, meaning that to achieve the same forces as a hydraulic system the electromagnetic suspension will require a greater system mass and volume [46]. Another downside of electromagnetic active suspensions is that in conventional designs, in order to affect the vehicle's attitude, a constant force is required. This means that changes in ride height and deviations from the vehicle's equilibrium position are very demanding in terms of energy consumption [46].

The Bose active suspension is one of the current prototypes whose excellent vibration isolation capabilities have been demonstrated. The system replaces the typical shock absorber with a high broadband linear motor. In an article by the company they explained that due to the absence of 'off

the shelf' motors and amplifiers which satisfy the size and power requirements, Bose were forced to develop their own [53]. The high forces required for fully active suspensions means that for electrical actuators operating on typical vehicle battery voltages of 12-14 V, large electrical currents are required [46]. Despite the potential for high power consumption due to the large currents, Bose claimed that the power consumption was reduced to a third of the 100 W typically required of a typical vehicle's air conditioning system [53]. Compared to the Mercedes ABC suspension, the Bose active suspension is significantly heavier, adding to the unsprung mass. This is undesirable in terms of vehicle dynamics and stability control [50].

Another fully active suspension showing great promise is the Electronically Controlled Suspension System (ECASS) developed by Texas University. The system was specifically designed for use with heavy vehicles and off road applications using rotary motors and a capacitor bank for energy regeneration [54]. The ECASS technology has been licensed to private companies and extensively tested in US military trucks. Most recently the ECASS system is being developed in conjunction with Horstman and L-3 for tracked combat vehicles with rotational suspension units, eliminating the need for translation of the motor output into linear motion [55]. The motor is connected to the road arm via a planetary gear set which improves the regenerative efficiency of the system.

2.9 Variable Stiffness Suspensions

While the modulation of the damping coefficient is commonly used and can be easily obtained with different technologies, the control of the spring stiffness is a more difficult problem [56]. It is well known that load-levelling or slow-active suspensions based on hydro-pneumatic or pneumatic technologies are subject to spring-stiffness variations, but the stiffness change is more a side-effect than a real control variable [57, 58, 56]. Karnopp and Margolis noted that considerable energy is required to change a linear spring constant when the suspension is supporting a load [59].

A more viable method of varying stiffness is by using non-linear devices such as an air spring. Although the research area of variable-damping-and-stiffness suspensions in a semi-active framework is still largely unexplored, it is not surprising that most literature on the architecture for variable damping and stiffness suspensions has focused on pneumatic springs.

Spelta et al. conducted a study of three different variable-damping-stiffness architectures shown in Figure 2.9 and found that they have comparable performance and controllability [56].

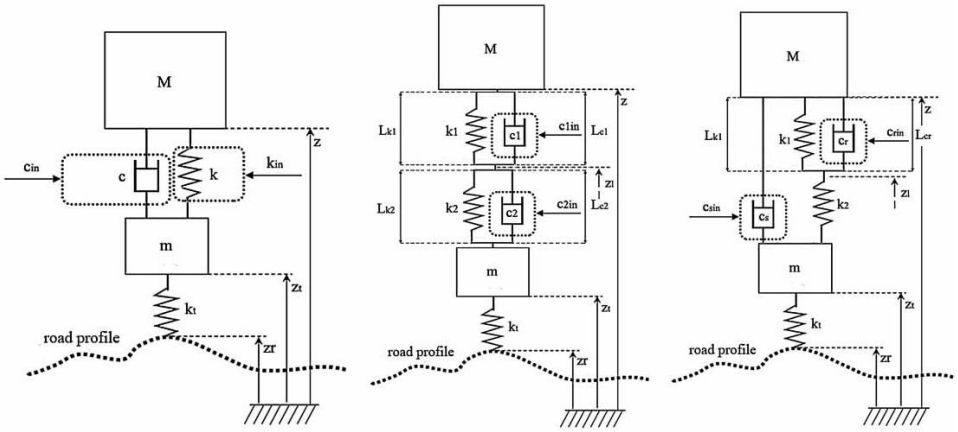

Figure 2.9 –1) Model 1: Ideal variable damping and stiffness suspension, 2) Model 2: Activation damper system (ADS), 3) Model 3: Double suspension system (DSS) [56].

Model 1:

Model 1 shows the mechanical diagram of an ideal semi-active suspension with variable damping and stiffness, where stiffness and damping are independently controlled.

Model 2:

If the damping coefficient $c1(t) \rightarrow \infty$, then the suspension system is reduced to an ideal quarter-car equipped with a classical semi-active suspension composed of the spring $k2$ and the variable damper $c2(t)$. Similarly, if the value of $c1(t)$ is comparable with $c2(t)$, the resulting suspension can be considered as an ideal quarter-car equipped with an equivalent spring given by the series of $k1$ and $k2$.

Model 3:

If $cr(t) \rightarrow 0$, then the suspension system is reduced to a standard semi-active system with the shock absorber $cs(t)$ and with an equivalent spring resulting from the series of $k1$ and $k2$. On the other hand, if $cr(t) \rightarrow \infty$ the equivalent suspension is made up of the spring $k2$ and the controllable damper $cs(t)$. The parallel variable damper and spring is sometimes referred to as a Voigt element.

Model 1 reveals the theoretical capabilities of a variable stiffness and damping system. However, Model 1 is difficult to implement physically with existing hardware. To this end Models 2 and 3 are simpler for practical implementation and are introduced as simplified approximations of Model 1. Figure 2.10 shows how the systems could be physically implemented and Figure 2.11 shows the performance of the two extreme configurations ($k = k\text{min}$; $c = c\text{min}$, and $k = k\text{max}$; $c = c\text{max}$) for the three different architectures. The bode plots are nearly indiscernible, confirming that the three suspension architectures provide the same results at the operating boundaries. Improved performance compared to variable-damping-fixed-stiffness systems was shown through analysis and simulation results.

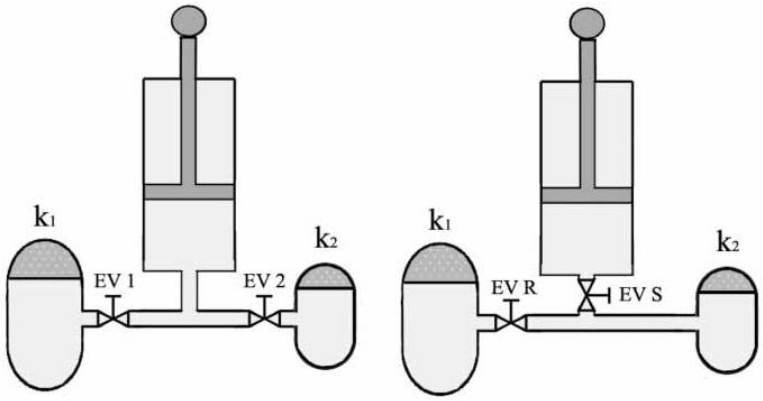

Figure 2.10 – Implementation of a DSS architecture (left) and an ADS architecture (right) [56].

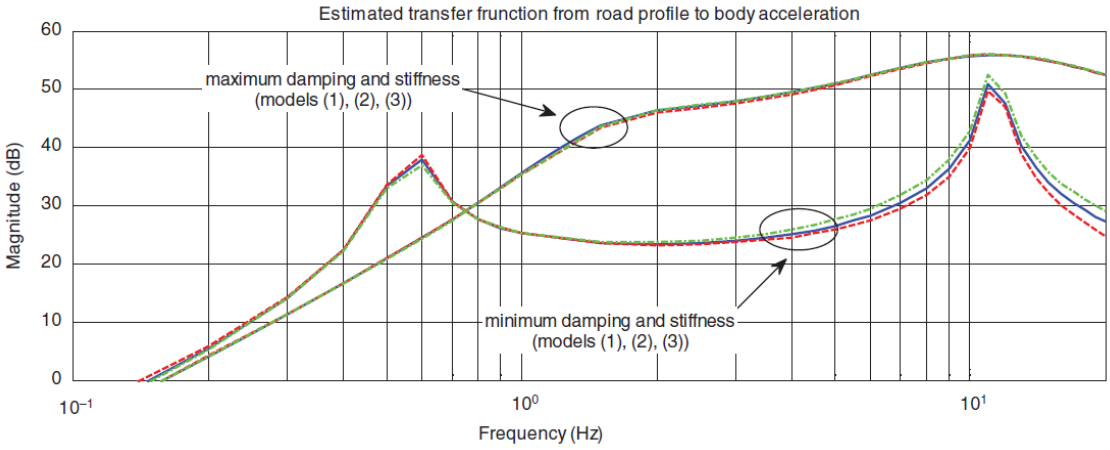

Figure 2.11 - Comparison of the bode magnitude plots in extreme configurations of the three suspension systems. Model (1), blue solid line; model (2), green dashed line; model (3), red dotted line [56].

One of the earlier studies of such variable stiffness suspension systems is illustrated in Figure 2.12 [60]. The suspension was able to vary stiffness to three discrete values and the stiffness was changed only when the desired control force could not be implemented by variable damping alone. The air spring consists of a main cylinder and two sub-chambers filled with pressurized gas, which are connected to the cylinder by air passages, each of which can be either opened or closed by the two valves. By opening and closing the airflow passages the effective volume of gas can vary to three different levels corresponding to both passages closed, one opened and both opened. This variation produces three distinct spring rates: soft, medium and firm. It should be noted that due to the loss of energy during the flow through the passages, the soft and medium spring rates have frequency dependent stiffness characteristics, showing hardening at high frequencies. This is because the quantity of air which can move from one volume to the other decreases with increasing frequency. The simulation results from the study demonstrated good performance when compared with semi-active suspensions with fixed stiffness.

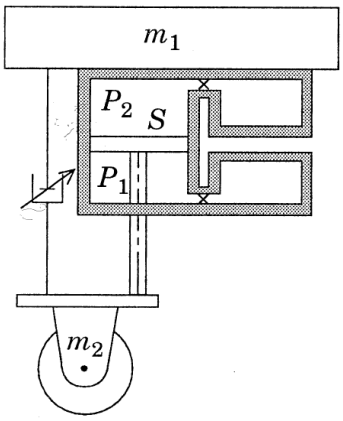

Figure 2.12 – Sketch of variable damping and stiffness mechanism [60].

A study of the performance of a similar semi-active variable damping and stiffness mechanism shown in Figure 2.13 was conducted by [57]. The high and low stiffness and damping characteristics are made possible by channeling hydraulic fluid with solenoid valves. The spring and damper units consist of a hydraulic strut (1), two gas filled accumulators (2 and 3), a hydraulic damper (4) and two solenoid valves (5 and 6). The low spring rate is achieved by compressing a large volume of gas in two separate chambers (2 and 3). By sealing off one of the chambers (2), a smaller gas volume (3) is compressed and a higher spring rate is achieved. Spring rates can be individually tailored by changing the two gas volumes. For low damping the hydraulic damper (4) is short circuited by opening a by-pass valve (5). For high damping this valve is closed and the hydraulic fluid is forced through the damper resulting in a high damping force.

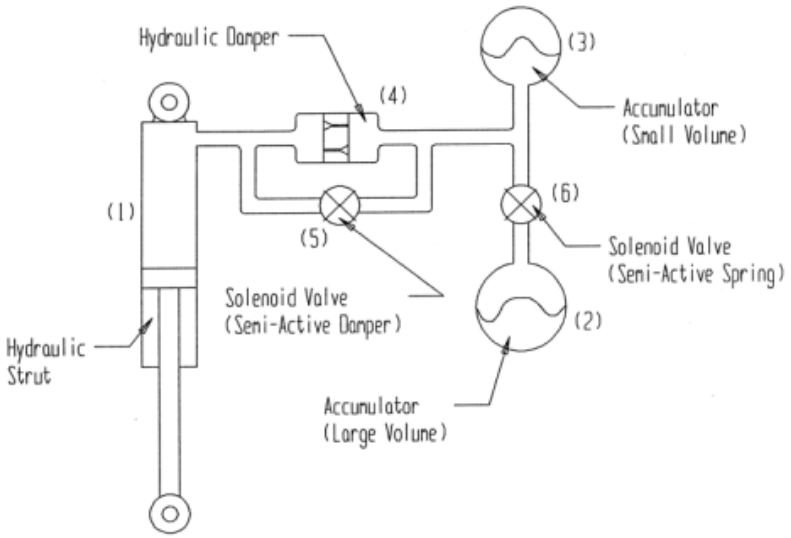

Figure 2.13 – Diagram of realisation of an ADS type suspension [57].

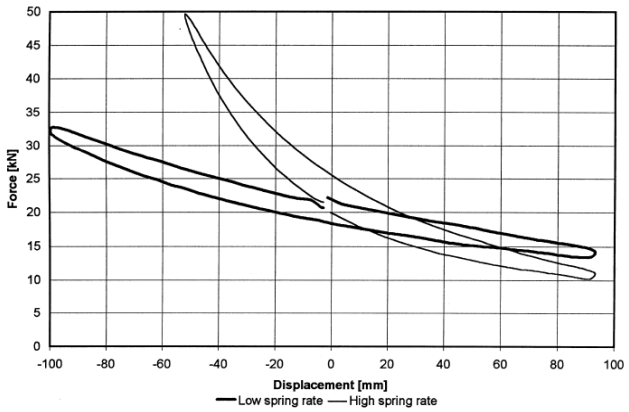

Figure 2.14 – Variable spring stiffness characteristic for system in Figure 2.13 [57].

A 160 kN Schenck hydraulic actuator was used to characterise the hydropneumatic spring and damper unit. This was done by measuring the force while compressing the spring. Figure 2.14 shows the result of the characterisation of both the hard (on) and the soft (off) spring settings. The hysteresis loop in the spring characteristic can be explained by the inherent damping effect of the hydropneumatic spring due to unavoidable heat exchange between the gas and the environment. This damping effect is dependent on the gas volume and pressure, the thermal time constant of the accumulator, the excitation frequency and the type of working fluid used. Since the desired spring force can be achieved by varying either piston area or gas pressure it is possible to design the hydropneumatic spring in such a way as to make optimal use of the thermal damping effect. The characterization of the spring was done at different excitation velocities using sinusoidal displacement inputs. Experimental tests using a practical realisation of the ADS architecture was achieved by using MR fluid dampers (RD 1097) provided by Lord Cooperation [61]. From the calculations and experimentation results, the authors concluded that the proposed control system has good performance for vibration isolation.

Although most research has focused on pneumatic springs, some studies have proposed other types of mechanism. An example is the torsional bar with discretely varying effective length is shown in Figure 2.15. In this design proposed by Kauer, a torsional bar features two discs, each of which can be interlocked with the body, preventing torsion of the remaining portion of the bar [60]. As a result the effective length, and hence the stiffness of the bar, may assume any of three different values.

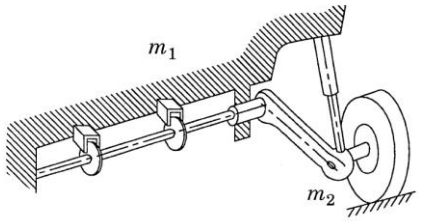

Figure 2.15 - Model including a torsional bar with variable effective length [60].

One semi-active variable damping and stiffness suspension currently available to road vehicles is the Citroen hydractive suspension [49, 62]. Citroen's hydractive suspension is a type of oleo-pneumatic

suspension with an architecture based on the ADS architecture (Model 2). There are four oleo-pneumatic spheres on each wheel of the vehicle, and solenoid valves which can interconnect the spheres with additional spheres. This is equivalent to connecting additional spring/damper units in series to effectively reduce both damping and stiffness.

2.10 Suspension Control

There are a number of issues that must be considered for the control of the suspension. The first distinction is between active and semi-active systems. Active systems can control ride height, correct vehicle attitude during maneuvers and react to preview information. The semi-active systems can only partially improve suspension performance in these aspects compared with a passive suspension. Since semi-active systems can only produce the desired force required by an active suspension for half of the time, generally semi-active systems utilize similar algorithms to active systems when possible and default to low damping when not. This approach to semi-active control by adapting active control laws has been termed the “clipped” control approach.

Initial developments of control strategies for active and semi-active suspensions were made with the assumption that the force producing element is perfect in the sense that there is no force tracking delay or errors. This method allows control engineers to investigate the ideal performance of various control strategies without having to consider the dynamics of the force producing element. Given this assumption of perfect actuators and linear springs and linear dampers, analyses of control methods are therefore commonly based on linear control theory.

Many actuators and variable dampers generally exhibit non-linear behavior which introduces difficulties into the control. Linear interpolation of these processes will only be valid under certain conditions. Typically, in conditions of extreme velocity, unpredictable results will be observed as a result of non-linearity [63]. Additionally, active suspension studies may use electric linear motors [64] as actuators to maintain linearity in the vehicle model. However, if the output cannot be written as a linear combination of its input, the system is said to be non-linear. Strategies for suspension control assuming perfect actuators have been extensively studied for many decades. These serve as an outer loop control strategy which calculates a desired suspension force based upon control objectives, road input and suspension motions. More recent work has focused upon how to implement force tracking given the practical limitations of the specific actuators and their dynamics.

2.10.1 Skyhook Control and Variants

Optimal control theory provides an important tool in obtaining the gains of full state feedback designs for active suspensions. However many test suspensions have not adopted optimal control mainly due to difficulties in implementation such as the sensing of some system states such as tyre deflection and also the limited bandwidth of actuators or limitations in processing speed. Therefore it is sometimes preferable to simplify the optimal strategies by only utilising a limited number of system states [3].

Optimal control has helped shed light on the effects of the various feedback gains and how they influence the conflicting multi-criteria goals. It was found that sufficient performance can be

achieved by using body velocity, suspension velocity and suspension deflection for feedback. The utilisation of body velocity feedback is analogous to attaching a damper between the body and virtual sky and the latter two terms are basically linear spring and linear force terms [65]. A slight variation of skyhook, by utilising the sprung mass acceleration instead of velocity, was termed acceleration-driven damper (ADD) control and was shown to be an effective strategy [66]. Extensions of skyhook algorithms have been implemented by numerous researchers including a gain scheduling scheme [67], and an adaptive scheme [68].

Ground-hook control theory has been proposed to improve road holding capabilities for controllable suspensions [11]. In this method, the fictitious damper is placed on a stationary ground instead of a stationary sky and this will give consideration to the road holding capabilities of the suspension system. This control scheme was mainly applied to truck and heavy-vehicles due to the importance of minimizing tyre load variations and their associated contribution to the durability of suspension components and the reduction of road damage. Another variant of skyhook control has been termed balance control. Balance control aims to cancel out the suspension force by using the active element to generate a force equal and opposite to the spring and/or the damping force [19]. The combination of various feedback signals based on skyhook controllers and their variant, such as a combination of skyhook and groundhook, has been termed hybrid control and was shown to achieve an effective compromise between the two strategies [69]. Another example of promising hybrid control is the combination of skyhook and ADD control which has been benchmarked in a study which compares it to other semi-active control strategies [70].

2.10.2 Optimal Control

The application of optimal control theory to active suspensions has been extensively recorded for many decades. Most research was based on fully active configurations where an actuator replaces spring and damper. It is convenient to have a direct method for finding the best possible performance of feedback control laws and linear stochastic optimal control theory has been widely used for the purpose [7]. Hrovat gave a very compressive review of existing optimal control studies [3].

Because of this, the ride optimization problem could be viewed as an equivalent optimal filtering problem where the aim is to eliminate the negative effects of vibrations caused by road roughness [3]. Road inputs are shown to approximate to a white noise in the form of a power spectral density where the signal conveniently matches the well-known, standard Linear–Quadratic–Gaussian (LQG) assumptions for process noise.

The most common forms of optimal control are the Linear Quadratric Regulator (LQR) and the Linear Quadratic Gaussian (LQG) [71]. For design of the controller using LQR theory requires that the system input is white noise, that the performance index to be minimised by the optimal control will be of quadratic form, and, in its simplest form, that all state variables will be measurable [72]. This normally includes body velocity, wheel velocity, suspension and tyre deflection. Typically the performance index will be a weighted sum of mean square values of output variables including body acceleration, suspension deflection, dynamic tyre load and, possibly, actuator force [73, 74].

The underlying assumption in much of the previous work was that all the states are exactly known while in practice, some of the states may not be easily accessible. For the simple quarter-car model,

typical viable measurements are the sprung mass acceleration and suspension deflection, whereas the tyre deflection is difficult to measure. Fortunately, the latter can often be neglected in the feedback control law without significant loss of performance, although there are operations, such as the stiffer suspension settings with minimal tyre vibration where performance is poor, necessitating a full state feedback, most likely based on a full-state estimation [3].

It is possible to estimate the full state vector using, for example, a Kalman filter in the context of the Linear–Quadratic-Gaussian (LQG) methodology [3]. While such systems may reduce sensor requirements, it is important to remember that they typically lead to a degradation in performance. In addition, the LQG controller is in general less robust with respect to modeling errors [3].

To address various forms of modelling uncertainties a number of recently developed optimal robust control techniques can be considered, especially promising being the ones based on frequency domain analysis such as H-infinity and H-2 [75]. In 1994 Yamashita et al. presented a control law for a full car model using the actual characteristics of hydraulic actuators based on H-infinity control theory [76] The results showed that the system is robust even when the closed loop system is perturbed by limited uncertainty [77]. This work was extended and made more practically feasible by simplifying the vehicle model into decoupled modes to make the implementation of the output feedback control simpler and realizable. The method proposed is reduced in complexity and does not require full state feedback and was also tested experimentally on a commercial vehicle. Subsequently there have been many studies of H-infinity controllers in active suspension applications.

As a result for optimizing the controller for robustness against unstructured uncertainties, there were reported issues of over damping due to the tendency of H-infinity to minimize the peaks in frequency response curves [3]. To improve the performance of H-infinity controllers from their overcompensation for uncertainties, many studies have combined these with methods such as linear parameter varying (LPV) controllers which aim to reduce model uncertainties by switching between numerous linearised models dependent upon different operating conditions [78].

Model predictive control (MPC) is another type of optimal control based upon repetitive computations which calculates for a control signal based on the plant model which will cause the plant to follow a particular trajectory in a specified time [79]. The major drawback of MPC is that it requires very intensive computation, such that for practical implementation of a simple plant, large time steps and a short prediction horizon is required to reduce the computation effort. Given the real-time requirements of MPC this may lead to performance degradation or instability. A fast MPC method was investigated and was compared favourably against skyhook for a realistic model of a semi-active half car suspension system [80].

2.10.3 Preview Control

A preview system aims to improve suspension performance by using feed forward knowledge of future road inputs. Knowledge of future road disturbances is obtained ahead of the vehicle by using a “look-ahead” sensor [81]. The preview information is obtained by reconstruction from the online measurement of acceleration and suspension deflection. Most studies assume that the road input to the rear wheels are delayed and identical to that experienced by the front wheels and therefore only preview sensors in the front of the vehicle are required. A cheaper alternative to the look-ahead

preview is the “wheel-base” preview, where road information is gathered by extrapolation of the vehicle and suspension displacements either obtained from accelerometers and/or displacement sensors using the assumption that the wheel is in contact with the ground and that tyre deflections are negligible [81]. In the wheel-base preview scenario preview information is only available for the rear wheels.

The concept of preview control for active suspensions was first introduced by Bender in 1968 [82]. It is possible to extend upon optimal LQR control methods by adding a preview of the road profile. The control laws contain a feed forward part using the preview information and a feedback part as from a typical LQG system [79]. Most studies into preview control have been associated with this optimal control path due to its ability to determine the theoretical improvements preview can offer to active suspensions [83]. Most control studies, especially the earlier ones, were conducted assuming perfect road information is available.

It is not clear how much preview time is needed to bring forth significant improvements. Earlier studies by Thompson et al. in 1980 suggested 200 ms while Louam et al. in 1988 suggested 300 ms, although the details are dependent on the control algorithm and vehicle speed [81]. Youn and Hac compared semi-active preview suspensions with variable stiffness and damping against active preview suspensions with 200 ms preview and found that both showed comparably good performance improvements across almost the entire frequency range [60]. The performance improvement was much less when a semi-active suspension with only variable damping is considered; this can be explained by the fact that active optimal preview requires more energy than in the non-preview case.

A simulation study by Hac in 1992 showed improvements of all aspects of suspension performance especially road holding and also a drastic reduction in the power consumption when compared to active suspensions with no preview [84]. Another simulation study also confirmed power reductions and an improvement in both comfort and road holding [83]. The authors here also demonstrated the improvement when preview is used to compensate for the delays of actuators. Vahidi and Eskandarian studied the effect of sensor noise on active preview systems and concluded that tyre vibration is most sensitive to sensor noise and satisfactory performance is maintained when sensor noise is within 10-20% [85]. Additionally performance of the control system with longer preview time degrades at a faster rate with increasing levels of noise.

A comprehensive review of optimal preview control suspensions by Sharp and Peng concluded from literature that limited bandwidth active preview systems can enhance ride comfort and at the same time reduce suspension working space [79]. In the case of limited bandwidth systems the preview can only deal with the body-hop mode and that typically 250 ms preview is required for 1 Hz mode and 100 ms for a 10 Hz mode. They also noted that there are diminishing returns from additional preview. Depending on the amount of preview available, MPC is considered an attractive method since it can optimise the suspension system over a restricted preview [79]. Thus MPC has been studied for preview control by numerous researchers [86].

A drawback of “look-ahead” sensors is that they recognize a heap of leaves as a serious obstacle, while a pothole filled with water, will not be detected at all. Moreover, if it is assumed that the road surface at the rear wheel is same as front wheel, then a brick detected by the front wheel might be pushed away, so it will not enter the rear wheel. In addition, the track of the rear wheels can differ

from that of front wheel especially during cornering. Wheel base preview is relatively reliable and cheap when compared with look-ahead sensors and is less likely to incorrectly predict road imperfections unless the wheel is not touching the ground. However, Sharp and Peng also noted that wheel-base preview, even with much lower cost than preview sensors, offers little value at usual vehicle speeds [79]. Overall they concluded that obtaining sufficient and accurate preview is currently unfeasible.

2.10.4 Non-Linear Control

Suspension systems are intrinsically non-linear, uncertain and are subjected to a variety of road profiles and suspension dynamics, although in many circumstances linear approximations are valid. There are nonlinearities in the road profile are due to the irregular roughness and discrete events such as bumps and potholes of the road surface while the suspension dynamics are affected by the non-linearities of the actuator and other passive components [3]. In reality the conventional MacPherson strut is non-linear and the bottoming of the strut and friction introduce further non-linearities.

Many control strategies used in active and semi-active suspensions are focused upon determining the desired actuator force and do not include actuator dynamics. Often in the practical implementation of these controllers, the suspension control strategy serves as an outer loop controller which determines the demanded active force, an inner loop controller is then designed to deal with the dynamics of the actuation system. Due to the non-linearity of the actuation systems, it is therefore appropriate to utilise non-linear control methods. Methods such as adaptive control, sliding mode control (SMC), backstepping control and linear parameter varying (LPV) control have been widely studied and successfully implemented on active and semi-active suspensions.

Adaptive control methods are systems which in general vary slowly to uncertain parameters or changing system states. The adaptation of the control system parameters may relate to changes in ground input disturbance or system parameters such as vehicle load or non-linear suspension component characteristics [87]. The adaptation can take on the role of self-tuning feedback gains and is designed to improve the performance of the control system in response to changing or uncertain system parameters and must be used in combination with other suspension control strategies.

Backstepping is a popular method for the control of active suspensions since it provides a systematic procedure to formulate the Lypuanov functions to ensure the stability of nonlinear dynamic systems in incremental steps. An adaptive non-linear backstepping design for the control of quarter car active hydraulic suspension was developed by Lin and Kanellakopoulos which utilised a non-linear low pass filter whose bandwidth increased with suspension travel [88]. This intentional introduction of non-linearity into the controller allows the suspension to remain soft over small suspension travels and stiffen during more severe oscillations. Suspensions using backstepping with similar strategies which deal with suspension bottoming can be found in [89, 90]. Fukao et al. used the combination of the H-infinity and adaptive backstepping control technique for an active suspension system with hydraulic actuators [91]. H-infinity control was used for the outer loop control in demanding the desired suspension force while an inner loop controller dealt with non-linearities by using an adaptive backstepping design. A backstepping controller has been used to consider the non-linearity of servo valves and changes in cylinder volume in an active hydraulic system [92].

SMC has origins in bang-bang control and is advantageous in terms of robustness to external disturbances and parameter variations. The concept is to force the systems onto a desired state space trajectory called the switching hyperplane and remain there [17]. The controller has a bang-bang character in that the sign of the controller switches depending on the direction of approach to the hyperplane.

SMC has been shown experimentally to give superior performance in force tracking of electro-hydraulic actuators especially at high frequency when compared to feedback linearised controller [93]. The downside of the feedback linearised control method is that although it yields good results given an accurate model, slight model errors of approximately 10% cause the controller to become unstable. This work was extended by combining the SMC with an adaptive controller that deals with uncertain parameters of the hydraulic system [94]. A SMC suspension used by Kim and Ro showed good performance and robustness against realistic suspension non-linearities in the form of a cubic spring force, a quadratic damper force and tyre lift off phenomena. Optimal linear quadratic control combined with an inner loop sliding mode controller for an active pneumatic actuator was shown to yield superior performance compared to the linear quadratic controller alone [95]. A SMC with a proportional-integral sliding surface was devised and simulated showing superior performance and robustness to LQR [96].

LPV control is a method of gain scheduling in which non-linear systems can be described using a set of linear models or to vary the performance of the controller by introducing linear parameters [97]. Thus LPV is most commonly used as an extension to H-infinity control methods as it helps to reduce the conservatism of robust controllers by providing a more precise linear model for the various operating regimes [78]. LPV control has also been implemented in combination with other control methods such as backstepping [98].

2.10.5 Intelligent Control

Intelligent control techniques based on soft computing have a number of advantages in the application of active suspension control. Often practical implementation of conventional control techniques based upon linear models are inadequate due to system non-linearity, while non-linear techniques are problematic as they require complex accurate models which can be costly. One approach in dealing with these problems is to utilise intelligent control methods that rely on soft computing which can tolerate uncertainty and imprecision. A comprehensive review on the state of the art of intelligent control methods for active suspension systems can be found in [87].

Intelligent computation methods that have been applied to active suspension problems include fuzzy logic, neural networks and genetic algorithms. Fuzzy logic lends itself to decision making processes through approximation and can deal with imprecision. Neural networks are beneficial for modeling non-linearity and capable of machine learning. Genetic algorithms are a promising method for global optimization but are too computationally intensive for real time applications. Both fuzzy logic and neural networks could be used for real-time control.

Adaptive fuzzy control has been explored by a number of researchers. Its popularity in dealing with non-linear and uncertain systems stem from it being model free, tolerant to sensor noise and is highly robust [87]. Fuzzy control systems have the ability to deal with linguistic and experts' knowledge through the design of fuzzy rules and membership functions. However to deal with

numerical and linguistic uncertainties with changing dynamic conditions an adaptive self-tuning fuzzy controller may be employed [87]. A fuzzy control system for an active suspension was developed and experimentally evaluated in [99]. Fuzzy control has also been successfully combined with SMC, the reason being that the properties of fuzzy control can help overcome problems faced by SMCs in terms of, chattering, susceptibility to noise at the switching surface, large sliding gains and the development of equivalent models [87]. Generally the stability and performance of fuzzy controllers must be tested through trial and error for all possible dynamic conditions to give certainty that the control system will behave as desired and this is rather impractical [17]. The combination of a fuzzy logic controller and SMC helps to ensure the stability of the control system.

Neural networks are a popular control method among active suspension researchers due to their adaptive ability to learn non-linear mappings. The control architecture consists of layers of interconnected artificial neurons; each neuron has an output which is a non-linear function of inputs. Neural networks have been extensively applied to the control of MR dampers because of their highly non-linear characteristics, by learning inverse mapping of the plant to be controlled [100, 101, 102]. The downside of neural networks is that the control system performance is highly dependent on the data sets used in training, therefore the training sets must be representative of all possible dynamic conditions to ensure good performance and stability. The behavior of the neural network can be unpredictable if it encounters states not covered by training sets and this is a barrier to practical implementation especially given the requirement of safety when working with vehicles. Moreover these intelligent methods may be used in combination, such as a combined genetic algorithm and fuzzy logic for the automatic design of rule acquisition, and a combined neural network and genetic algorithm where the neural network tracks the optimised output from the genetic algorithm [87].

2.11 Hybrid Numerical-Experimental Testing

2.11.1 Background

Hybrid numerical-experimental testing is not a new concept and has received considerable attention mainly in the field of civil engineering. The concept refers to the combination of real experimentation with computer numerical simulation with the aim of obtaining more reliable results than pure simulations, but normally at much shorter time scales and lower costs than would otherwise be required in full experimental testing. In this Thesis a hybrid test rig is designed and implemented with the goal of testing vehicle suspensions. Due to issues discovered with the method in terms of accuracy and stability, a large portion of discussion and analysis of hybrid tests is conducted in Chapter 5.

A number of terms have been used to describe different types of hybrid numerical-experimental testing due to their separate development in a variety of fields. Despite the differences in name, these testing methods are very similar. These terms are hardware in the loop (HIL) testing, model in the loop (MIL) testing and substructuring.

Most literature on numerical-experimental testing of active and semi-active suspensions has been termed HIL testing. Originally HIL testing was developed for evaluating electronic control units on simulated physical systems which did not require mechanical interfaces [5]. In this example the term refers to the inclusion of physical hardware (an electronic control unit) into a computer simulation loop of the physical plant, such that there is dynamic interaction between the physical hardware and the simulation loop. Later it was extended to include testing of physical hardware with mechanical interactions such as the suspension system [5].

When HIL testing is used in the context of active and semi-active suspensions, the physical hardware is the active or semi-active actuation system, whose output is detected using sensors. The real-time information from the sensors is then used as the input into a computer simulation model of the vehicle dynamics. The output of the simulation model is realised physically through an actuator connected to the physical test piece. Here the computer simulation contains all other relevant components for the simulation of the entire vehicle dynamics minus the test piece in question. Typically a quarter car HIL in the loop suspension will contain one physical test piece system mechanically connected to one actuator. Research utilising this type of quarter car HIL suspension test rig can be found readily in numerous literatures [22, 23, 25].

Another term which can be found in some literature is MIL testing. MIL has been defined as a “test specimen which is part real and part virtual”, meaning that a simulated system is physically realised mechanically through the use of an actuator [6]. The actuated simulation (MIL) then interacts dynamically with the rest of the rest of the system which is physical hardware (HIL).

From this perspective a mechanical HIL system must also contain a MIL system and vice versa; they are in fact dualities of a hybrid numerical-experimental system. For the example of the HIL suspension system, the real test piece is a HIL system while the simulated system whose output interacts with the test piece via an actuator is a MIL system. The difference between the uses of HIL or MIL terminology lies more in the focused interest of the researcher; for HIL systems the

researcher is interested in the performance real test piece while for MIL systems the researcher is interested in the performance of the actuated simulation.

Work on hybrid numerical-experimental systems has been studied extensively by University of Bristol researchers where the substructuring terminology has been adopted [103]. In essence substructured systems are the same as those mechanical HIL and MIL systems where there is dynamic interaction between real physical part (HIL) and actuated simulation part (MIL). A schematic diagram of a hybrid system is depicted in Figure 2.16.

Studies with HIL systems have benefits under the following conditions:

- Simulation models are inadequate for the representation of interested test piece and related phenomena or that accurate models are too computationally costly [5].
- Laboratory machine testing do not offer dynamic interaction [5].
- Pure experimental tests are costly in terms of time and finance [5].

The benefits of MIL systems can be summarised as follows:

- Newly designed systems can be tested without having to be physically realised and configurations can be easily varied via simulation [6].
- Some physical phenomena are difficult to be realised experimentally such as aerodynamic forces but can be more easily and accurately simulated [6].
- Lends to testing scaled systems and also expansion of time scales, namely pseudo-dynamic testing, since simulation models can be easily scaled [4].

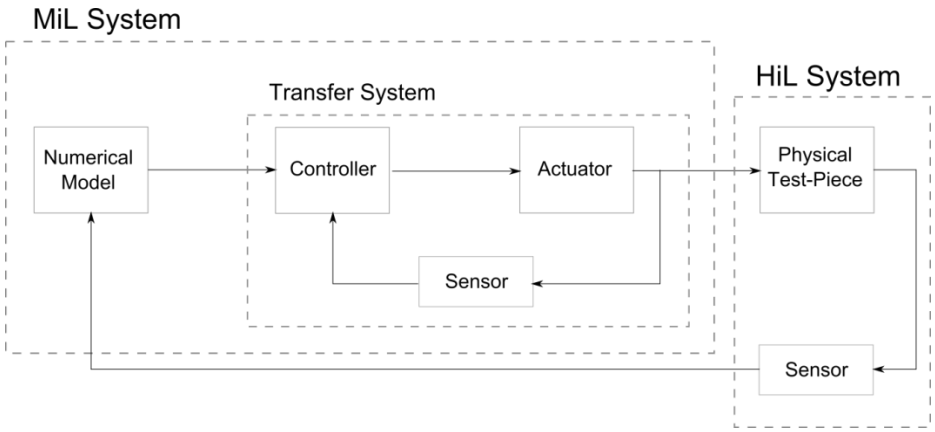

Figure 2.16 – Schematic diagram of hybrid numerical-experimental test rig.

Despite the many benefit of hybrid testing there are also a number of concerns in their practical implementation:

- Test rig accuracy is affected by errors and time delays caused by the MIL transfer function, namely sensor, actuator and control system dynamics.

- The transfer function dynamics could lead to instability and robustness issues.
- Can be affected by noise due to sensors required for HIL and MIL interaction at the mechanical interface.
- Computational costs affect model complexity due to real-time requirements and efficient numerical methods are required.

2.11.2 Previous Applications

Hybrid numerical-experimental testing has potential benefits in many applications. This involves the dynamic testing of structures and components and is applicable to a range of fields such as automotive, aerospace, civil engineering, biomedical, rail and defence [104]. Early development of the substructuring techniques was concentrated in the field of civil engineering, particularly the testing of building structures subjected to seismic loads [4]. In the earlier hybrid testing studies, a method often utilised was pseudo-dynamic testing, in which experiments were conducted on a greatly expanded time scale [4]. This approach was beneficial as it reduced the requirements for fast actuator response and the reduced system frequencies meant that system stability is easier to achieve. The limitation is that the technique could not capture rate dependent characteristics of physical components. More recently there has been increasing hybrid tests conducted in real time [4]. Although there exist a wealth of substructuring literature in the area of seismic testing, often these systems are limited to a single MIL system and a single HIL system [105, 106, 107].

The rest of the literature will focus on generic applications of hybrid testing such as systems consisting of only linear mass spring dampers. Spring mass dampers are also building blocks of the suspension model and a number of researchers have studied the hybrid testing of vehicle suspensions.

Most previous applications of dynamic testing using MIL systems have been focused on a system single MIL part. This typically involves a single actuator which tracks the output of the MIL numerical model. The simplest of this system is a single mass spring damper system with one degree of freedom as shown in Figure 2.17. Here the numerical model is a spring mass damper system while the physical HIL element is a spring attached to a wall.

Another widely studied model for MIL testing is the slightly more complicated two degree of freedom system. One configuration of two masses is the quarter car suspension where the one of the mass at the end is not fixed to wall. Due to its application to suspension and vibration isolation systems this model has been studied by several researchers [6, 108, 109]. Another two mass system configuration is where the masses are fixed to a wall at both ends; this was studied in [110] and [109].

In the studies by Stoten et al. [108] the experiments were conducted with hydraulic actuators operating in position control mode, as the numerical model function has an input in terms of force and an output in terms of position. A mathematical framework for the closed loop system was formulated analytically for a MIL quarter car suspension system. Two possible system modes of operation were proposed, where the MIL system can represent either tyre or the sprung mass element. The actuator dynamics were modelled as a simple first order lag and justified by

comparison to experimental results from system identification. From the proposed mathematical framework a novel closed looped controller termed the Linear Substructuring Controller (LSC) is devised. The LSC controller is based on a feedforward and feedback part such that the feedforward transfer function completely cancels out the dynamics of the closed loop test rig and not only that of the actuator. Additionally the MCSEF controller is proposed, this is an adaptive implementation LSC to improve robustness.

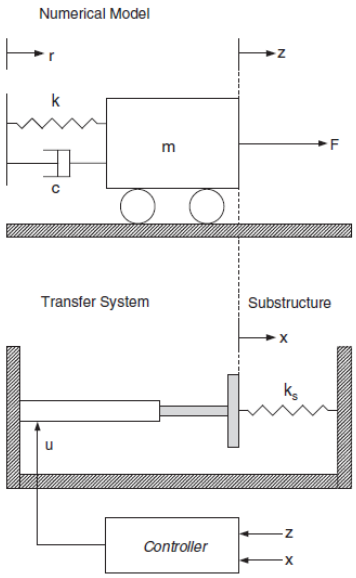

Figure 2.17 – Schematic representation of a substructured system with one transfer system. State variable for the numerical model: $z(t)$, state variable for the output of the combined actuator and controller transfer function (also called Transfer System in substructuring literature): $x(t)$, control input to the actuator (voltage): $u(t)$ [111].

The flexible nature of MIL systems is that multiple MIL systems can be used in combination within a single test rig. Compared to the single MIL test rig, here are few studies with experimental evaluation for hybrid tests with two MIL systems such as those conducted in [6, 103, 109, 112]

One of the simplest configurations for a test rig with two MIL systems is a three mass system. A three mass spring damper system connected in series was studied in [109, 112]. Both papers was configured such that the masses at both end were represented by MIL systems while the middle mass spring damper was realised physically. Here the MIL systems are connected in parallel since they both simultaneously receive inputs from the physical system and their outputs feedback directly into the physical system and not each other. Results in both studies showed that additional MIL systems lead to increasing difficulty in controlling the test rig to achieve the desired response due to the combination of errors from each MIL system.

In [6] Plummer conducted hybrid experiments on a half car model where the sprung mass heave and pitch motions are used as input to the MIL tyres. Corresponding forces from the input motion is calculated by the MIL tyre numerical model and tracked by the actuators. This test rig contains two parallel MIL systems, one for each actuator. In the same paper Plummer also conducted an experiment using MIL numerical model of aerodynamic forces to impart forces on a half car model [6]. The half car model used was simplified 'bicycle model' which limited the system to 2 degree of

freedoms. The aerodynamic forces were modelled to be dependent on the vehicle velocity and the front and rear ride heights. Again this hybrid test rig contains two MIL systems whose outputs are tracked with an actuator. Both experiments conducted by Plummer showed that although the MIL systems can effectively capture the qualitative trends of the system dynamics, significant deviation and stability can occur from the actuator delay [6].

One of the most complex hybrid experiments for a suspension application is a full motorcycle test rig conducted by Stoten et al. [103]. The test rig consisted of the full motorcycle tyres, suspension system and sprung mass as shown in Figure 2.18. The distinctive feature of the test rig is that the physical components are not physically linked. Each wheel and tyre unit is connected to an actuator, and the combined sprung mass and suspension are connected to two actuators. This configuration means that the test rig is capable of implementing any combination of real and virtual components via control of the actuators. With this approach the mimicking actuators are similar to MIL systems, but instead of following the output of a numerical model, the actuators follow the output from a physical system.

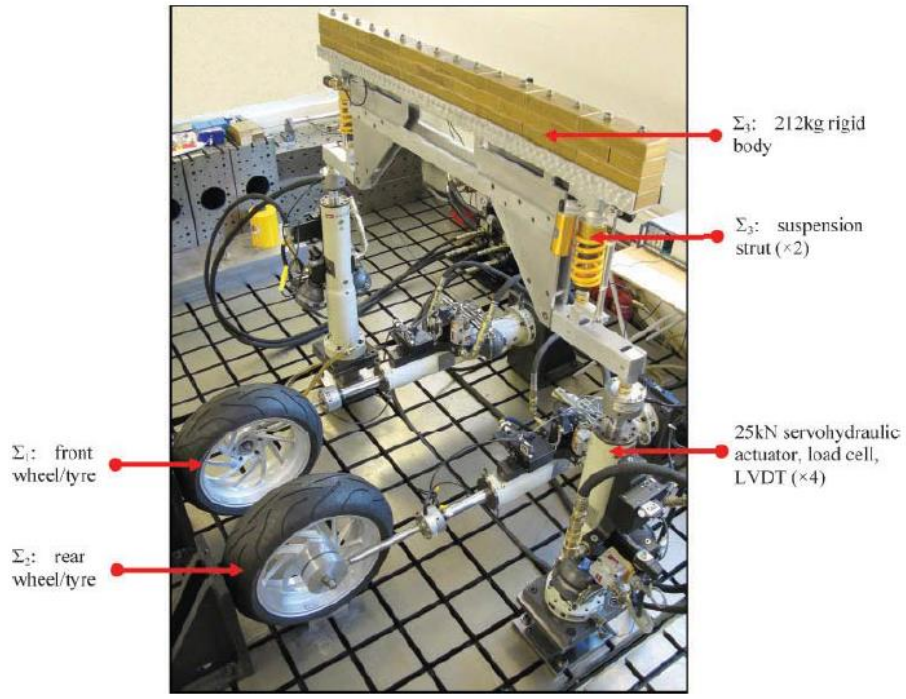

Figure 2.18 – Photo of quasi-motorcycle substructuring test rig [113].

Moreover this setup interestingly allows for “geographically remote physical experiments to be conducted as a seamless whole” [113]. Even if the test rig experiments were conducted with purely real components, there will still be considerable control challenges due to actuator delays as the separate physical systems are connected via actuators that aim to reproduce the displacements or forces from connecting subsystems.

Using the motorcycle test rig Stoten et al. demonstrated its capability to conduct a single MIL quarter car test and also extended to experiment with the multiple inputs and outputs. The configuration chosen used one physical wheel, one physical sprung mass and suspension, and one MIL wheel and tyre. With this arrangement the combined system has control complexity which is

equivalent to three MIL systems connected in series. Under this configuration the authors conducted experiments comparing performance of the LSC against MCSEF controller. The results showed that both controllers were able to achieve stability and that the MCSEF was superior when the system is subjected to parameter uncertainty and variation.

One of the novel aspects of the work presented in thesis is the application of a new configuration of hybrid numerical/experimental test rig which is presented in Chapter 3. The proposed test rig is a quarter car suspension test rig consisting of a real HIL wheel and tyre, and a MIL suspension component and a MIL sprung mass connected in series. To the author's knowledge this test configuration has never been experimented on before. Although the motorcycle rig by Stoten et al. has similarities in the sense that separate hybrid test systems are connected in series, the type of vehicle tested and choice of the MIL/HIL components differ. Another novel aspect of the thesis is the representation of the MIL sprung mass as a flexible structural model representing for which experimental results are discussed in Chapter 7.

2.11.3 Delay Compensation

It is widely known that tracking errors and specifically actuator delays lead to performance degradation and possibly instability of hybrid numerical-experimental test systems. Therefore a large amount of effort has been devoted to delay compensation of the MIL systems. The delays of MIL systems are due to the combination of sensing, computation and actuator response time. Additionally the system stability also depend on the dynamic interaction between numerical model and the physical system [110]. Study of the simplest single mass spring damper with a single MIL system as shown in Figure 2.17, showed that the critical delay for system stability is c/k_s [111, 114].

A very comprehensive review of delay compensation schemes for hybrid numerical-experimental testing was given by Bonnet et al. [109]. Delay compensation techniques can be classified into two general categories:

1. Methods based on classical control theory and its mathematical models of systems.
2. Methods based on adjustment of the actuator command signal depending on known or estimated actuator delay and amplitude error.

Model Based Methods

Model based methods of control theory are based on quantifying feedforward and feedback functions of the controller. The simplest formulation is when only the actuator is considered. Zero delay can be achieved by using a feedforward of an inverse of the actuator plant model. The downside of this technique is that it requires an accurate model of the plant, and inaccuracy can easily lead to poor performance and instability. Moreover model inversion also has physical implementation difficulties if the inversed plant model has numerator degree of freedom greater than the denominator. Experimental results with the basic inverse model feedforward controller with error feedback for a substructuring test rig can be found in [110].

Plummer used system identification results to devise a special command filter which cancels the phase lag of the actuator at higher frequencies, this is basically an implementation of frequency domain model inversion [6]. Although a significant improvement the test rig dynamics was achieved using a command filter, this solution had a undesired effect of large noise amplification at very high

frequencies. The Smith predictor is more complex strategy for the formulation of an inverse model feedforward with error feedback and a Smith predictor controller was implemented for a HIL test rig [115]. The Smith predictor only considers the delay of the MIL system using the representation of a constant time delay. Experimental results showed that while without compensation the test rig was unstable test rig, the Smith predictor controller achieved stability and dynamics resembling the emulated system.

A more complete method of inverse feedforward control for substructuring systems is the LSC which provides an exact feedforward transfer function which completely cancels out the dynamics of the physical plant, numerical model and actuator dynamics [110]. Moreover the technique was proposed in a framework which is directly applicable to other linear hybrid numerical/experimental test rigs. Although improved performance compared to the basic inverse model controller was achieved, the performance of the LSC controller is highly dependent on the accuracy of the model, and so to improve the robustness of the controller adaptive gains were proposed following the structure of minimal control synthesis (MCS). The adaptive controllers have been termed MCSEF and MCSmd and have been demonstrated experimentally to give significant improvement [108, 110].

Demand Altering Methods

Demand altering methods are based on the knowledge of the actuator time delay and amplitude errors. If these are known then using forward prediction, the demand signal can be extrapolated forward equal to the amount of time delay, such that they cancel each other. Therefore this separates the demand altering methods into two aspects of estimation and prediction.

Many studies in literature have assumed constant time delay and neglected actuator amplitude error. For robustness and high performance an estimation scheme for time delay and amplitude error will be necessary. A well-established method for on-line delay estimation is the Darby delay updates. This method uses the real-time displacement error and a velocity estimate to the system time delay. It has also been suggested that this method can also be applied to amplitude errors by finding the local peaks [109]. An improvement of the technique has been termed Modified Darby updates and was shown to be superior experimentally. Another method for delay estimation is based on measuring the time delay between crossings of a predefined threshold. A similar approach can be done for the amplitude error by finding the amplitude difference between local peaks. This method was implemented on a two MIL system in [112]. The downside of this method is that for a good delay estimation, the crossing threshold must be crossed sufficiently during the test. Although this is not an issue for earthquake engineering applications, it is unrealistic for vehicle suspension applications when subjected to random road inputs.

The first implementation of delay compensation using forward prediction was by Horiuchi et al. who used an exact polynomial extrapolation. He fitted an exact polynomial to the last few data points and the extrapolation can only be an integer number of time steps. The number of data points used was one greater than the polynomial order [116]. An alternative method based on least squares approximation rather than exact fitting was proposed by Wallace et al. [112]. This method allowed a forward extrapolation equal to any amount of time and also utilised a larger number of data points.

Another form of extrapolation is based on linearly predicted acceleration introduced in [117] where it was shown to be theoretically superior in terms of stability to the polynomial fitting method. This

requires knowledge of acceleration at the current and previous time step and assumes that acceleration varies linearly [109]. A different form of polynomial extrapolation is the use of Laguerre polynomials which only requires the current data points. All of these forward prediction methods are compared experimentally in three separate tests in [109].

Comparison results conducted by Bonnet et al. showed that delay compensation does greatly improve the performance of hybrid test rigs [109]. For three different configurations of tests conducted all were unstable when no compensation scheme is applied. Most of the compensation strategies applied was able to stabilize the system even when subjected to the demanding test configuration of a three mass system with two MIL systems. However the MCSEF method was incapable of achieving stability in the demanding three mass test, while the demand altering schemes performed better and with stability.

2.11.4 Performance Evaluation

Performance indicators for the evaluation of the substructuring test rig accuracy are measured by the deviation of the test rig output compared to the ideal emulated system [112]. The ideal emulated system is the system which the test rig should behave like, it is the case where there is no sensor/actuator error or delay such that the MIL actuator perfectly tracks the output of the MIL numerical model. Two indicators are suggested for evaluation of test rig accuracy, the numerical model accuracy and the transfer function accuracy [112]. The numerical model accuracy is the error between ideal output and the test rig numerical simulation output. The transfer function accuracy is the error between numerical simulation output and the sensed output from the actuation transfer function.

The numerical model accuracy e_1 is,

$$e_1 = z^* - z \tag{3.1}$$

The transfer function accuracy e_2 is,

$$e_2 = z - x \tag{3.2}$$

Here the idealized emulated system output is z^*, numerical simulation output is z and the sensed actuator output is x. The overall accuracy of the test rig is the combination of numerical model and transfer function accuracy. The transfer function accuracy may never be zero and there is coupling between e_1 and e_2 such that if $e_2 \rightarrow 0$ then $e_1 \rightarrow 0$. Any error in e_2 will lead to error in e_1 which will propagate into the next time step in a feedback loop and may lead to instability.

2.12 Conclusions

The literature has shown evidence of vehicle ride and handling performance improvements through the use of active and semi-active suspensions. Active suspensions are shown to have superior performance compared with semi-active counterparts due to the ability to impart forces upon the suspension allowing attitude correction and ride height alteration, which are important aspects for

automobiles. Within active systems there is a clear distinction between fully active (high bandwidth) and slow active (narrow bandwidth) suspensions, where fully active suspensions can deal with wheel hop resonance in addition to low frequency body modes. The performance benefits of fully active systems are difficult to justify given that most comfort and handling characteristics are heavily influenced by low frequency vibrations. Additionally, there are significant increases in the cost of the actuator and power consumption for fully active suspensions over slow active alternatives.

In suspension applications where attitude correction and ride height alteration are not a major requirement, it is difficult to justify the use of active suspensions over semi-active alternatives, especially when active suspensions are inferior in terms of weight, cost, complexity, reliability and safety. Within semi-active suspensions there are two prime candidates for generating variable damping namely variable orifice actuators or MR fluids. MR fluids have benefits in terms of fast response times, high force capabilities and reliability due to the lack of moving parts but are more difficult to control and expensive due to the immaturity of the technology.

Usually, when semi-active suspensions are considered, it is assumed that only variable damping is possible, however recent research has been conducted into suspensions with both variable damping and variable stiffness. These are mainly achieved through the use of hydropneumatic suspensions with variable dampers and gas accumulators. These suspensions offer significant improvements over suspensions with only variable damping and lie somewhere in between traditional active and semi-active systems. However the addition of gas accumulators and variable dampers in these suspensions will lead to increased costs, complexity, weight and size of the semi-active suspension.

In the last decade much effort has been made into the commercialization of active and semi-active suspensions. Some successful implementations have been achieved in the automotive industry in high end vehicles such as those fitted by Daimler Chrysler, Citroen, Nissan, McLaren, Chevrolet, Ferrari and Audi. In addition, the significant investment made by companies such as Bose, Sachs and the Lord Coorporation suggests a level of confidence in the technology. Although real flight applications for active/semi-active landing gear are yet to be seen, many researchers have successfully tested the principles using drop test facilities.

Many of the active and semi-active systems depend highly on the capability of the actuation and control systems utilised. While traditional research has focused on suspension control by assuming perfect actuators, researchers are now building on this work by incorporating more non-linear actuator dynamics into the control design and utilising more advanced control and intelligent computing methods.

From this summary it can be concluded that there is no clear winner between active and semi-active suspensions since the choice of technology is most dependent on application and budget. A typical suspension test rig using real components will be restricted to a single specific configuration. A more flexible and multi-purpose test rig can be achieved by utilising hybrid numerical-experimental testing. From this reasoning a hybrid test rig is proposed in the Chapter 3 of this thesis and a brief literature review of hybrid test systems is addressed covering advantages, disadvantages, possible issues and solutions.

3. Suspension Test Rig

3.1 Motivation for Rig Design

Typical suspension test rigs are based upon the quarter car model, which has been shown to be an appropriate representation for a limited range of applications. The many types of passive, semi-active and active suspensions and components available to suspension designers mean that experimentation cannot proceed without specification of all the suspension parts. This includes the wheel, tyre, spring, damper, active actuators, semi-active actuators and any other connecting structures. A suspension designer has to design and manufacture suspension parts or otherwise order pre made parts from suppliers. Additionally the suspension will have dynamic interaction with the vehicle structure. Inclusion of vehicle structure will allow for inclusion of dynamics of vehicle attitude as well as possible flexible vibration modes which could be significant for structures such as aircrafts. Researchers in the area of landing gears have made calls for development of suspension control in conjunction with modelling of interaction with airframe dynamics [118].

The aim of the test rig proposed in this thesis has two major capabilities in addition to a typical quarter car test rig:

- To enable rapid testing and comparison of different suspension types and components.
- Engage rapid testing of flexible vehicle structure as opposed to simple point mass representation.

A test rig that can successfully achieve these two objectives would possibly be capable of rapidly testing different suspension and vehicle types. This type of test rig can be achieved by including an actuator which emulates a mechanical system. Two actuators are required, one for the emulation of the suspension system and another for the emulation of the vehicle structural system.

The goals outlined here can be achieved using numerical-experimental testing since it combines real experimental physical part with numerically modelled part. It has been suggested by researchers in hybrid testing that the method has great potential in the automobile industry for rapid product development, noting in particular that a numerical vehicle model can be utilized [4].

3.2 Test Rig Concept Design

The test rig developed here can be represented by two MIL systems, which is the same as a multi-actuator substructuring [112]. This method entails using one actuator to emulate the suspension components; this will be the suspension MIL. Another actuator could emulate the vehicle structure; this will be the vehicle structure MIL. Within this setup a real wheel and tyre could be used, which can be considered as the HIL system. Furthermore the system is designed such that other real suspension components may be incorporated into the test rig as additional HIL systems. The concept for incorporating HIL suspensions is that for preliminary testing or for easy to model components it is

more convenient to use MIL suspensions, while for more extensive testing or for difficult to model components testing could be achieved by physically adding those suspension components which may replace or operate alongside the MIL suspension. An additional actuator will be required to provide ground excitation input. A diagram of the test rig architecture is shown in Figure 3.2. To the author's knowledge, this configuration of a quarter car hybrid numerical-experimental test rig, with an MIL suspension and MIL vehicle structure connected in series, has never been conducted before.

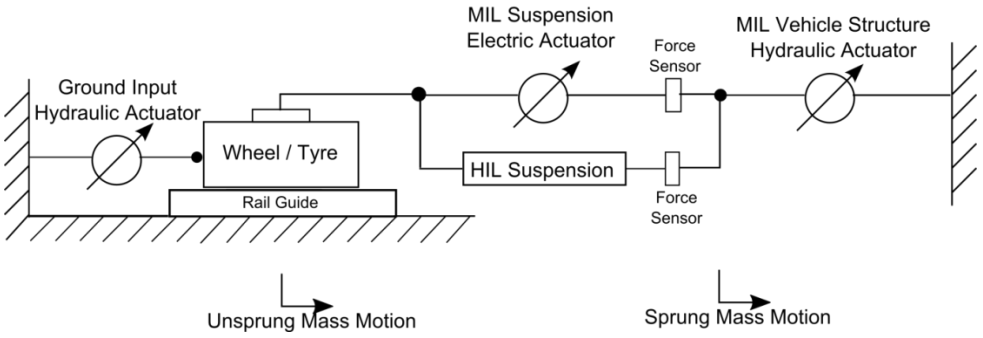

Figure 3.2 –Diagram of test rig (side view).

There are two control choices for MIL systems, they can be in either force control or position control, defined by the choice of the numerical model input and output. For force controlled MIL systems, the output of the numerical model is a demand force which is then controlled by the actuator, while inputs to the model are typically displacements. Conversely for position controlled MIL systems, the output of the numerical model is a demand position while the model input is typically a force. The reason either formulation can be used is that forces and motions are coupled entities in dynamic systems governed by the motion equations. The choice of force or position control in the MIL suspension and the MIL vehicle structure is discussed next.

MIL suspension control:

In typical MIL systems displacement control is used. These are systems that have force as an input to the numerical model, and a displacement resulting from input force as the output. In the case of MIL suspension it does not make sense to operate in displacement control since almost all suspension control strategies are conceptualised in terms of suspension force generation. Furthermore, passive suspension components are naturally modelled as functions of motions, for example a spring is a function of displacement and a damper is a function of velocity. Although it is possible to formulate the MIL suspension in displacement control mode, the author believes it will be more conceptually straight forward in the context of suspension force generation strategies to utilise force control mode and use suspension motions as the numerical model input. If MIL suspension is in position control, two force sensors will be required for forces acting on the sprung mass node and the wheel mass node as well as sensor for suspension velocity for the damper model. Therefore in position control mode one more force sensor will be required compared to force control mode.

MIL vehicle structure control:

As discussed for the MIL suspension control mode selection, the same applies to the MIL vehicle structure control, which can be achieved either using force or displacement control. Considering the

case where both actuators could be operating in force control, this would mean that resulting displacements would be the physical consequences of the force interactions and this method can be considered the most realistic as it does not require any numerical integrations of sprung mass accelerations into displacement. To achieve the correct displacements from the force interactions, the force sensors are required to be extremely precise. In this configuration the input to the MIL suspension are the sensed suspension motion parameters as required for the numerically modelled components. The input to the MIL vehicle structure is the sprung mass displacement which could then be used to calculate demand force from the resulting structure. The downside of this configuration is the demanding requirement for accurate force sensors. Displacement control is achieved by using the sensed suspension force as an input from which the resulting structural acceleration response is calculated and then double integrated to output demand sprung mass position.

The experimental rig designed here will use force control for the MIL suspension and position control for the MIL vehicle structure. Three actuators are required, for the ground actuator a large hydraulic actuator is chosen because of its high power so that dynamic interaction with the tyre will negligibly affect the ground actuator motion. For the MIL suspension an actuator with high bandwidth is required as the suspension vibration frequency is substantially higher than the sprung mass body hop frequency. Like the ground actuator, a hydraulic actuator is chosen for the MIL vehicle structure actuator since it has the strength to not be affected to the mechanical forces exerted by the suspension and also due to less demanding frequency requirement.

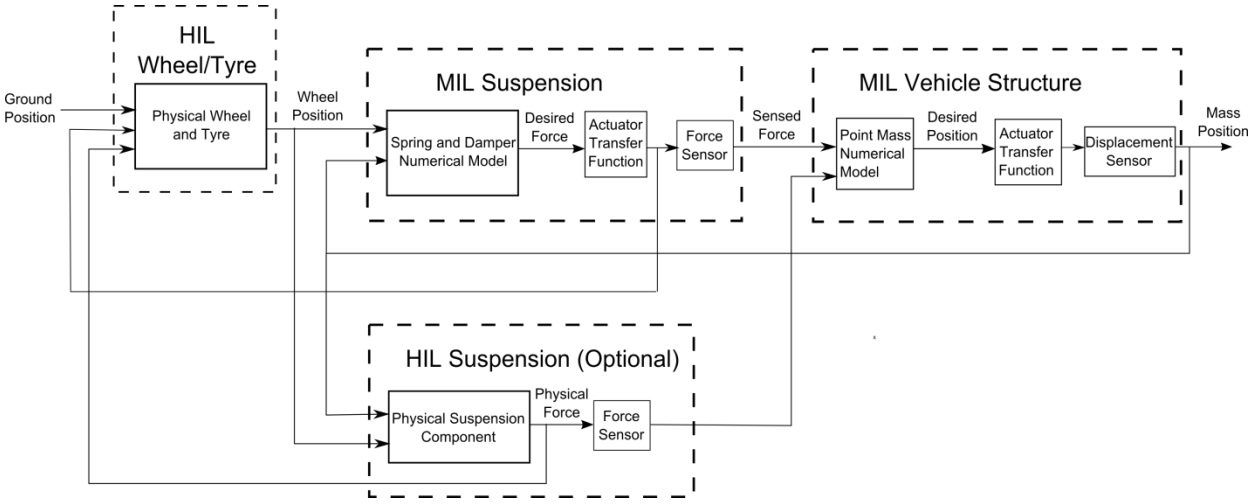

Figure 3.3 – Signal flow schematic of closed loop test rig.

Figure 3.3 shows a control schematic of the flow of signals within the test rig closed loop system. The ground input serves as a physical input of external disturbance that acts directly upon the physical tyre and wheel.

The MIL suspension model has inputs as required by the components being modelled, for the example of passive spring and damper the MIL suspension would require suspension displacement for spring force calculation, and suspension velocity for damping force calculation. The diagram shows inputs of wheel position and sprung mass position because suspension displacement is the difference between the two positions and velocity can be obtained from differentiation of

displacement signal. If other MIL components were used then the inputs required for the numerical model will vary according to the force generation function of the particular component, or if the component modelled is active/semi-active, then the inputs will also depend on the suspension control strategy and the feedback employed. A passive HIL suspension component will not require an input signal since it is a real hardware.

The force generated by the MIL suspension and the HIL suspension combined is the input to the MIL vehicle structure model. The vehicle structure model is based upon calculation of the resulting displacement as a consequence of the input force. The vehicle model in the simplest form is a point mass, but could be a full vehicle model with heave, pitch, roll and warp, or a complex finite element type model consisting of many interconnected masses with springs and dampers. The displacement output of the simulation model is tracked by the hydraulic actuator control system and the sensed displacement is fed back into the MIL suspension, completing the closed loop system.

The final experimental results presented in Chapter 6 and 7 do not contain a HIL suspension part. This is because the experimental test results in Section 6.2 with HIL suspension gas spring which was sized with the intention for the scaled Boeing 707 configuration showed instability. Therefore subsequent tests were conducted with quarter car configurations which did not suit the specification of the sized gas spring. Moreover conducting the tests with purely MIL systems gives an indication of the worst case scenario of tests, which is of more interest to the research here, since delays from MIL systems will always be greater than HIL systems.

3.3 Test Rig Mechanical Design

A hydraulic actuator capable of delivering 23 kN at 100 bar pressure was chosen for the MIL vehicle structure actuator such that suspension forces would not significantly affect its controlled position tracking. The hydraulic cylinder manufactured by Vickers is double sided and has a total volume of 0.172 m^3. To ensure sufficient flow to the two hydraulic cylinders a pump with 48 l/min was used. The servo valves for the cylinders are custom made Moog valves with rated flow of 259 l/min at 35 bar. Experimental tests on the hydraulic actuators showed they could achieve a maximum velocity of 0.3 m/s. The two hydraulic cylinders for the ground input and MIL vehicle structure are identical, with identical valves and connected together in a parallel fashion in a single hydraulic circuit.

The important aspects considered are the stroke length, maximum velocity and bandwidth. A simple hydraulic circuit as shown in Figure 3.4 proved to be sufficient for the application, allowing maximum velocity of both actuators to be achieved simultaneously. The hydraulic actuators were found to perform good tracking using proportional controller, the feedback displacement is obtained from a LVDT sensor built into the cylinder. Test and system identification results in Chapter 6 showed that the hydraulic actuator has a bandwidth up to approximately 10 Hz. This will mean that tests conducted will require that the sprung mass frequency is below 10 Hz.

The other critical component to be sized is the MIL suspension actuator. Here a linear electric motor is chosen for its high bandwidth and absence of gearing. A Dunkermotoern STB3810 linear motor was found to fit the force, speed and bandwidth requirements. The STB3810 has manufacture's specification for peak force of 1860 N, continuous force of 276 N, stroke of 0.21 m, maximum speed

of 4.4 m/s, maximum acceleration of 196 m/s^2 and time constant of 1.26 ms. Testing of linear motor presented in Chapter 6 showed bandwidth of approximately 20 Hz and good tracking using Proportional plus Integral controller; the force feedback was obtained from a 1010AF-2.5kN-B load cell manufactured by Interface. The arrangement of the actuator in series with a spring (the tyre) was found to significantly worsen the control response of the actuator due to their dynamic interaction, reducing bandwidth from approximately 125 to 20 Hz. This means that the maximum wheel motion frequency of the experiments conducted must be less than 20 Hz.

For ease of construction, assembly and safety issues it was decided that the rig would be constructed horizontally. Since the rig's primary purpose was for a proof of concept, it was not considered essential that the rig be made vertical. Additionally, in scaled testing it is quite possible that acceleration due to gravity is scaled, this will be easier to implement on a horizontal setup where there is no gravity force acting on any rig degree of freedom. Aiding on this aspect was that the sprung mass, represented by an actuator, has to account for gravity forces through numerical simulation. The gravity forces of the wheel could also be implemented physically using the MIL suspension actuator. To aid a horizontal setup, a support mechanism is required for the wheels and a SKF low friction rail guide was chosen. After experiemental tests were conducted friction in the rail guide was found to be a major issue as it damped out wheel mass vibrations. With hindsight this issue would not be present if the test rig was arranged vertically.

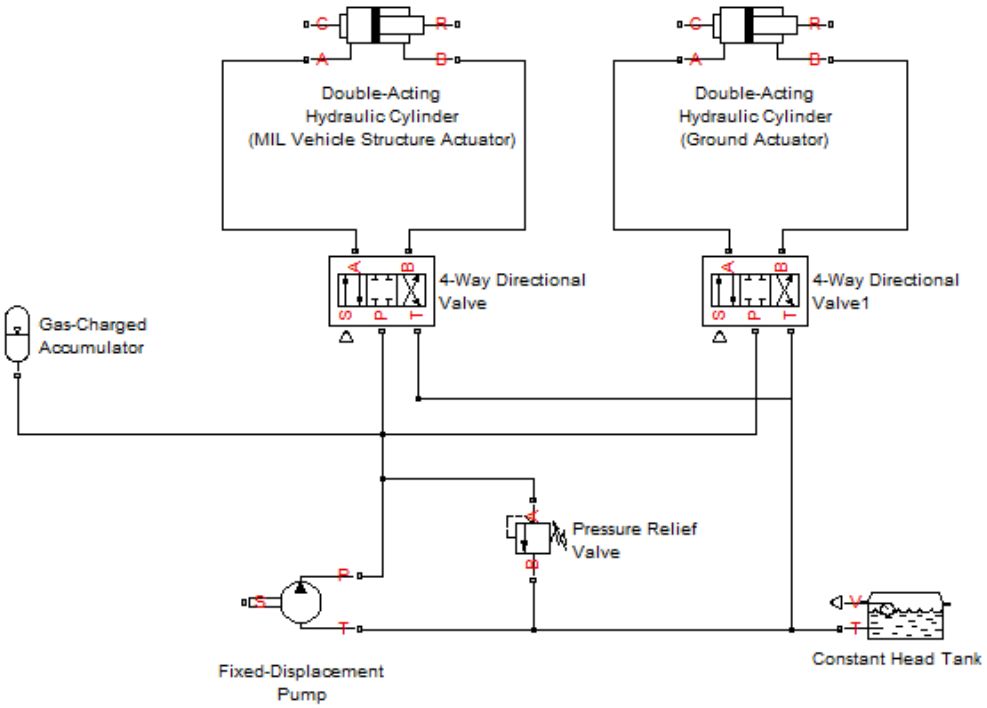

Figure 3.4 – Hydraulic circuit diagram.

After establishing the three actuators to be used for the TEST rig, mechanical parts were designed to house and connect the actuators into a system. Other off the shelf components required other than the actuators are force sensors for measuring the suspension force, a LVDT for measuring suspension displacement, linear rail guide and an actual vehicle wheel. All other parts such as plates,

brackets, housing and connecting blocks were designed and manufactured in house at the University of Bath. The drawing of the complete assembled test rig is shown in Figure 3.5.

The mechanical design includes the wheel assembly housing and base plate that rests upon the rail guide carriage. The base plate then supports the wheel, and contains a housing on which the suspension components sits as illustrated in Figure 3.6. The diagram shows an electric actuator and a hydraulic cylinder sitting on top of the wheel assembly.

The sprung mass in the test rig is virtual, and therefore simply consists of the connection between the MIL suspension actuator rods, and the MIL vehicle structure actuator rod. The plate is bolted on the end of the hydraulic actuator rod, from the plate connections are made to the MIL suspension actuator and any other HIL suspension components via a force sensor and rose joint to ensure alignment and therefore low friction of the suspension struts in spite of low manufacturing tolerances. A diagram of the sprung mass connection assembly is depicted in Figure 3.7.

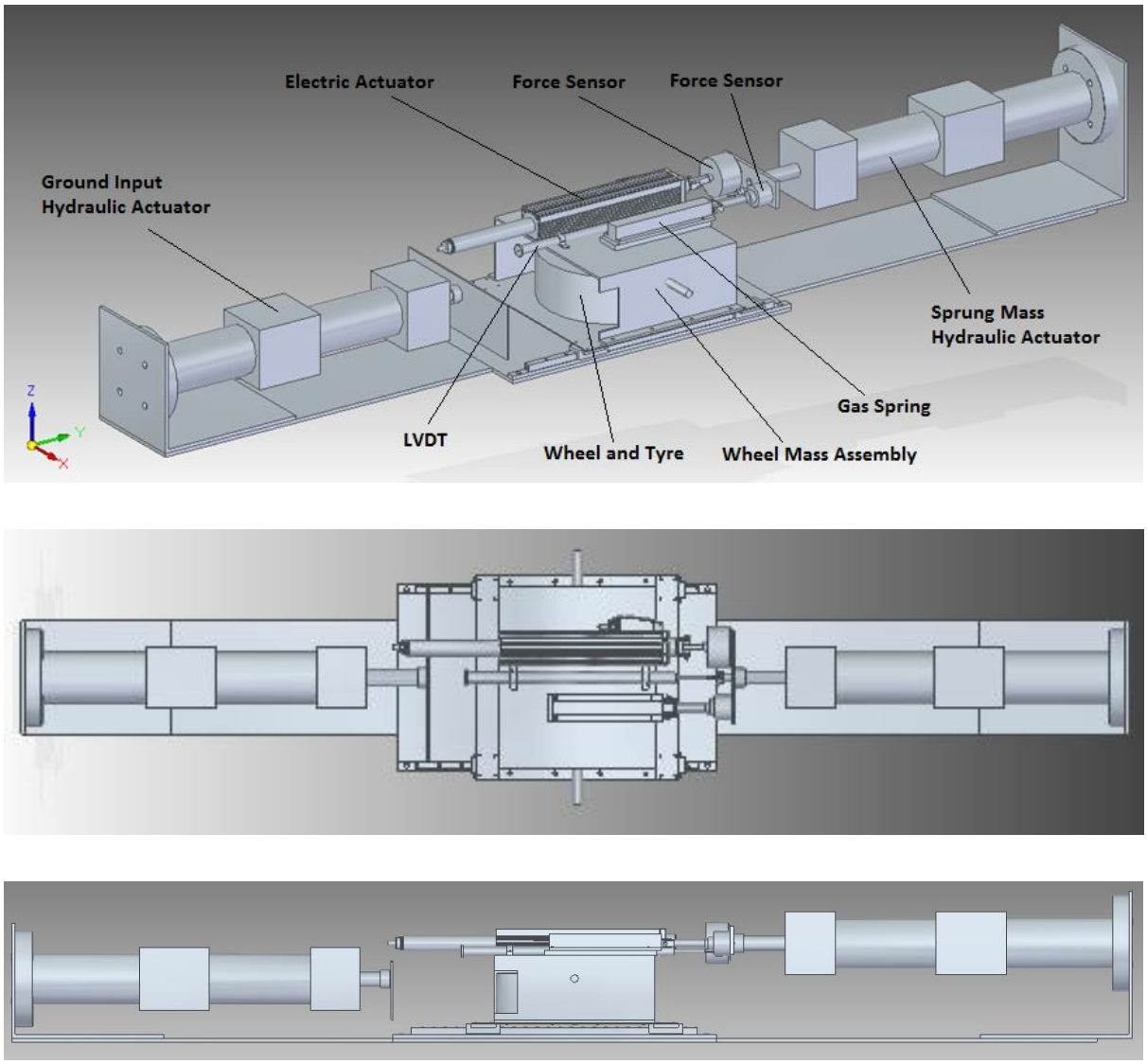

Figure 3.5 – Assembly drawing of horizontal TEST rig. From top to bottom, a) perspective view, b) top view, c) side view

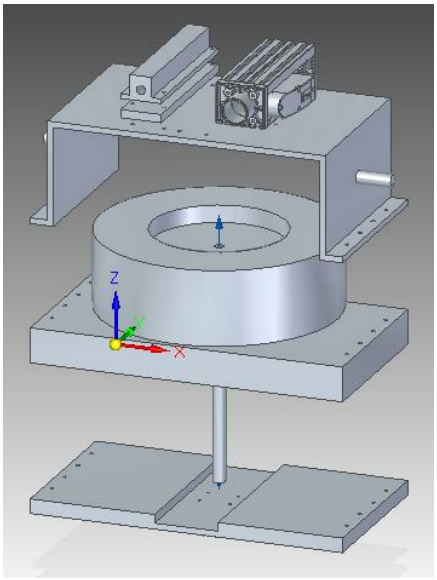

Figure 3.6 – Wheel mass assembly.

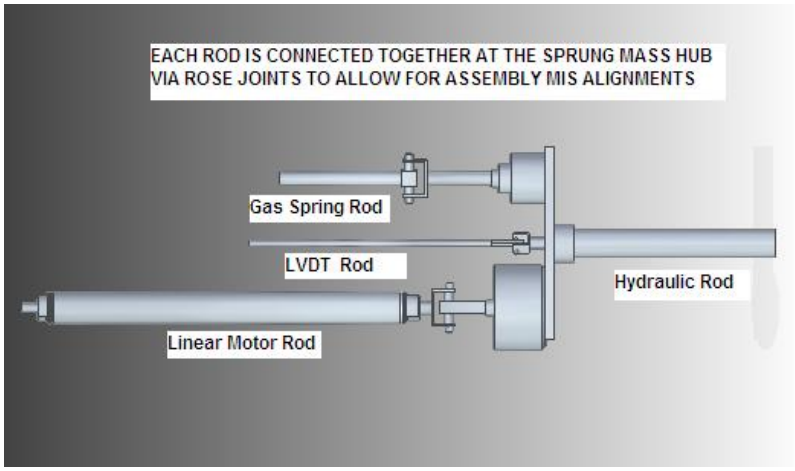

Figure 3.8 – Sprung mass connection assembly.

3.4 Test Rig Sensors and Signal Processing

The sensors used in the test rig are LVDTs and a force sensor. The force sensor is used for force control of the MIL suspension electric actuator and three LVDTs are used to measure the displacement of the suspension and two hydraulic actuators.

From experimentation the noise level from the LVDT signal was determined to be $+/-5x10^{-4}$m which is dominated around the frequency of 50Hz. This is contributed by its close proximity to the linear motor which contains a permanent magnet shaft and the electro-magnetic effects from the three phase mains electricity. Therefore a filter with cut-off frequency of 40Hz was applied reducing noise levels to $+/-2x10^{-4}$ m. Suspension velocity readings are used as inputs to the MIL suspension

numerical model for velocity dependent dampers. These readings are obtained by differentiation of the LVDT signal. Due to amplification of noise during differentiation up to +/-0.02 m/s, a low pass filter with a lower cut-off frequency of 25Hz was applied to give noise levels of +/-0.005 m/s.

The force sensor used is the Interface 101AF-2.5kN-B rated at 2.5 kN and natural frequency of 6.9 kHz. Although the error of the sensor is listed as +/-0.7 N, in reality due to close proximity with the linear permanent magnet motor the noise levels were as high as +/-12 N and also occurring around 50 Hz. A first order filter was applied with cut-off frequency of 40 Hz is applied and reduced noise levels to +/-1 N.

Later on in the Thesis simulation and experimental results show that delays within the test rig control loop have detrimental effects on control stability. One of the major sources of delays in the experimental system was found to be due to filtering applied on the sensor signals. This includes the displacement and velocity of the suspension which is used as an input to the MIL suspension numerical model, the displacement of the hydraulic actuator which is used to control the sprung mass position, and force readings for suspension force control and as input into the MIL vehicle structure model.

Delays emanating from low pass filters for the listed sensors will add up to the overall system delay. With hindsight more effort should have been made to improve the test rig performance by utilising filters with better delay characteristics. Alternative filters that could possibly be applied to improve delay times are higher order filters, non-causal filters and notch filters. Another solution would be to use a velocity transducer which will circumvent the need for filtering of the differentiated displacement signal.

3.5 Dynamic Similitude Testing

One of the benefits of hybrid test rigs is that they lend themselves to dynamic similitude scaled testing. It is a lot easier to conduct dynamic similitude scaling when a test rig comprises of actuators with a wide force range and long stroke, rather than the alternative of finding actual scaled components. First of all it is difficult to find components that will fit the scaling requirements. In some circumstances scaling could result in a component which is not physically realizable. Another example could be a case where it is beneficial to scale the density of a hydraulic fluid, in reality it may be difficult to find a practical hydraulic system based upon the scaled fluid density. In these cases where similitude scaling is difficult to achieve, hybrid MIL systems offer a simple way of scaling by simply altering the numerical model MIL simulation. In this section a background introduction of dynamic similitude scaling is discussed.

The Buckingham Pi Theorem is an estabilished method for dimensionless analysis. It allows the scaling of systems dimensions so that the resulting scaled system could be scaled back to the original system as long as the scaling factors are known.

Given n variables and m primary dimensions in a given system of homogenous set of equations, there will be $n - m$ dimensionless groups, also called Pi groups, which define the system. A system is

scaled by applying a scaling factor to the Pi groups. The Pi groups are chosen arbitrarily, normally in terms of ratios that have physical significance.

Dynamic Similitude of Boeing 707

Here an example of similitude scaling is demonstrated. The landing gear application is suitable for this rig because:

1. The MIL vehicle structure allows modelling of an aircraft flexible structure which will have coupling with the landing gear suspension.
2. Landing gear systems are very difficult to test experimentally due to their large physical size and costs associated, especially when the vibration of the aircraft structure is considered.

The scaling conducted here will be done assuming a real time configuration that uses a HIL gas spring in combination with a MIL damping suspension. The incorporation of a HIL component here is to demonstrate the ability of the technique to size real scaled components. The parameters of a Boeing 707 aircraft is obtained from a study on semi-active landing gear control [119] and shown in Table 3.1.

m_s	68210 kg
m_u	1140 kg
k_s	11250000 N/m
b_s	105400 Ns/m
k_t	8461000 N/m
b_t	0 Ns/m

Table 3.1 – Parameters of Boeing 707 landing gear.

For typical landing gear of large aircrafts such as Boeing 707, the suspension stiffness is non-linear function due to the gas spring design. Design information of landing gear by Norman Currey offers important data and guidelines in landing gear components sizing [120]. Given in the textbook the landing gear strut stroke of a Boeing 707 is 0.589m. A guide to sizing the gas spring advises that for large cargo type aircrafts the fully extended gas spring force is a quarter of the rated static load and the fully compressed gas spring force should be four times the rated static load. Using the rated load and gas strut stroke force requirements, parameters for the Boeing 707 are estimated as follows,

$$F_{gs} = P_i A_g \left(\frac{L}{L-x}\right)^{\gamma} \tag{3.3}$$

Where $F_{gs}$is the gas spring force, P_i is the initial gas charge pressure, A_g is the gas action area, x is the suspension stroke and L the gas strut length. To satisfy the design requirements from Norman Currey, the available strut stroke x is 0.589m, the gas strut force at no compression stroke is 167285N and the gas strut length L is 0.673m.

For this estimated gas spring the suspension stiffness is 3.79 MN/m at equilibrium and 24.7 MN/m at fully compressed position. The rated landing gear stiffness of 11.25 MN/m [119] does fall in between this range. The defined gas spring has an equilibrium position at 76% stroke compression compared to the rated equilibrium stroke for a Boeing 707 at 84% compression [120] but this difference is not significant.

Now with a defined gas spring, dynamical similitude scaling could be conducted so that a scaled down testing could be done using a real scaled HIL gas spring. The HIL gas spring could be constructed by connecting a hydraulic cylinder to a charged accumulator. For scaling the Buckingham Pi's theorem is applied to the quarter car equation of motion of the two masses,

$$m_s\ddot{x}_s = P_i A_g \left(\frac{L}{L-(x_s-x_u)}\right) + b_s(\dot{x}_s - \dot{x}_u) - m_s g \tag{3.4}$$

$$m_u\ddot{x}_u = -P_i A_g \left(\frac{L}{L-(x_s-x_u)}\right) - b_s(\dot{x}_s - \dot{x}_u) - k_t(x_s - x_u) - b_t(\dot{x}_s - \dot{x}_u)u \tag{3.5}$$

The two equations here have a combined total of 12 variables or n = 12. The variables are; m_u, m_s, x_s, $x_{u,}$, u, L, P_iA_g, b_s, b_t, k_t, g and t. Choosing the primary dimensions of [Mass], [Length] and [Time] to be m_s, x_s, and t the Pi groups are,

$$\pi_1 = \frac{m_u}{m_s} \qquad \pi_2 = \frac{x_u}{x_s} \qquad \pi_3 = \frac{u}{x_s} \qquad \pi_4 = \frac{L}{x_s} \qquad \pi_4 = \frac{t^2 P_i A_g}{x_s m_s} \tag{3.6}$$

$$\pi_5 = \frac{t b_s}{m_s} \qquad \pi_6 = \frac{t b_t}{m_s} \qquad \pi_7 = \frac{t^2 k_t}{m_s} \qquad \pi_8 = \frac{t^2 g}{x_s}$$

The scaling factor is defined as,

$$\lambda_{x_s} = \frac{x_{s\,Rig}}{x_{s\,Real}} \tag{3.7}$$

From the Pi groups and definition of the scaling factor, relationships of the scaling factors in order to remain dynamical similitude is given by,

$$\lambda_{m_s} = \lambda_{m_u} \qquad \lambda_{x_s} = \lambda_{x_u} \qquad \lambda_{x_s} = \lambda_u \qquad \lambda_{x_s} = \lambda_L \qquad \lambda_{m_s}\lambda_{x_s} = \lambda_{P_iA_g}\lambda_t^2 \tag{3.8}$$

$$\lambda_{m_s} = \lambda_{b_s}\lambda_t \qquad \lambda_{m_s} = \lambda_{b_t}\lambda_t \qquad \lambda_{m_s} = \lambda_{k_t}\lambda_t^2 \qquad \lambda_{x_s} = \lambda_g\lambda_t^2$$

The requirements of the test rig and their components will help determine the scaling of the Boeing 707 down to a size which is compatible. The scaling is done under the assumption that a HIL gas spring will provide the spring force while a MIL suspension damper provides the damping force. The requirement is a suspension stroke that is within the electric actuator stroke of 0.21 m and force generation capability of 1860 N.

Rig Suspension Stroke	0.18 m
Rig Sprung Mass	200 kg
Time Scaling Factor	1
Boeing 707 Landing Velocity	3 m/s

Table 3.2 – Defined rig parameters used for calculating other scaled parameters.

The requirements for the rig shown in Table 3.2 provides the basis for deriving other scaled parameters.

Rig Gas Spring Force Constant	395 N
Rig Damping Coefficient	772 Ns/m
Rig Maximum Velocity	0.966 m/s
Rig Maximum Damping Force	747 N
Rig Wheel Mass	8.36 kg

Table 3.3 – Calculated scaled rig parmeters from scaling law and rig requirements.

From the parameters of the rig in Table 3.2, the parameters of the Boeing 707 landing gear in Table 3.1 but with the gas spring strut in Eq. 3.3 and the scaling factors in Eq. 3.8, the rest of the rig parameters are calculated as shown in Table 3.3.

The rig maximum damping force is calculated from the scaled landing velocity multiplied with the scaled damping coefficient, which at 747 N is well within the electric actuator force capability. Now with a gas spring force constant of 395 N a cylinder and accumulator can be chosen to fit the requirement. The stroke of the cylinder stroke should be chosen to be equal to that of the suspension at 0.18 m, and the area of the cylinder determines the accumulator initial gas pressure. To maintain similitude the ratio of the volume of cylinder to the volume of the accumulator must satisfy the ratio of x to L. For example if a cylinder with 0.18m stroke and a piston area of 0.0012 m^2 and volume of 209e-3 m^3, the initial accumulator pressure should be at 3.41 bar at a volume of 334e-3 m^3. It should be noted that the effect of displacement scaling, without scaling time, results in velocity and acceleration scaling factors that are not unitary. A non-unitary acceleration scaling factor would mean that acceleration due to gravity is also altered. In a horizontal rig setup scaling of gravitational acceleration is much easier to achieve compared to a vertical setup.

The example above is conducted arbitrarily for a HIL gas spring and MIL damping suspension as a demonstration of application of Buckingham Pi theorem to the test rig. The example was also conducted for real time testing, or in other words the time scale is kept at unity. Pseudo-dynamic testing can also be achieved by introducing an expanded time scale which would lessen the real time frequency requirement for MIL actuators. For the example above, the sprung mass maximum velocity requirement of 0.966 m/s is greater than the hydraulic actuator maximum velocity of 0.3 m/s. It is circumstances like this that pseudo-dynamic time scaling could be applied to lower the velocity requirement. In principle pseudo-dynamic scaling follows the same procedure as for real time scaling apart from the assignment of the time scaling factor and is therefore not exhibited here.

3.6 Rig Performance Validation

In this Section experimental results are presented and compared to a simulation of the ideal emulated system. The results provide a basis for the assessment and validation of the test rig's capability in capturing correct system dynamics. The accuracy of the test rig can only be made by comparison of the rig with a pure simulation model. This comparison is made difficult by real components within the rig such as the wheel and tyre as this would necessitate comparing the rig performance with a simulation which also models the experimental wheel and tyre. With this approach it will be impossible to distinguish whether the discrepancy between the rig and the pure simulation model are results of test rig errors, or the modelling errors of the real components in the simulation. Furthermore there is friction in the railings which would also have to be modelled to allow a comparison.

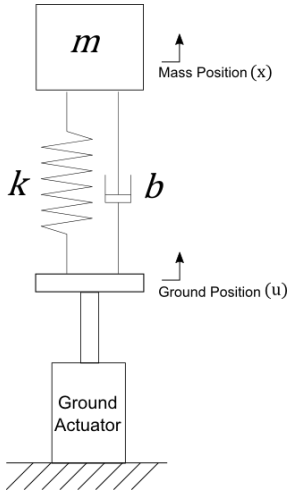

Figure 3.9 – Equivalent mechanical diagram of rig for single mass spring damper emulation test.

To evaluate the performance of the actuator and sensor transfer function, a simple linear spring and damper system was modelled. Figure 3.9 illustrates the equivalent mechanical diagram of the emulated test rig when the wheel and tyre is ignored and thus simplifying the two mass system into a one mass system.

Figure 3.10 shows the closed loop control schematic of the single mass test setup. Here the wheel and tyre is ignored by using ground position as an input to the MIL suspension numerical model instead of the wheel position, in effect the suspension displacement becomes the difference between mass and ground position, as opposed to mass and wheel position. For the emulation test the suspension is purely MIL and there are no HIL components in order to aid the comparison between test rig results and the pure simulation model.

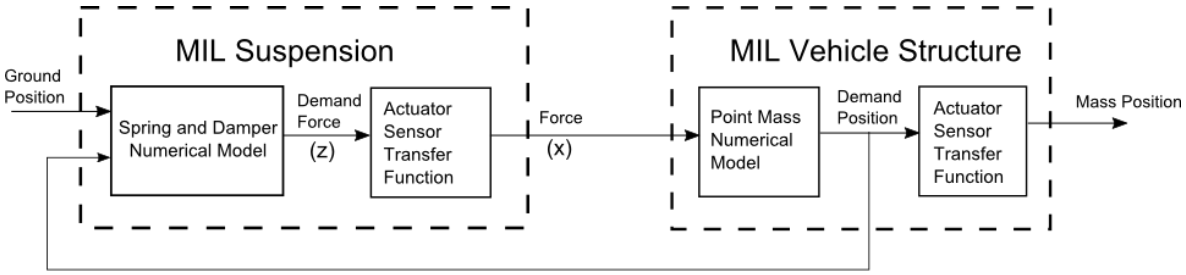

Figure 3.10 – Control schematic of single mass spring damper emulation test.

For the rig validation test the MIL suspension model comprises of a linear spring and linear damper and MIL vehicle structure formulated as a point mass. The parameters of the test are chosen arbitrarily and shown in Table 3.4.

Sprung Mass	25 kg
Suspension Stiffness	350 N/m + 220 N preload
Suspension Damping	30 Ns/m

Table 3.4 – Single mass spring damper parameters for rig validation test.

Results of a drop mass test with no ground input are shown in Figure 3.11 and 3.12. The initial conditions of the test are zero sprung mass velocity and the suspension in extension of 0.072m above equilibrium. This type of drop test is equivalent to an aircraft landing at zero vertical velocity; it is also a demonstrative test of a vehicle's responsiveness to settling down due to a positional disturbance.

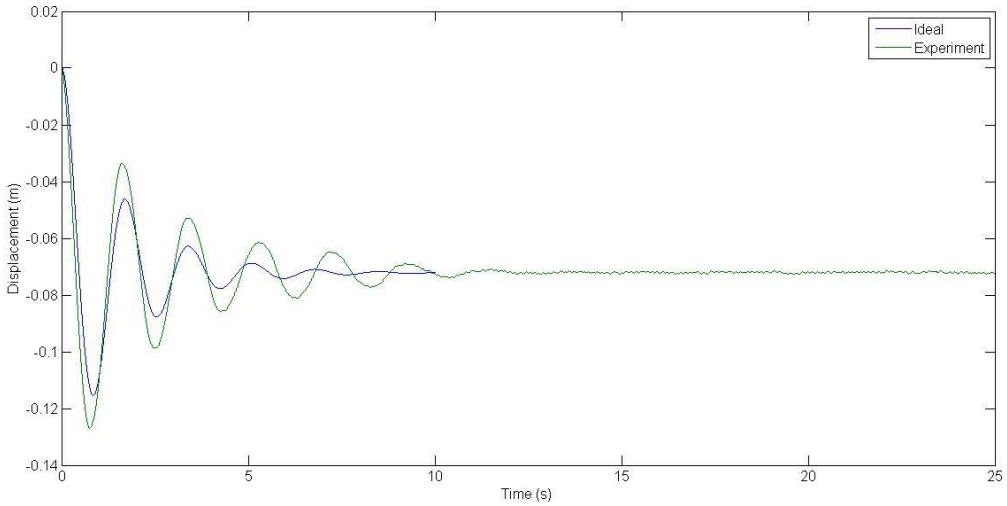

Figure 3.11 – Command sprung mass position time history for drop test with no ground input.

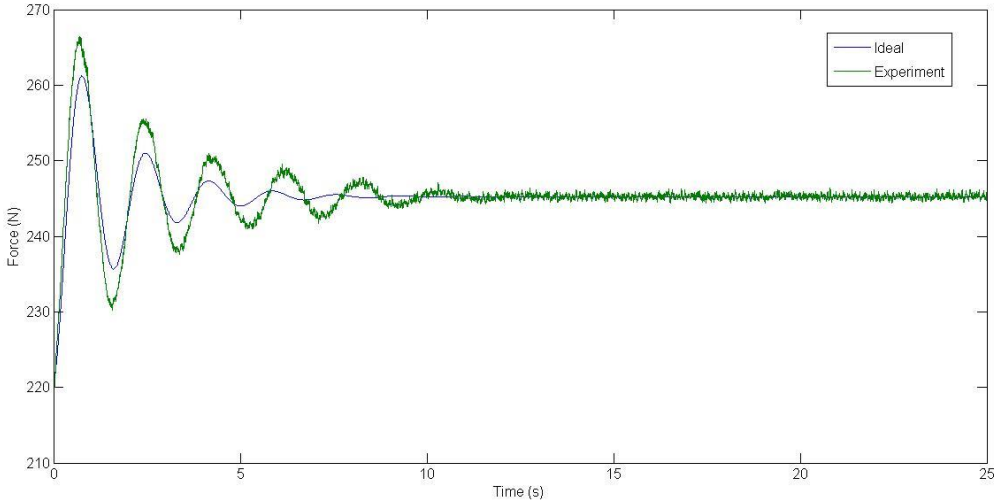

Figure 3.12 – Command force time history for drop test with no ground input.

The results from Figure 3.11 and 3.12 show the same trend because the sprung mass position and suspension force are directly linked entities within one closed loop, as governed by the numerical model, such that high peak mass displacement leads to high peak force determined by the spring stiffness. From the drop test displacement response observed in Figure 3.11, there is peak amplitude overshoot and a slight difference in the natural frequency when comparing the ideal and the experiment.

The coupling between sprung mass position and suspension means that the error of each MIL is propagated into the next MIL in a recurring loop that accumulates numerical model errors. Because of this the numerical model accuracy (e_1) of the rig may either be measured in terms of force error or in terms of mass position error.

The numerical accuracy of transfer function is described by the error e_1 observed in Figure 3.11 and 3.12. The tracking errors of the mass position and suspension force are presented in Figure 3.13 and 3.14 respectively. From the figures it can be seen that for both systems the actual output is always lagging the demand. Reduction of the transfer function delay would lead to a reduction in numerical model error and improved test rig accuracy. Another source of error that is clearly visible in Figure 3.14 is force error due to friction. The Coulomb friction in the actuator causes a sign change in the friction level which adds to the actuator force resulting in a step change in real suspension force. The errors due to friction and compensation methods are discussed in detail in the next chapter.

The drop test is repeated with ground input excitation. The ground input is pseudo random made up of a summation of sine waves of different frequencies, amplitudes and randomised initial phase. The amplitude of the sine wave at each frequency follows the spectral density model of motorway road [25]. The ground input is depicted in Figure 3.15 has a frequency range 0.0158 – 0.576 Hz and is representative of vehicle travelling at a velocity of 65 km/h.

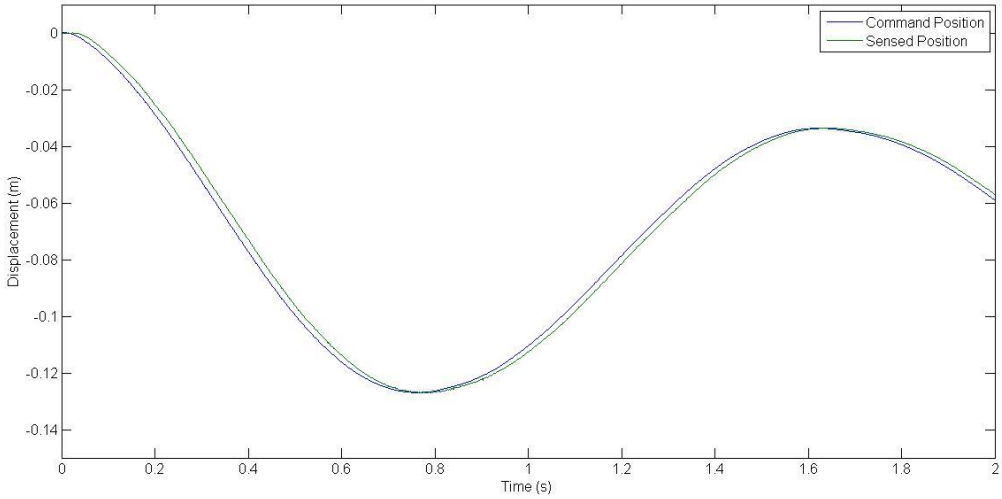

Figure 3.13 – Sprung mass position tracking error.

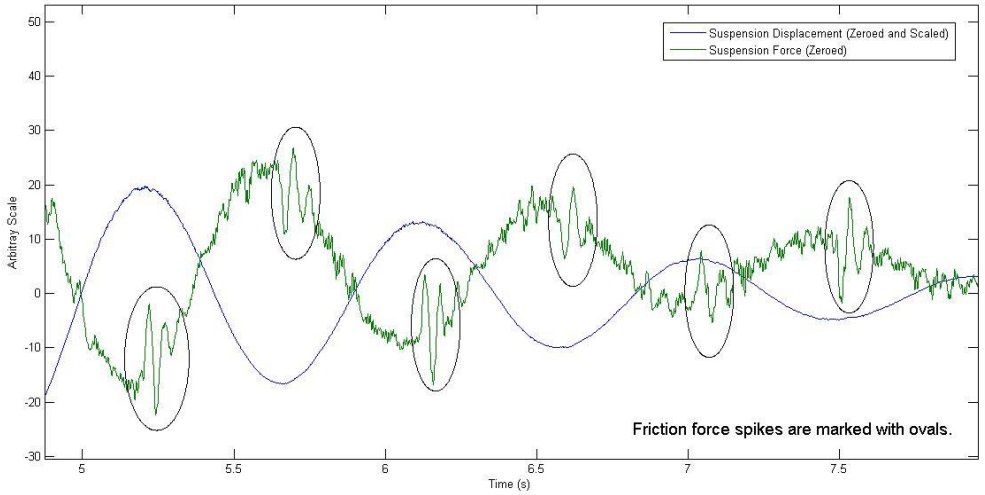

Figure 3.14 – Coulomb friction force spikes within the suspension electric actuator occurs when there is a change of direction in the suspension motion.

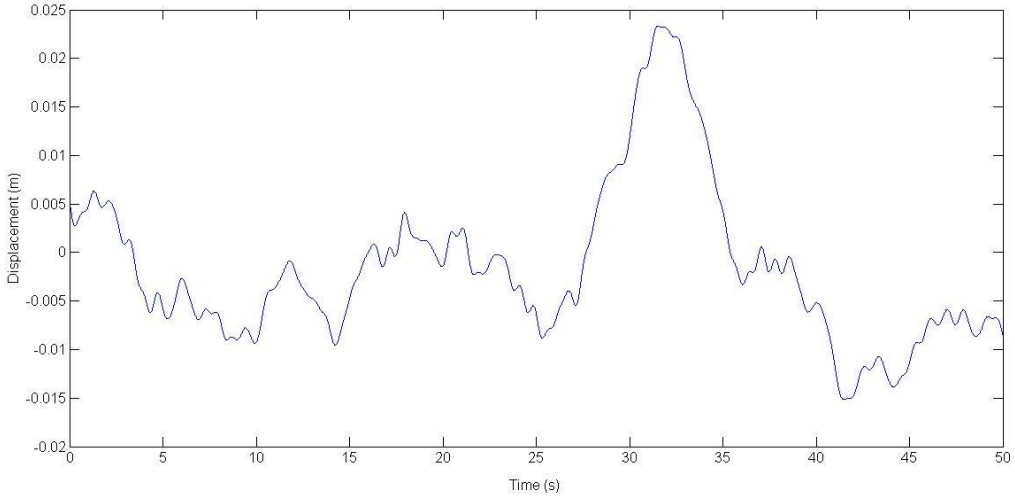

Figure 3.15 – Pseudo random ground input excitation.

Figures 3.16 and 3.17 depicts the mass displacement and suspension force time responses of the rig subjected to the ground displacement input in Figure 3.15. The results show that after the decay of the transient from the initial conditions the effect of subsequent ground inputs forces the response to closely match that of the ideal case. It is when there is no external excitation that the transient decay of the and the ideal case start to diverge as the closed loop states trajectory becomes dominated by delays which accumulate through each loop. The ground input acts as an excitation which forces the rig to a new state and hence reduces the contribution of accumulated errors from the previous excitation to the overall response.

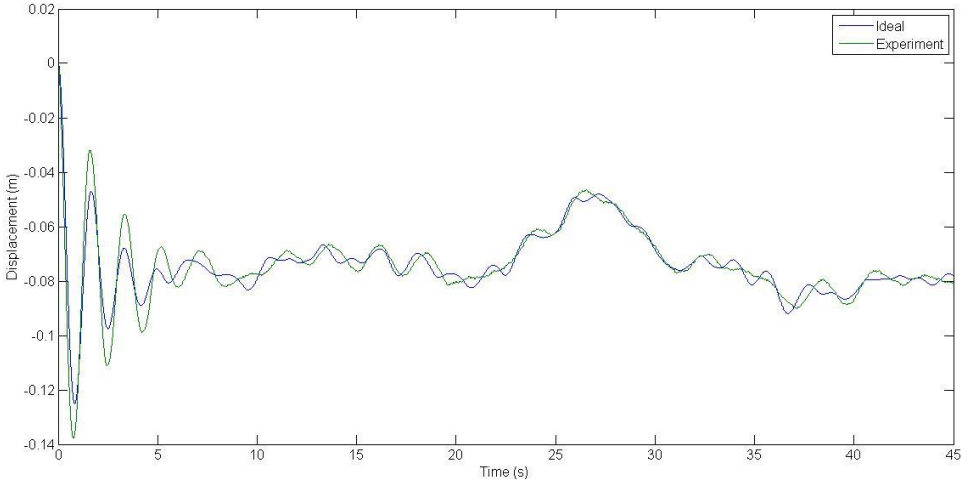

Figure 3.16 – Command sprung mass position time history for drop test with pseudo random ground input.

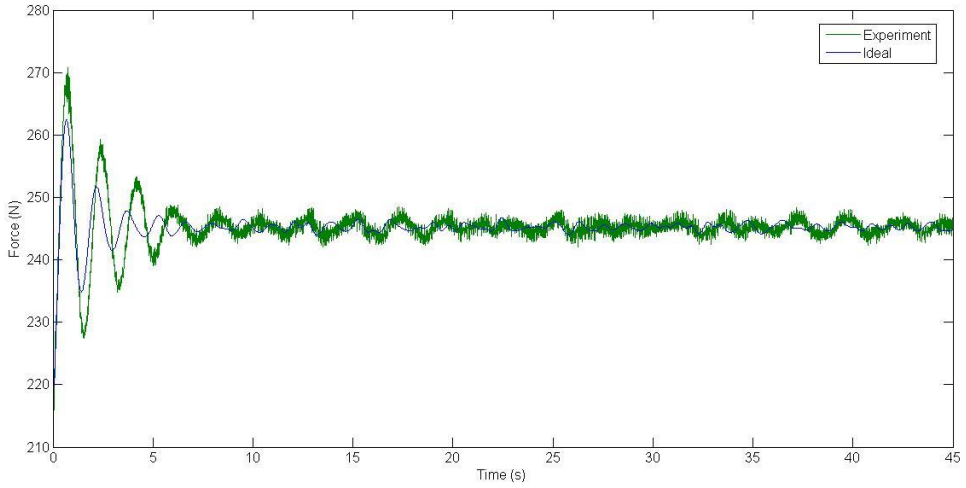

Figure 3.17 - Command force time history for drop test with pseudo random ground input.

A comparison between the rig and ideal simulated system in terms of frequency response is shown in Figure 3.18. Overall the rig exhibits a natural frequency peak close to the ideal system. At higher frequencies the response is dominated by noise. This high frequency noise is the result of double differentiation of displacement readings from the LVDT sensor.

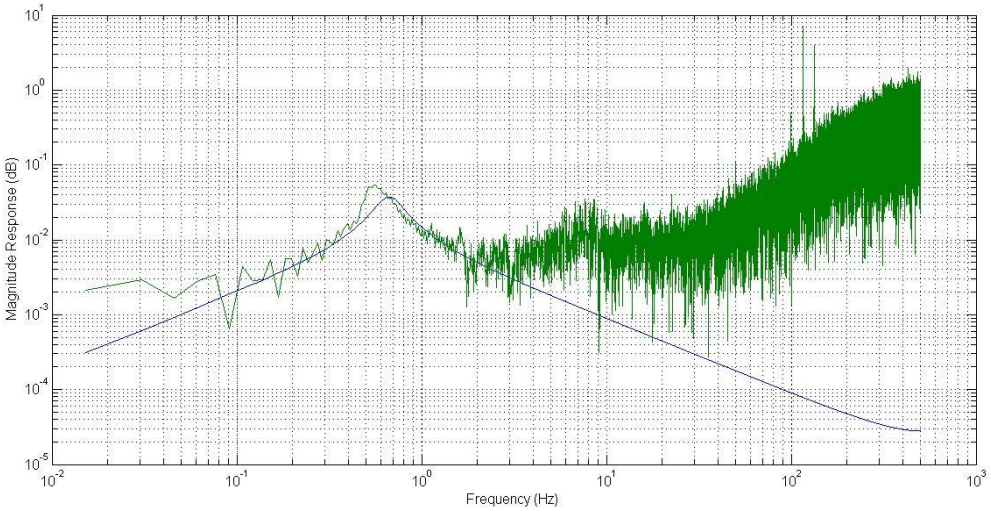

Figure 3.18 – Sprung mass acceleration against ground input velocity frequency response.

RMS error	No Ground Input	Ground Input
Position Numerical Error (Pe_1)	0.00772	0.00448
Position Tracking Error (Pe_2)	0.000777	0.000671
Total Position Error (Pe_1+Pe_2)	0.00850	0.00515
Force Numerical Error (Fe_1)	2.70	2.68
Force Tracking (Fe_2)	9.53	8.79
Total Force Error (Fe_1+Fe_2)	12.2	11.5

Table 3.5 – RMS tracking error of test rig for MIL position and force systems.

Table 3.5 presents the RMS response from the 45 s drop test for the conditions with and without ground excitation. Figures 3.19 and 3.20 shows a plot of test rig accuracy for the case without and with ground input respectively. The green line represent the test rig experimental results while the blue line is the ideal emulated simulation. For perfect actuator tracking the rig response would result in a completely diagonal line and match the ideal case. Both Table 3.5 and Figure 3.19 and 3.20 informs that for the position MIL system, the transfer function error is low, and is lower than the numerical model error while for the force MIL system, the transfer function error is high, and is higher than the numerical model error. Overall the error of the force MIL system is shown to be much higher than that of the position MIL both graphically and in terms of root mean square error. The major source of error for the force transfer function apart from time delay is Coulomb friction which occur every suspension direction change. The major source of error for the position MIL is a typical transfer function time delay seen in position tracking systems.

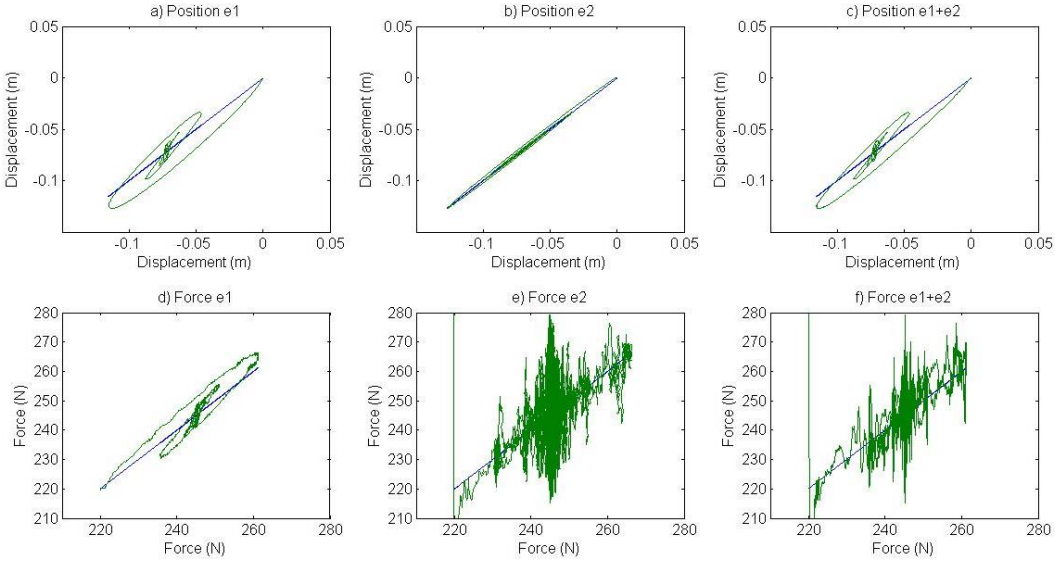

Figure 3.19 –Plot for no ground input case of rig numerical model accuracy (e_1), transfer function accuracy (e_2) and overall accuracy (e_1+e_2) for force MIL and position MIL systems.

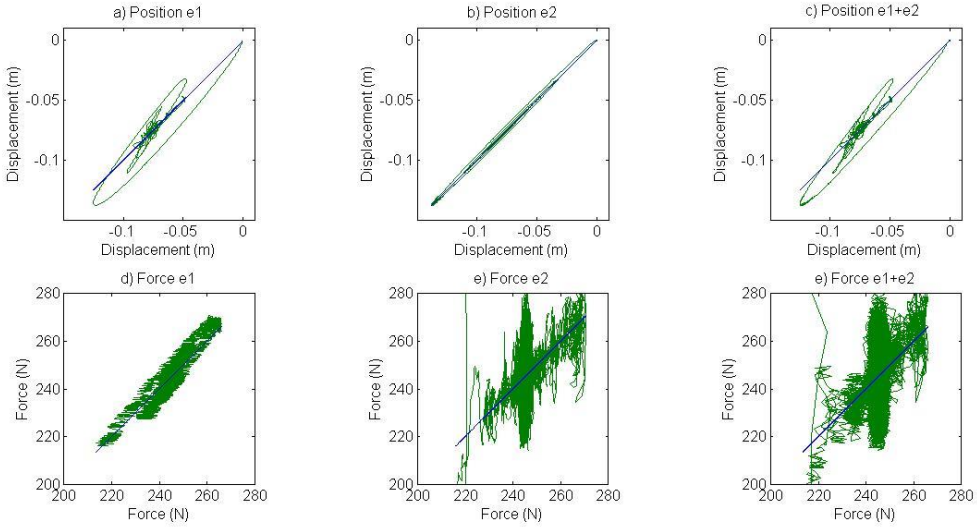

Figure 3.20 –Plot for pseudo random ground input case of rig numerical model accuracy (e_1), transfer function accuracy (e_2) and overall accuracy (e_1+e_2) for force MIL and position MIL systems.

3.7 Conclusions

In this chapter a brief literature background on hybrid numerical-experimental testing is discussed along with advantages and disadvantages of the method. It was concluded that a suspension test rig with a suspension MIL and a vehicle structure MIL is ideal for the rapid prototyping and comparison of various suspensions even though there may be a number of complications that affect the test rig performance.

The mechanical design of the test rig is both discussed and presented in this chapter. Detailed information is also given on the components utilised such as actuators and sensors. The control schematic of the rig is described showing mechanical and numerical interactions between the physical and the virtual components. One of the major benefits of a MIL hybrid test rig is that it is highly feasible for scaled testing. After the description of the test rig, a demonstration of dynamic similitude scaling is used to show how testing large scale structures such as a commercial aircraft landing gear could be implemented.

Finally, the chapter contains experimental results for the test rig validation. The results showed that for the conditions chosen, the rig has a reasonable performance and accuracy. The major sources of rig errors are due to delays in the actuator transfer function and also friction within the linear motor. Since the linear motor is in force control, reversals in actuator velocity will cause friction to change sign, which is analogous to adding a step disturbance to the force output. The results in this chapter showed that the numerical and transfer function errors are far greater for the suspension MIL than the hydraulic actuator MIL. Therefore the focus on performance should be in improving the tracking performance of the electric actuator using friction compensation; this is the topic of the next chapter.

4. Friction Compensation

4.1 Introduction

This chapter contains work on improving the accuracy of a MIL suspension test rig by using a controller which compensates for the friction forces. A novel friction compensation method is proposed and has been pubished at the UKACC conference, the paper is tittled “Friction compensation for a force controlled electric actuator with unknown sinusoidal disturbance motion” [121] . A submission of an extended version, which is based on the complete Chapter 4 of this thesis has been accepted for publication in Proceedings of the IMecE Part C Journal of Mechanical Engineering Science on 12 Janaury 2015 and is awaiting publication, the paper is titled “Friction Compensation using Coulomb Friction Model with Zero Velocity Crossing Estimator for a Force Controlled Model in the Loop Suspension Test Rig”.

Results for the friction compensation method are only exhibited in Chapter 4 and not the final experiments in Chapter 6 and 7. This is because the same performance improvements due to friction compensation will be seen in the results and therefore considered unnecessary. Furthermore in Chapter 6 and 7 the focus was upon validating test rig capabilities as studied in Chapter 5.

Friction compensation is an extensively studied topic in engineering control literature [122]. A common class of friction compensation technique is feedforward and feedback model based compensation. Here friction is estimated using a motion based model where the input into the model is either the reference motion signal (feedforward) or a measured motion signal (feedback) [122]. Many applications of friction compensation that have been studied are for actuator positioning systems. The general lack of force sensors in typical position control systems has driven research to focus on implementing friction compensation without measuring the friction force directly. Instead friction forces are estimated using friction models based upon motion, also known as model based compensation [123]. In these systems the motion reference is known in advance so both feedforward and feedback motion based models can be used.

Classical models of friction include Coulomb and Stribeck friction models where the friction force is a simple function of velocity [122]. More complex dynamical models, such as the Lugre model incorporate rate dependent characteristics such as varying break away force and frictional lag [122]. Despite the comprehensiveness of dynamical friction models they present certain drawbacks in practical friction compensation. Complex friction models require well calibrated parameter identification and can be subject to variation from wear and tear or changes in alignment of the rig set up. Although complex dynamic models take into account the effect of small pre-sliding displacement, usually the effects are too small to be measured by typical position sensors [123]. Another difficulty with dynamic models such as the Lugre model is the requirement of an internal friction state with fast dynamics. It has been reported that the delays in the dynamic internal friction state which results from digital control are poorest at velocity reversals which may also lead to limit cycles [123].

For these reasons, although the Lugre model receives widespread attention, there has been limited practical implementation due to realization difficulties [124]. The authors here also successfully demonstrated feedback friction compensation for position control in a table drive mechanism with linear motors using the Lugre model and a disturbance observer. To avoid difficulties of applying dynamic friction models to typical CNC machine tools, in addition to PID control, a double pulse compensation signal was devised based on analysis of the transient friction error at velocity reversal where friction effects were greatest [125].

Other than computational issues, the practical benefits of using a friction model depend largely on the quality of motion measurements available. Velocity information obtained from the differentiation of position signals can be inaccurate due to the noise in position sensors, with the errors more significant at low velocities. Methods of filtering or estimating a more precise value of velocity usually involve a trade off in terms of signal delay and accuracy. Some studies have concentrated efforts on improving velocity estimation, especially at low velocities, for the application of friction compensation, such as in [126] and [127]. In [126] velocity estimation was obtained by varying the sampling period of encoder counts, depending on the actuator velocity. In [127] an adaptive differential filter for velocity estimation is presented.

The task of force control and friction compensation for the MIL suspension test rig has a lot of similarities to force control in haptic interface applications, more so than force control in actuator positioning systems. Haptic interface devices with force feedback are required to transmit a force towards a user who is physically controlling the device motion, here precise force control in presence of motion disturbance is needed for transparent force rendering [123, 128]. In these studies a force sensor is used for force feedback as it gives a more direct, reliable and accurate reading of force compared to the estimation of force from motor current. In both [123] and [128] force feedback is utilised in combination with model based friction compensation, and in [128] a comparison was also conducted between different friction models. In [129] a HIL test rig for an aircraft load simulator was achieved using force feedback in combination with a feedback Lugre friction compensation model; the experimental results verified high force tracking performance.

Similar to force feedback haptic interface applications, the test rig studied here attempts to output actuator forces independent of actuator motion disturbance, prohibiting the use of feedforward model based friction compensation since suspension motion is not pre-determined. This leaves only the option of model based feedback friction compensation in conjunction with force feedback as a practical approach. Initial testing of the actuator showed that a proportional-integral force feedback controller is capable of compensating for friction except in velocity reversal regions. This suggests that performance levels similar to a complex dynamical model such as the Lugre model can be achieved using a simple Coulomb friction model. Research on friction compensation for a position controlled table drive in [130] demonstrated that friction characteristics are predominantly Coulomb during dynamic motion when examined using a dynamic friction model with elastic bristles.

In this chapter a method of Coulomb friction compensation with force feedback control is presented. To deal with issues of motion sensor inadequacies, an algorithm which detects when velocity reversal occurs using information from both force and position sensors is utilised. The proposed method offers a simple and effective method of compensation for systems equipped with force sensors.

4.2 Experimental Rig

The rig is setup according to Figure 3.9 and Figure 3.10 where rig accuracy tests can be conducted and compared to the ideal emulated simulation since the test setup contains no real components. To investigate the accuracy of the substructure rig, the suspension numerical model is chosen as a passive linear spring and damper. The choice of suspension components to be emulated by the numerical model would affect the accuracy of the test rig if the profile of output forces cannot be satisfactorily achieved by the chosen actuator, or if the chosen pseudo mass of the structure is so small such that small force tracking errors lead to large mass accelerations.

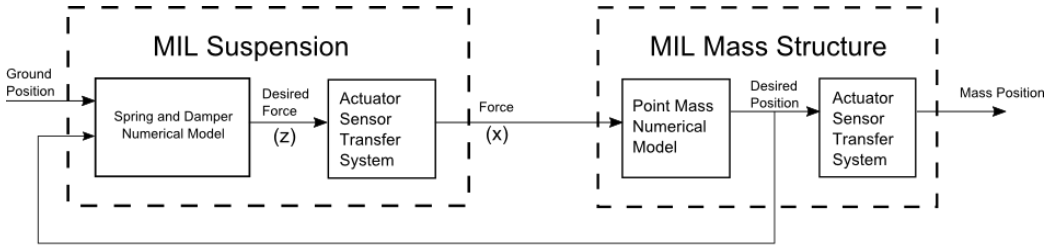

Figure 4.1 – Control schematic for the MIL suspension force only test rig.

Since the aim here is concerned with friction compensation for a MIL suspension force tracking application, rig tests were performed assuming that the sprung mass transfer function and position measurement system has no error or delays. This was achieved by feeding back the sprung mass structure numerical model output of command position and velocity as inputs into the force numerical model as shown by Figure 4.1. With this setup all the errors in the system would be solely caused by errors in the force MIL suspension.

4.3 Controller Structure

The MIL suspension actuator used in the test rig is a Dunkermotoren permanent linear magnet motor STB38 which has a built in amplifier and current controller. The built in proportional, integral and derivative (PID) current control loop acts as the inner control loop. An outer control loop is designed to control the force of the actuator via force feedback and the control gains acting upon the force error provide a demand current input to the inner control loop.

The force controller has the structure of a standard PI feedback controller shown in Figure 4.2. Furthermore a feed forward reference signal is incorporated to improve the performance of the actuator since motors force and current are typically proportional. Following the concept of Coulomb friction compensation the control architecture is designed to input a step command current which cancels out the Coulomb friction step change at the instance of velocity reversal.

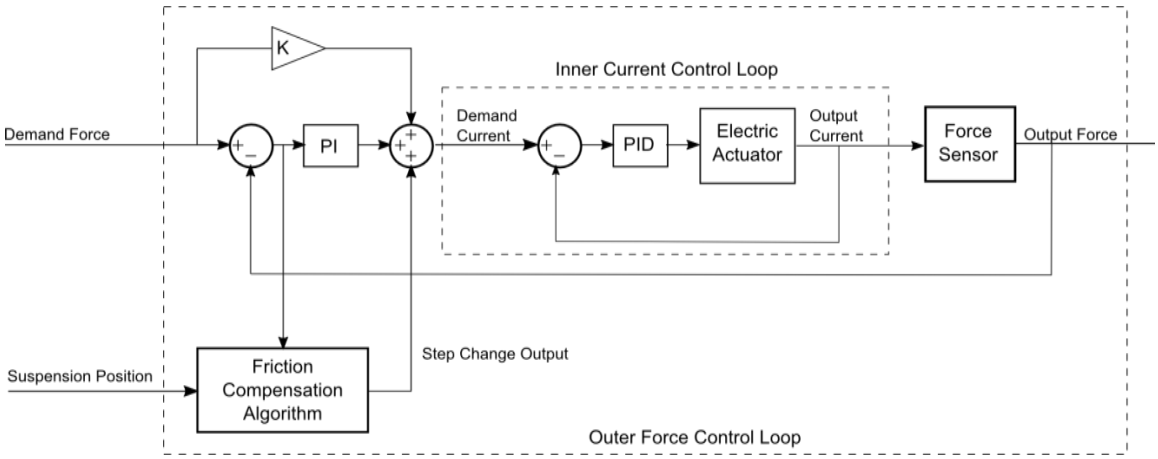

Figure 4.2 – Force Controller Structure.

4.4 Friction Compensation for Deterministic Systems

The suspension test rig shown in Figure 3.9 and following the block diagram shown in Figure 4.1 was subjected to a road input displacement signal as shown in Figure 4.3 (a). The disturbance ground input is a superposition of sine waves with random phases and amplitudes following the spectral density profile of a motorway road obtained from [25]. It corresponds to a vehicle travelling at 225 km/h from with frequencies limited between 0.1 and 5 Hz. The period of the pseudo random input is 10 seconds and repeating cycles were used for experiments. Figure 4.3(b) and Figure 4.3(c) show the resulting suspension displacement and velocity respectively. Here the suspension displacement denotes the displacement between the ground and the sprung mass.

Figure 4.4 presents the suspension force error (e_2) when subject to the road input in Figure 4.3. This shows that at higher velocities the force tracking error magnitude is relatively small, suggesting that most viscous friction is compensated for. This indicates that the error caused by Coulomb friction is much more severe than viscous friction as shown by the large force error at zero velocity. From Figure 4.4 'no motion' represents the experimental case where the ground and sprung mass position are kept constant. Here the suspension velocity is actually zero and the presence of non-zero velocity in Figure 4.4 is a result of noise from velocity readings.

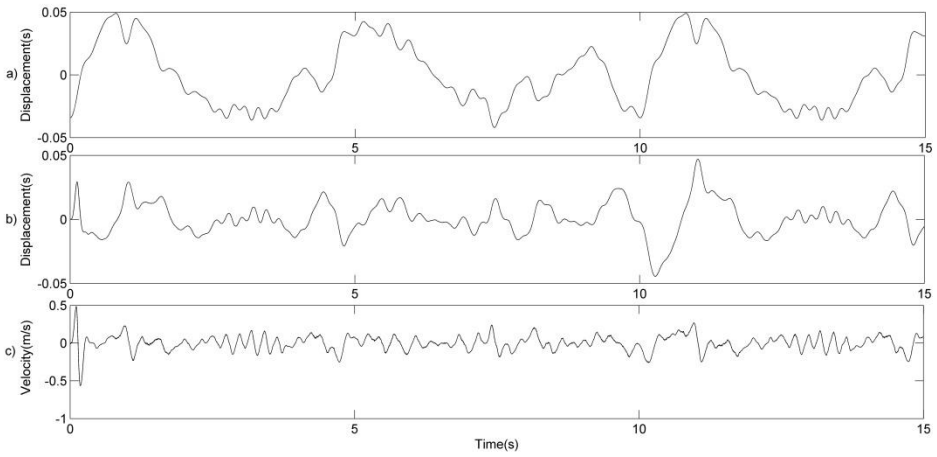

Figure 4.3 – Road input disturbance and the resulting rig motion profile. a) Road displacement, b) suspension displacement, c) suspension velocity.

These results suggest that major improvements in force tracking could be achieved by compensating for friction only at velocity reversal. The Coulomb friction model, shown in Figure 4.5 is chosen since it is the simplest method which captures the characteristic of friction at velocity sign changes. More complex static models and dynamic friction models are also avoided due to the difficulty of parameter identification and the requirement of very precise motion sensors [123]. This is in agreement with the finding in [130] that the non-linear friction characteristic of a table drive is expected to behave as simple Coulomb friction when under dynamic table motion. Furthermore the friction characteristics of permanent magnet linear motors are commonly modeled using classical static friction models as illustrated in Figure 4.5 [131, 132, 133].

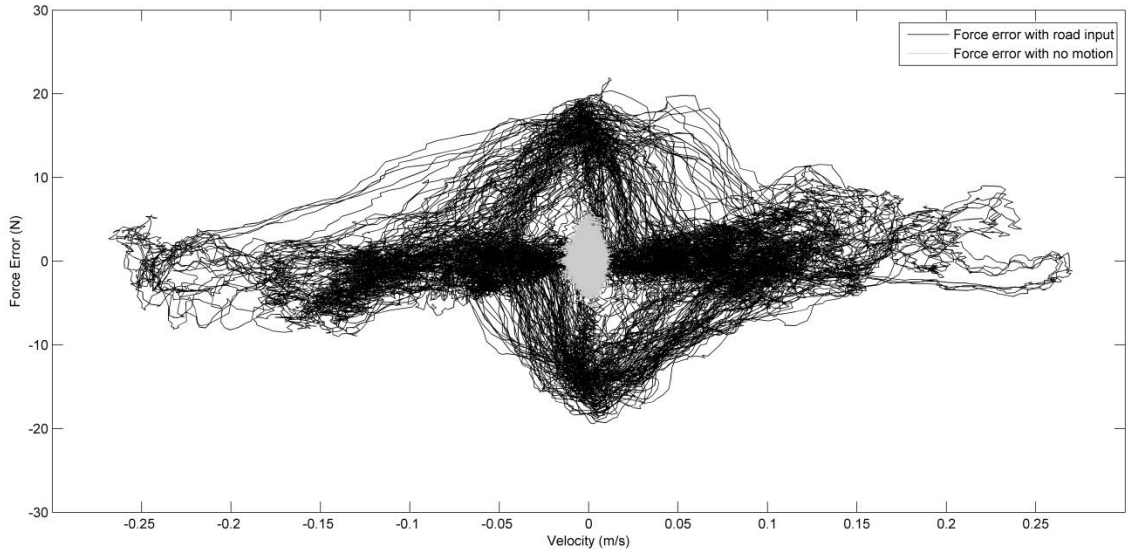

Figure 4.4 - Suspension force error vs. velocity for a constant demand force.

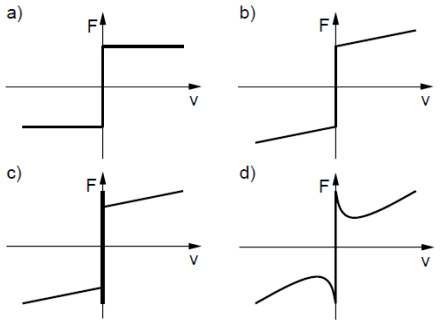

Figure 4.5 – Diagram of static friction models relating friction force as a function of velocity: a) Coulomb, b) Coulomb and viscous, c) Coulomb, viscous and stiction d) Stribeck [122].

The Coulomb friction model chosen for this study is described by,

$$f(v) = \begin{cases} F_c \times sign(v), & if\ v\ \neq 0 \\ -F_c \leq f(v) \leq F_c, & if\ v = 0 \end{cases} \quad (4.1)$$

Here *f(v)* is the friction force as a function of velocity *v* and F_c is the Coulomb friction force.

The results of experimental friction compensation tests using a simple Coulomb friction model are shown in Figure 4.6 where the control goal is constant force tracking while the suspension in Figure 3.9 is subjected to a sinusoidal input motion disturbance. This demonstrates the principle of Coulomb model friction compensation assuming the zero velocity points are known in advance. Here the compensation signal is a step change of 0.15 V, which results in a force equivalent to the step change in force due to Coulomb friction.

The results in Figure 4.6(a) show that the simple Coulomb model is effective at reducing the friction force spikes when compensation occurs within +/- 0.005s of the velocity reversal. Figure 4.6(b) and (c) show the effect of late and early compensation applied +/- 0.015s from the velocity reversal, which result in large force error spikes and no performance improvement. If the zero velocity estimation is determined too early then the compensation signal produces a force spike, or if too late the friction spike grows before compensation occurs.

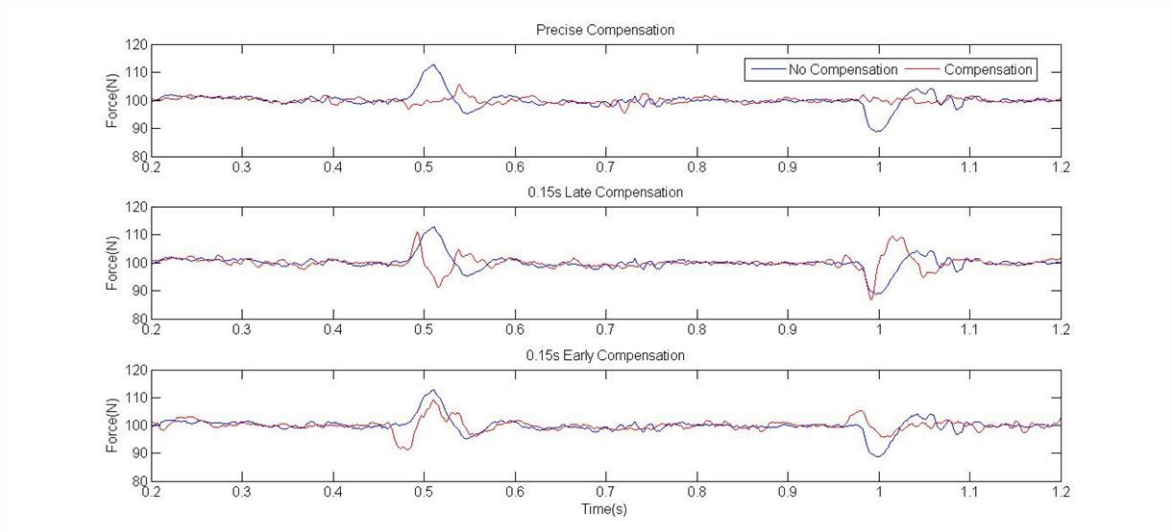

Figure 4.6 – Comparison of friction compensation step triggering times on 1 Hz suspension motion.

These experimental results suggest that the Coulomb friction model is effective at cancelling force spikes due to friction sign change at velocity reversal for permanent linear magnet motors, if velocity reversal times are known in advance (ie. the system is deterministic). This is possible for motion controlled systems where velocity reversal times are determined by the reference position profile. However for the case of a MIL suspension force control system the motion of the suspension is not determined by the suspension forces alone but in combination with the road disturbance input and sprung mass dynamics. Since suspension motion is one of the unknowns to be investigated by the test rig, there is no easy model based method of estimating suspension velocity, especially if the road input was random. Furthermore the friction compensation for the test rig is intended to be generic and perform independently of disturbance. The only way of estimating or detecting zero velocity crossing for such non-deterministic systems is through investigation of the position signals from sensors and force sensors. The aim of friction compensation presented in this paper is to form a generic method for any force controlled system by utilising a simple Coulomb friction model. Despite the simplicity of the model the previous section highlights the possible benefits and also the importance of applying the compensation signal at the precise time. The challenge therefore becomes detecting when velocity reversal has occurred, or is about to occur.

4.5 Friction Compensation for Non-Deterministic Systems

Direct velocity measurement is difficult, so often velocity is estimated from position and or acceleration measurements. The major difficulty associated with this approach is that the friction spike occurs before the obtained velocity crosses zero. This is due to both the nature of Stribeck friction and lag associated position or acceleration signal filtering.

The method described in this paper attempts to maximize the effectiveness of detecting velocity reversal by using both motion and force information in a two stage method. The first stage is to create a window where velocity reversal is likely to occur. The second stage is then to look within the velocity window for a force profile which matches a known example friction spike which is experimentally obtained beforehand in a parameter identification process. The major benefit of using this force information to apply the compensation trigger is that it guarantees that the friction compensation signal is applied at the correct time provided that the detection is correct.

4.5.1 Zero Velocity Crossing Estimation

The velocity crossing window is estimated simply by using velocity and acceleration data at the current time step. Assuming constant acceleration, the predicted time to velocity zero crossing can be obtained from:

$$T_0 = -v/\dot{v}, \tag{4.2}$$

Here T_0 is the estimated time until velocity crossing and v and $\dot{v}$ are respectively the velocity and acceleration of the linear electric actuator.

Tests conducted on the suspension rig for different frequencies and amplitudes of sine wave motions indicated that the start of a friction spike consistently occurred within 0.02 seconds before the zero crossing of the filtered velocity signal. Therefore a threshold of estimated velocity zero crossing time of 0.03 seconds could be used to ensure that a window is activated within a force spike. This difference in time between the force spike and the velocity crossing zero varies depending on the frequency and amplitude of the sine wave motions and also the bandwidth of the velocity filter. An appropriate time till velocity zero crossing threshold T_T can be easily determined experimentally for any rig. Window activation rules are presented in Rule 1.

Rule 1 - Window Activation

Window = 1 if ($T_0 > 0$) AND ($T_0 < T_T$) AND ($v > 0$),	*Positive to negative crossing activation.*
Window = -1 if ($T_0 > 0$) AND ($T_0 < T_T$) AND ($v < 0$),	*Negative to positive crossing activation.*
Window = 0 if ($T_0 < 0$) OR ($T_0 > T_T$),	*Window inactive.*

One implementation difficulty with this method is that, if the acceleration signal is lagging the velocity signal, then in certain cases velocity reversal can occur without the window being activated.

This lag would be the present if acceleration is obtained by differentiating the velocity signal which would likely require filtering to reduce noise.

Another solution explored here is to forward predict the velocity signal using a polynomial extrapolation which is then differentiated. Although this reduces the accuracy of the acceleration signal the improved experimental results suggest that the window is sensitive to lag of acceleration signal. Although this method is effective in certain cases, there are also instances where because of future prediction, the obtained acceleration could be leading the velocity signal such that acceleration switches sign prior to the actual velocity zero crossing. In these cases although a window is initiated it may be cut short before a friction force spike could be detected. To alleviate this problem two estimation windows were used in combination to ensure that both cases are dealt with, one based on a short time lag acceleration signal obtained from forward prediction and the other a low pass filtered acceleration signal with a longer time lag but less noise.

Another problem that could occur is that, due to the noise in the velocity signal, it is possible that at low velocities the signal could switch sign momentarily before the real zero crossing. This means that due to noise the window could change from active to inactive before a force spike occurs. The algorithm is adapted to deal with this issue by extending the window for a few time steps after zero velocity crossing as a preemptive action that the velocity zero crossing may be due to noise.

4.5.2 Force Spike Detection

The friction force spike detection algorithm is only active when the velocity zero crossing window is active. Since the force spikes are a result of the interaction between controller, sensors, friction, motion and force trajectories, the profile of the force error spike is not predictable. However there are still generalities that can be established, such as a minimum gradient of the rise, and a force error threshold which can be used to distinguish the friction spike from those caused by other errors. The aim is to detect the initial rise of the force error spike so that compensation is applied as quickly as possible for maximum effectiveness. Rule 2 demonstrates the concept and application of the force spike detection algorithm.

Rule 2 - Friction Force Spike Detection Algorithm

Conceptual Rule:

1. Window Condition: Velocity zero crossing window is active, the direction of the expected crossing determines the direction of the expected gradient change and force error.
2. Force Error Condition: The absolute force error value of the current time step must be equal or greater than the force threshold.
3. Force Error Rise Profile Envelope Condition: For a specified number of previous time steps, define a minimum absolute gradient between the force error for each subsequent time step.

Algorithm:

$$Force\ Detect = True,$$

$$If\ for\ n = 1{:}N\ (Window = 1)\ \&\ (F_E(i) > F_T)\ \ \&\ \ \left(|F_E(i-n+1) - F_E(i-n)|\ > G_T(n)\right)$$

$$Else\ If\ for\ \ = 1{:}N\ (Window = -1)\ \&\ (F_E(i) < F_T)\ \ \&\ \ \left(|F_E(i-n+1) - F_E(i-n)| < G_T(n)\right)$$

$$Else$$

$$Force\ Detect = False,$$

For logics in Rule 2, *i* is the sample of the current time step, F_E is the force error, F_T the force error threshold, G_T the gradient threshold and *N* is the number of samples. For the test conducted in this study the specific thresholds and number of samples chosen for Condition 2 and Condition 3 were determined by examination of a friction force spike obtained experimentally. An example for this process is illustrated in Figure 4.7.

Condition 1 defines the expected direction of the force error and gradient change which is determined by the direction of the expected zero velocity crossing. This constrains the direction of force error and gradient in Condition 2 and 3.

Condition 2 assigns a minimum force error threshold so that the friction force spike is detected only when a substantial force error has occurred. Choosing a low error threshold allows earlier detection of friction force spikes but also increases the likelihood of false detections due to noise in force readings. To ensure an improvement in force tracking performance the error threshold should be chosen so that it is within the bounds of force tracking error not caused by friction. For the example in Figure 4.7, the force error threshold is chosen at 4N, this is below the no motion force tracking error which is between +/- 6N shown in Figure 4.4.

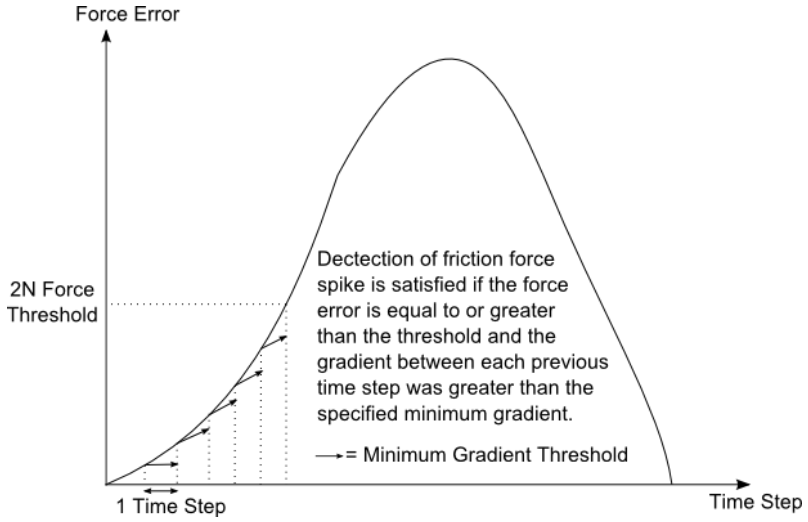

Figure 4.7 – Example diagram of force spike profile envelope for Condition 2 and 3 used in this study for a force threshold of 4N.

Condition 3 introduces a gradient threshold which is also obtained from observation of the friction force spike. After choosing a force error threshold, from the friction force spike diagram, the number of samples can be chosen so that gradient change from the beginning of the force error rise up to the threshold is constrained. This is simply creating a gradient change envelope constraining the shape of the friction force spike rise. Force error due to noise tends to be more oscillatory without such consecutive force changes in the same direction. The force profile envelope condition could be further defined to include not just the gradient but the complete force versus time profile of the friction force error spike rise. For this study, experimental results showed that good detection performance was achieved using a simple gradient envelope. The choice of the gradient envelope is illustrated by an example in Figure 4.7; five gradient samples are chosen to cover the majority of the force error rise, the initial sample has a minimum gradient of zero and the subsequent samples a minimum gradient of 0.2. The minimum gradient threshold is chosen to be substantially lower than the gradient of the actual friction force spike, this is to improve robustness and demonstrates that the capability of the algorithm does not require tight force error envelope constraint.

4.6 Experimental Results

The friction compensation algorithm was first tested with constant force tracking and single frequency and amplitude sine wave suspension motions. Figure 4.8 illustrates the performance of the detection algorithm for a 1Hz sine wave motion and Figure 4.9 for 5 Hz without actually implementing the compensation step signal. The force threshold was set to 2 to demonstrate the ability of the algorithm to correct for the friction spike early in the spike rise. Throughout a test of 25 seconds the algorithm successfully detected all friction force error spikes in early stages of the spike rise demonstrating good robustness.

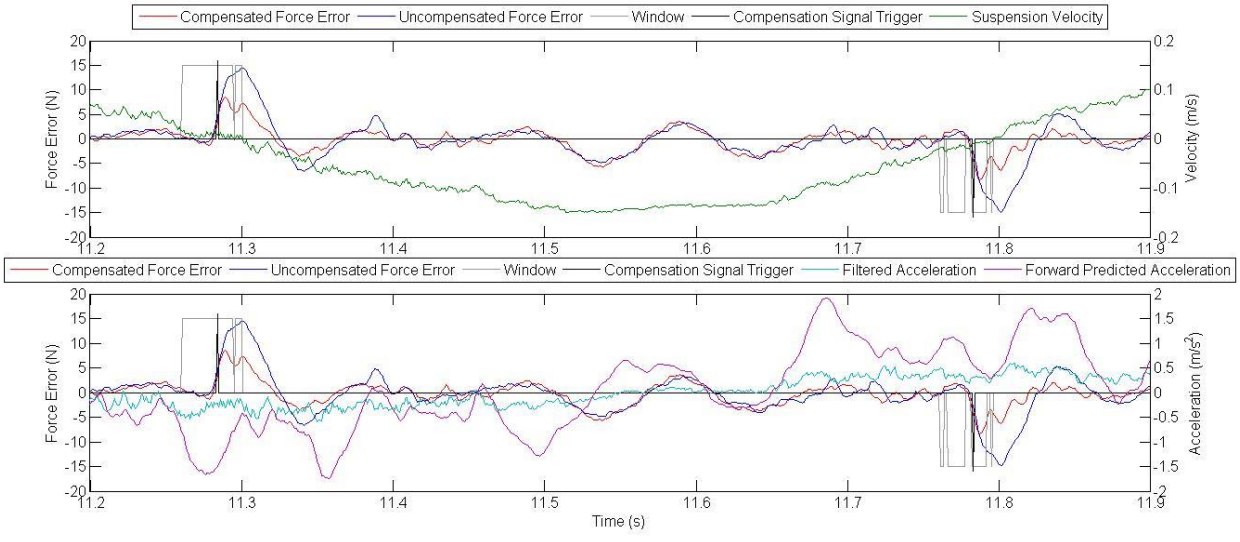

Figure 4.8 – Friction force spike detection algorithm for 1 Hz and 20 mm amplitude sine wave motion.

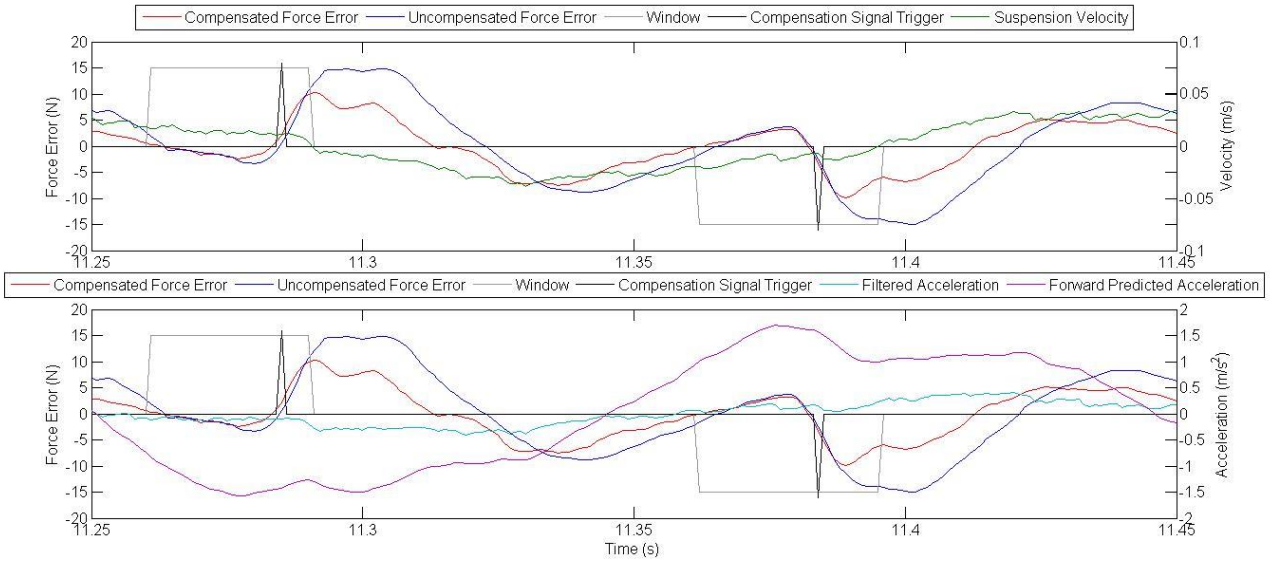

Figure 4.9 – Friction force spike detection algorithm for 5Hz and 1 mm amplitude sine wave motion.

The next step was to test the performance of the friction detection with the rig configuration emulating a single mass spring damper, using the pseudo random input disturbance as in Figure 4.3. The resulting suspension motions are a result of the interaction of the disturbance and a virtual sprung mass damper with values of; m = 25 kg, k = 350 N/m and c = 50 Ns/m. This test would differ from previous tests in that now the electric actuator is tracking a varying force as defined by the numerical model unlike in earlier demonstrations whereby the force tracking was of a constant demand. The friction compensation algorithm is applied onwards after the first second and the force demand during this period is shown in Figure 4.10.

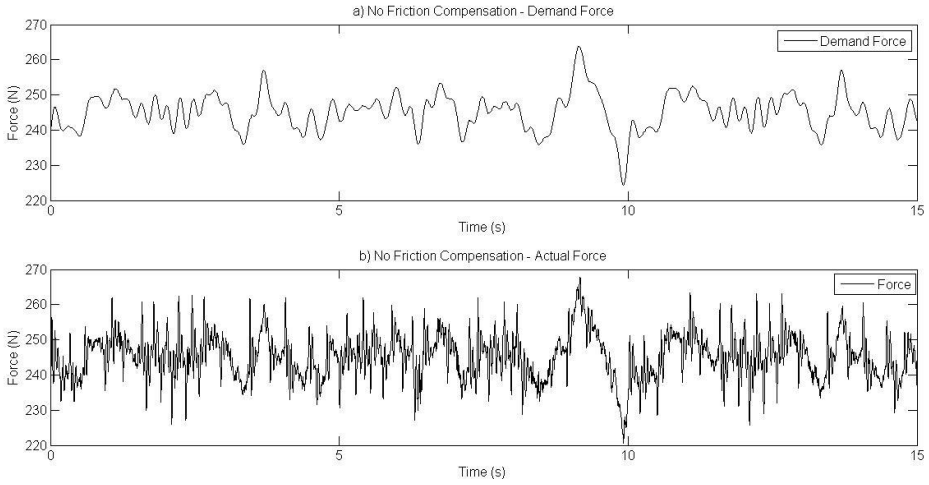

Figure 4.10 – Demand and real force for rig single spring mass damper emulation test with no friction compensation.

With the introduction of random motion the algorithm will be far less successful for two primary reasons. The first is that motion of the suspension may indicate that the velocity is crossing zero but

actually approach zero only to reverse and this would falsely trigger the zero crossing velocity windows. Secondly there are regions where suspension velocity remains low and close to zero with high levels of noise in the acceleration signal. In these conditions windows may easily be falsely activated or not activated.

The force tracking of the force profile in Figure 4.10 is likely to increase tracking errors and worsen the performance of the friction detection algorithm when compared to the constant force tracking case. Increased force tracking errors lead to greater possibility of the triggering of false friction force spike detections.

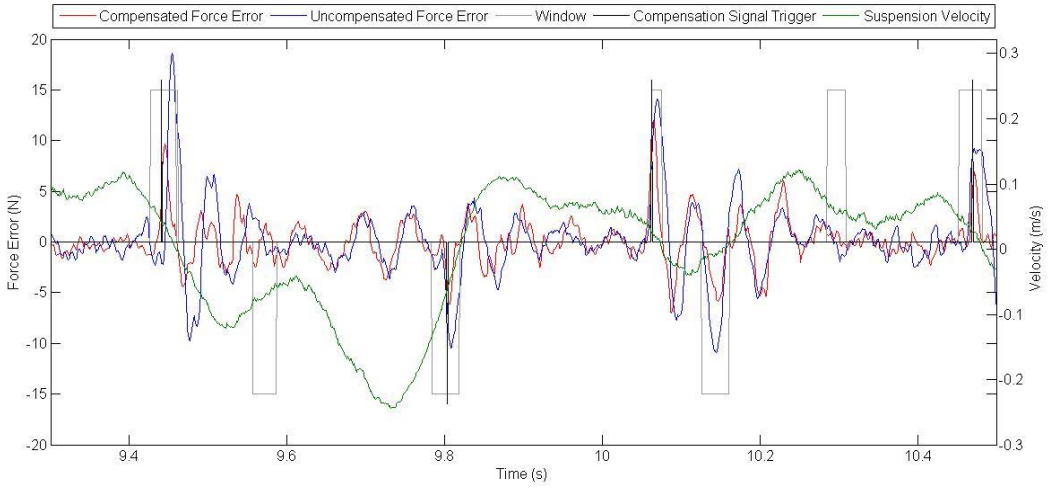

Figure 4.11 –Friction detection and compensation demonstration for single mass spring damper emulation test subjected to 0.1-5.0 Hz random road input for algorithm with 4 N force threshold.

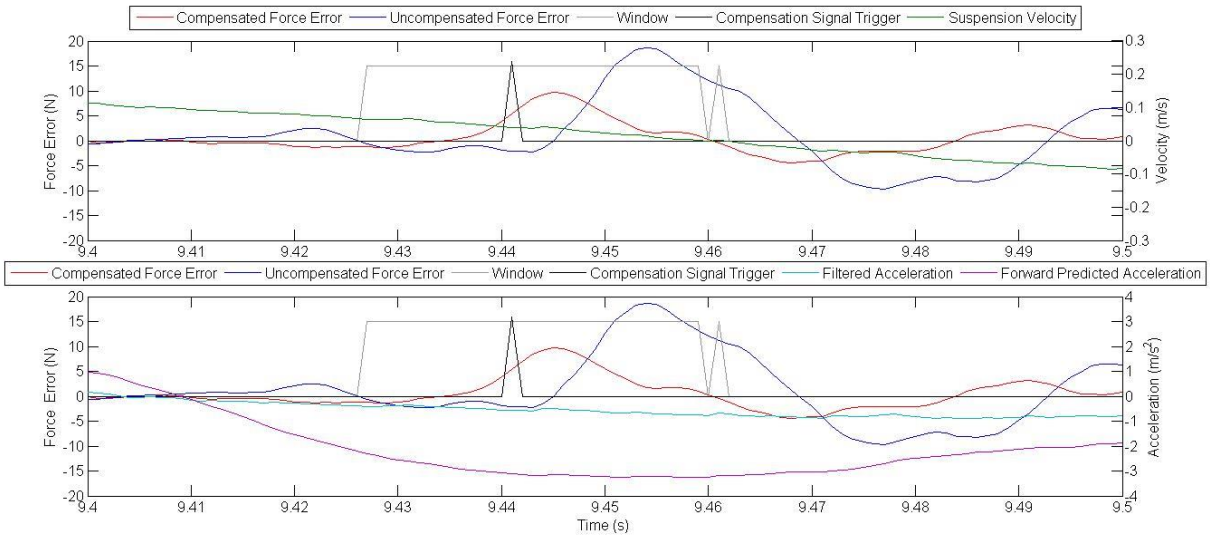

Figure 4.12 – Enlarged view of friction force spike detection and compensation from Figure 4.11.

Figure 4.11 demonstrates the typical performance of the detection algorithm on a section of the time response. The figure also compares the result on the force error of applying a 0.15V compensation step signal and the case of no compensation, showing that compensation is more effective when the correction signal is applied in the early stages of the force spike rise. Figure 4.12 shows an enlarged view of a friction force spike compensation in Figure 4.11. The figures show that a window is activated when velocity and acceleration indicate that a zero crossing is expected and that the window remains open beyond the friction force spike. This allows for force spike detection to occur within the activated window when force error increases above the threshold as shown in Figure 4.12.

Performance of the algorithm is quantified in terms of the RMS tracking error of the friction compensation algorithm compared with no compensation. The RMS force error is taken across the entire test run of 44 seconds and is presented in Table 4.1. To show that the window plays an important role in the performance, other algorithms without the window are also compared.

		RMS Error (N)		
Algorithm	Force Threshold (N)	Force Tracking Error	Numerical Model Error	Total Error
No Compensation		3.955	0.281	4.236
Complete Algorithm	1	2.714	0.240	2.954
Complete Algorithm	2	2.689	0.221	2.910
Complete Algorithm	3	2.718	0.215	2.933
Complete Algorithm	4	2.663	0.220	2.883
Complete Algorithm	5	2.943	0.224	3.167
Force Profile Only	1	4.285	1.119	A1.184
Force Profile Only	2	4.074	0.828	4.902
Force Profile Only	3	3.760	0.606	4.366
Force Profile Only	4	3.444	0.519	3.963
Force Profile Only	5	3.135	0.353	3.488
Force Threshold Only	2	7.276	0.333	7.609
Force Threshold Only	4	6.115	0.300	6.415
Force Threshold Only	6	4.061	0.231	4.292
Force Threshold Only	8	3.440	0.227	3.667
Force Threshold Only	10	3.622	0.255	3.877
Force Threshold Only	12	3.854	0.318	4.172

Table 4.1 – Comparison of RMS error for full and partial friction compensation algorithms operating at different error force thresholds for friction force spike detection.

This capability to improve performance while using a lower force threshold compared to the no motion force tracking error is shown in Table 4.1 where the ‘force profile only’ algorithm

outperforms the ‘force threshold only’ algorithm. From the table it is evident that ‘force profile only’ algorithms perform worse when the force threshold is lowered. This is as expected since false detections should increase. This is in contrast with the complete algorithm which maintains comparable performance irrespective of the force threshold since the velocity window helps to reduce the chance of false detections.

The results from the Table 4.1 clearly indicate that force error reduction is highest when using all elements of the designed friction compensation algorithm. All the algorithms utilize a 40ms buffer as the minimum time between compensation signals, meaning that two triggers will not occur within 40ms. This buffer is applied to prevent multiple triggering of force spike detections from a single force spike. There are two criterias for choosing the buffer time. First the buffer time period must be a lot smaller than the time period of the highest frequency in the system to prevent the buffer from missing detections. Here the test is subjected to a maximum frequency of 5 Hz or a period of 200ms. Secondly the buffer time must be greater than the time span of a single friction spike which is approximately 20ms.

4.6 Two Step Compensation

Results from section 4.5 demonstrated the performance of friction compensation where the compensation step signal has amplitude equal to that of the Coulomb friction. It can be seen from Figure 4.12 that the reduction of the friction force error spike does not commence immediately after triggering of the compensation step signal; the absolute force error continues to increase for a short time before decreasing. This is due to the step response dynamics of the linear electric motor and its controller. This means that increasing the amplitude of the step input compensation signal would result in a faster reduction of the force error. However, application of a step input larger than the Coulomb friction level would also result in a change of the equilibrium point of the integral term in order to maintain the same demand force.

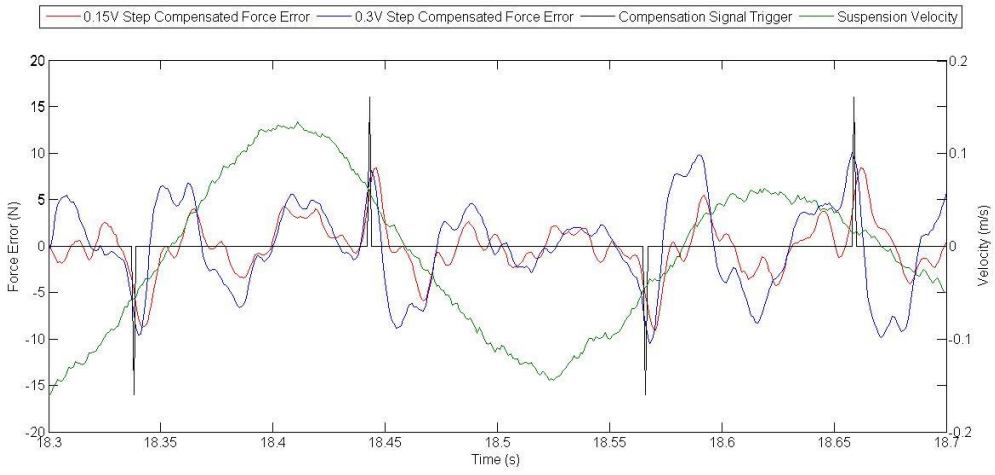

Figure 4.13 – Experiment result comparing force error of 0.15 V against 0.3 V step compensation.

Figure 4.13 illustrates the effect of applying a compensation signal twice that of the friction level. Although the friction spike error reduction occurs swiftly, the force errors after the friction spike are increased as the integral term drives towards a new equilibrium point.

One way to enable a large compensation step to be used while not altering the integral term's equilibrium point is to add a second step input in the opposite direction shortly after the first step so that the summation of the two step inputs equate to the friction level. In this case this mean adding a second step with magnitude 0.15 V opposing the first step.

To test the effect of the timing of the second compensation step signal a simulation was conducted and results are shown in Figure 4.14. The simulation was simplified so that the outer loop force controller consisted of only an integral term. Since the controller consists of an outer force loop and inner current loop, there are two equilibrium conditions to be satisfied, namely force and current equilibrium. The current equilibrium is determined by the demand force and the friction force while the force equilibrium is at zero force error. The timing of the second step is crucial and should be triggered so that the motor current settles to the new equilibrium before the force error from the friction force spike returns to zero. This is to ensure that as the friction force error is driven to equilibrium at zero error, the current would already be close to the equilibrium current allowing the system to settle quickly. Under this arrangement, as the second step is applied it is opposing the action of the force integral controller and in doing so a gradual approach to zero force error can be achieved.

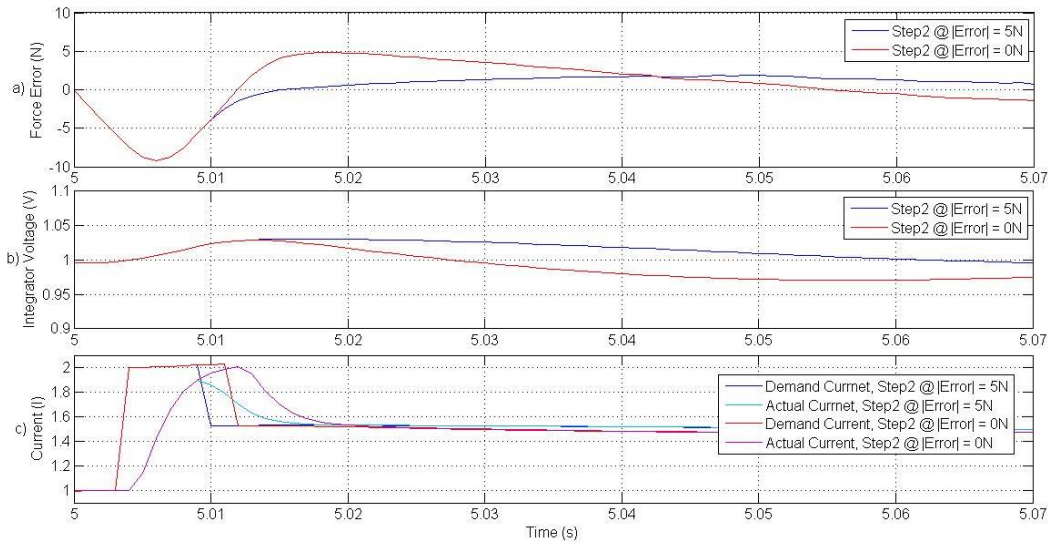

Figure 4.14 - Simulation Result Illustrating the effect of the timing of Step 2 triggering. Step 1 compensation is applied at 5.004 second. a) Force error plot, b) Force controller integrator voltage, c) Current controller demand and actual current.

If the second step is applied late then the motor current is driven to the demand current defined by the first compensation step as the force error approaches zero. After the force error changes sign the integral controller will act in the opposite direction and drive the motor current to the equilibrium. If at this moment the second step is applied, both the force integral controller and the

second step signal will be pushing the system in the same direction causing the force output to overshoot and oscillate as shown in Figure 4.14. In effect the purpose of the two step compensation signals is to drive the motor current to its new equilibrium position such that action is done by the force controller integral term is reduced. This is beneficial since high integral gains lead to oscillatory responses when correcting force errors.

This technique allows for any combination of step magnitudes of the two steps as long as their summation is equal and opposite to the Coulomb friction. This would mean that the larger the steps magnitudes the quicker the compensation signals will correct for the friction force spike as long as the current response to the second step settles before force error zero crossing. Figure 4.15 compares the simulated response of two sets of step magnitudes showing superior performance when the step magnitudes are larger.

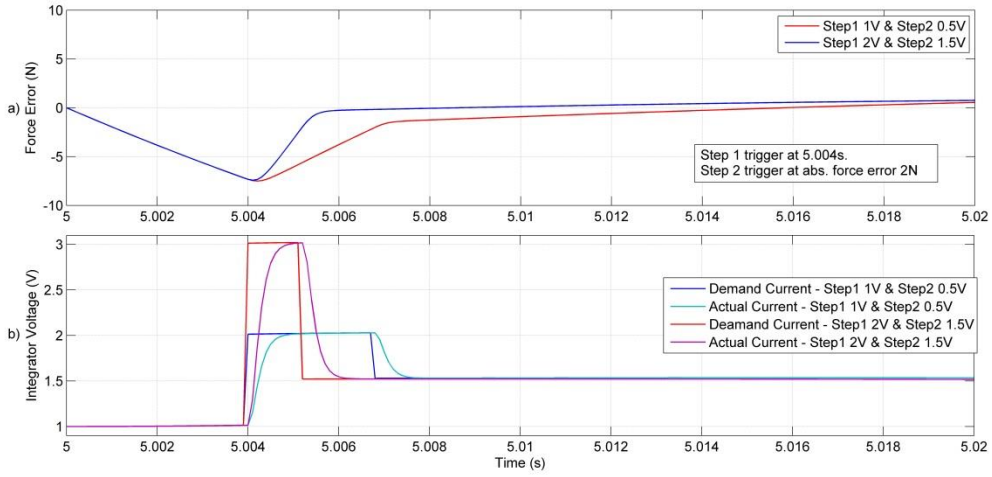

Figure 4.15 - Simulation Result illustrating the effect of choosing steps with larger magnitude. a) Force error plot, b) Current controller demand and actual current.

The two step compensation algorithm was applied to the same system as presented in section 4.6. The second step was triggered when the force error crossed the level of 4N after application of the first step. Experimental tests indicated that 4N was a sensible option as it ensured a safety margin such that the motor current would settle before force zero crossing. Figure 4.16 shows a section of the result in a time series comparing one step compensation against two step compensation. It is clear that for a friction cancellation step input of 0.3V, the two step compensation is better at reducing the subsequent force oscillations after the Coulomb friction spike. The RMS error from the complete 44s time response displayed in Table 4.2 confirms that the two step algorithm is superior compared to the one step algorithm. The two step compensation algorithm reduces the total error (e_1+e_2) of the test rig by 37%. Figure 4.17 demonstrates the two step algorithms ability to cancel out the friction spike compared to the no compensation case. The plot shows an approximate reduction in Coulomb friction force error spike of 50% from 20N to 10N.

RMS error	No Compensation	1 Step Compensation	2 Step Compensation
Synchronisation (e_1)	3.955	2.663	2.474
Force Tracking (e_2)	0.281	0.212	0.196
Overall (e_1+e_2)	4.236	2.875	2.670

TABLE 4.2 – RMS tracking error of *e1* and *e2* and overall system error *e1+e2* for compensation using 4 N force error threshold.

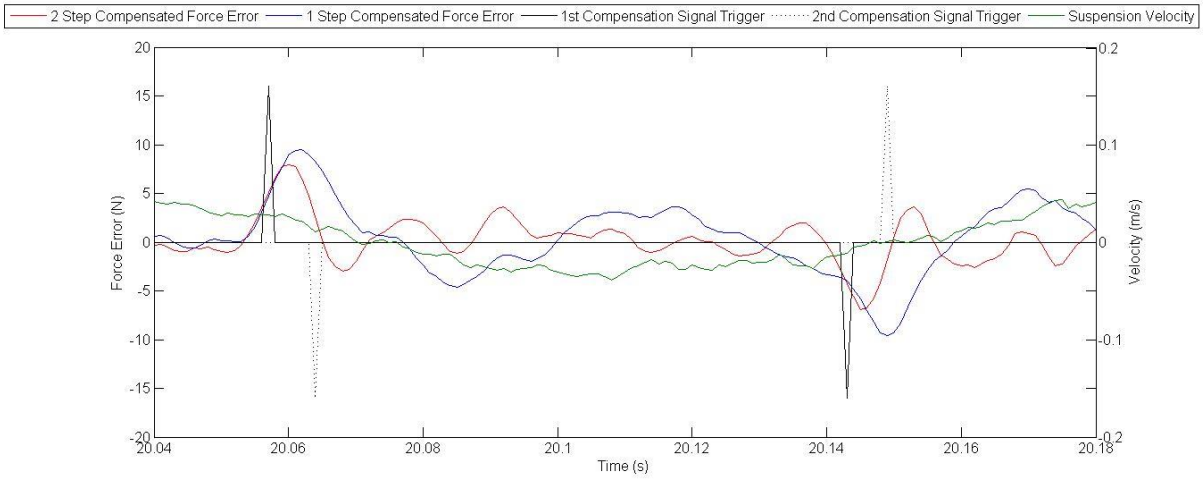

Figure 4.16 – Experiment result comparing 1 vs. 2 step compensation. Force error threshold for step 1 compensation is 4 N. Step 2 is triggered when force error re-crosses 4 N.

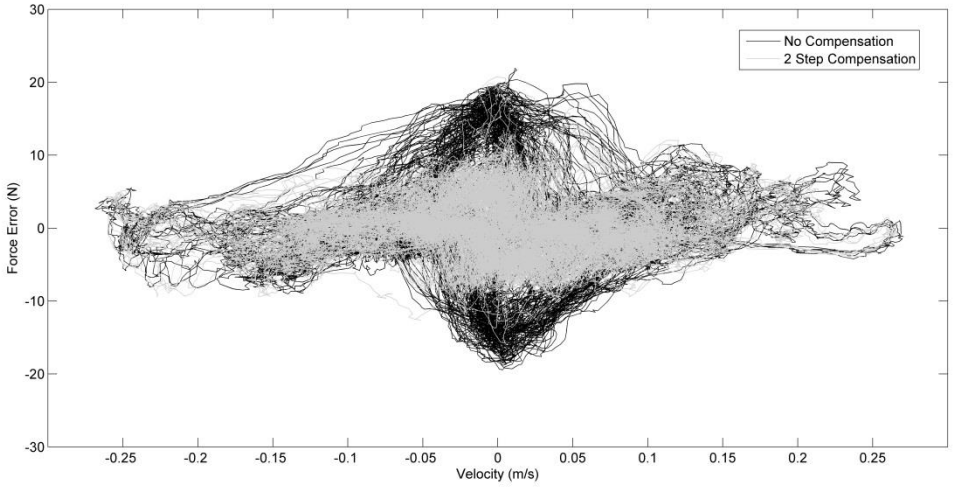

Figure 4.17 – Force velocity plot comparing no compensation and 2 step compensation.

4.7 Conclusions

The friction compensation technique presented in this paper demonstrated the ability to improve the performance of MIL force control systems. The algorithm achieved approximately 50% reduction in friction force error spike for an actuator subjected to a pseudo random disturbance motion of 0.1-5Hz. In regards to the single mass spring damper MIL suspension test rig the two step friction compensation algorithm reduced the combined RMS force tracking and synchronisation error by 37% when compared with a situation in which no friction compensation algorithm was applied. The biggest advantage of this technique is that it could be implemented without comprehensive modeling of the actuator, or friction characteristics except for a simple Coulomb model and a few other parameters. Friction parameter identification, which can be troublesome for complex models is avoided. This algorithm requires the determination of the integrator level change caused by Coulomb friction and observation of the friction force error spike in relation to velocity signal in order to choose the appropriate time till velocity zero crossing threshold, force error threshold and the friction spike rise envelope. A force sensor and position sensor for the actuator stroke are the sensing instruments required. This means that this technique could be implemented with relative ease on any force control system, especially for systems with non-deterministic actuator motion to achieve significant improvement in force tracking.

5. Test Rig Control Loop Analysis

5.1 Single Mass Model

Insight into analysis of the suspension MIL and vehicle structure MIL systems can be gained by simplifying the numerical-experimental system into a single mass-spring-damper system. The quarter car suspension has two masses, the sprung and unsprung mass. Both the suspension MIL and structure position MIL systems can be implemented in a single mass system by ignoring the unsprung mass as conducted for experiments in Chapter 3 and Chapter 4. The aim here is that if system stability is well understood in terms of a single mass system, the results can be extended to a two mass system such that stability is maintained.

5.1.1 Single Mass Model

A single mass damper is excited from the base as shown in Figure 5.1.

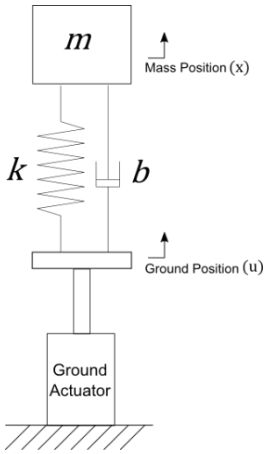

Figure 5.1 – Mechanical diagram of single mass spring damper.

The system is well known and has a second order response. The system equation at equilibrium is given by,

$$m\ddot{x} = -k(x-u) - b(\dot{x}-\dot{u}) \tag{5.1}$$

This can be rearranged to,

$$m\ddot{x} + b\dot{x} + kx = ku + b\dot{u} = \mu \tag{5.2}$$

Here μ is a function of the ground input which is later used in the state space formulation of system equation. Taking the Laplace transform with output as displacement $X(s)$ and input of $U(s)$,

$$\frac{X(s)}{U(s)} = \frac{bs+k}{ms^2+bs+k} \tag{5.3}$$

The system could also be described in state space form,

$$\mathbf{A\dot{z} + Bz = Cu} \tag{5.4}$$

The states of the system are,

$$z_1 = x \tag{5.5}$$

$$z_2 = \dot{x} \tag{5.6}$$

Giving the state space equation,

$$\begin{bmatrix} 1 & 0 \\ 0 & m \end{bmatrix} \begin{bmatrix} \dot{x} \\ \ddot{x} \end{bmatrix} + \begin{bmatrix} 0 & -1 \\ -k & -b \end{bmatrix} \begin{bmatrix} x \\ \dot{x} \end{bmatrix} = \begin{bmatrix} 0 \\ 1 \end{bmatrix} \mu \tag{5.7}$$

The roots of the system can be determined from both the closed loop transfer function and the state space model. This analysis will reveal properties of the system such as the vibration mode and their rate of decay and frequency. From the state space equation the characteristic equation which yields the eigenvalues, λ, of the system is evaluated by solving the determinant,

$$\left|\mathbf{A^{-1}B + \lambda I}\right| = 0 \tag{5.8}$$

Here $\mathbf{I}$ denotes an identity matrix. After obtaining the eigenvalues, the eigenvectors, v, are obtained by solving,

$$\left(\mathbf{A^{-1}B + \lambda I}\right)\mathbf{v} = 0 \tag{5.9}$$

5.1.2 Single Mass System - Suspension MIL Model

The state space single mass spring damper system equation can be extended to include the dynamics of the MIL transfer function. Investigation of the effect of MIL suspension and MIL vehicle structure can be conducted separately. The transfer function delay is modeled in the simplest form of a first order lag low pass filter. A first order lag can better capture the nature of delays in actuators which are frequency dependent as opposed to using a constant time delay.

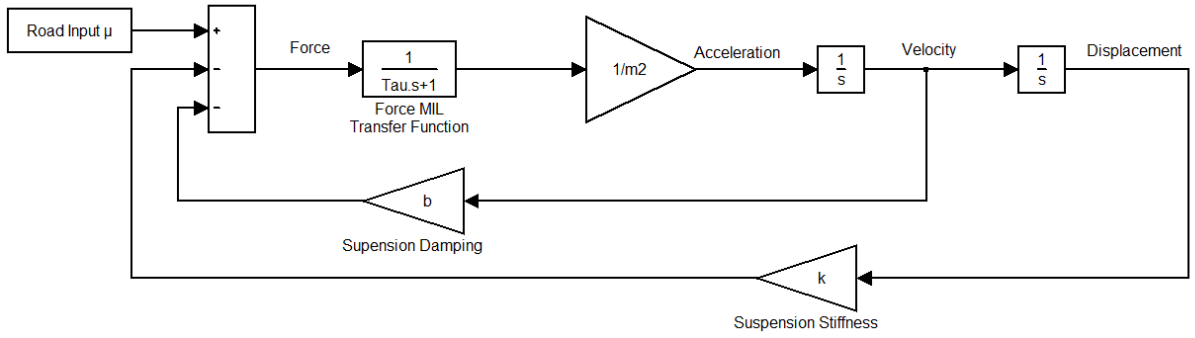

Figure 5.2 – Block diagram of suspension MIL on single mass spring damper.

In hybrid numerical-experimental testing literature, transfer functions of MIL actuators have been commonly modeled as a first order lag [6, 110, 114]. Although this might not be the most accurate representation of actuators, its simplicity allows more insight to be gained and its consistent use in literature gives a basis for comparison to other studies. The bode plots of actuator transfer functions in Chapter 6 show that magnitude and phase responses have shapes similar to that of a first order lag. Moreover experimental results in Chapter 6 confirm the analysis derived from first order lag approximation used in Chapter 5. A first order low pass filter in the frequency domain is represented by the transfer function,

$$\frac{Y(s)}{X(s)} = \frac{1}{1+\tau s} \tag{5.10}$$

Here X is the input and Y the output of the filter in the Laplace domain and τ is the filter time constant. The first order low pass filter has a time domain equation of,

$$\tau\dot{y} + y = x \tag{5.11}$$

For the force MIL system the filter is applied to the suspension force signal as shown in Figure 5.2, causing the force output to lag the demand force from the numerical model output. Applying the first order filter to the output force yields an extra state in the state space equation. This extra state is the filter output, f, and the equation is,

$$\tau\dot{f} + f = kx + b\dot{x} \tag{5.12}$$

Incorporating the force filter dynamics into the single mass state space equation and adjusting the sprung mass equation of motion so that it is a function of filter output,

$$\begin{bmatrix} 1 & 0 & 0 \\ 0 & 1 & 0 \\ 0 & 0 & m \end{bmatrix}\begin{bmatrix} \dot{f} \\ \dot{x} \\ \ddot{x} \end{bmatrix} + \begin{bmatrix} \tau^{-1} & -k\tau^{-1} & -b\tau^{-1} \\ 0 & 0 & -1 \\ 1 & 0 & 0 \end{bmatrix}\begin{bmatrix} f \\ x \\ \dot{x} \end{bmatrix} = \begin{bmatrix} 0 \\ 0 \\ 1 \end{bmatrix}\mu \tag{5.13}$$

5.1.3 Single Mass System – Vehicle Structure MIL Model

For a sprung mass position MIL system a transfer function delay is applied to the output of the sprung mass position as shown in Figure 5.3. The delay in sprung mass position here also entails that there is an equal delay in the sprung mass velocity. This means that for an equivalent state space formulation two delays must be applied, to the sprung mass position and to the sprung mass velocity as these are realised as separate states in the state space system. On the block diagram in Figure 5.3, the equivalent of applying two separate filters in the feedback position and velocity is to apply a single filter on the velocity output.

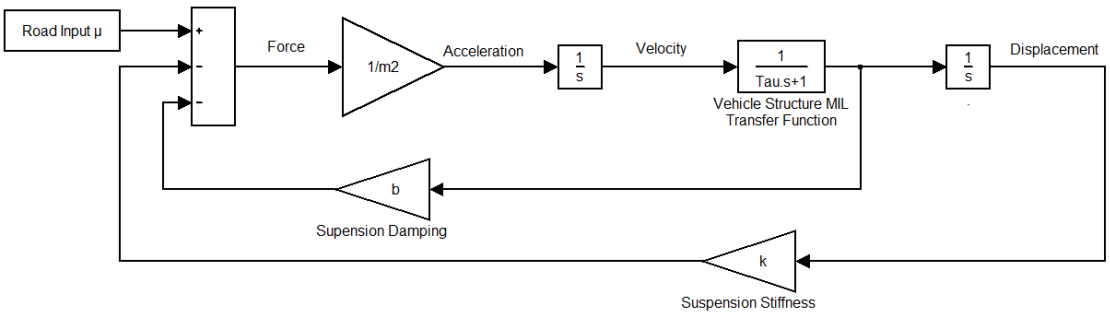

Figure 5.3 - Block diagram of suspension MIL on single mass spring damper.

Let f_{mp} denote the filter output applied to the sprung mass position,

$$\tau \dot{f}_{mp} + f_{mp} = x \tag{5.14}$$

Let f_{mv} denote the filter output applied to the sprung mass velocity,

$$\tau \dot{f}_{mv} + f_{mv} = \dot{x} \tag{5.15}$$

Incorporating the two additional filter states to the state space equation yields,

$$\begin{bmatrix} 1 & 0 & 0 & 0 \\ 0 & 1 & 0 & 0 \\ 0 & 0 & 1 & 0 \\ 0 & 0 & 0 & m \end{bmatrix} \begin{bmatrix} \dot{f}_{mp} \\ \dot{f}_{mv} \\ \dot{x} \\ \ddot{x} \end{bmatrix} + \begin{bmatrix} \tau^{-1} & 0 & -\tau^{-1} & 0 \\ 0 & \tau^{-1} & 0 & \tau^{-1} \\ 0 & 0 & 0 & -1 \\ -k & -b & 0 & 0 \end{bmatrix} \begin{bmatrix} f_{mp} \\ f_{mv} \\ x \\ \dot{x} \end{bmatrix} = \begin{bmatrix} 0 \\ 0 \\ 0 \\ 1 \end{bmatrix} \mu \tag{5.16}$$

This equation has four states due to choice of state variables for the state space equation. Since the system has three degrees of freedom an alternative choice of state space variables can yield a system with three states.

5.1.4 Equivalence of Suspension MIL and Sprung Mass Position MIL

A delay applied to the suspension MIL and the sprung mass position MIL have different effects on a two mass system. This is because suspension MIL acts on both the sprung and unsprung mass while the vehicle structure MIL only acts on the sprung mass. However in the single mass case there is no unsprung mass, which means both MIL systems act purely on the sprung mass. In this case whether the delay is applied to output force or the output position the systems are equivalent. This equivalence is shown by the block diagrams for the suspension MIL and the sprung mass MIL in Figure 5.2 and Figure 5.3 respectively. A delay applied to the plant at either the force output or the velocity output yield identical systems.

The transfer function of the block diagram given in Figure 5.2 and Figure 5.3 is,

$$\frac{X(s)}{U(s)} = \frac{bs + k}{m\tau s^3 + ms^2 + bs + k} \tag{5.17}$$

Although the MIL vehicle structure state space equation yields a fourth order equation, see Equation 5.16, the eigenvalues analysis of the state space equations in Table 5.1 shows that the state space representations of MIL vehicle structure and MIL suspension force are identical. The system parameters chosen are arbitrary with $m = 50\ kg$, $k = 500\ N/m$ and $b = 100\ kg$.

		Eigenvalues			
		Pole1	Pole2	Pole3	Pole4
$\tau = 0.01$	MIL vehicle structure	-100	-98.06	-0.9677 + 3.043i	-0.9677 - 3.043i
	MIL suspension		-98.06	-0.9677 + 3.043i	-0.9677 - 3.043i
$\tau = 0.1$	MIL vehicle structure	-10	-9.012	-0.4940 + 3.294i	-0.4940 - 3.294i
	MIL suspension		-9.012	-0.4940 + 3.294i	-0.4940 - 3.294i
$\tau = 0.2$	MIL vehicle structure	-5	-5	3.162i	- 3.162i
	MIL suspension		-5	3.162i	- 3.162i
$\tau = 0.5$	MIL vehicle structure	-4	-2.946	0.4732 + 2.562i	0.4732 - 2.562i
	MIL suspension		-2.946	0.4732 + 2.562i	0.4732 - 2.562i

Table 5.1 – Eigenvalues from state space model for MIL vehicle structure and MIL suspension at different time constants.

5.1.5 Critical Time Delay of Single Mass MIL System

The critical time delay for a given system is the maximum allowable delay which ensures system stability. By varying the time delay for a given system the critical delay can be found from the eigenvalue analysis of the characteristic equation. The characteristic equation for the single mass MIL is a third order polynomial where λ is the eigenvalue,

$$\lambda^3 + \frac{1}{\tau}\lambda^2 + \frac{b}{\tau m}\lambda + \frac{k}{\tau m} = 0 \tag{5.17}$$

By solving the third order polynomial an expression for λ in terms of system parameters can be found. Equating the real part of λ to zero would reveal the critical delay at the stability boundary. Unfortunately solving the cubic polynomial does not yield an expression which is simple enough to provide meaningful understanding. The equation may be solved using Cardano's formula [134] to give three solutions of λ,

$$\lambda_1 = S + T - \frac{1}{3\tau} \tag{5.18}$$

$$\lambda_2 = -\frac{1}{2}(S + T) + \frac{1}{2}i\sqrt{3}(S - T) - \frac{1}{3\tau} \tag{5.19}$$

$$\lambda_3 = -\frac{1}{2}(S+T) - \frac{1}{2}i\sqrt{3}(S-T) - \frac{1}{3\tau} \tag{5.20}$$

Where,

$$S = \sqrt[3]{A + \sqrt{A^2 + B^3}} \tag{5.21}$$

$$T = \sqrt[3]{A - \sqrt{A^2 + B^3}} \tag{5.22}$$

$$A = \frac{1}{27\tau^3} - \frac{b}{6m\tau^2} - \frac{k}{2m\tau} \tag{5.23}$$

$$B = \frac{1}{9\tau^2} + \frac{b}{3m\tau} \tag{5.24}$$

The equation for λ contains square root nested in cube root which make the expression difficult to evaluate and could also contain imaginary numbers. From this equation it is not clear for understanding at what critical time constant does the real part of λ becomes zero. From Descartes Rules of Sign [134] this characteristic polynomial will have either 3 real and negative roots, or one real negative root and two complex conjugates. Note that since there is always at least one negative real root, instability must occur at the complex conjugate poles.

The Routh-Hurwitz stability criterion is a method for testing the stability of a characteristic equation by checking if any roots have real positive parts. For a third order polynomial of the form,

$$a_0x^3 + a_1x^2 + a_2x + a_3 = 0 \tag{5.25}$$

From Routh-Hurwitz stability criterion, the system is stable if,

$$a_1a_2 > a_0a_3 \tag{5.26}$$

Therefore the MIL single mass spring damper is stable if,

$$\tau < \frac{b}{k} \tag{5.27}$$

This gives a critical time constant τ_c for which the system will be on the stability boundary,

$$\tau_c = \frac{b}{k} \tag{5.28}$$

From the equation a stability region mapping for the system can be plotted as shown in Figure 5.4. From the expression it is clear that for a given transfer function time delay, systems will be more stable with low stiffness and high damping. One hypothesis of why high stiffness leads to instability could be that it increases the natural frequency of the system and thus requires that time delay is small to ensure non-negative damping. But if the natural frequency is the reason then changes in mass inertia must also have an effect on the critical time constant, this is not the case. It is intuitive that high damping will lead to system stability but it will be shown in Section 5.3 that this is not so straight forward. At critical time delay the MIL system becomes equivalent to the same mass spring

system with no delay and zero damping. At critical damping system real pole is zero and the imaginary part is equal to the natural frequency and the additional filter pole is real and negative.

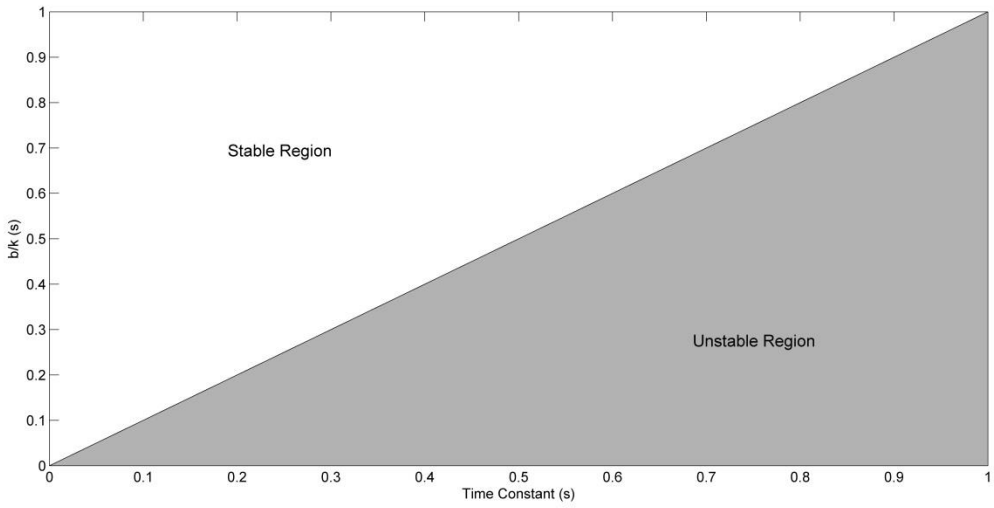

Figure 5.4 – Stability region mapping for single mass spring damper with single MIL. The stability of the system is defined by the suspension damping, stiffness and MIL system time delay.

5.1.6 Critical Time Delay of Double MIL

For a single mass spring damper with a suspension MIL and vehicle structure MIL, the total time delay dynamics is a product of transfer function delays as shown in Figure 5.5.

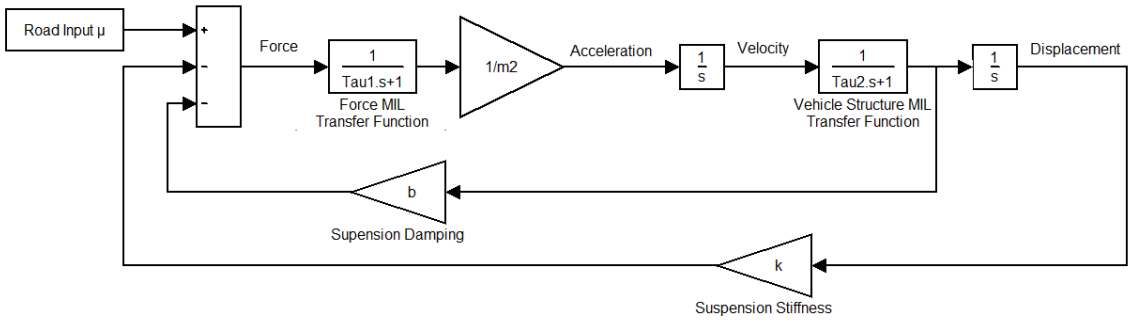

Figure 5.5 – Block diagram of single mass spring damper with suspension MIL and mass position MIL.

The total transfer function delay is now a second order low pass filter in the form,

$$H(s) = \frac{\omega_n^2}{s^2 + 2\xi\omega_n s + \omega_n^2} = \left(\frac{1}{\tau_1 s + 1}\right)\left(\frac{1}{\tau_2 s + 1}\right) = \frac{\frac{1}{\tau_1\tau_2}}{s^2 + \frac{(\tau_1 + \tau_2)}{\tau_1\tau_2}s + \frac{1}{\tau_1\tau_2}} \tag{5.29}$$

The phase response of this second order system is,

$$Phase\ Angle\ = tan^{-1}\left(\frac{-\frac{2\xi\omega}{\omega_n}}{1-\frac{\omega^2}{\omega_n^2}}\right) \tag{5.30}$$

A single mass spring damper with a second order MIL transfer function can be approximated to a first order filter so that an estimated critical time constant for the second order system can be found. The instability of MIL systems is dependent on the delay of the transfer function which is defined by the phase response. By finding the frequency of the second order system at 45° phase lag, this gives the cut off frequency of a first order low pass filter which also occurs at 45° phase lag. If $\tau_1$and $\tau_2$are equal then ξ will equal one, else if unequal ξ will be greater than one. This ensures that the response of the second order low pass filter will be over damped with no resonance peak and therefore have a phase response similar to that of a first order filter up to the 45° point.

Figure 5.6 shows that second order low pass filter from Equation A1.9 with $\xi = 1$ has a frequency response shape that is similar to a first order low pass filter and therefore it is possible to approximate a second order low pass filter to a first order low pass filter. The frequency at 45° phase lag of the second order filter, Equation A1.9, is calculated using Equation A1.8. This gives a frequency of 41.4 rad/s. This frequency is used to approximate a first order low pass filter given by Equation A1.10. From the phase response in Figure 5.6 it can be seen that up to the 45° point, the first order filter has slightly larger phase lags, this ensures that the approximate first order filter will be a safe approximation.

$$Second\ Order\ Filter = \left(\frac{1}{\frac{1}{100}s+1}\right)\left(\frac{1}{\frac{1}{100}s+1}\right) \tag{5.31}$$

$$First\ Order\ Filter\ Approxmation = \left(\frac{1}{\frac{1}{41.4}s+1}\right) \tag{5.32}$$

A MIL system with transfer function (A1.10) will be marginally stable for $k/b = 41.6$. To test the accuracy of this approximation, the poles of the system are compared as shown in Table 5.2. At the same k/b ratio the second order filter system is more stable and becomes marginally stable when $k/b = 49.5$.

	Eigenvalues			
	Pole1	Pole2	Pole3	Pole4
1st Order Filter	0 + 0.91i	0 - 0.91i	-41.4	-
2nd Order Filter	-1.7e-5 + 0.91i	-1.7e-5 - 0.91i	-101	-98.9

Table 5.2 – Eigenvalues of single mass spring damper with first and second order transfer function from (A1.9) and (A1.10) respectively, with $b = 1\ Ns/m,\ k = 41.4\ N/m$ and $m = 50\ kg$.

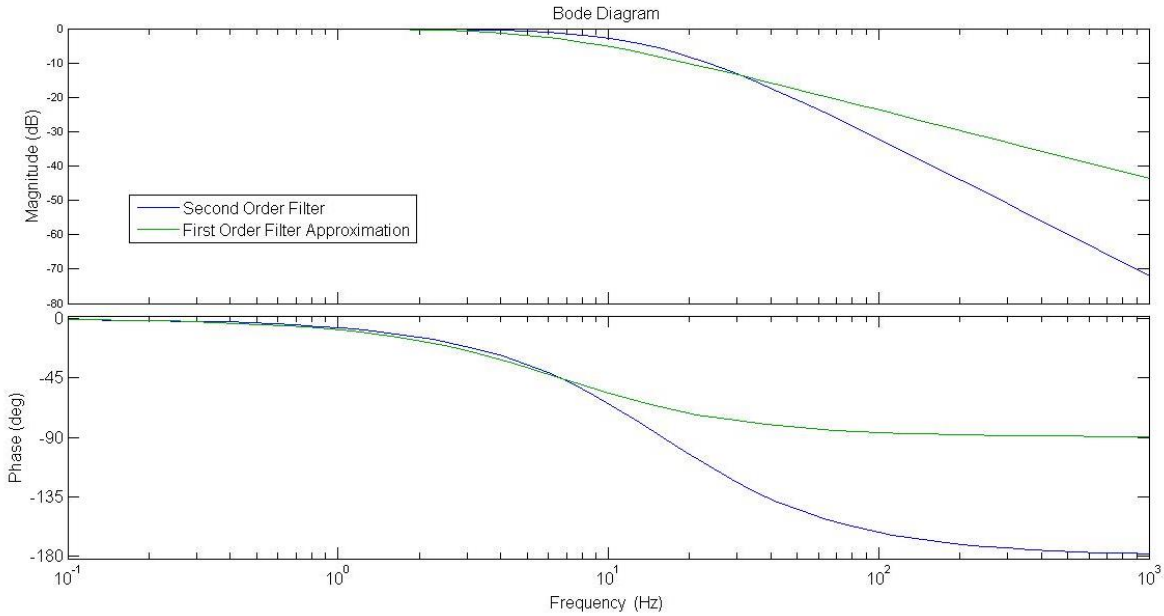

Figure 5.6 – Bode plot of second order filter and its approximated first order filter.

5.2 Single Mass Model Parameters Variation

The performance of MIL systems is evaluated in terms of accuracy in comparison to the ideal emulated response. To help with this understanding a root locus plots for system parameter variation will be conducted. This is done in a generic manner so that limitations and possible applications for the test rig can be estimated. This will reveal the changes to the response decay rate and frequency of the system resonant modes.

5.2.1 Variation of Time Constant

The system parameters chosen are arbitrary as shown below in Table 5.3.

	Variable Parameter: $\tau = 0.001s \; to \; 1s$	
	Case 1	**Case 2**
Damping Ratio	1	0.5
$m\ (kg)$	50	50
$k\ (N/m)$	500	500
$b\ (Ns/m)$	316.2	158.1

Table 5.3 – Parameters for variation of time constant for single mass spring damper MIL system.

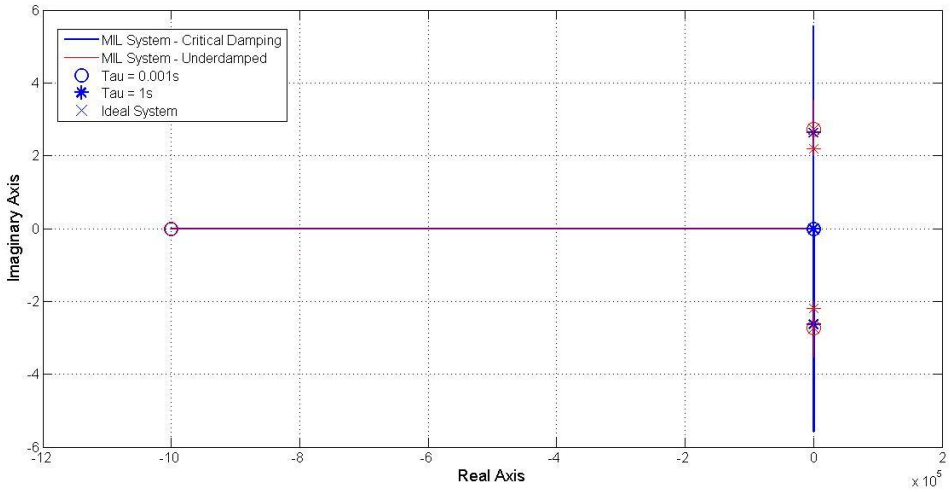

Figure 5.7 – Root locus plot for variation of time constant.

As the time delay constant increases the system is expected to become more unstable. Figure 5.7 shows the root locus plot for the variation of time constant for a critically damped and an underdamped system. From Figure 5.7, at small time constant the extra pole introduced by the filter is not dominant, lying to the far left of root locus plot. From Figure 5.8, the focused view of the root locus shows that at low time constant the poles of the MIL system match those of the ideal system for both critically and under damped systems. As the time constants increase both MIL systems eventually become unstable. For a critically or over damped system the root locus moves away from the zero imaginary axis as the delay has the effect of reducing the apparent damping of the system such that the system becomes underdamped with conjugate poles. For the under damped system the poles also move generally towards the right, due to reduced apparent damping. At the critical time constant where the real part of the body hop poles is zero the system resembles an undamped mass spring system, therefore at this point the poles of the critically and under damped systems intersect.

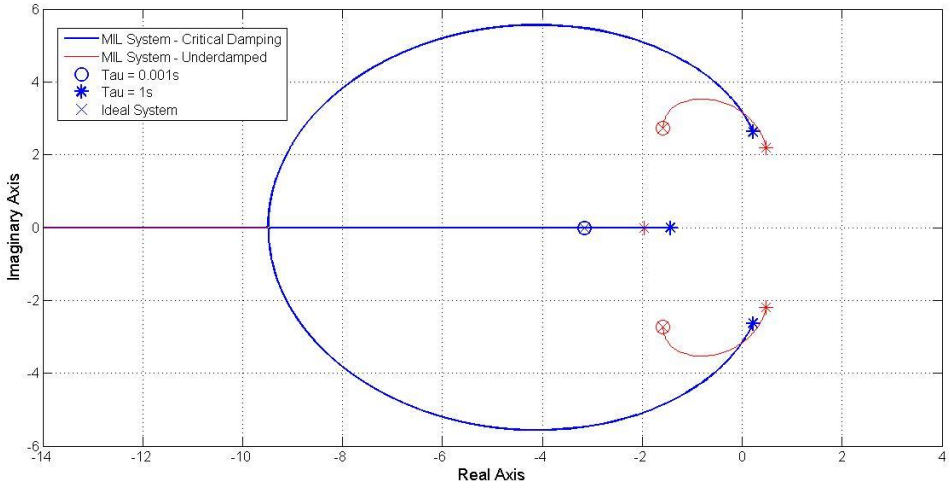

Figure 5.8 – Exploded view of root locus plot for variation of time constant.

5.2.2 Variation of Natural Frequency

The natural frequency of the system is varied by changing the stiffness, keeping the mass constant, and the damping ratio constant by altering the damping, the parameters are given in Table 5.4.

	Variable Parameter: $k = 1\ to\ 100000N/m$					
	Case 1	**Case 2**	**Case 3**	**Case 4**	**Case 5**	**Case 6**
Damping Ratio	1	1.5	0.5	1	1.5	0.5
$m\ (kg)$	50	50	50	50	50	50
$\tau\ (s)$	0.2	0.2	0.2	0.01	0.01	0.01

Table 5.4 - Parmeters for variation of natural frequency for single mass spring damper MIL system.

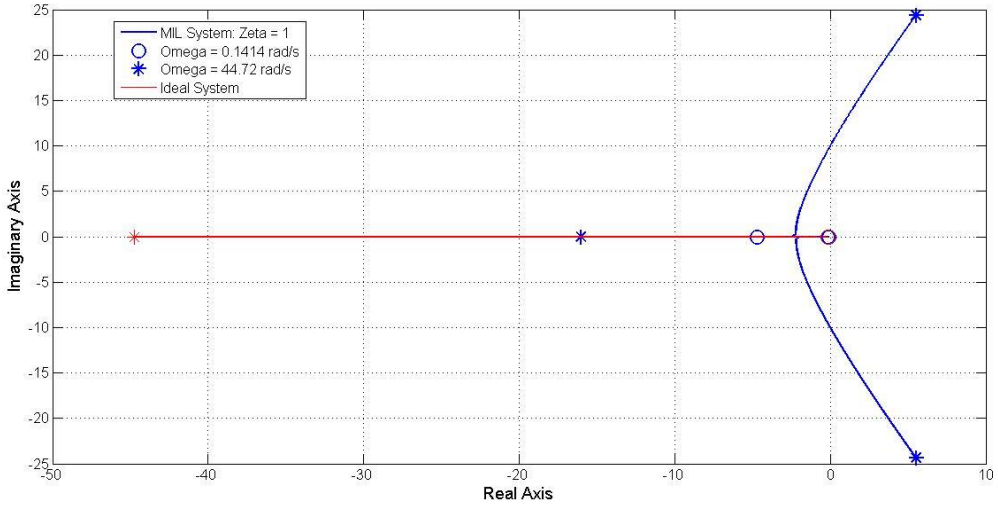

Figure 5.9 – Case 1: Root locus of natural frequency variation for critical damping ratio, $\tau = 0.2s$.

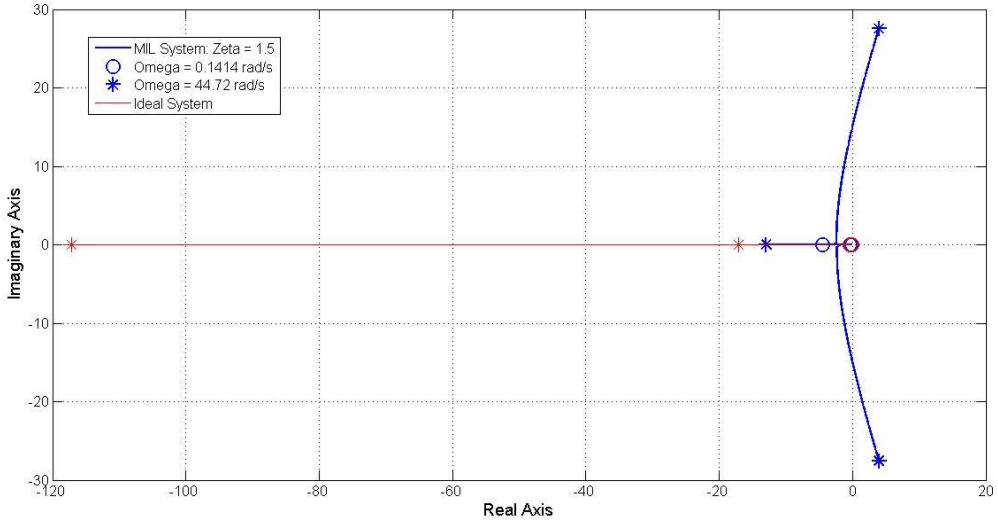

Figure 5.10 – Case 2: Root locus of natural frequency variation for over damped system, $\tau = 0.2s$.

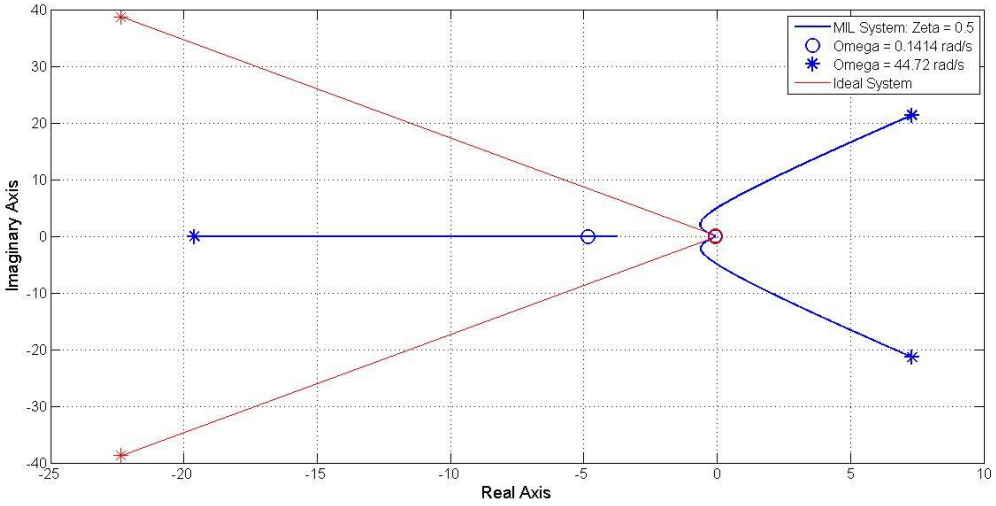

Figure 5.11 – Case 3: Root locus of natural frequency variation for underdamped system, $\tau = 0.2s$.

With a large time delay constant of 0.2s of Cases 1, 2 and 3, for all damping ratios, shown in Figure 5.9, Figure 5.10 and Figure 5.11, the system poles become unstable as the natural frequency of the system increases. The reason for this is because the instability condition is determined by,

$$\tau_c = \frac{b}{k} \tag{5.33}$$

Therefore as natural frequency increases, the only way to keep the same stability margin would be to increase the damping proportionally with stiffness. However in achieving the same damping ratio the damping has to increase proportionally with square root of stiffness, since,

$$\xi = \frac{b}{2\sqrt{km}} \tag{5.34}$$

This means that for a constant damping ratio, as the natural frequency increases, the critical time constant decreases which leads to system instability. Following this reasoning systems which are highly damped will be more stable as shown by comparing Figure 5.9 - 5.11, note that the end point of unstable pole is further to the right for lower damping ratios.

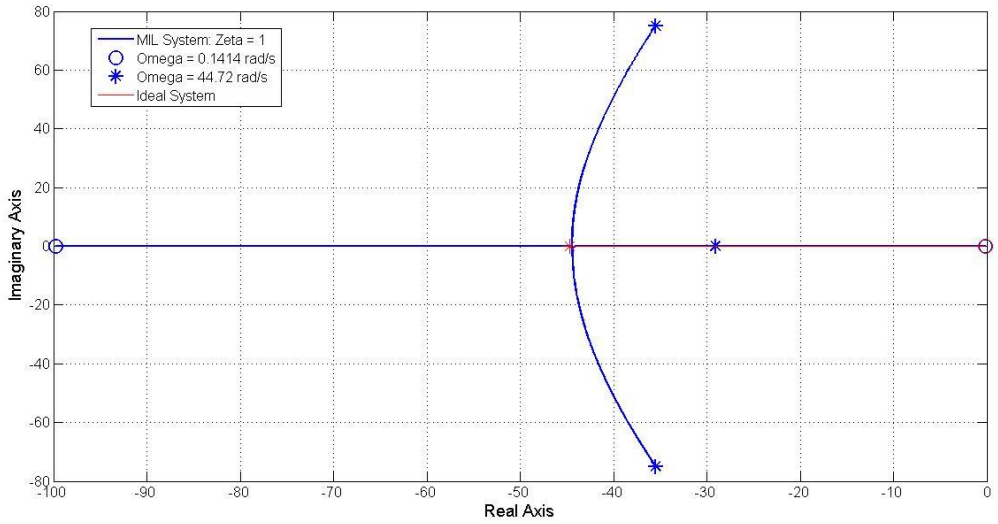

Figure 5.12 – Case 4: Root locus of natural frequency variation for critical damping ratio, $\tau = 0.01s$.

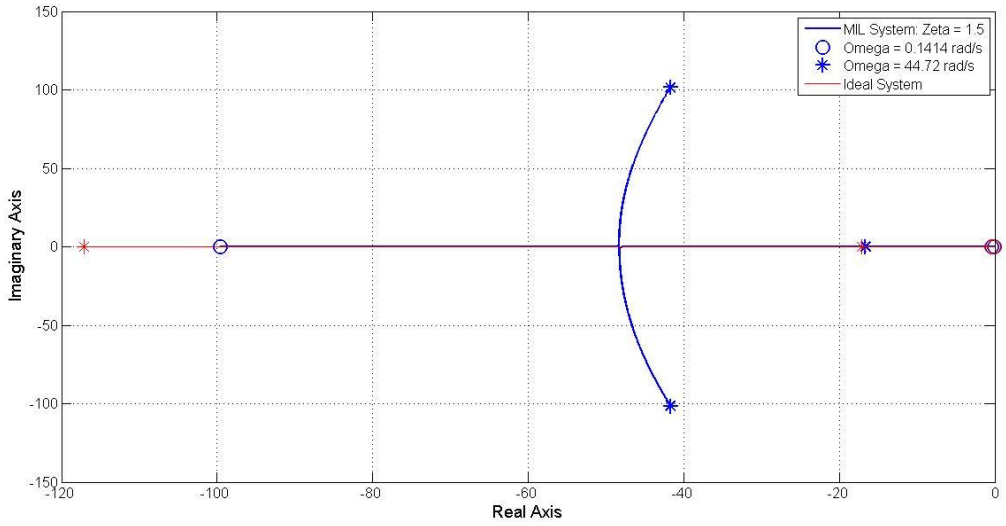

Figure 5.13 – Case 5: Root locus of natural frequency variation for over damped system, $\tau = 0.01s$.

For smaller time delay constant of 0.01s the root locus plots are shown in Figure 5.12 - 5.14. Unlike in the large time delay case, the MIL system with smaller time delays did not show instability at a system natural frequency of 44.72 rad/s. It is interesting to note that for the critically and over damped cases the root locus in Figure 5.12 and 5.13 has the same shape as the root locus plots in Figure 5.9 and 5.10. The effect of the smaller time delay is that the breakaway point is shifted further to the left of the root locus giving the system greater stability. However the conjugate poles after the breakaway point for the time delay constant of 0.01s reach much higher natural frequencies than the 0.2s time delay case. This shows a substantial difference from the desired system dynamics occur even with small time delays. Furthermore any dynamics introduced by the MIL system which are of a high frequency, although stable in the root locus, could be unstable in the real time implementation if the controller sampling rate is too low.

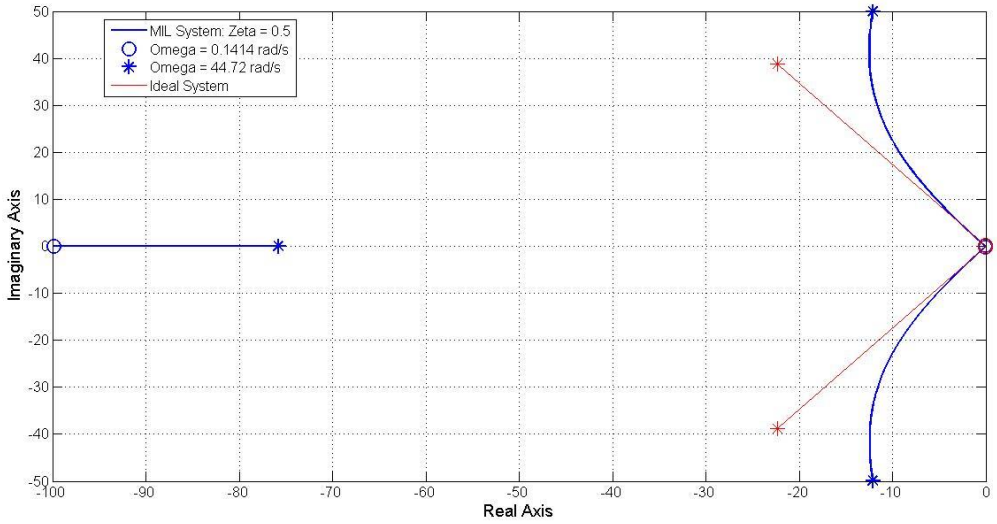

Figure 5.14 – Case 6: Root locus of natural frequency variation for under damped system, $\tau = 0.01s$.

5.2.3 Variation of Damping Ratio

Variation of damping ratio is achieved by varying stiffness and mass equally while keeping the damping coefficient constant. The variation was conducted for three cases of delay time constant as shown below in Table 5.5.

	Parameter Variation: $k = m = 1\ to\ 100000$		
	Case 1	**Case 2**	**Case 3**
Natural Frequency (rad/s)	1	1	1
$b\ (Ns/m)$	100	100	100
$\tau\ (s)$	0.2	0.01	0.001

Table 5.5 - Parmeters for variation of damping ratio for single mass spring damper MIL system.

Root locus plot for Case 1-6 are shown in Figures 5.15 – 5.20. Instability is expected to occur for low damping ratios because, for a given system natural frequency, low damping coefficients lead to a small critical time delay. This instability at low damping ratio is shown if Figure 5.16. With smaller time constants, the damping ratio of 0.005 does not cause instability as shown by Figure 5.18 and 5.20. An interesting phenomenon observed here is that, for large time constants, there is an asymptote for large damping ratios as shown in Figure 5.15 and 5.17. This asymptote, although stable, has its frequency tending to infinity as the damping ratio increases. The effect of this is that when implemented in real time control, the very high frequency introduced into the system could lead to instability if the control loop sampling frequency too low. Comparing Figure 5.15 and 5.17, as time constant decreases the asymptote point moves to the left on the root locus and the frequencies at the asymptote becomes higher. The presence of this asymptote means that although the system is stable for high damping ratios, the MIL system resembles the ideal system much more closely when the damping ratio is low. With a very small time constant of 0.001s, shown in Figure 5.18 and 5.19, this asymptote disappears and the MIL system matches well with the ideal system across the entire damping ratio range.

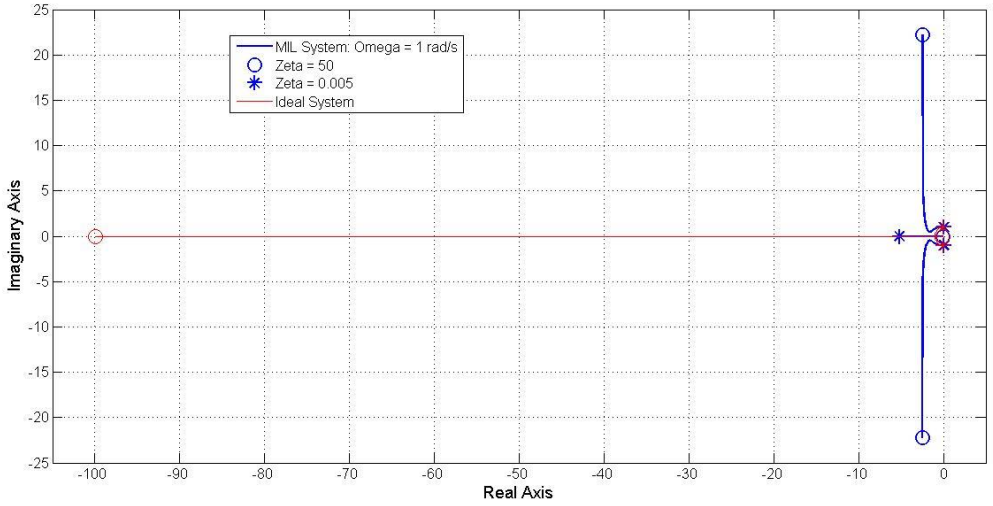

Figure 5.15 – Case 1: Root locus of damping ratio variation for time constant of 0.2s.

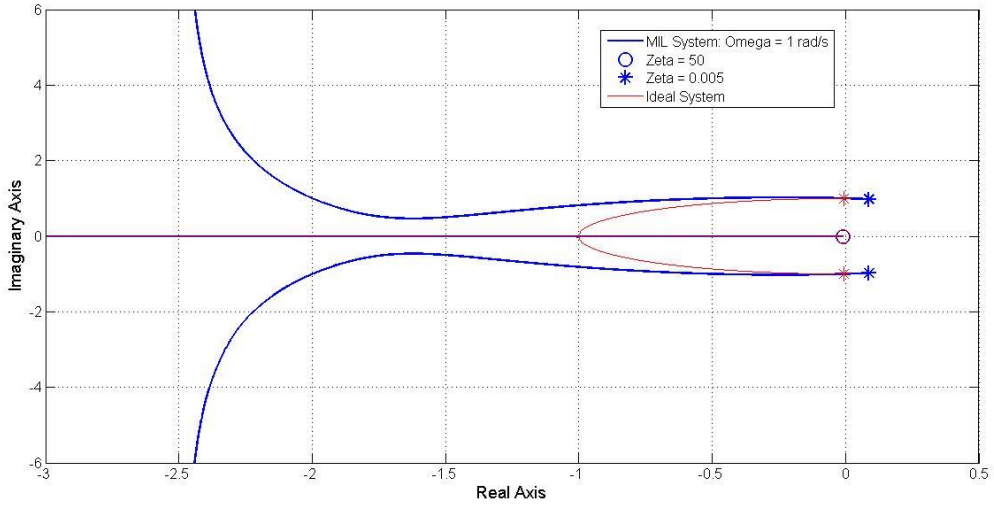

Figure 5.16 – Case 1: Exploded root locus of damping ratio variation for time constant of 0.2s.

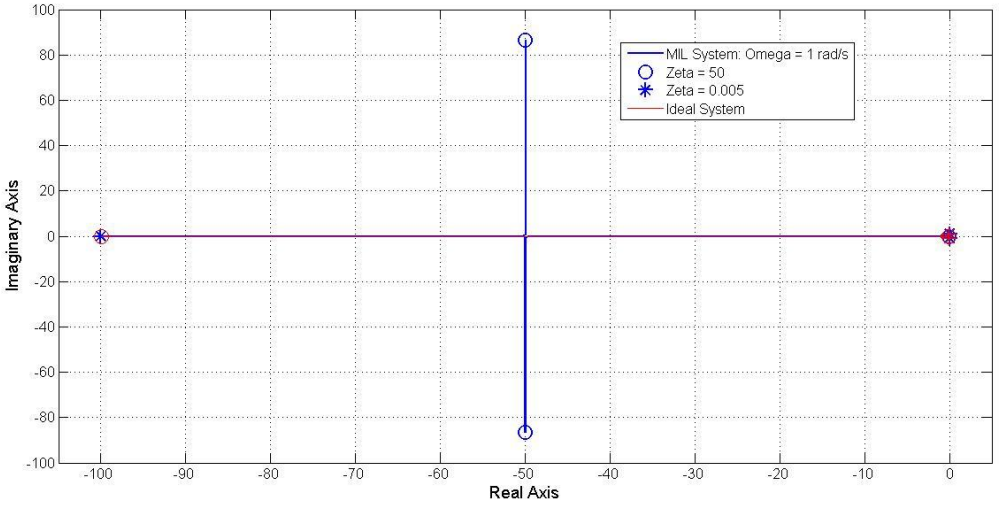

Figure 5.17 – Case 2: Root locus of damping ratio variation for time constant of 0.01s.

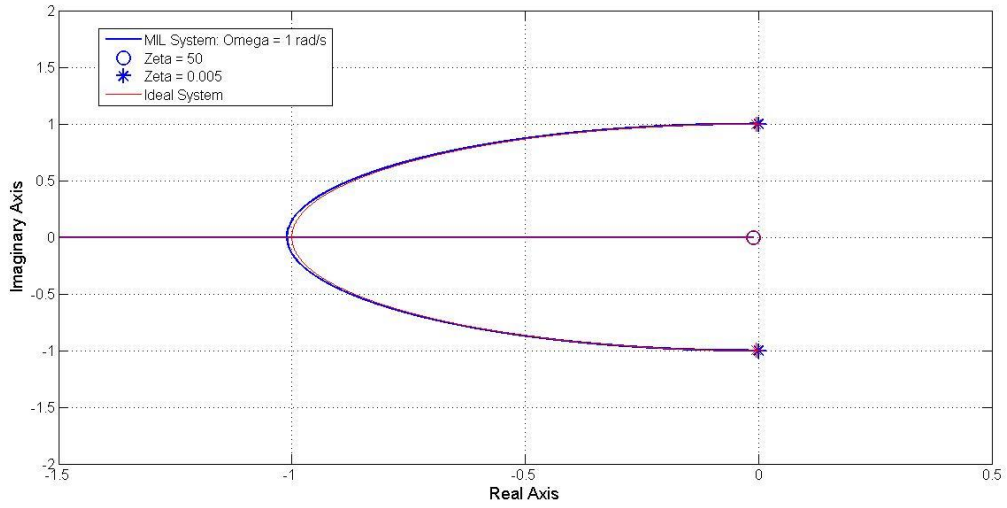

Figure 5.18 – Case 2: Exploded root locus of damping ratio variation for time constant of 0.01s.

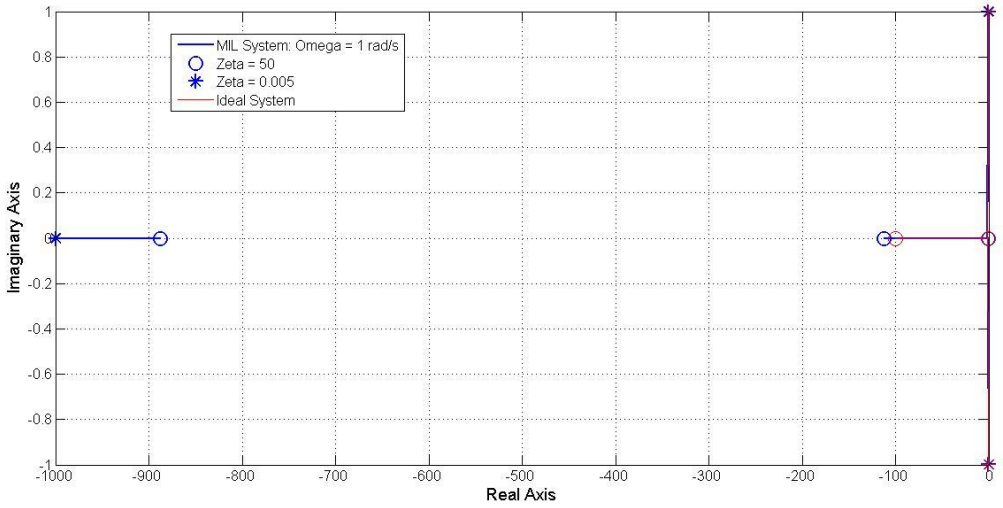

Figure 5.19 – Case 3: Root locus of damping ratio variation for time constant of 0.001s.

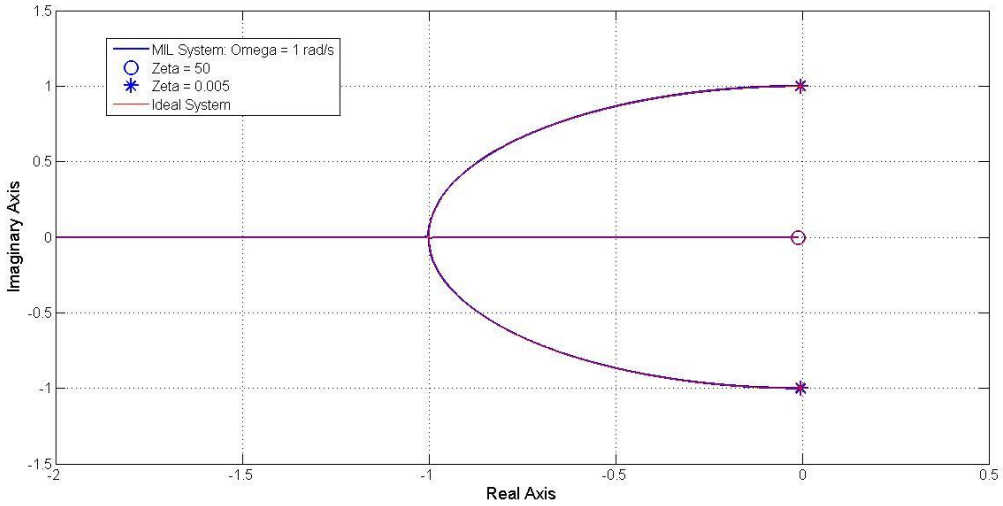

Figure 5.20 – Case 3: Exploded root locus of damping ratio variation for time constant of 0.001s.

5.2.4 Conclusion

The findings from parameter variation of single mass-spring-damper MIL system show that for root locus stability only the damping to stiffness ratio is relevant. Stability is easier to achieve when damping is high and stiffness low. Increasing the time delay constant will in general move system roots towards positive real axis. From this reasoning systems with higher natural frequencies will lead to instability for a given damping ratio and time delay. Conversely high damping ratios for a given time delay and natural frequency will ensure stability. If the time delay is not sufficiently small, even for a system with stable eigenvalues, an asymptote tending to very high frequencies appears when damping ratio is very high, or when system natural frequency is very high. Reduction of time delay moves the breakaway point further to the left of the root locus, if the time delay is very small then there is no asymptote as shown in Figure 5.19. However if damping ratio is increased further in Figure 5.19 then an asymptote would occur further to the left of the root locus. These results show that it is not enough that a given time delay yield stable eigenvalues, but that the time delay is small enough such that MIL does not introduce high frequency dynamics. Firstly the introductions of these dynamics diverge the MIL system response from the emulated system and secondly it could lead to instability in real time implementation.

5.3 Two Mass Model

Extending from the one mass case, formation of system equations and their analysis is conducted for a two mass spring damper system with MIL delays.

5.3.1 State Space Quarter Car Model

Here a quarter car model is developed and formulated into a state space model. The system equation of motion about the equilibrium position is given by,

$$m_u\ddot{x}_u = b_s(\dot{x}_s - \dot{x}_u) + k_s(x_s - x_u) - b_t(\dot{x}_u - \dot{u}) - k_t(x_u - u) \tag{5.35}$$

$$m_s\ddot{x}_s = -b_s(\dot{x}_s - \dot{x}_u) - k_s(x_s - x_u) \tag{5.36}$$

Here m_u and m_s denote the sprung and unsprung mass respectively. The suspension stiffness and damping are k_s and b_s respectively, and the tyre stiffness and damping are k_t and b_t. Rearranging the equation so that the system inputs are on the right hand side,

$$m_u\ddot{x}_u - b_s(\dot{x}_s - \dot{x}_u) - k_s(x_s - x_u) + b_t\dot{x}_u + k_t x_u = b_t\dot{u} + b_s u = \mu \tag{5.37}$$

$$m_s\ddot{x}_s + b_s(\dot{x}_s - \dot{x}_u) + k_t(x_s - x_u) = 0 \tag{5.38}$$

Defining the system states as,

$$z_1 = x_u \tag{5.39}$$

$$z_2 = x_s \tag{5.40}$$

$$z_3 = \dot{x}_u \tag{5.41}$$

$$z_4 = \dot{x}_s \tag{5.42}$$

Yields the following state space matrix,

$$\begin{bmatrix} 1 & 0 & 0 & 0 \\ 0 & 1 & 0 & 0 \\ 0 & 0 & m_u & 0 \\ 0 & 0 & 0 & m_s \end{bmatrix} \begin{bmatrix} \dot{x}_u \\ \dot{x}_s \\ \ddot{x}_u \\ \ddot{x}_s \end{bmatrix} + \begin{bmatrix} 0 & 0 & -1 & 0 \\ 0 & 0 & 0 & -1 \\ k_t + k_s & -k_s & b_t + b_s & -b_s \\ -k_s & k_s & -b_s & b_s \end{bmatrix} \begin{bmatrix} x_u \\ x_s \\ \dot{x}_u \\ \dot{x}_s \end{bmatrix} = \begin{bmatrix} 0 \\ 0 \\ 1 \\ 0 \end{bmatrix} \mu \tag{5.43}$$

This is a fourth order system and will have four eigenvalues of λ and four eigenvectors v. The system has two degrees of freedom so it will have two resonance modes, such that there are two pairs of conjugate poles if the system is underdamped. The mode shape is given by the eigenvector where the masses are either travelling in the same direction (Body Hop Mode) or in opposite directions (Wheel Hop Mode). A passive quarter car system will always be stable with all eigenvalues having negative real part.

5.3.2 MIL Suspension Model

As for the single mass system, the transfer function of the two mass MIL suspension is approximated as a first order delay. A block diagram of the resulting closed loop control system is shown in Figure 5.21.

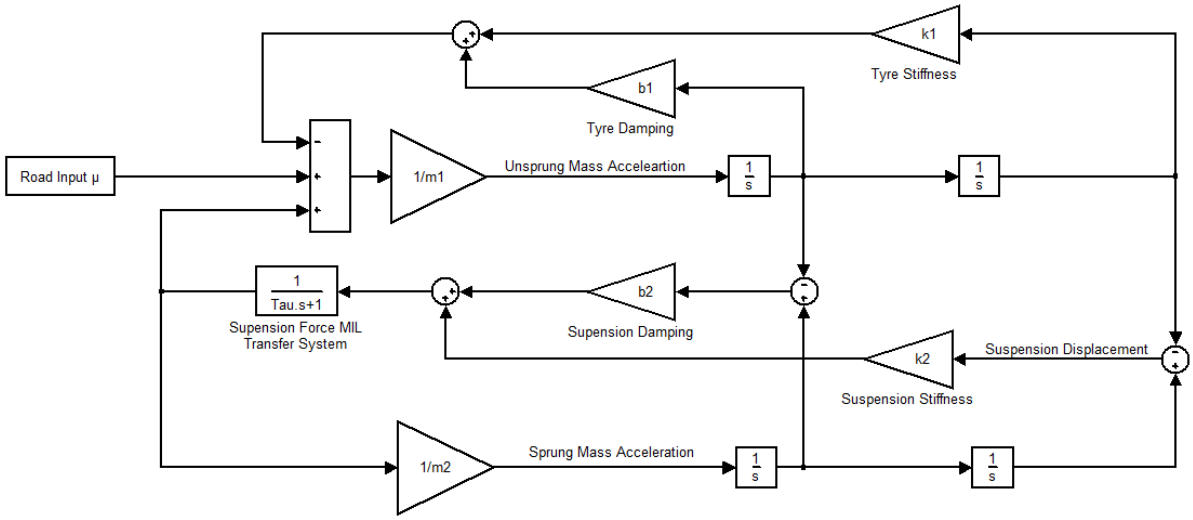

Figure 5.21 – Block diagram of closed loop control system with suspension MIL transfer function.

A first order filter is applied to the suspension force signal,

$$\tau_s \dot{f}_s + f_s = k_s(x_s - x_u) + b_s(\dot{x}_s - \dot{x}_u) \tag{5.44}$$

$$\dot{f}_s + \frac{1}{\tau_s} f_s + \frac{k_s}{\tau_s} x_u - \frac{k_s}{\tau_s} x_s + \frac{b_s}{\tau_s} \dot{x}_u - \frac{b_s}{\tau_s} \dot{x}_s = 0 \tag{5.45}$$

Here f_s represents the output of the suspension force transfer function and τ_s is the time constant of the first order filter. Now the equation of motion is rearranged so that suspension forces are obtained directly from the filtered force f_s,

$$m_u \ddot{x}_u - f_s + k_t x_u + b_t \dot{x}_u = \mu \tag{5.46}$$

$$m_s \ddot{x}_s + f_s = 0 \tag{5.47}$$

Arranging the new equations in state space matrix,

$$\begin{bmatrix} 1 & 0 & 0 & 0 & 0 \\ 0 & 1 & 0 & 0 & 0 \\ 0 & 0 & 1 & 0 & 0 \\ 0 & 0 & 0 & m_u & 0 \\ 0 & 0 & 0 & 0 & m_s \end{bmatrix} \begin{bmatrix} \dot{f}_s \\ \dot{x}_u \\ \dot{x}_s \\ \ddot{x}_u \\ \ddot{x}_s \end{bmatrix} + \begin{bmatrix} \tau_s^{-1} & k_s\tau_s^{-1} & -k_s\tau_s^{-1} & b_s\tau_s^{-1} & -b_s\tau_s^{-1} \\ 0 & 0 & 0 & -1 & 0 \\ 0 & 0 & 0 & 0 & -1 \\ -1 & k_t & 0 & b_t & 0 \\ 1 & 0 & 0 & 0 & 0 \end{bmatrix} \begin{bmatrix} f_s \\ x_u \\ x_s \\ \dot{x}_u \\ \dot{x}_s \end{bmatrix} = \begin{bmatrix} 0 \\ 0 \\ 0 \\ 1 \\ 0 \end{bmatrix} \mu \tag{5.48}$$

This system will yield 5 eigenvalues from which there are the two conjugate pole pairs representing the modes of vibration if the system is underdamped, and one additional pole for the decay of first order filter dynamics.

5.3.3 MIL vehicle structure Model

For the MIL vehicle structure the transfer function delay is approximated as a first order filter and applied to the sprung mass position output. A block diagram of the resulting system is illustrated in Figure 5.22. The delay of sprung mass position also results in an equal delay in sprung velocity. To incorporate this into the state space model two additional first order lags are required, one acting on the position output and one acting on the velocity output.

The time domain equation for the sprung mass postion filter given by,

$$\tau_m \dot{f}_{mp} + f_{mp} = x_s \tag{5.49}$$

$$\dot{f}_{mp} + \frac{1}{\tau_m} f_{mp} - \frac{1}{\tau_m} x_s = 0 \tag{5.50}$$

Where f_{mp} denote the position filter output and τ_m the time delay constant. The time domain equation for the sprung mass velocity filter is given by,

$$\tau_m \dot{f}_{mv} + f_{mv} = \dot{x}_s \tag{5.51}$$

$$\dot{f}_{mv} + \frac{1}{\tau_m} f_{mv} - \frac{1}{\tau_m} \dot{x}_s = 0 \tag{5.52}$$

Where f_{mv} is the velocity filter output. This introduces two additional degrees of freedom to the quarter car state space model. The equation of motion must also be altered to utilise the delayed position and velocity,

$$m_u \ddot{x}_u - b_s(f_{mv} - \dot{x}_u) - k_s\left(f_{mp} - x_u\right) + b_t \dot{x}_u + k_t x_u = \mu \tag{5.53}$$

$$m_s \ddot{x}_s + b_s(f_{mv} - \dot{x}_u) + k_s(f_{mp} - x_u) = 0 \tag{5.54}$$

Arranging the new equations in state space matrix,

$$\begin{bmatrix} 1 & 0 & 0 & 0 & 0 & 0 \\ 0 & 1 & 0 & 0 & 0 & 0 \\ 0 & 0 & 1 & 0 & 0 & 0 \\ 0 & 0 & 0 & 1 & 0 & 0 \\ 0 & 0 & 0 & 0 & m_1 & 0 \\ 0 & 0 & 0 & 0 & 0 & m_2 \end{bmatrix} \begin{bmatrix} \dot{f}_{mp} \\ \dot{f}_{mv} \\ \dot{x}_u \\ \dot{x}_s \\ \ddot{x}_u \\ \ddot{x}_s \end{bmatrix} + \begin{bmatrix} \tau_m^{-1} & 0 & 0 & -\tau_m^{-1} & 0 & 0 \\ 0 & \tau_m^{-1} & 0 & 0 & 0 & -\tau_m^{-1} \\ 0 & 0 & 0 & 0 & -1 & 0 \\ 0 & 0 & 0 & 0 & 0 & -1 \\ -k_s & -b_s & k_t + k_s & 0 & b_t + b_s & 0 \\ k_s & b_s & -k_s & 0 & -b_s & 0 \end{bmatrix} \begin{bmatrix} f_{mp} \\ f_{mv} \\ x_u \\ x_s \\ \dot{x}_u \\ \dot{x}_s \end{bmatrix} = \begin{bmatrix} 0 \\ 0 \\ 0 \\ 0 \\ 1 \\ 0 \end{bmatrix} \mu \tag{5.55}$$

This system will yield 6 eigenvalues from which there are the two conjugate pole pairs representing the modes of vibration if the system is underdamped, and two additional poles for the two first order filter dynamics.

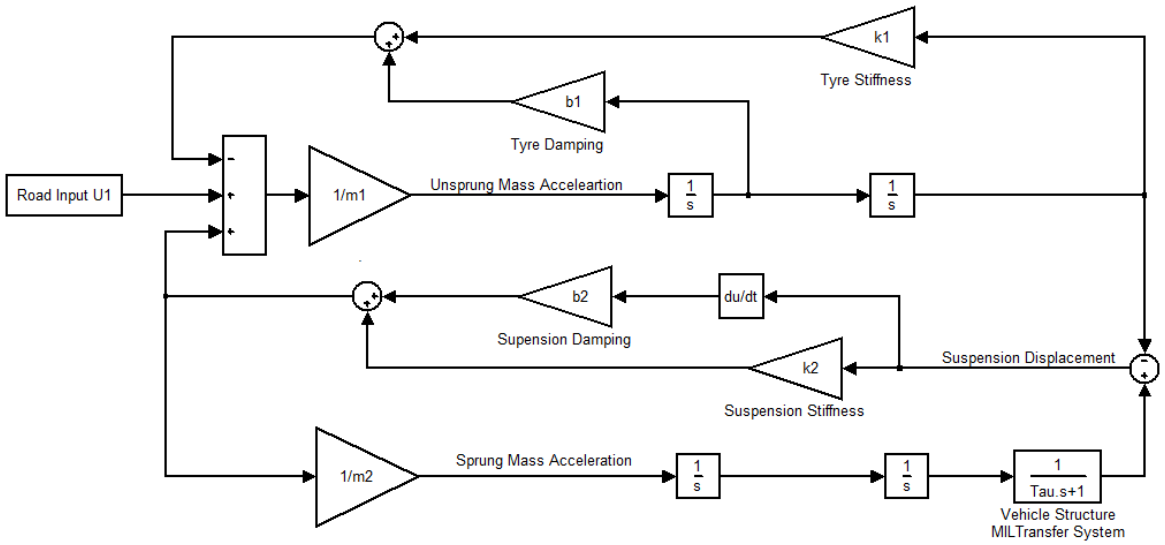

Figure 5.22 - Block diagram of closed loop control system with vehicle structure MIL transfer function.

5.3.4 Combined Suspension MIL and Vehicle structure MIL

A combined suspension MIL and vehicle structure MIL is implemented by combining the additional state space equation from the filter poles. The block diagram of the system will have the combined MIL systems as shown in Figure 5.21 and 5.22. The equation for the suspension force filter is altered to utilise the delayed sprung mass position and velocity instead. This yields the following state space equation,

$$\begin{bmatrix} 1 & 0 & 0 & 0 & 0 & 0 & 0 \\ 0 & 1 & 0 & 0 & 0 & 0 & 0 \\ 0 & 0 & 1 & 0 & 0 & 0 & 0 \\ 0 & 0 & 0 & 1 & 0 & 0 & 0 \\ 0 & 0 & 0 & 0 & 1 & 0 & 0 \\ 0 & 0 & 0 & 0 & 0 & m_u & 0 \\ 0 & 0 & 0 & 0 & 0 & 0 & m_s \end{bmatrix} \begin{bmatrix} \dot{f}_{mp} \\ \dot{f}_{mv} \\ \dot{f}_s \\ \dot{x}_u \\ \dot{x}_s \\ \ddot{x}_u \\ \ddot{x}_s \end{bmatrix} + \begin{bmatrix} \tau_m^{-1} & 0 & 0 & 0 & -\tau_m^{-1} & 0 & 0 \\ 0 & \tau_m^{-1} & 0 & 0 & 0 & 0 & -\tau_m^{-1} \\ -k_s\tau_s^{-1} & -b_s\tau_s^{-1} & \tau^{-1} & k_s\tau_s^{-1} & 0 & b_s\tau_s^{-1} & 0 \\ 0 & 0 & 0 & 0 & 0 & -1 & 0 \\ 0 & 0 & 0 & 0 & 1 & 0 & -1 \\ 0 & 0 & -1 & k_t & 0 & b_t & 0 \\ 0 & 0 & 1 & 0 & 0 & 0 & 0 \end{bmatrix} \begin{bmatrix} f_{mp} \\ f_{mv} \\ f_s \\ x_u \\ x_s \\ \dot{x}_u \\ \dot{x}_s \end{bmatrix} = \begin{bmatrix} 0 \\ 0 \\ 0 \\ 0 \\ 0 \\ 1 \\ 0 \end{bmatrix} U_1 \tag{5.56}$$

5.3.5 Stability of Suspension MIL

	Case 1	Case 2	Case 3	Case 4
$k_t\ (N/m)$	500	600	500	500
$k_s\ (N/m)$	500	500	500	500
$m_u\ (kg)$	50	50	60	50
$m_s\ (kg)$	50	50	50	50
$b_t\ (Ns/m)$	0	0	0	10
$b_s\ (Ns/m)$	100	100	100	100
$\tau\ (s)$	0.2	0.2	0.2	0.2
Real Part of Body Hop Pole	0	0	0	0
Real Part of Wheel Hop Pole	0	0	0	0

Table 5.6 – Variation of system parameters other than suspension stiffness and damping.

The quartercar MIL system has a system order higher than 3 which means that the roots of the system cannot be solved analytically to obtain an expression for critical time constant. As shown in Section 5.1.5 an expression for τ_c cannot be achieved for a 3rd order system from eigenvalue analysis and therefore it is also not possible for system of higher orders. While the Routh-Hurwitz Criterion could be used to solve for τ_c for a single mass system, for higher order systems such as the suspension MIL and vehicle structure MIL, the Routh-Hurwitz criterion yields multiple expressions which are extremely long with high order terms.

To help understand what causes the instability of MIL systems a set of arbitrary quartercar parameters are chosen with a MIL time delay constant such that the system is at the limit of stability. The stability condition of the suspension MIL quarter car is found to be exactly the same as the single mass suspension MIL since only variation of suspension damping and suspension stiffness can nudge the purely oscillatory system into stability or instability. The results of this are shown in Table 5.6. For the quarter car suspension MIL system the instability point occurs simultaneously for wheel and body hop modes. The critical time constant for the quarter car suspension MIL is given by,

$$\tau_c = \frac{b}{k} \tag{5.57}$$

5.3.6 Stability of Vehicle structure MIL

For the vehicle structure MIL system only the body hop poles can become unstable regardless of system parameters. The following Tables 5.7 – 5.12 shows the effect of varying each quarter car model parameter to investigate instability.

The results from the tables, in terms of the sprung mass system, high suspension stiffness and low sprung mass lead to instability. This means that as expected, higher sprung mass natural frequency will lead to deteriorating rig accuracy. As for suspension damping, instability occurs if the damping is too low or too high. For the unsprung mass system, high tyre stiffness and low unsprung mass lead to system stability. Therefore for stability the unsprung mass natural frequency should be low. More over increasing the tyre damping has a stabilising effect on the MIL system.

$k_t\ (N/m)$	500	500	500
$k_s\ (N/m)$	500	600	400
$m_u\ (kg)$	50	50	50
$m_s\ (kg)$	50	50	50
$b_t\ (Ns/m)$	0	0	0
$b_s\ (Ns/m)$	100	100	100
$\tau\ (s)$	0.06895	0.06895	0.06895
Real Part of Body Hop Pole	0	0.0242	-0.0394

Table 5.7 – Variation of suspension stiffness.

$k_t\ (N/m)$	500	500	500	500
$k_s\ (N/m)$	500	500	500	500
$m_u\ (kg)$	50	50	50	50
$m_s\ (kg)$	50	50	50	50
$b_t\ (Ns/m)$	0	0	0	0
$b_s\ (Ns/m)$	100	200	50	1000
$\tau\ (s)$	0.06895	0.06895	0.06895	0.06895
Real Part of Body Hop Pole	0	-0.0487	0.0432	0.0256

Table 5.8 – Variation of suspension damping.

$k_t\ (N/m)$	500	500	500
$k_s\ (N/m)$	500	500	500
$m_u\ (kg)$	50	50	50
$m_s\ (kg)$	50	60	40
$b_t\ (Ns/m)$	0	0	0
$b_s\ (Ns/m)$	100	100	100
$\tau\ (s)$	0.06895	0.06895	0.06895
Real Part of Body Hop Pole	0	-0.0057	0.0087

Table 5.9 – Variation of sprung mass.

$k_t\ (N/m)$	500	600	400
$k_s\ (N/m)$	500	500	500
$m_u\ (kg)$	50	50	50
$m_s\ (kg)$	50	50	50
$b_t\ (Ns/m)$	0	0	0
$b_s\ (Ns/m)$	100	100	100
$\tau\ (s)$	0.06895	0.06895	0.06895
Real Part of Body Hop Pole	0	-0.0148	0.0112

Table 5.10 – Variation of tyre stiffness.

$k_t\ (N/m)$	500	500	500
$k_s\ (N/m)$	500	500	500
$m_u\ (kg)$	50	60	40
$m_s\ (kg)$	50	50	50
$b_t\ (Ns/m)$	0	0	0
$b_s\ (Ns/m)$	100	100	100
$\tau\ (s)$	0.06895	0.06895	0.06895
Real Part of Body Hop Pole	0	0.0043	-0.0061

Table 5.11 – Variation of unsprung mass.

$k_t\ (N/m)$	500	500	500
$k_s\ (N/m)$	500	500	500
$m_u\ (kg)$	50	50	50
$m_s\ (kg)$	50	50	50
$b_t\ (Ns/m)$	0	10	100
$b_s\ (Ns/m)$	100	100	100
$\tau\ (s)$	0.06895	0.06895	0.06895
Real Part of Body Hop Pole	0	-0.0299	-0.2926

Table 5.12 – Variation of tyre damping.

5.4 Quarter Car MIL Suspension Parameters Variation

The state space model formulated in section 5.3 reveals the poles of the closed loop system and their frequency. The location of the poles indicates the stability of the system, the response decay rate and the frequency of each mode. It is expected that the larger the transfer function delay the more unstable the system will become as in the single mass case. However it is not as clear how variations of other parameters such as stiffness, damping and mass inertias would affect the system response. These analyses of parameter variations could be conducted using the state space model, here the case of suspension MIL and vehicle structure MIL are evaluated separately. As to not overload the reader with graphical information of root locus due to parameter variation, only a qualitative trends from the analysis will be discussed here, for complete presentation of root locus results see Appendix A.

The root locus results for the quarter car MIL suspension shows the same behavior as seen in the single MIL system. As shown in Section 5.3, the two systems have the same stability condition which is only dependent on the suspension stiffness and damping. Interestingly the wheel and body hop poles of the quarter car MIL suspension always cross the stability boundary together. As for the unsprung mass system, results show that best performance is achieved when tyre natural frequency is low. This would place lower demands on the actuator in terms of frequency, and therefore allow a larger time delay to be used.

Variation of Time Delay

For increasing delay the quarter car MIL suspension behaves similarly to the single mass MIL system. For the sprung mass critical damping ratio case, with low time delays there is a close resemblance and the test rig wheel hop mode is overdamped as in the ideal case. As time delay increases the underdamped body hop poles move to the right and become unstable like in the single mass MIL system. For the wheel hop poles, they move from overdamped to underdamped and then continue rightwards reaching instability at the same time delay value as the body hop poles. At the instability point the system behaves as the ideal quarter car suspension with zero suspension and tyre damping. The root locus plots for these results are shown in Appendix A1.1.

Variation of Natural Frequency

As in the single mass MIL system, here the best performance is achieved when the sprung mass natural frequency is low and the damping ratio high. The root locus plots are shown in Appendix A1.2. As natural frequency increases both the body and wheel hop poles begin diverging from the ideal poles and move to the right becoming unstable together. The quarter car MIL suspension has the same critical time delay as the single mass MIL.

Variation of Damping Ratio

Like the single mass MIL system, instability of the quarter car suspension MIL occurs when the sprung mass damping ratio is high. Additionally root locus plots shown in Appendix A1.3 shows that there are vertical asymptotes when the damping ratio is low. Even when time delay is small the vertical asymptote can still exist but is shifted to left of the root locus and the asymptote reaches higher frequencies for the same damping ratio. This phenomena is also seen for the single mass MIL

system. This means that there could be issues with instability even when the damping ratio is low, since the high frequency dynamics from the asymptotes may mean that control loop sampling times are insufficient. Only when the time delay is small that no vertical asymptote is observed at low damping ratios, and good resemblance to the ideal system is achieved across all damping ratios.

Variation of Tyre Stiffness

The root locus plots for tyre stiffness variation are shown in Appendix A1.4. The results show that variation of tyre stiffness cannot cause system instability, as stability only depend only on the time delay, suspension spring and damping parameters. As tyre stiffness increases the wheel hop poles diverge from the ideal case leading to poor performance. However instead of reaching instability, at high tyre stiffness the wheel hop poles form a vertical asymptote at zero real axes.

Variation of Wheel Mass

The root locus plots for wheel mass variation are shown in Appendix A1.5. The results show that variation of wheel mass cannot cause system instability, as stability only depend on the time delay, suspension spring and damping parameters. Best performance is achieved when wheel mass is high, while a vertical asymptote occurs when wheel mass is low. The vertical asymptote can lead to system instability if sampling rate is insufficient.

5.5 Quarter Car MIL Vehicle Structure Parameters Variation

Parameters variations are conducted for the quarter car MIL vehicle structure and root locus results are presented in Appendix A2. Here general discussions of effects due to parameter changes are given. For the quarter car MIL vehicle structure only the body hop poles become unstable and the wheel hop poles always stable. Like in the MIL systems previously studied, high sprung mass natural frequency and low sprung mass damping ratio leads to instability. A dramatic difference from the MIL suspension is that the unsprung mass system can also cause instability. It is shown that low unsprung mass natural frequency leads to worse performance and instability, unlike the MIL suspension where resemblance to the ideal case is achieved when unsprung mass frequency is low.

Variation of Time Delay

As expected, increases in time delay move the system poles to the right leading to instability. For the underdamped case, increasing time delay moves wheel hop poles from being overdamped to underdamped. This is also observed in the quarter car MIL suspension. The most notable difference for the quarter car MIL vehicle structure is that, although both wheel and body hop poles move to the right, only the body hop poles become unstable. This maybe because the MIL vehicle structure only acts on the sprung mass, while the MIL suspension acts on both sprung and unsprung masses.

Variation of Natural Frequency

The root locus plots in Appendix A2.2 confirm that increasing sprung mass natural frequency decreases system performance and could lead to instability. Here as observed for the quarter car MIL vehicle structure, only the body hop mode becomes unstable. Interestingly, as natural frequency increases the wheel hop poles generally move to the left, rather than to the right as seen in single mass MIL and quarter car MIL suspension systems.

Damping Ratio

In all the root locus plots shown in Appendix A2.3, the body hop poles become unstable at low sprung mass damping ratios and the wheel hop mode is always stable. The shape of the body hop poles is similar to that in the suspension MIL case except that it continues moving rightwards towards instability region when the damping ratio is low. In terms of the wheel hop mode, at low frequencies the wheel hop does not become unstable and actually approaches the ideal wheel hop poles. However at high damping ratios a vertical asymptote is seen for the wheel hop poles as observed in all other MIL systems. The results here show that for the quarter car MIL vehicle structure system instability occurs when sprung mass damping ratio is high or low.

Variation of Tyre Stiffness

Interestingly the variation of tyre stiffness has the opposite effect on the quarter car MIL vehicle structure compared to the MIL suspension. Here best performance is achieved when tyre stiffness is high. As tyre stiffness decreases the body hop poles move to the right and become unstable. If the system is stable, the plots show that divergence from the ideal dynamics is greatest for the wheel hop mode when tyre stiffness is low, and greatest for the body hop mode when the tyre stiffness is high.

Variation of Wheel Mass

Again in contrary to the quarter car MIL suspension, here instability for the body hop modes occurs when wheel mass is high. For the wheel hop poles, good resemblance to the ideal dynamics is greatest when wheel mass is high and worse when low.

5.6 Quarter Car Combined MIL vehicle structure and MIL Suspension Parameters Variation

Root locus results for parameters variations are conducted for the combined quarter car MIL suspension and MIL vehicle structure and presented in Appendix A3. Here general discussions of effects due to parameter changes are given. The results show that the combined MIL vehicle structure and MIL suspension exhibits the combination of properties seen in the individual quarter MIL vehicle structure and the individual quarter car MIL suspension.

Variation of Time Delay

The combined qualities of the quarter car MIL suspension and MIL vehicle structure can be seen in the root locus plots in Appendix A3.1. Here increasing time delay leads to system instability with both body and wheel hop poles moving to the right. Instability first occurs for the body hop mode and if time delay increases further then the wheel hop mode will also become unstable. The results also show that the combination of time delays from two sources lead to greater system instability, shifting real poles to the right.

Variation of Natural Frequency

For the sprung mass natural frequency variation, the combination of general trends from the quarter car MIL suspension and MIL vehicle structure are observed. System instability occurs when the natural frequency is high and occurs for both the body and wheel hop modes, but occurs in the body mode first.

Variation of Damping Ratio

The combined qualities from the quarter car MIL suspension and the quarter car MIL vehicle structure can be seen in the combined system root locus as shown in Appendix A3.3. Body hop poles are unstable at both low and high damping ratios, this is the same as in the quarter car MIL vehicle structure. The wheel hop poles exhibit a stable vertical asymptote at low damping ratios and unstable at high damping ratios. For the combined system, as always the body hop poles reach instability prior to the wheel hop poles.

Variation of Tyre Stiffness

The variation of tyre stiffness in Appendix A3.4 shows that body hop poles are unstable when stiffness is low as in the vehicle structure MIL. When tyre stiffness is high, the wheel hop poles diverge from the ideal trajectory and approach a vertical asymptote at zero real axes as seen in the MIL suspension.

Variation of Wheel Mass

The variation of wheel mass in Appendix A3.5 shows that body hop poles are unstable when wheel mass is high as in the MIL vehicle structure. When wheel mass is low, the wheel hop poles diverge from the ideal trajectory and approach a vertical asymptote at zero real axes as seen in the MIL suspension.

5.7 Conclusion

The closed loop system analysis of MIL hybrid systems was conducted in this chapter by approximating the MIL system delay as a first order lag. The analysis shows that for all MIL systems large time delay constant of the first order lag lead to poor performance and instability. A comparative summary of stability condition for the various configurations of MIL systems is shown in Table 5.13.

It is shown that, for a single mass-spring-damper, suspension MIL and vehicle structure MIL systems are equivalent with identical dynamics. The stability of a single mass MIL system is dependent only on the damping to stiffness ratio and is guaranteed if the time constant is lower than the ratio.

The quarter car suspension MIL system has the same stability condition as the one mass case which means that, if the isolated sprung mass system is stable, the two mass system will also be stable. For good performance the sprung mass natural frequency should be low while the sprung mass damping ratio is high. However with very high sprung mass damping ratio there could be additional high frequency dynamics introduced to the system which deteriorates performance and could lead to instability if closed loop control sampling rate is not sufficiently high. In regards to the wheel and tyre, the mass should be high and the stiffness low.

The quarter car MIL vehicle structure stability criteria are more complex. In general, the sprung mass should be high and the suspension stiffness low. Therefore like the quarter car MIL suspension, systems with low sprung mass natural frequency are desirable. Another interesting difference is that, for quarter car MIL vehicle structure systems, both low and high suspension damping ratios cause instability. Moreover, the tyre stiffness should be high and the wheel mass low such that the unsprung mass natural frequency is high.

When both quarter car suspension MIL and vehicle structure MIL systems are within one closed loop system, the overall dynamic response is a combination of both systems. This means that a smaller delay time constant will be required from each MIL system and instability could be caused by the trends seen from the individual investigation of each MIL system but with a few differences. In the next Chapter experimental tests are conducted which verify the findings from the analysis conducted here.

	Stability					
	Sprung Mass				Unsprung Mass	
	Natural Frequency		Damping Ratio		Natural Frequency	
	Low	High	Low	High	Low	High
Single Mass MIL	✔	✘	✘	✔	-	-
Quarter Car MIL Suspension	✔	✘	✘	✔	✔	✔
Quarter Car MIL Vehicle Structure	✔	✘	✘	✘	✘	✔
Quarter Car MIL Combined	✔	✘	✘	✘	✘	✔

Table 5.13 – Summary of stability conditions for various MIL systems. A tick denotes stability and a cross denotes instability.

6. Quarter Car Experimental Validation

6.1 Test System Description

In this section a test rig is used to test a quarter car model subjected to a drop test and ground disturbance. The drop test is representative of an aircraft landing touchdown while response to ground input is representative for taxiing. The test conditions are chosen because an aircraft has considerable flexible structural dynamics which could be modelled by the sprung vehicle structure MIL system, flexible structure test results are presented in Chapter 7.

6.1.1 Overall System

The test rig is controlled using MATLAB XPC software run on a desk top computer using a National Instruments input/output card PCI-6229. Inputs to the card are sensor readings and outputs are the command position and force to the actuators. A schematic of the signal flow of the control loop is shown in Figure 6.1 and a mechanical diagram in Figure 6.2

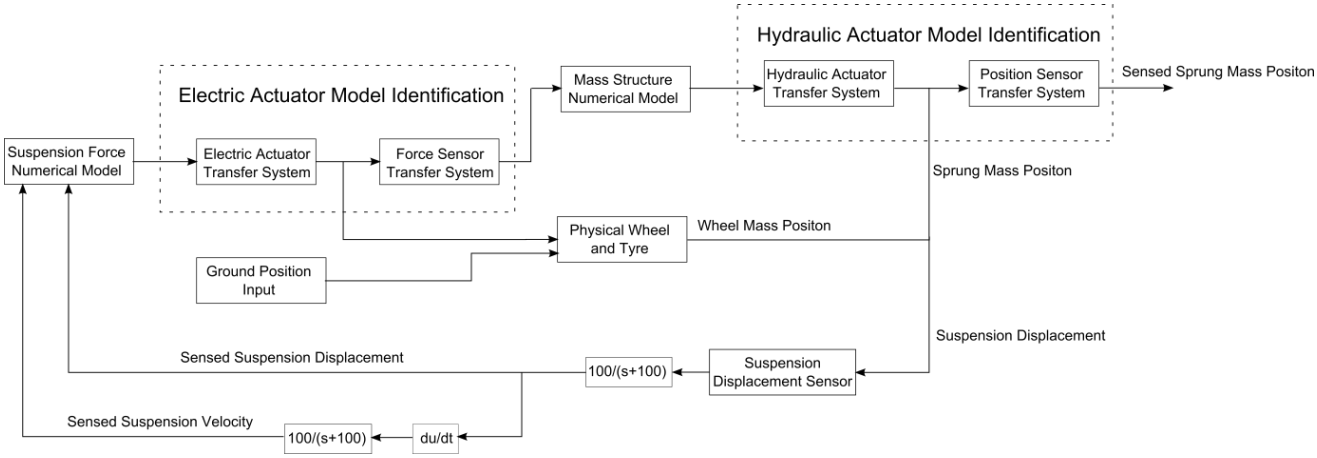

Figure 6.1 – Signal flow schematic of numerical-experimental test rig.

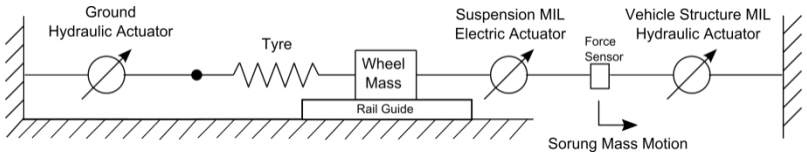

Figure 6.2 – Mechanical diagram of experimental test, here the spring represent a real tyre.

6.1.2 Electric Actuator Controller

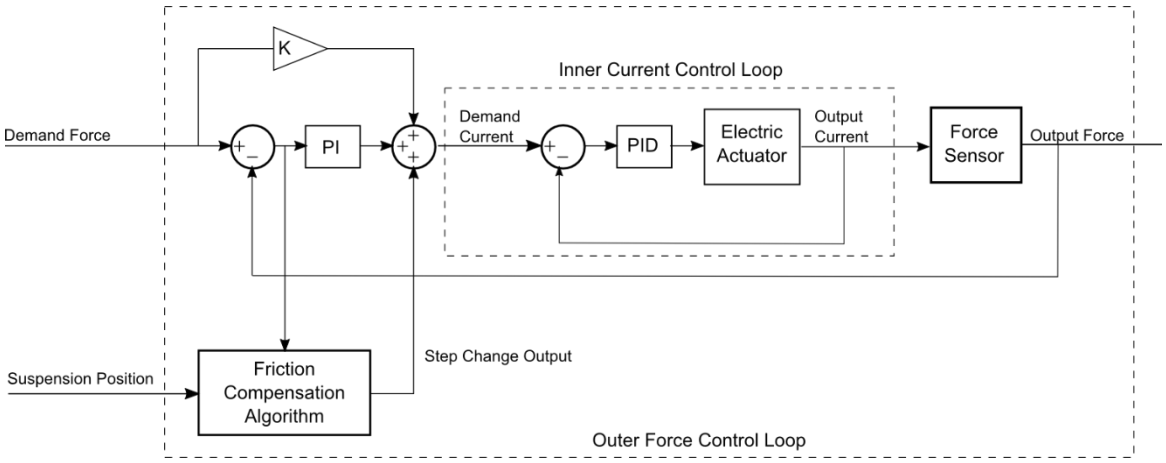

Figure 6.3 – Block diagram of electric actuator controller.

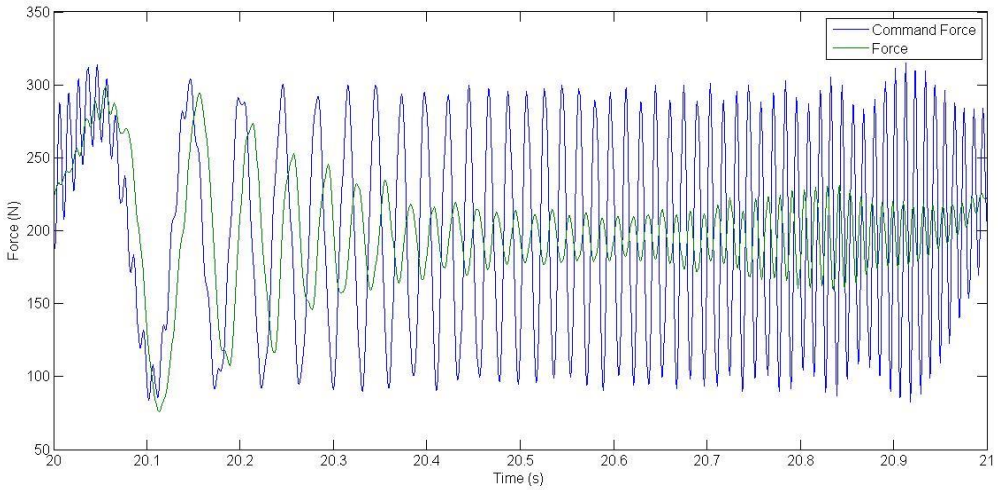

Figure 6.4 – Force tracking time response with SPHS input signal.

The block diagram of the electric actuator controller is the same as shown in Figure 6.3. The control consists of an inner current control loop and an outer force control loop. A first order lag filter with time constant 0.01 second is used to filter noise from the force sensor signal. The inner current control loop was tuned for high speed response using the software provided by the manufacturer of the actuator. The outer control loop was tuned using Ziegler-Nichols method [135].

Electric actuator model identification was conducted using a Schroeder Phased Harmonic Signal (SPHS) input signal. The SPHS signal contains integer frequencies of 1-100 Hz with equal magnitudes, to ensure that the electric actuator frequencies of interest are excited. The major benefit of this is much reduced testing times compared to excitation by sine waves of a single frequency. The SPHS achieves this by selecting the relative phase of each frequency component such that the overall signal has the lowest possible peak value, this is so that saturation of actuator can be avoided [136]. The time trace of the input and output signal is shown in Figure 6.4.

The system identification toolbox in MATLAB was utilised where transfer functions up to eight order were fitted to the time response. The results showed that the best fit was obtained when the transfer function is third order with a single zero described in Equation (6.1). The time response output of the transfer function is shown in Figure 6.5 and the bode plot in Figure 6.6. The RMS error of the model is 27% when the 200 N point is taken as the equilibrium zero.

The model has a good fit with the experimental results apart for two regions in particular. At low frequencies, see from 20-20.1 second, the experimental result contains a higher frequency component. At higher frequencies, see from 20.7-20.95 seconds, the experimental force increases in amplitude and this effect could not be captured by any of the tested transfer functions. In terms of phase response there is a good match with the experimental results, for most of the entire frequency range.

$$TF = \frac{0.1562\,s^2 - 68.9s + 4.716 \times 10^4}{s^2 + 438.8s + 4.706 \times 10^4} \tag{6.1}$$

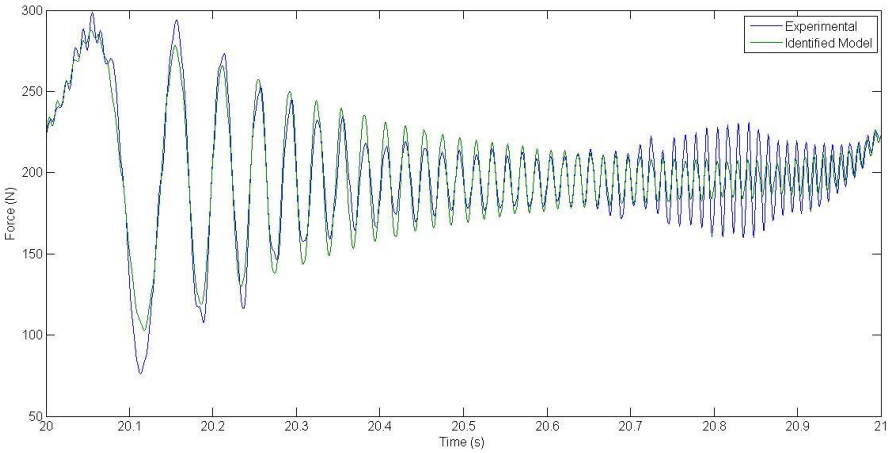

Figure 6.5 – Comparison of identified model response TF to the experimental result.

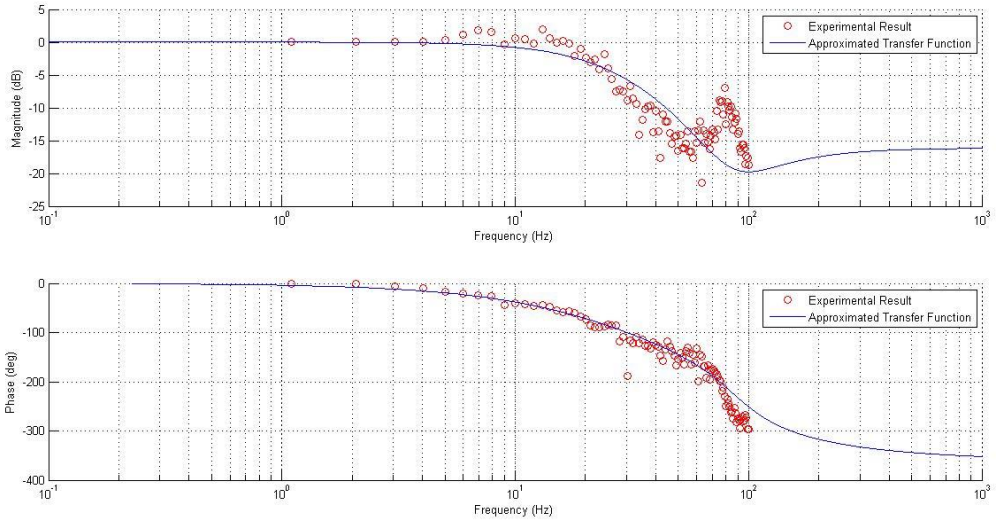

Figure 6.6 – Bode Plot of identified transfer function.

The bode plot contains the phase delay of the system at each frequency. Therefore a time delay can be calculated from the phase delay at each frequency. The time delay plot of the approximeted transfer function is shown in Figure 6.7. Since the model matches the experimental results in terms of phase response up to about 70-80 Hz and the tests will be conducted up to 10 Hz, the time delay shown in Figure 6.7 is a good representation of the system. The divergence of the identified model from the experimental results occurs at around 80-100Hz, most noticeably in terms of magnitude response as observed in Figure 6.5.

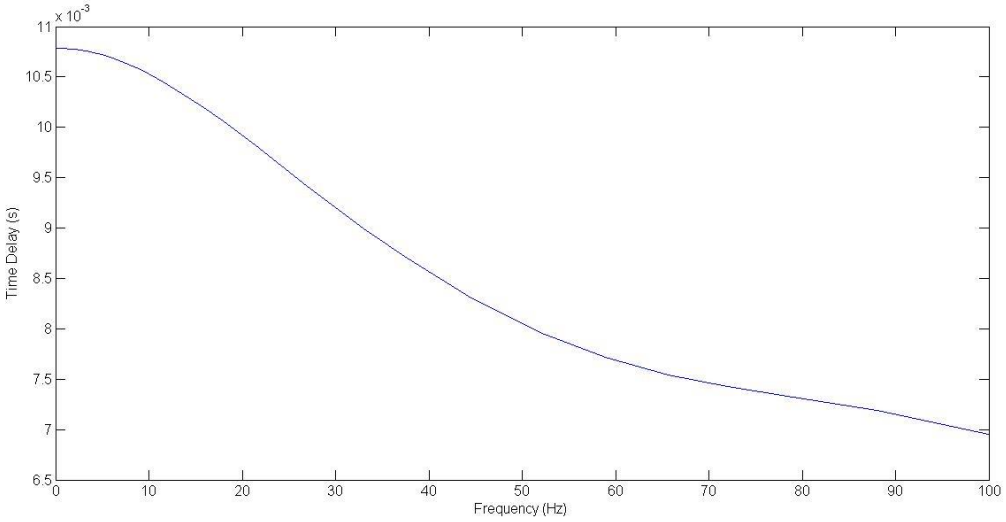

Figure 6.7 – Time delay of transfer function model.

6.1.3 Hydraulic Actuator Controller

The hydraulic actuator controller uses the PID controller which is also tuned by the Ziegler-Nichols method [135]. One hydraulic actuator is used for the vehicle structure MIL and another for the ground input.

The dynamic response and associated transfer function of the hydraulic actuator was identified using the same process as above. The hydraulic actuator is position controlled and the tracking of the SPHS input signal is shown in Figure 6.8. The results show that actuator has poor magnitude response, with very low gains beyond the -3dB point even at low frequencies below 10 Hz. Using the MATLAB system identification toolbox, a transfer function was obtained and the response of the transfer function to the SPHS input is shown in Figure 6.9. The identified transfer function shows a good match to the real system in terms of phase response while the amplitude response is too low for low frequencies but still sufficiently captures the general trend. The identified transfer function is fourth order with two zeroes and has a RMS percentage error of 28% when compared to the real output,

$$TF = \frac{1817s^2 + 7.719 \times 10^4 s + 6.243 \times 10^5}{s^4 + 165.9s^3 + 6674s^2 + 8.598 \times 10^4 s + 6.281 \times 10^5} \tag{6.2}$$

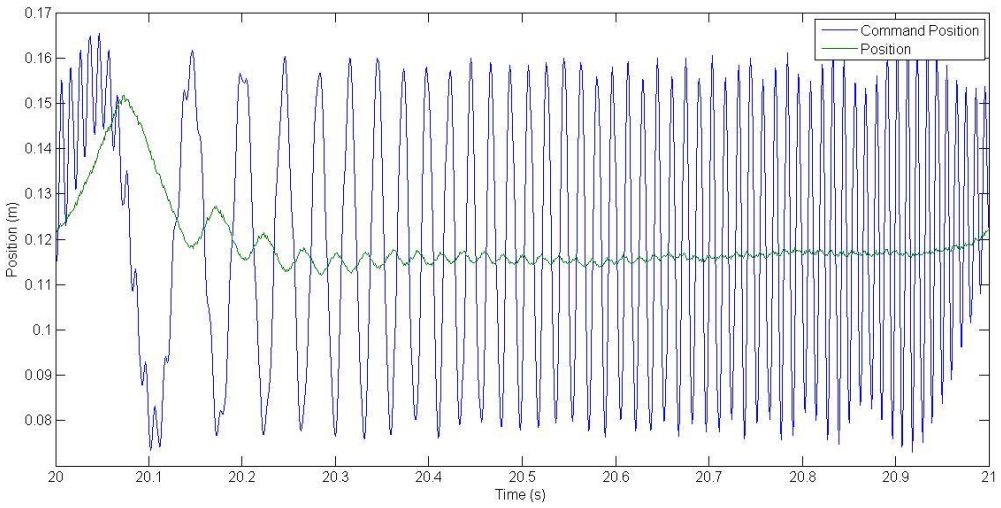

Figure 6.8 - Position tracking time response with SPHS input signal.

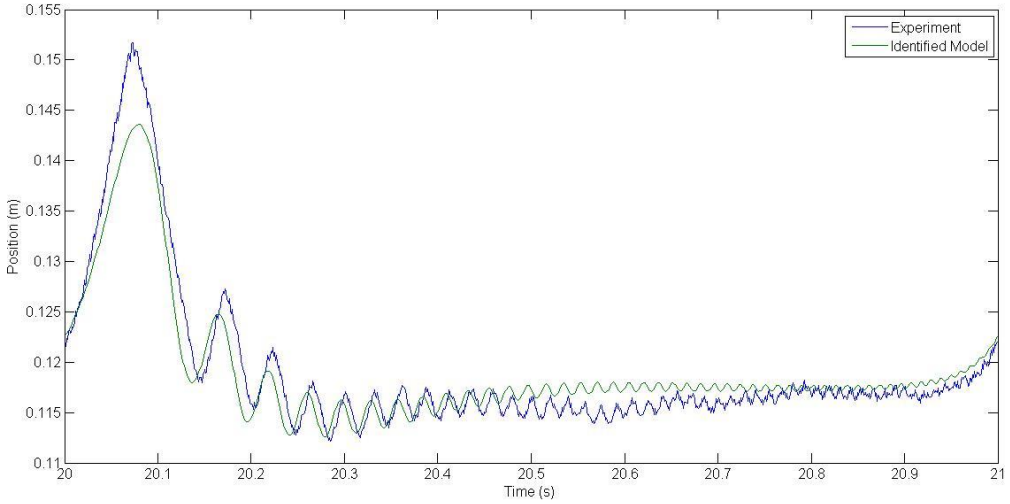

Figure 6.9 - Comparison of identified model response TF to the experimental result.

Figure 6.10 shows the bode plot of the identified transfer function in comparison to experimental data. There is a good agreement in terms of magnitude response across the entire test freuency range. In terms of phase response there is good agreement up to approximatly 13 Hz, this is because after 13 Hz the rate of change of phase lag becomes greater and this could not be captured by the approximated transfer functions while maintining the correct magnitude response. However this approximation remains valid since hybrid tests that are conducted in Chapter 6 and 7 has a maximum forced frequency of 10Hz.

It can be seen that the phase shift of the transfer function is quite large, even at 1 Hz the phase shift is already approximatly 90 degrees. This is likely to cause issues to the test rig performance and stability since the large phase shift implies a large time delay. The time delay plot in Figure 6.11 derived from the bode plot confirms that the hydrualic actuator has large time delay with a peak occuring at approimately 3Hz.

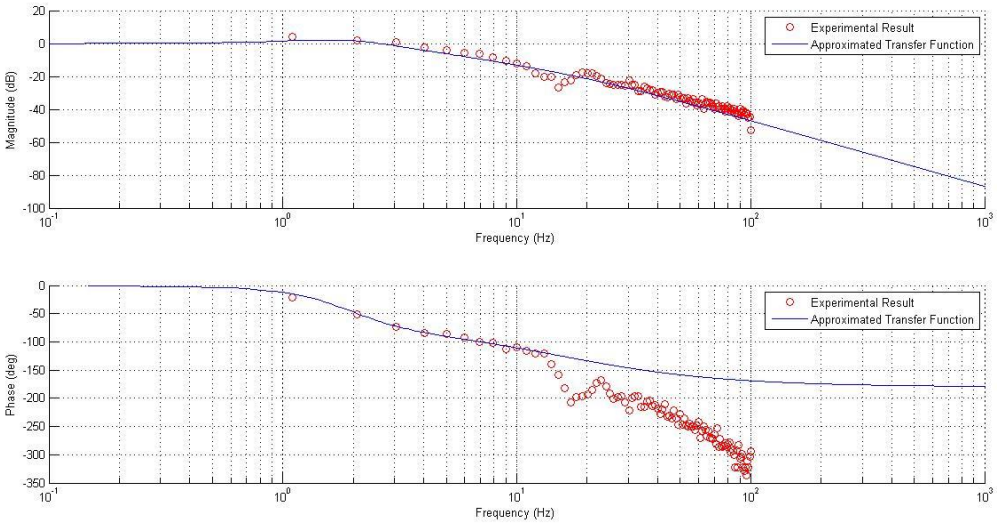

Figure 6.10 – Bode plot of identified transfer function.

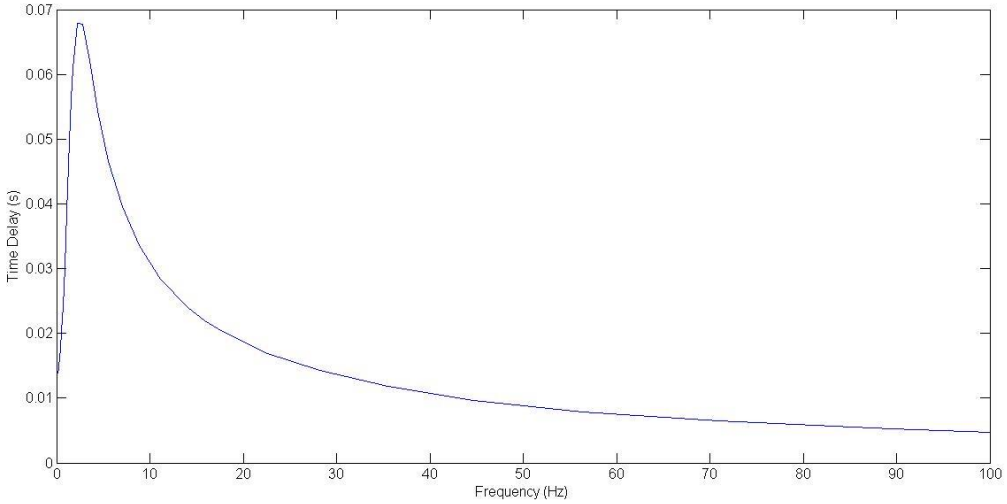

Figure 6.11 – Time delay of identified transfer function.

6.1.3 Tyre Stiffness Identification

The tyre stiffness was tested using a static Instron force/displacement testing machine. The result of the test is shown in Figure 6.12. The plot shows that tyre stiffness is non-linear and could be well described by a fifth order polynomial. A best fit straight line through the origin yields a tyre stiffness of approximately 23000N/m. Due to limitations of the Instron test machine test the tyre is compressed with contacts on opposite sides of the tyre, unlike in a real operation where the tyre is compressed between the hub and tyre. This means that the stiffness result from the test can be approximated to compressing two springs in series; therefore the stiffness of the tyre in normal operation will be twice the measured value, approximately 46000 N/m.

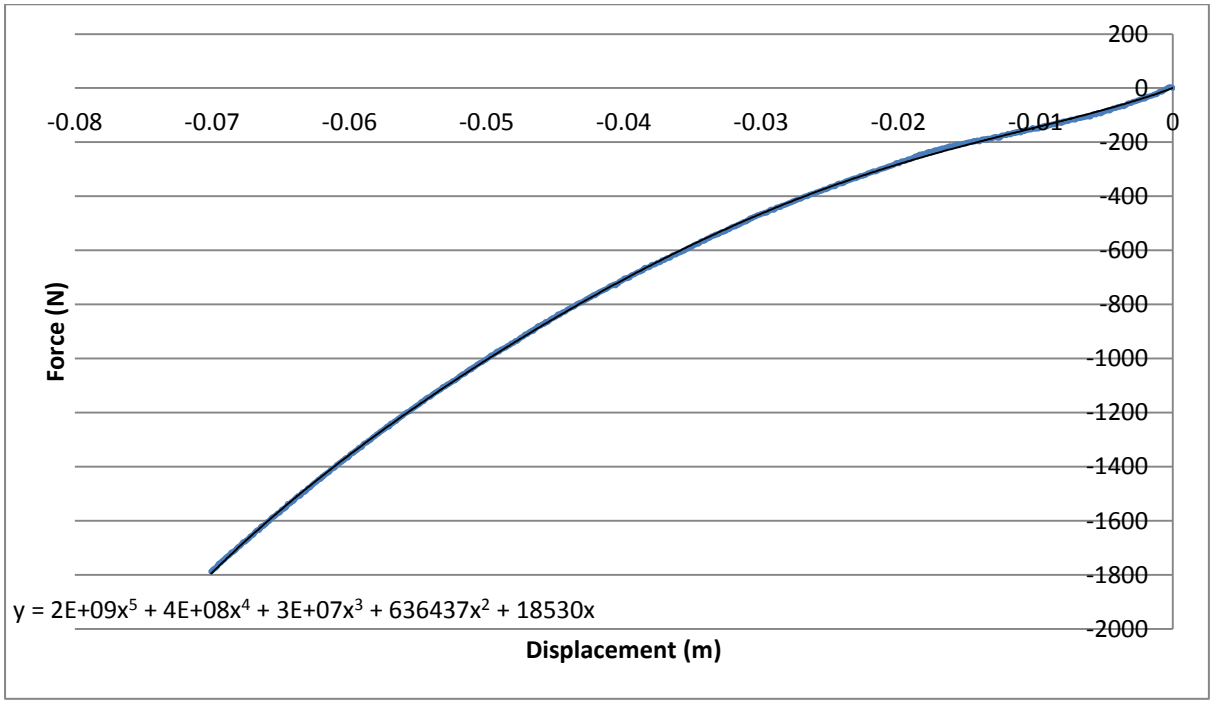

Figure 6.12 – Tyre force displacement relationship, static loading test.

6.1.3 Rail Guide Friction Identification

The rail guide on which the wheel mass assembly rests is subject to substantial friction forces. The static friction level was identified using the electric actuator to apply a ramping force until motion occurs. Repeating the test in both directions reveals that the static friction force is approximately 50N (Figure 6.13). Displacement units in the figure are arbitrary since the intention here is to show the level of force output required to overcome friction in the railings and initiate motion.

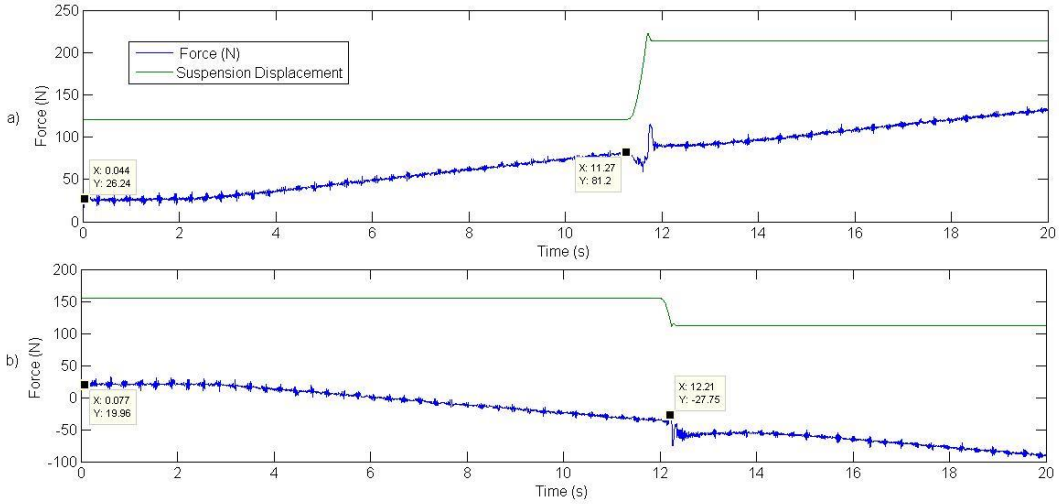

Figure 6.13 – Tyre force displacement relationship, static loading test. Here the displacement signals indicate the overcoming of railing friction force to initiate motion, therefore the displacement is shown in arbitrary units.

6.2 Real-Time Control Stability

The findings from Chapter 5 indicate that parameters of the quarter car system have an important impact on the performance and stability of the test rig. From the rig system parameters identified in Section 6.1 a simulation of test rig performance could be conducted. To simplify the simulations, the transfer functions of the hydraulic and electric actuator dynamics are considered to be dominated by their sensor filter. Additionally the simulation contains the low pass filters for the suspension position and velocity sensor readings. To get a good degree of noise attenuation, all low pass filters are of 1st order with a time constant of 0.01 s.

Experimental test for the Boeing 707 configuration is also conducted and the result shown in Figure 6.23 show agreement with the simulation. For the Boeing 707 configuration the MIL system delays and system natural frequencies are such that the system is unstable with negative damping.

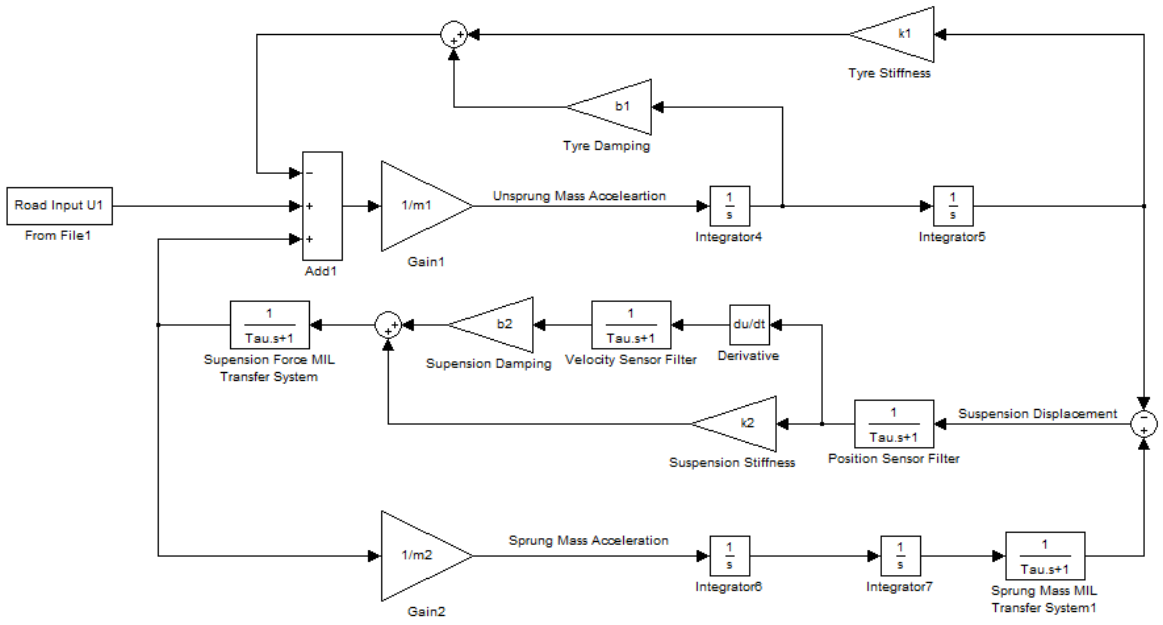

Figure 6.14 – Block diagram of simplified test rig simulation.

The simplified simulation shown in Figure 6.14 is used to simulate the test rig under different vehicle parameters. Vehicles are selected to represent a range of weight classes and the parameters of these vehicles are presented in Table 6.1. The parameters for the Boeing 707 is obtained from [119], the truck obtained from [25], the car obtained from [137] and the motorcycle obtained from [138]. For the truck, since suspension damping information was unavailable, it was assumed to be critically damped if the sprung mass was considered independently.

	k_t (N/m)	m_u (kg)	k_s (N/m)	b_s (Ns/m)	m_s (kg)	b_s/k_s
Boeing 707	8461000	1140	11250000	105400	68210	0.0094
Truck	500000	420	1950000	94300	4450	0.0484
Car	250000	400	20000	1300	400	0.0650
Motorcycle	180000	25	7600	750	72.5	0.0987

Table 6.1 – Single wheel station suspension parameters of various vehicle types.

Instability occurred in simulation for all the vehicle types indicated in Table 6.1. The time response of the simulations are shown in Figures 6.15-6.22. From the figures it can be seen that stability grows fastest for the aircraft, then the truck while the car and motorcycle has less exponential growth. This suggests that the parameters of larger vehicles result in more system instability for a given delay.

The results from Chapter 5 indicate that for stability the sprung mass undamped natural frequency should be low and the damping ratio bounded by a minimum and maximum value. However for these vehicle parameters and the simulated rig delays, it was found that the system was actually unstable for all damping values. For the suspension MIL system the stability is determined by the b_s/k_s ratio shown in Table 6.1; the low ratio implies that small time delays are required for stability. The simulated rig system has four sources of delay, each with a time constant of 0.01s, which will combine to give the total system delay. Increasing the suspension damping b_s helps with the stability of the suspension MIL but leads to instability for the vehicle structure MIL. Therefore for this set of vehicle parameters it is possible that instability occurs for all suspension damping values.

In terms of the unsprung mass system, the vehicle parameters selected have high stiffness and low unsprung mass when relating to results from Chapter 5. The high tyre stiffness leads to degradation in rig accurcy and a slower decay rate of the wheel vibration mode. Moreover a low unsprung mass will also lead to poor rig acrruracy characterised by very high wheel hop frequencies which could cause instability in real time closed loop control if the sampling rate is insufficient. Overall, the parameters of typical vehicle quarter cars are very demanding on the control and signal processing performance of real time hybrid testing with a combined suspension MIL and a vehicle structure MIL.

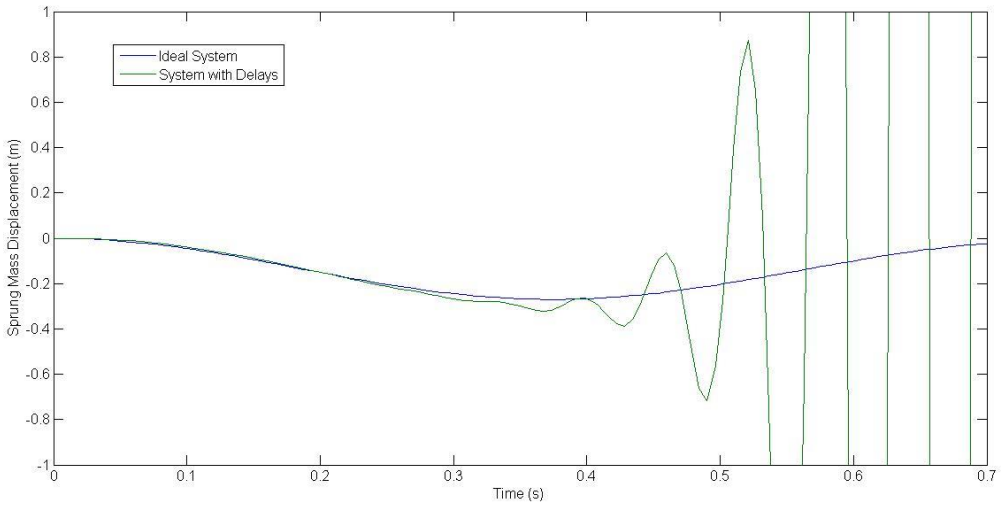

Figure 6.15 – Simulation of Boeing 707 sprung mass position.

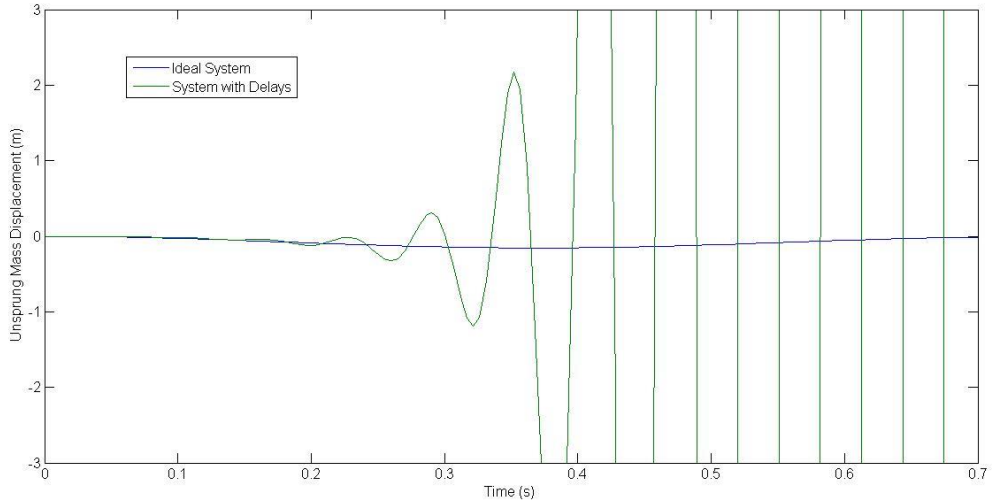

Figure 6.16 - Simulation of Boeing 707 sprung mass Position

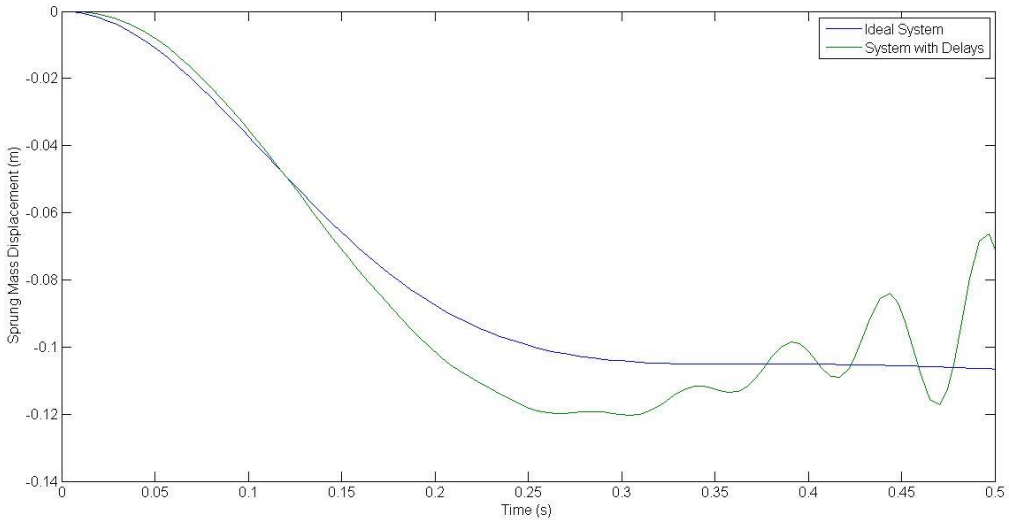

Figure 6.17 – Simulation of truck sprung mass position.

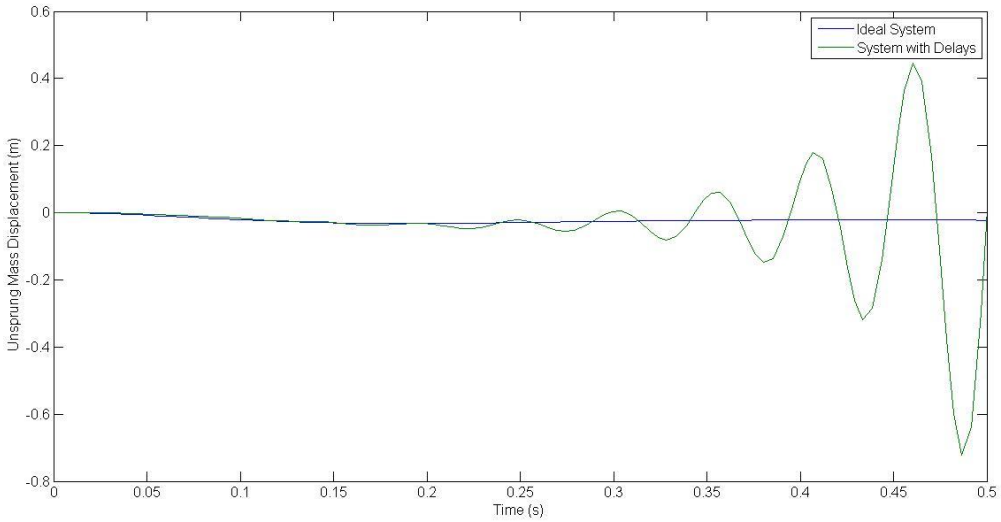

Figure 6.18 – Simulation of truck wheel mass position.

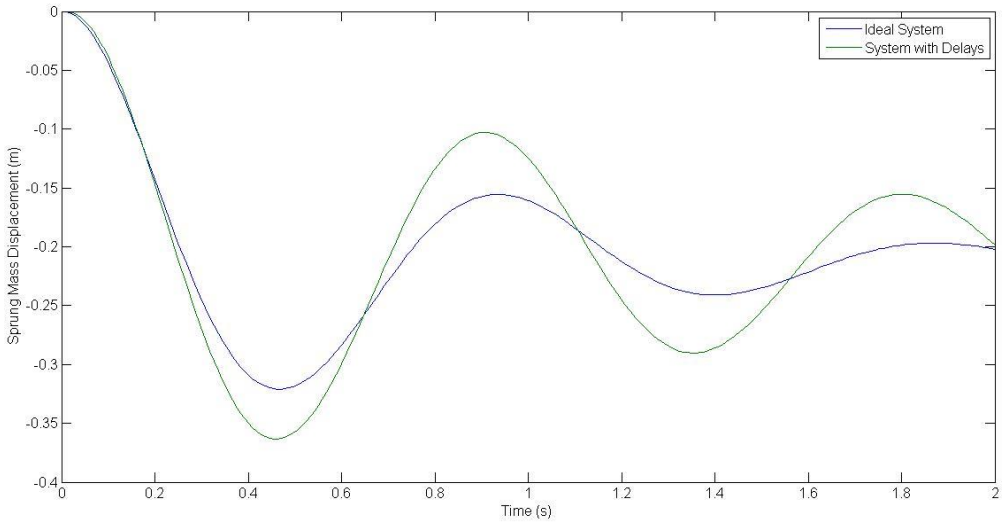

Figure 6.19 – Simulation of car sprung mass position.

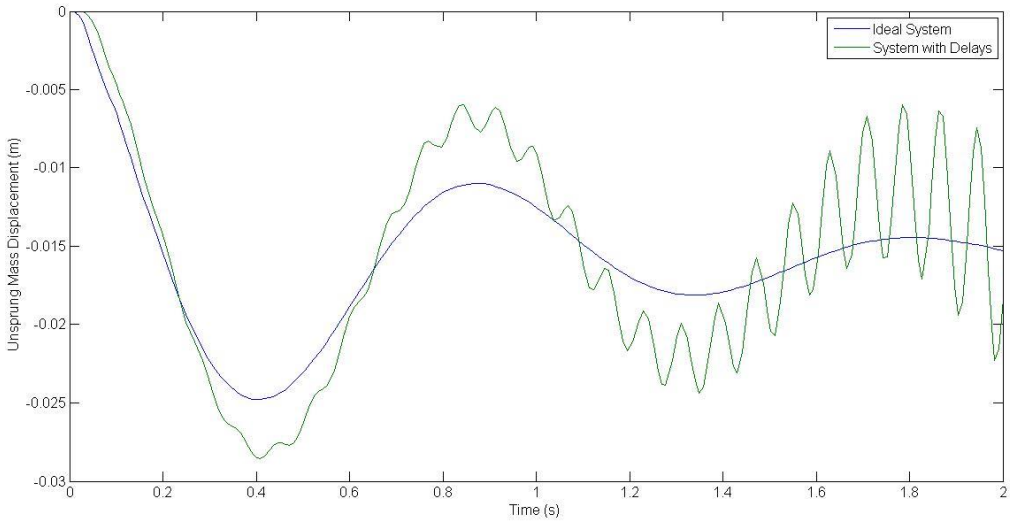

Figure 6.20 – Simulation of car wheel position.

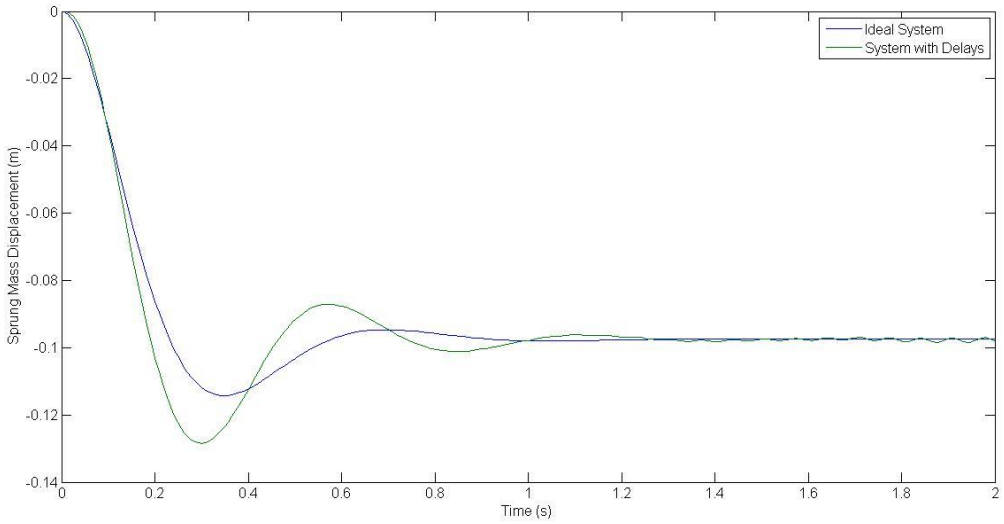

Figure 6.21 - Simulation of motorcycle sprung mass Position

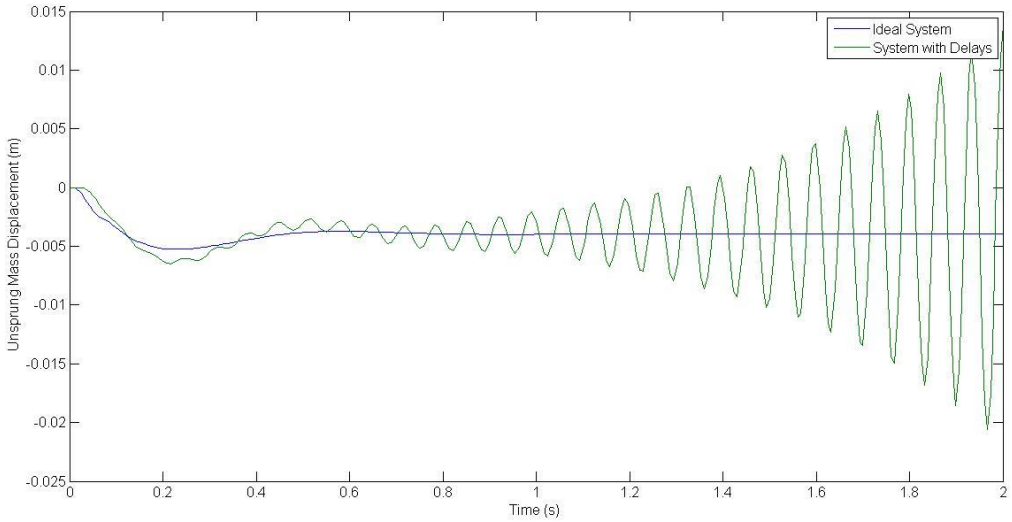

Figure 6.22 – Simulation of motorcycle wheel position.

An attempt was made to conduct experiments on the test rig using Boeing 707 quarter car parameters. After scaling as described in Section 3.5 the Boeing 707 parameters to the rig wheel mass and stiffness, the spring force range was too high to be achieved using the electric actuator. To overcome the problem a real spring was added to the suspension as a HIL component while the suspension MIL used a numerical model of a linear damper. Figure 6.23 shows the result of the test which is unstable. The blue line shows the command force that could be derived from an unfiltered velocity reading and the green line is the real command force after velocity is filtered. The red line shows the real damping force measured by the force sensor. The plot shows that the real damping force is completely out of phase with what otherwise should be the damping force if there were no sensor filters and transfer function delays. Since the damping force is completely out of phase there will be negative damping which results in exponentially increasing vibration amplitudes.

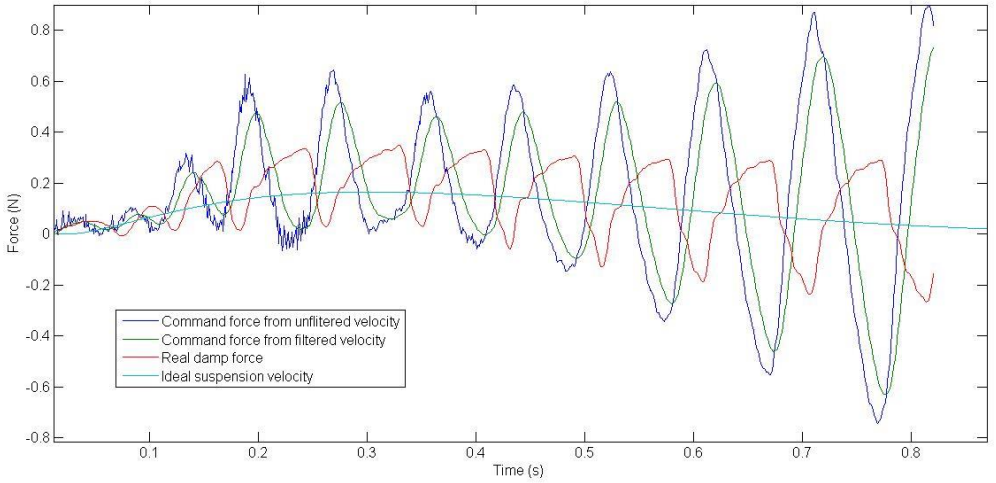

Figure 6.23 – Experimental test of Boeing 707 showing negative damping and instability. The suspension MIL numerical model is of a passive damper whilst another real spring is in operation.

6.3 Real-Time Test – Point Mass

A quarter car system parameters were chosen such that the experiment was stable. The parameters are given in Table 6.2. Although the tyre stiffness measured from the static test indicated a tyre stiffness of approximately 46000 N/m, comparison of experimental to simulation results suggested that best match in terms of steady state equilibrium position is achieved when the simulation tyre stiffness is set to 50000 N/m. This small difference may be associated with the non-linear tyre characteristics where stiffness is frequency dependant. Therefore the ideal emulated system used for verification with rig test results will adopt a tyre stiffness of 50000 N/m. In this section experimental tests are conducted and validated by comparison with the ideal emulated simulation.

Experimental Parameters	
$m_s\ (kg)$	25
$k_s\ (N/m)$	1000
$b_s\ (Ns/m)$	50
$m_u\ (kg)$	34
$k_t\ (N/m)$	50000
$b_t\ (Ns/m)$	0

Table 6.2 –Quarter car parameters for experimental tests and ideal emulated system.

6.3.1 Passive Drop Test - No Ground Disturbance

The first test conducted is for a case with no external road input excitation. The system is set to begin at an initial condition and the system response investigated. The initial conditions are that of a drop test, such that it resembles the landing touchdown of an aircraft. Initially the suspension is fully extended, the body mass is above its equilibrium position and the tyre is in contact with the ground.

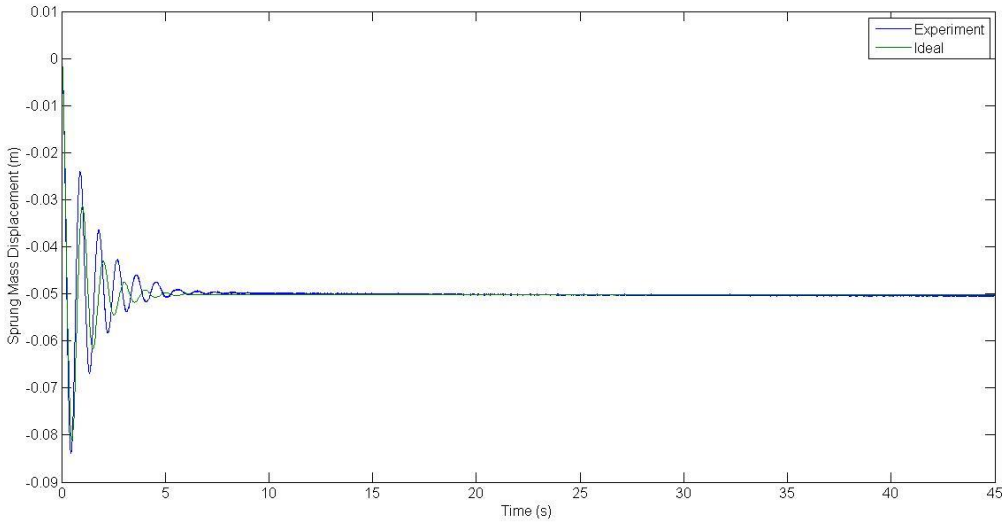

Figure 6.24 - Sprung mass displacement time response.

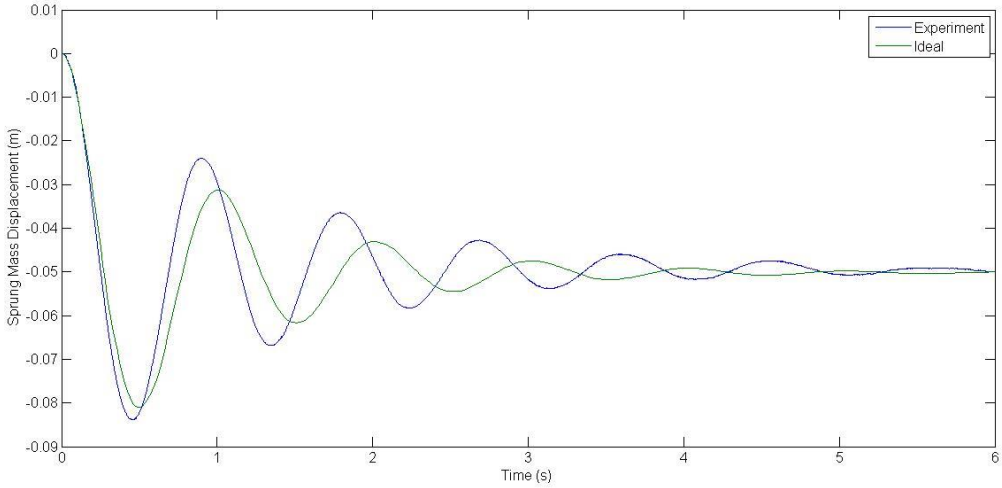

Figure 6.25 – Exploded view of sprung mass position time response.

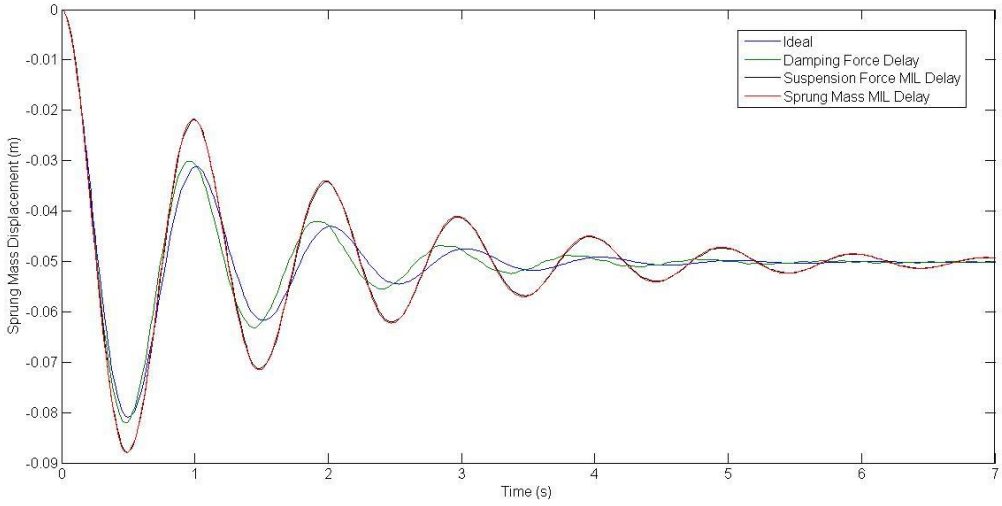

Figure 6.26 – Time response of first order low pass filter with 0.05s time constant applied to the damping force only, or low pass filter with 0.02s time constant applied to suspension force or sprung mass position.

Figure 6.24 and 6.25 shows the time response of the sprung mass position. The initial position of the mass is at zero displacement (this is not the equilibrium position) and zero velocity. At this point the spring is uncompressed and there is a 200N preload. The virtual gravity force acting on the sprung mass pushes the system to settle at an equilibrium position. The time response shows that there is a peak amplitude error as well as a phase shift when comparing the experimental results to the ideal case. Simulation results show that a MIL delay applied to the sprung mass position or to the suspension force produces a very similar time response (Figure 6.26). Here there is very little phase shift but a pronounced amplitude error. However if there is a phase difference between the spring and damping force, such as in the case where velocity is lagging position, this causes the system body hop frequency to shift to a slightly higher frequency. This effect, shown in the simulation result of Figure 6.26, is in agreement with the test rig experimental results, where to obtain a velocity

reading with appropriate noise levels a filter had to be applied after differentiation of the position sensor signal.

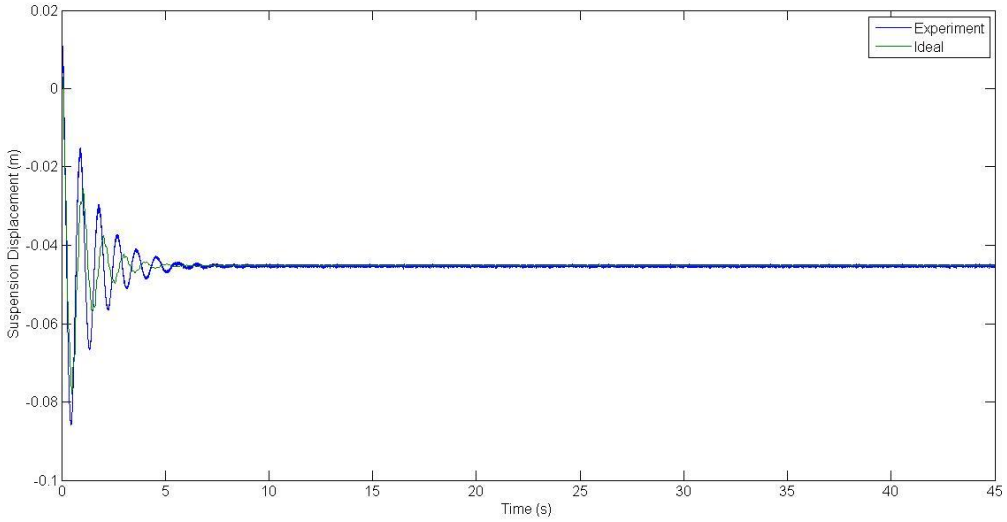

Figure 6.27 – Suspension displacement time response.

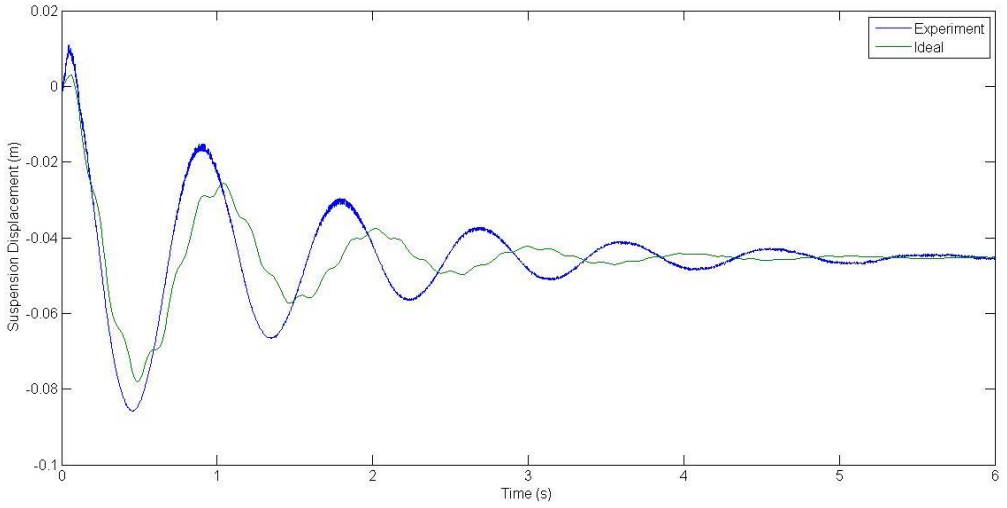

Figure 6.28 – Exploded view suspension displacement time response.

The suspension displacement is shown in Figure 6.27 and 6.28. Since the unsprung mass displacements are very small compared to the sprung mass displacements, the suspension displacement is dominated by the sprung mass response. In the ideal case, the unsprung mass motion contains a combination of the low frequency body hop and the high frequency wheel hop mode, however this high frequency vibration is absent in the experimental test.

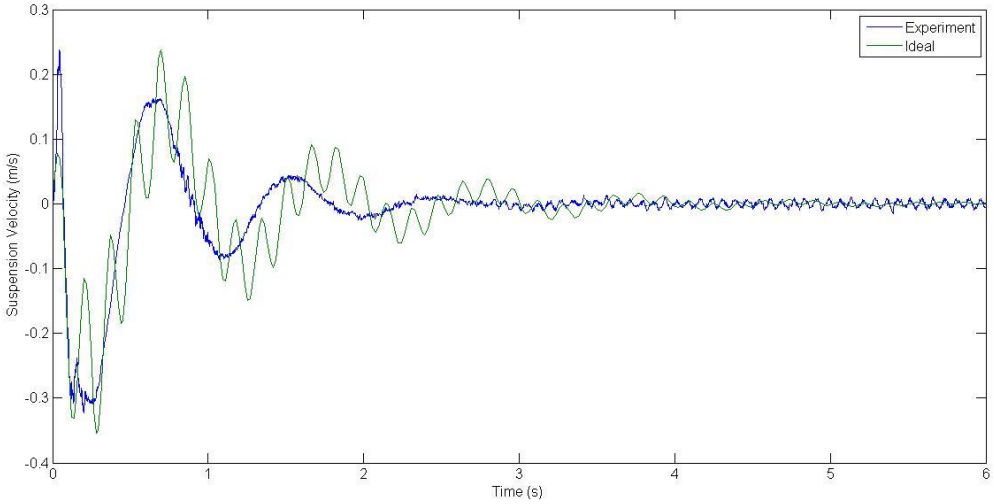

Figure 6.29 – Suspension velocity time response.

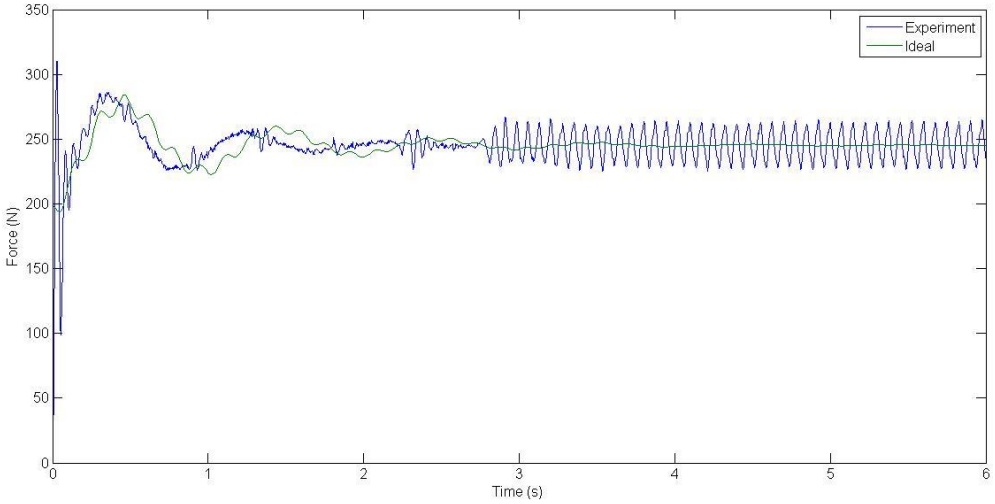

Figure 6.30 – Suspension force time response.

The suspension velocity time response is shown in Figure 6.29 and has a similar frequency content and peak amplitude error as the suspension displacement. From the figure it is seen that through low pass filtering, the noise levels of the velocity signal is reduced to approximately +/-0.005 m/s. From the suspension displacement and velocity signals, the suspension MIL calculates the demand force which is tracked by the electric actuator force controller. The plot of the real force time response is shown in Figure 6.30. It can be seen that again similar peak amplitude error and phase shift is observed which is expected since the force is simply a result of suspension motion. The force readings also show the effects of friction on the tracking error which occurs at suspension velocity reversals, and a limit cycle caused by friction when the system is stationary at the equilibrium point. Additionally the experimental force initial condition does not match the emulated system initial force of 200N. This is due to an error in setting up the experimental tests, but also demonstrates that acceptable results can be achieved even with initial force error.

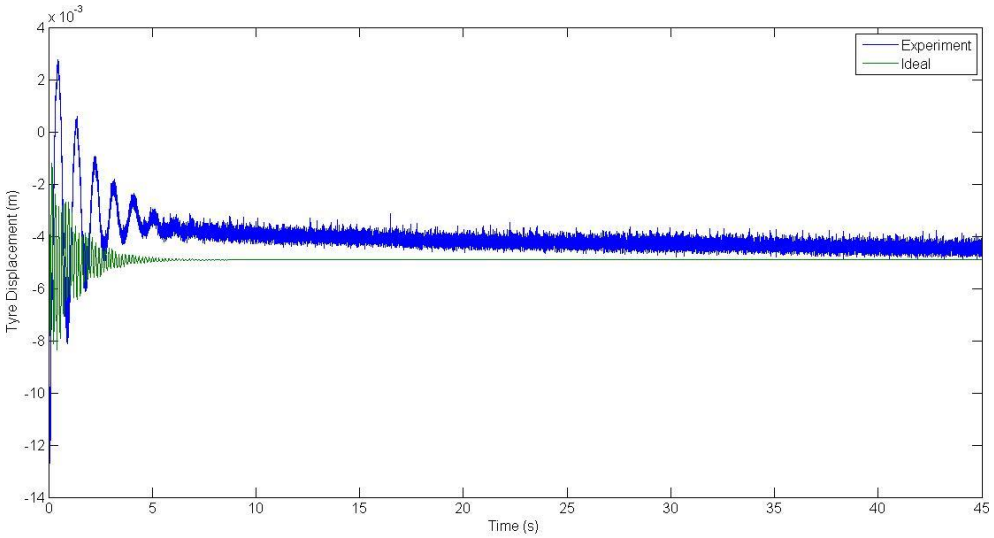

Figure 6.31 – Tyre Displacement time trace.

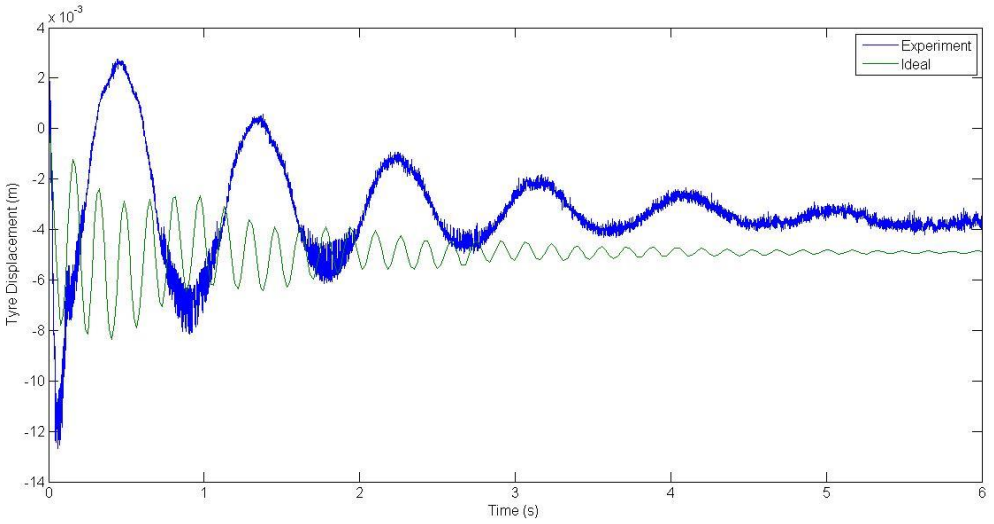

Figure 6.32 – Exploded view tyre displacement time trace.

The tyre displacement time response is shown in Figure 6.31 and 6.32. Since the ground is stationary, here the wheel position is equivalent to tyre displacement. From the plot there is a steady state error between the experimental test and the ideal emulated response of approximately 0.001m. If the emulated system tyre stiffness was increased the steady state unsprung mass position of both cases will be equal but this would also shift the sprung mass steady state position by the same amount. The absence of higher frequency tyre vibrations suggests they had been damped out very quickly. The damping of the tyre is not measured and could be quite high since the tyre has relatively low pressure. Moreover there is substantial friction in the wheel guide rails which include stiction, where viscous damping is equivalent to a damper attached between the wheel and virtual ground, similar to groundhook. By simply increasing the wheel damping in the emulated model, which could be considered as the combination of tyre damping and viscous damping of the rails, a similar response is obtained where the high frequency wheel mode decays very quickly. The tyre

displacement time response comparing a simulation of the rig with zero tyre damping and 1000Ns/m damping is shown in Figure 6.33. The plot shows that with high damping the high frequency wheel hop mode decays very quickly after only one oscillation, similar to the results observed from the experimental tests. With hindsight problems associated with railing friction could have been prevented with a vertical configuration test rig.

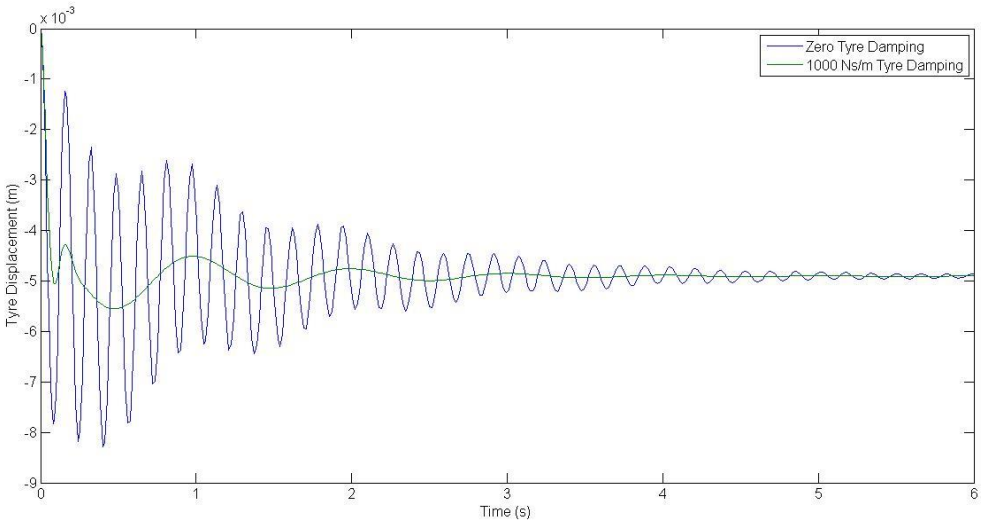

Figure 6.33 – Simulated effect of high wheel mass railing friction in dampening wheel hop mode.

Another curious phenomenon of the tyre vibration is that is seems to be out of phase with the low frequency component of the ideal response as shown in Figure 6.29. This could either be a real physical phenomena where the wheel is not vibrating as it should due to the unmodeled dynamics of the tyre such as friction and damping. An alternative explanation is that it is not a physical issue and a signals issue, for the out of phase wheel vibration or the steady state wheel position error could be due to errors in the LVDT position sensor. Since the wheel position is composed of the combined readings from the sprung mass position LVDT and the suspension displacement LVDT, if the 2 LVDTs are not equally calibrated or contain non-linearites, this could result in erroneous wheel positions. Furthermore since the tyre position is in the magnitude of millimeters, slight calibration issues will show up on the tyre response but not the suspension displacement or sprung mass position whose magnitude are in the order of centimeters. The reality is that there is probably a combination of both physical and sensor issues in obtaining accurate tyre displacement readings. Despite the possible issues in obtaining good tyre readings for the no ground input case, it will be shown in later sections that if the ground is moving, the wheel response is much better since the tyre displacements are very small compared to wheel displacements.

The sprung mass and tyre displacement time response shown in Figure 6.24 and 6.31 indicate a drift in the steady state position. The likely explanation is that during a steady state command force, the real force output is highly oscillatory due to limit cycles caused by friction and the double integration of the filtered force yields the command sprung mass position. The process of double integrating this filtered force signal could produce a drift in the command position, and hence the real output position if the limit cycle average force is not equal to the sprung mass virtual weight. As the suspension displacement is kept constant by the suspension MIL the steady state drift is also seen in the tyre displacement.

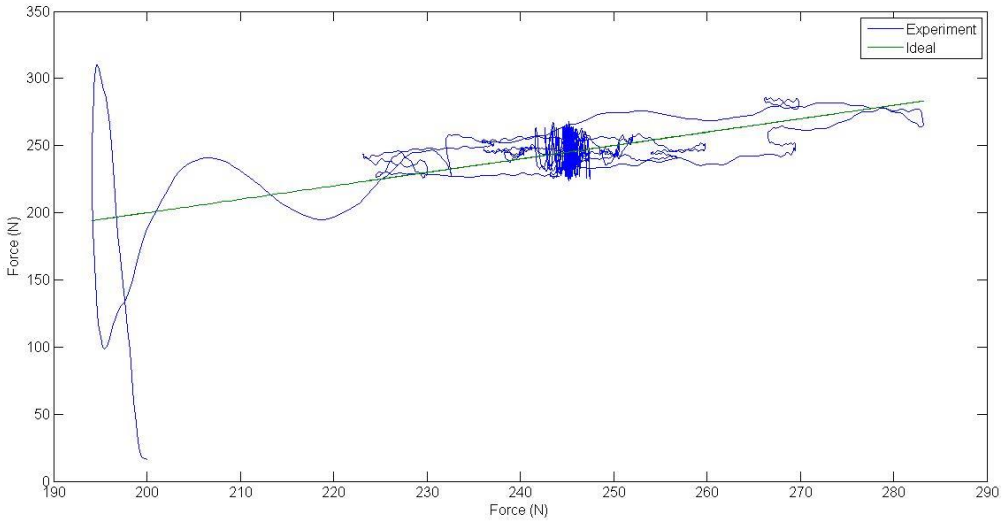

Figure 6.34 – Force error subspace plot.

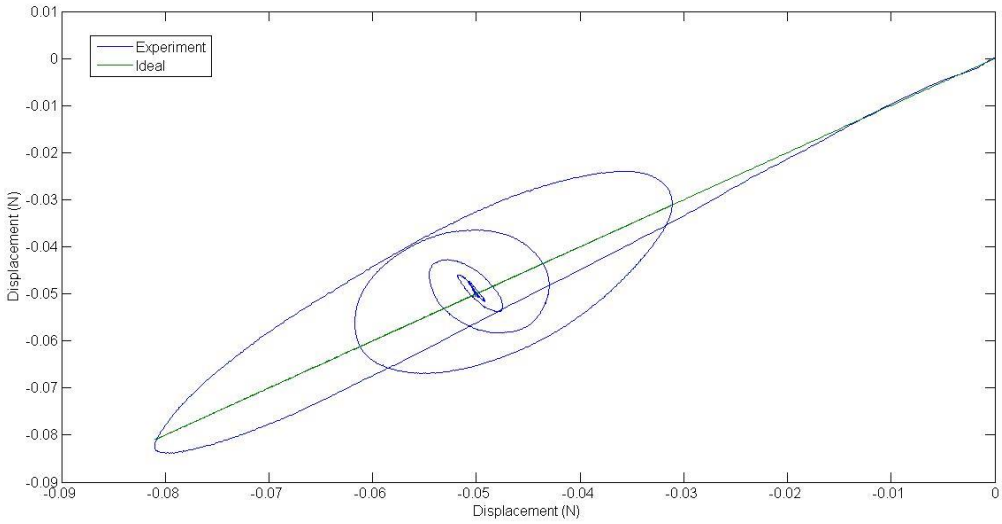

Figure 6.35 – Sprung mass position error subspace plot.

The accuracy of the test rig could be assessed by combining the numerical model error and the transfer function error as demonstrated in Chapter 3. This gives the total error of the test rig and is basically the difference between the ideal response and the actual MIL system output across the test time span. The test accuracy can be categorised by the total force MIL system error and the total sprung mass position MIL system error. Table 6.3 shows the RMS error of the suspension MIL and the vehicle structure MIL. Here the errors from the suspension MIL are much higher than the vehicle structure MIL. This is because the suspension control is more difficult because it is in dynamic interaction with the wheel and tyre which causes limit cycles due to friction. Figure 6.34 and 6.35 shows the comparison between the ideal output and experimental output at each point in time. In these plots a perfectly diagonal line denotes the perfect response while bigger loops denote bigger time delays and amplitude error.

	Suspension MIL	Vehicle structure MIL
Total RMS Error ($e_1 + e_2$)	12.4	0.0602
Percentage Error (%)	321	60

Table 6.3 – Overall test accuracy, the error denotes comparison of emulated to real output.

6.3.2 Passive Drop Test with 1.6Hz Pseudo Random Road

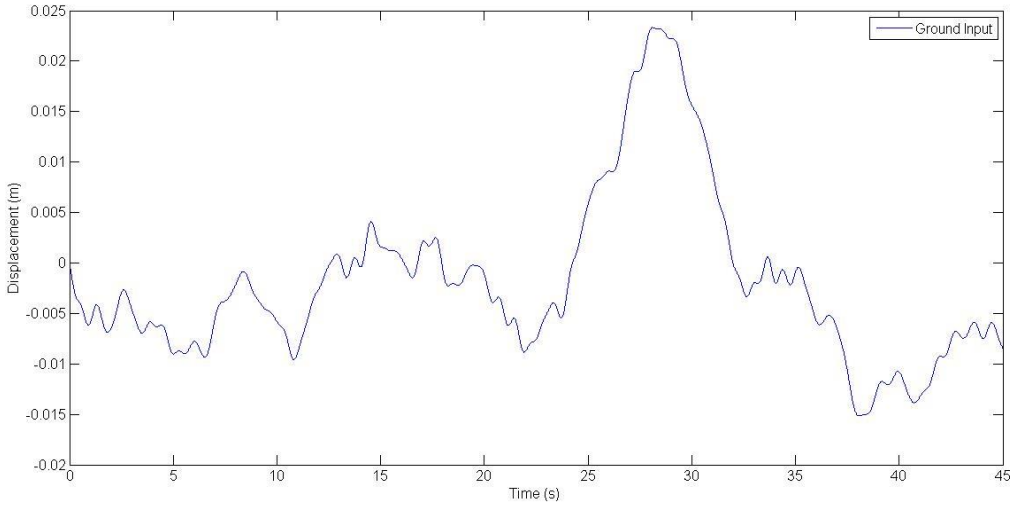

Figure 6.36 – Pseudo random ground input profile 0.02-1.6Hz.

The drop test from Section 6.3.1 is repeated but this time with a ground disturbance. The ground disturbance contains a combination of sine waves with randomised phase and frequencies ranging from 0.02-1.6Hz. This input is representative of a vehicle travelling at 25 km/h on a motorway road described by the spectral density function of Equation 6.3. The numerical parameters were obtained from [25]. A time response of the ground input is shown in Figure 6.36.

$$S_r(\gamma) = \frac{k}{\gamma^n}\ [m^2(cycle\ m^{-1})^{-1}] \tag{6.3}$$

Here,

$$\gamma = wave\ number\ (cycle\ per\ metre)$$

$$n = dimensionless\ exponent = 2.5$$

$$k = roughness\ coefficient = 7 \times 10^{-8}$$

In this test the quarter car is initially set as in Section 6.3.1. Hence the experimental results will contain two sections of responses. Initially the system is dominated by the response due to the initial conditions of a drop test and here the results are similar to that seen in Section 6.3.1. After reaching the equilibrium position from the initial steady state conditions, the response becomes dominated by the ground disturbance input which is representative of the vehicle taxiing.

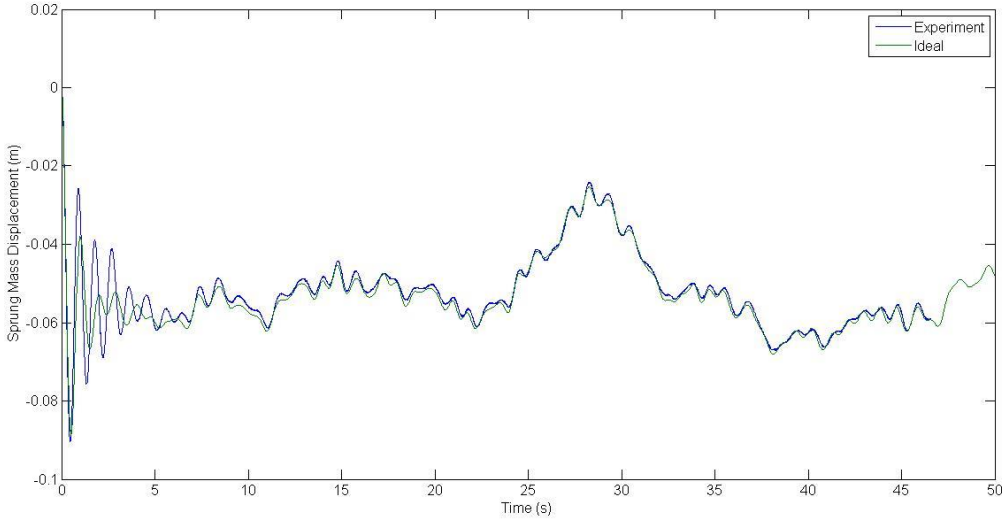

Figure 6.37 – Sprung mass displacement time trace.

The graph of the sprung mass position is shown in Figure 6.37. From 0-5 seconds the response is similar to that seen in Section 6.3.1 where there is a pronounced peak amplitude and phase shift error compared to the ideal emulated system. The response due to the ground input seen onwards has a much better accuracy. This is because after 5 seconds the system is responding to continuous state changes.

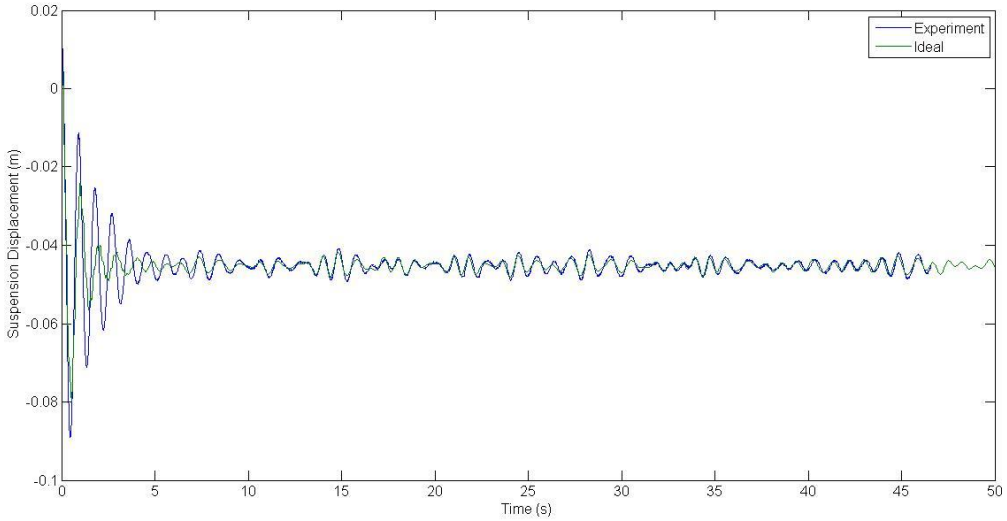

Figure 6.38 – Suspension displacement time trace.

The suspension displacement time response is shown in Figure 6.38. Like the sprung mass response the suspension displacement response performance is a lot better for ground displacement than the response due to a drop test. Also as in Section 6.3.1, the suspension displacement does not contain the higher frequency vibration due to the over damped wheel hop mode. The velocity is obtained by filtering the suspension displacement signal and is shown in Figure 6.39 to have appropriate delay and noise levels. The suspension displacement and velocity signal is the input for the spring and

damper forces and hence the output force shown in Figure 6.40 show similar errors. Again it is clear from the plot that friction forces are a source of force tracking error.

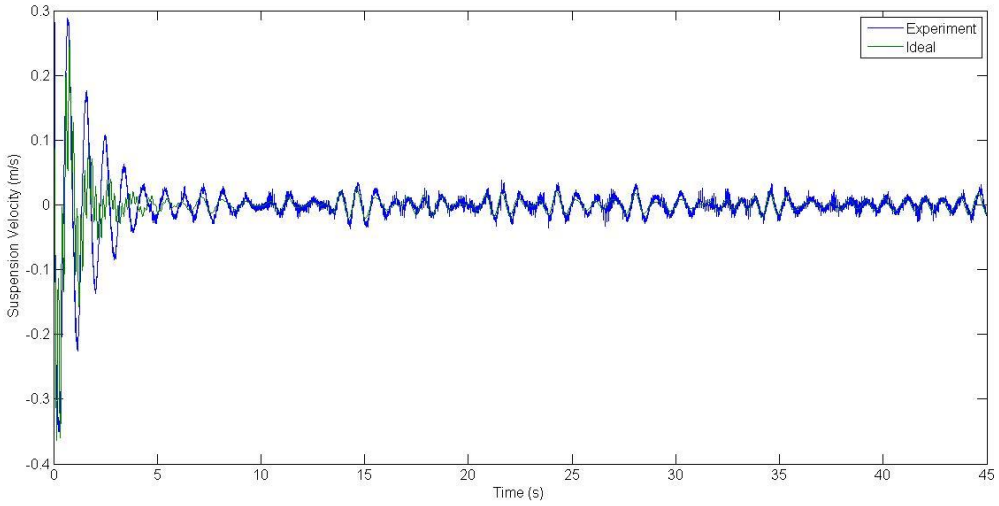

Figure 6.39 – Suspension velocity time response.

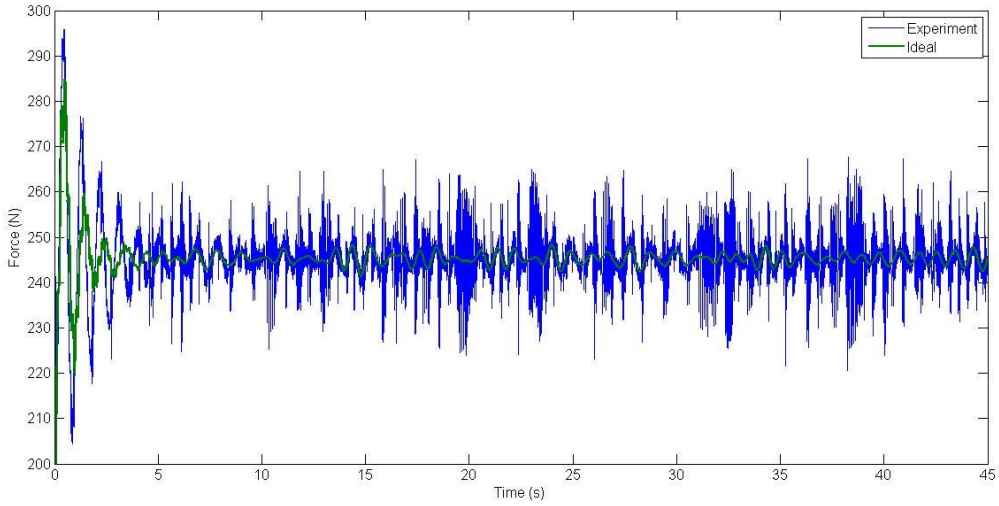

Figure 6.40 – Output force time response.

As in Section 6.3.1, here the tyre displacement time response here does not resemble the expected emulated system. Despite the poor tyre displacement performance, when viewed in terms of the wheel position the results are much better because tyre vibrations are very small (Figure 6.41).

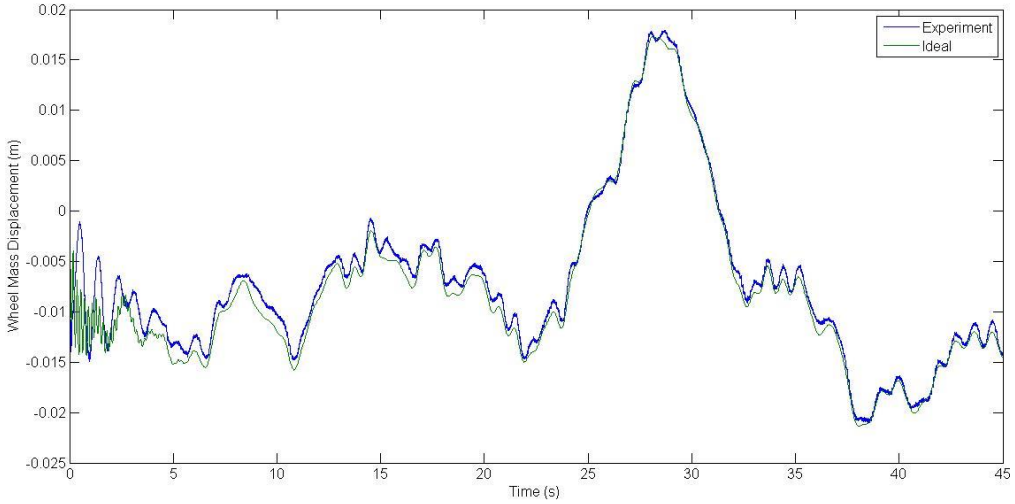

Figure 6.41 – Wheel mass displacement time response.

The accuracy of the test system is shown in terms of RMS values in Table 6.4 and through subspace plots in Figure 6.42 and 6.43. As seen in the Section 6.3.1, the force errors are again much higher than the position tracking errors. The mass position plot in Figure 6.42 shows that after the transient response from the initial drop test has decayed, the system performance becomes much better, illustrated by the smaller elliptical loops of the experimental response. This same effect is not possible to see in the force plot as the errors are dominated by friction.

	Suspension MIL	Vehicle structure MIL
Total RMS Error ($e_1 + e_2$)	7.60	0.0606
Percentage Error (%)	187	59

Table 6.4 – Overall test accuracy, the error denotes comparison of emulated to real output.

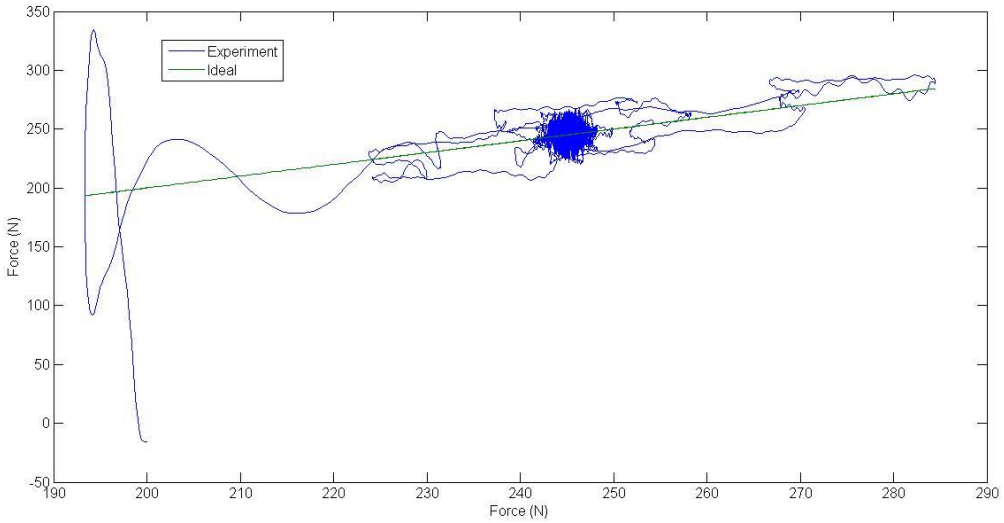

Figure 6.42 – Force error subspace plot.

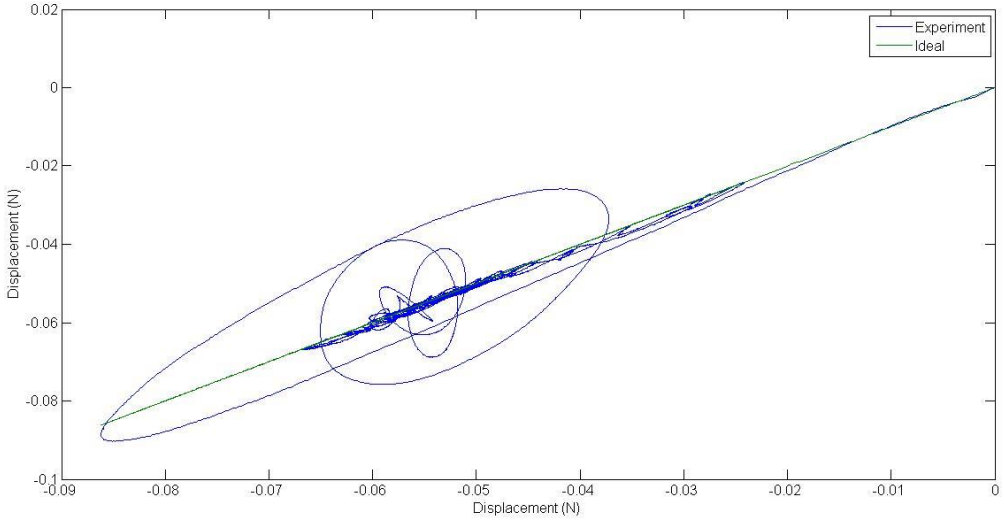

Figure 6.43 – Sprung mass position error subspace plot.

6.3.3 Passive Drop Test with 10Hz Pseudo Random Road

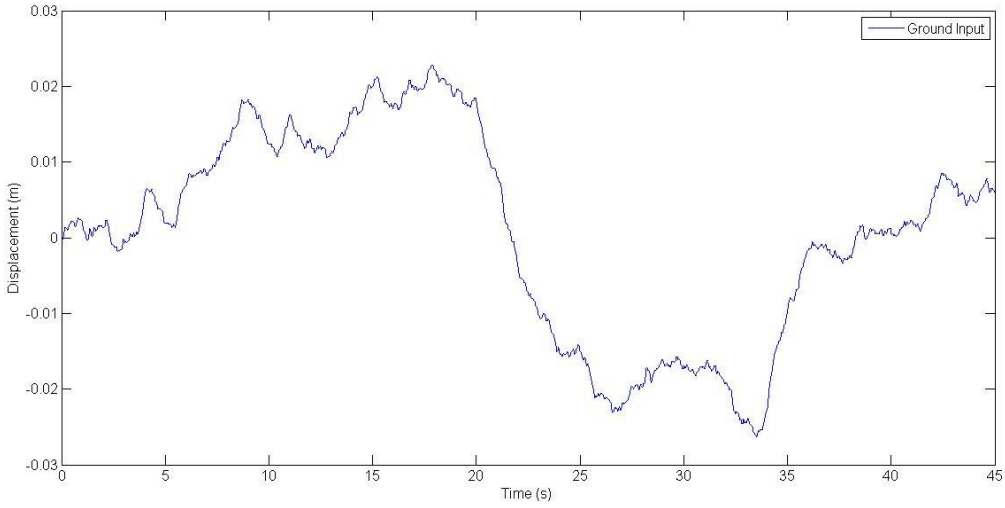

Figure 6.44 – Pseudo random ground input profile 0.01-10Hz.

In this test the road profile is made up of frequencies ranging from 0.01-10Hz and is representative of a vehicle travelling at 15 km/h on a motorway road with the same parameters as in Section 6.3.2. The road profile is shown in Figure 6.44.

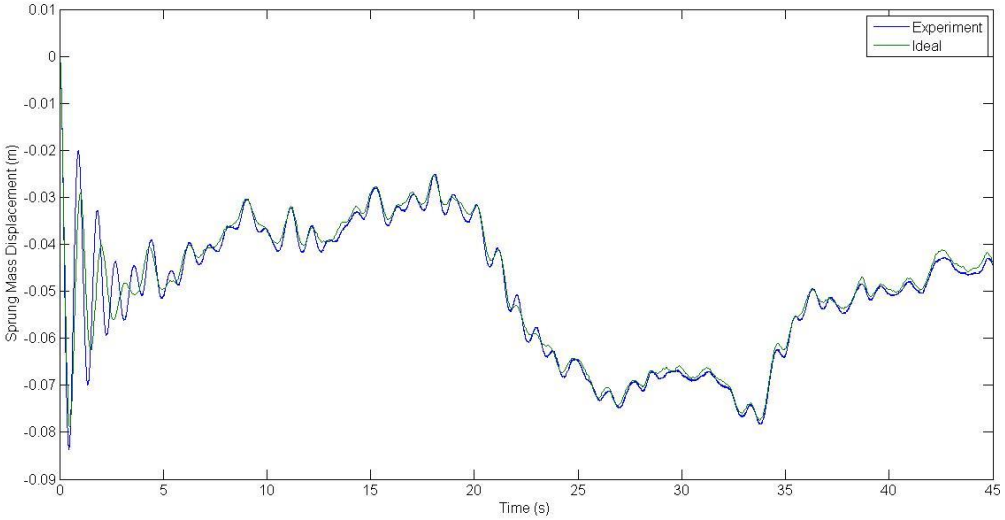

Figure 6.45 – Sprung mass displacement time response.

The time responses are shown in Figure 6.45-6.47. The consequence of higher ground input frequencies is that the sprung and unsprung masses will also be excited at the higher forced frequencies. The sprung mass position time response shown in Figure 6.45 has good accuracy as the ideal sprung mass response is dominated by the body mode which occurs at approximately 1.2Hz.

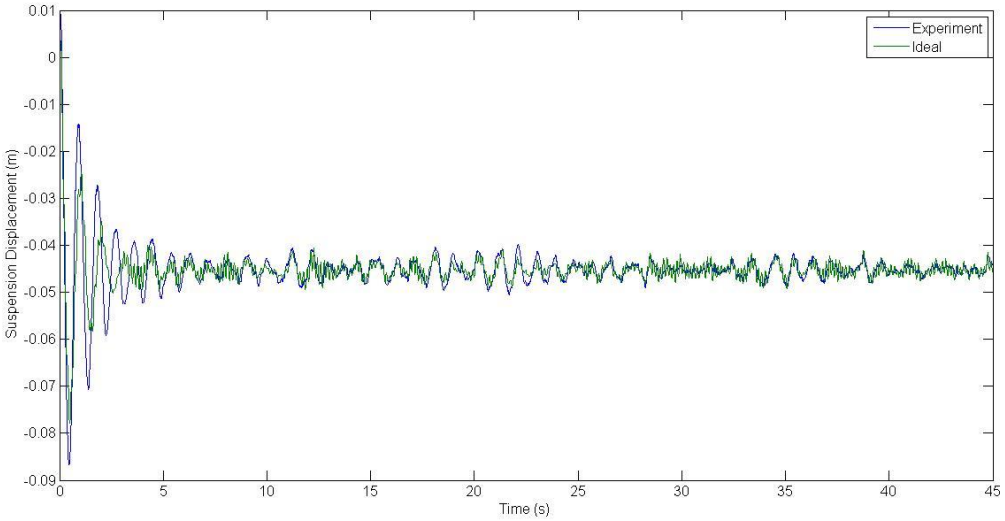

Figure 6.46 – Suspension displacement time response.

The time response of suspension displacement is shown in Figure 6.46. As in previous experiments the tyre vibration has low accuracy compared to the ideal response. Wheel vibration in Figure 6.47 shows that the wheel hop motion is highly damped due to rail friction and contains no higher forced frequencies from the ground input. Therefore the suspension displacement is lacking a high frequency wheel hop mode. Ignoring the higher frequency contribution from the wheel vibration, the suspension displacement low frequency component has a good resemblance to the ideal case.

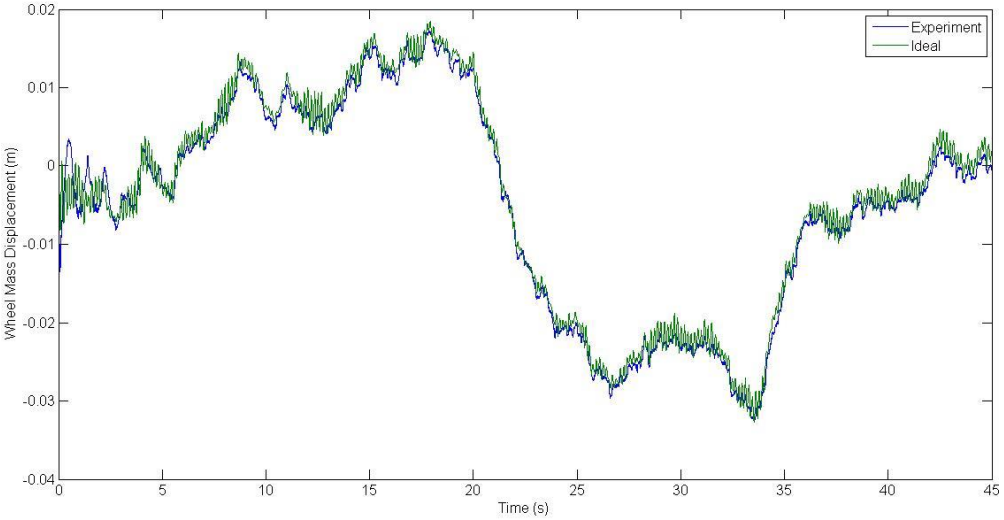

Figure 6.47 – Wheel displacement time response.

A frequency response plot for sprung mass position and suspension displacement of the experimental results are shown in Figure 6.48 and 6.49 respectively. For the sprung mass frequency response the ideal case and the experimental match up closely. The differences occur around the body hop resonance peak, the experimental results have a larger resonance peak which occurs at a slightly higher frequency. The shift of the resonant frequency was demonstrated in Figure 6.26 as an effect of varying delays between spring and damper forces. The frequency response of the suspension displacement shows a pronounced wheel hop resonance peak at around 6-7 Hz for the ideal emulated simulation. This wheel hop resonance could not be captured by the experimental tests due to wheel mass damping caused by the raid guides friction.

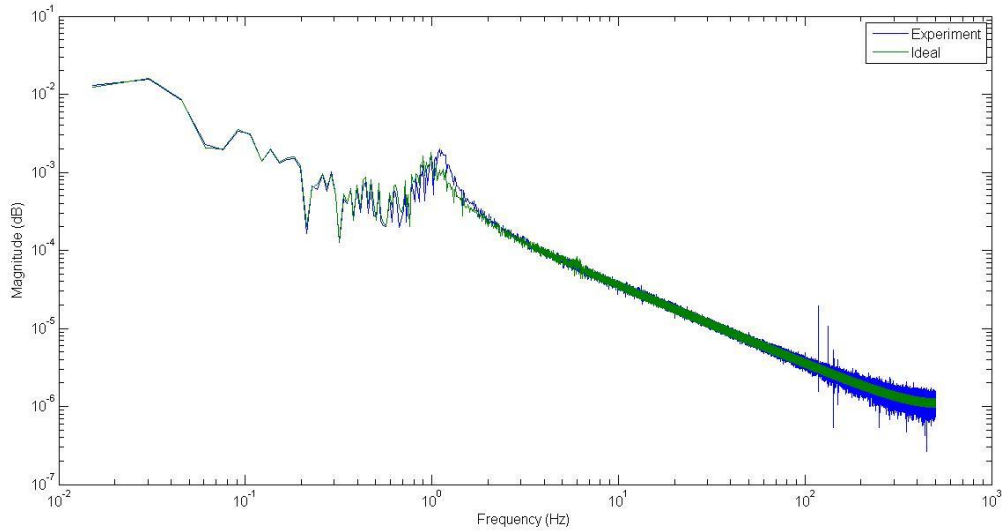

Figure 6.48 – Frequency response of sprung mass position for 0.01-10 Hz ground input.

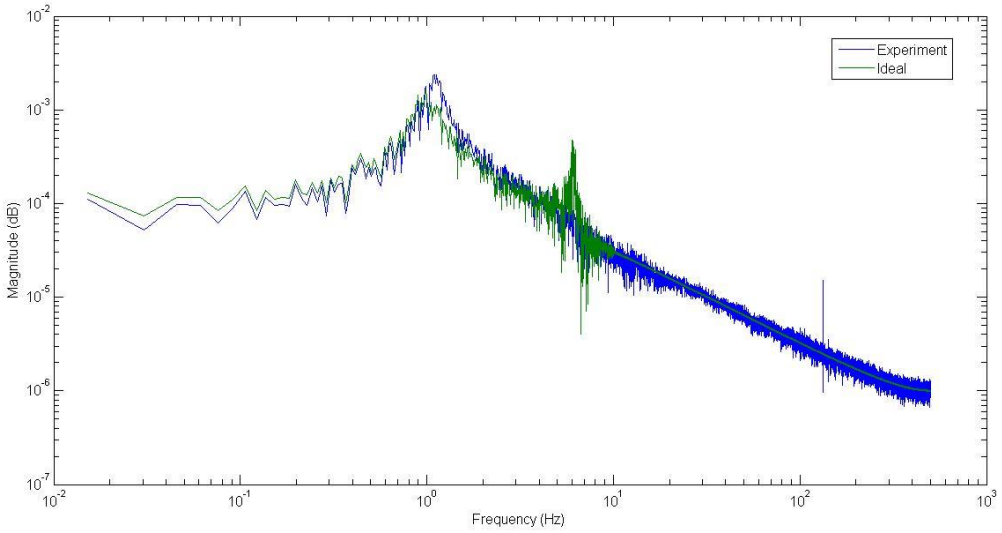

Figure 6.49 – Frequency response of suspension displacement for 0.01-10 Hz ground input.

The errors of the test rig results are shown in Table 6.5 and in Figures 6.50 and 6.51. The RMS errors are very similar to the values seen in Section 6.3.1 and 6.3.2. The errors shown in Figures 6.50 again indicate a reduction of errors after the transient response from the initial conditions has decayed.

	Suspension MIL	Vehicle structure MIL
Total RMS Error ($e_1 + e_2$)	7.86	0.0609
Percentage Error (%)	173	61

Table 6.5 – Overall test accuracy, the error denotes comparison of emulated to real output.

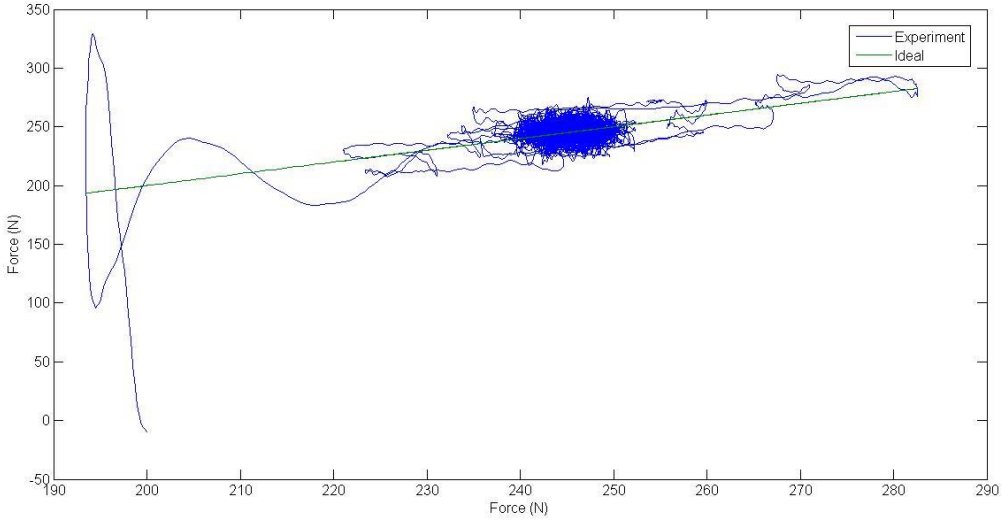

Figure 6.50 – Force error subspace plot.

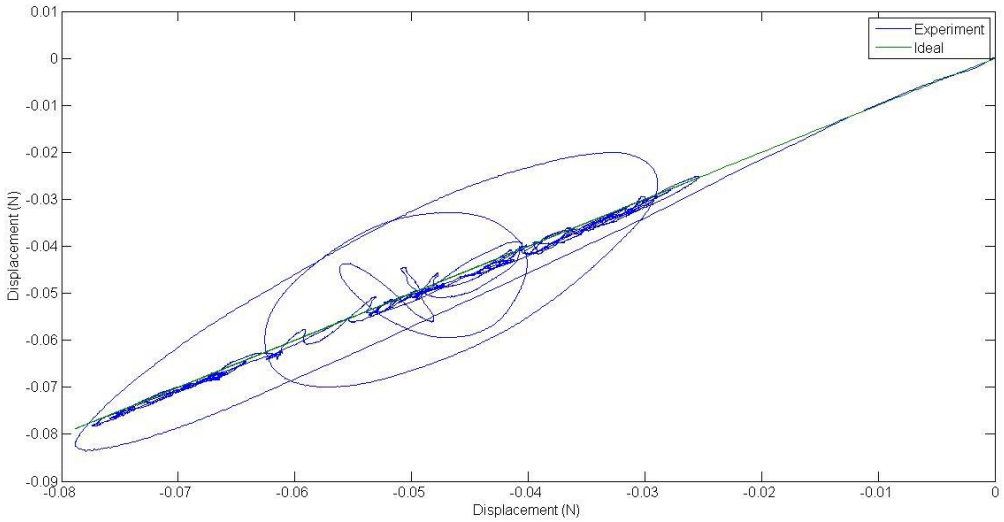

Figure 6.51 – Sprung mass position error subspace plot.

6.4 Conclusion

The experimental results presented in this chapter have confirmed the analysis of numerical-experimental test rigs conducted in Chapter 5. The simulation and experimental result in Section 6.2 shows that given the delays of the MIL based test rig, representative experimental tests of a single wheel station motorcycle, car, truck or aircraft cannot be conducted. This is because the test rig has too much time delay from various sources such as the electric actuator control system, hydraulic actuator control system, suspension displacement sensor transfer function and filters. All these sources of delay are combined in a control loop and are the limiting factor of system performance. However for a given delay, the test rig performance will also depend on the quarter car parameters as identified in Chapter 5. Unfortunately real vehicle suspensions have natural frequencies which are too high, suspension damping to stiffness ratios that are too low, low sprung mass and high stiffness which are all undesirable in terms of rig performance. The only method of successfully undertaking the real-time testing of real vehicle suspensions with this test rig would be to reduce the delays of the system. This may be achieved by using actuator controllers which compensate for time delay and by using sensors that have less noise properties so that the time delay from low pass filtering is kept to a minimum.

In Section 6.3, experimental results were conducted for a quarter car suspension system whose parameters yield a stable system given the test rig time delays. Although the quarter parameters used are unrealistic the results still help gain insight into the feasibility and performance of such test rigs and suspension systems. However the performance in terms of tyre displacement was poor for all experimental tests and it is possible that it is down to a sensor calibration issue. For all the tests, results were poorest when responding to a step input represented by a drop test while response to continuous inputs such as the ground disturbance is a lot better. This is because when responding to a step input the experimental result diverges from the ideal result with time as they decay at different rates while with continuous input test rig is constantly in forced readjustment.

The next chapter will present experimental results for semi-active and active suspensions. The vehicle structure MIL system is also altered from a point mass to a flexible structure model. The experimental results are compared and discussed.

7. Active and Flexible Structure Testing

In this Chapter experimental tests are conducted for semi-active and active suspensions with comparisons to the passive case. After a review of the results the test is extended to include a flexible structure. To the author's knowledge there is no existing literature with suspension test rigs with MIL sprung mass systems which contains significant flexible vibration modes, such as that of an aircraft, and therefore this is one of the novel contributions of this Thesis.

7.1 Active and Semi-Active Point Mass

7.1.1 Semi-Active Skyhook

A semi-active skyhook suspension was experimentally tested with the 0.2-1.6Hz ground input as in Section 6.3.2. The semi-active damper model used in the suspension MIL is a continuously variable damper with instantaneous force capability. The parameters for the semi-active quarter car are given in Table 7.1. Validation of this test result is given in Appendix B1.

Experimental Parameters	
$m_s\ (kg)$	25
$k_s\ (N/m)$	1000
$b_s\ (Ns/m)$	50
$b_{sky}\ (Ns/m)$	200
$b_{variable-max}\ (Ns/m)$	500
$b_{variable-min}\ (Ns/m)$	10
$m_u\ (kg)$	34
$k_t\ (N/m)$	50000
$b_t\ (Ns/m)$	0

Table 7.1 –Quarter car parameters for experimental tests.

Before discussing the test results in detail, note that Section 7.1.3 presents a comparative study for results of passive, semi-active and fully active skyhook. So that figures are not redundantly replicated again in this section, readers are referred to Section 7.1.3 for semi-active skyhook test result figures.

The test results shown in Figure 7.7, in Section 7.1.3, demonstrate that the semi-active suspension is effective at reducing sprung mass vibrations. The RMS sprung mass acceleration values in Table 7.3 show that there is 61.4% reduction comparing semi-active to passive suspension. Not only is the sprung mass vibration reduced, the usage of suspension displacement is also reduced, meaning that the semi-active suspension can be designed with a smaller available suspension stroke. Figure 7.8 shows the time response of the suspension displacement. The semi-active algorithm also reduces tyre vibrations during the drop test response, shown in Figure 7.9.

The superior sprung mass vibration isolation is expected from a skyhook algorithm where the objective of the semi-active damper is to oppose the sprung mass velocity. A plot showing the command force for the semi-active and passive damper is shown in Figure 7.1. From the plot it is clear that the semi-active force is much higher than the passive damper force, and that reduction in

sprung mass vibration is a consequence of the semi-active force. There are two reasons for the low passive damping force. One reason is because the passive damping coefficient is lower than the semi-active damping coefficient. Another reason is because the semi-active damping forces act to stabilize both the sprung mass and suspension displacement, thus requiring less action from the passive damper.

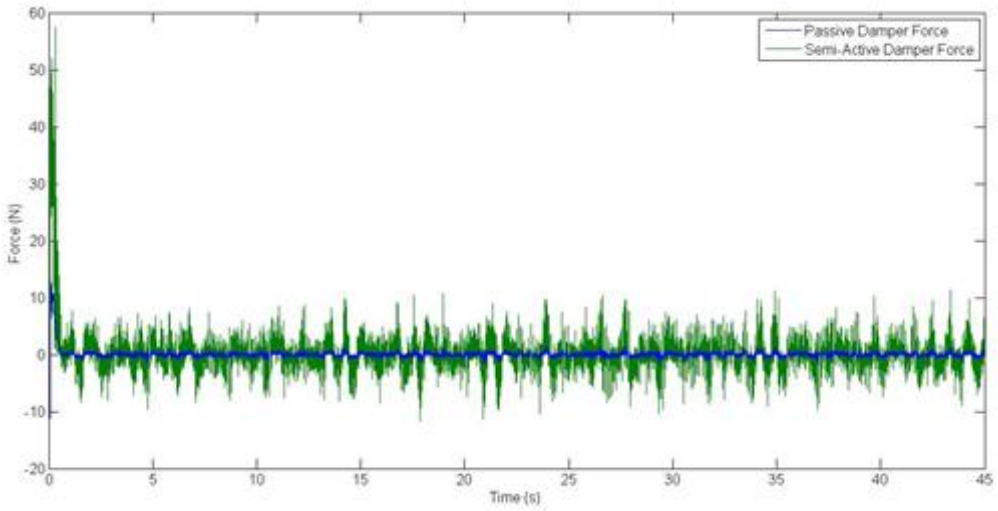

Figure 7.1 – Time response of command passive damper and semi-active damper force.

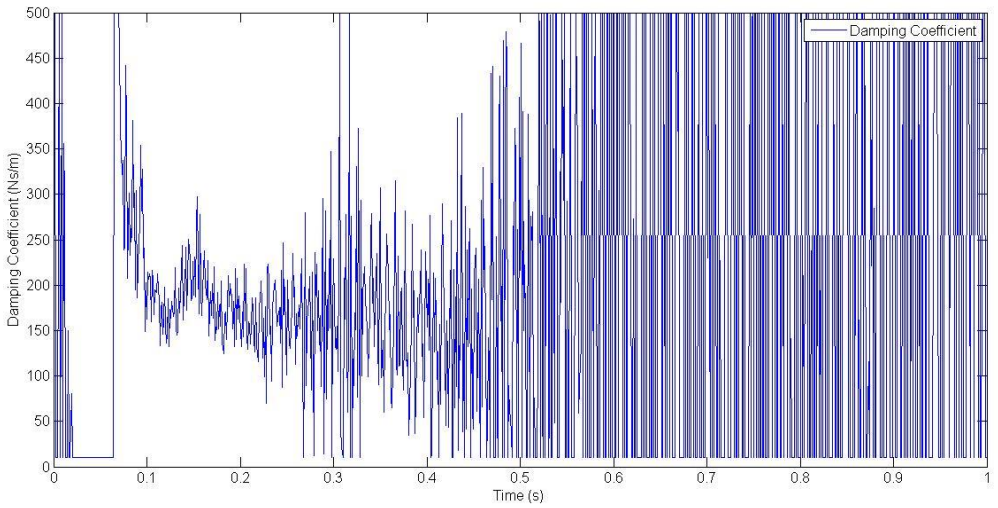

Figure 7.2 – Time response of semi-active damper damping coefficient.

The semi-active skyhook force is switched between skyhook damping force and minimum damping coefficient when the correct sign of the skyhook damping force cannot be delivered. This result in damping forces which are highly non-linear characterized by jumps in the demand semi-active force as seen in Figure 7.1. High frequency limit cycle switching between on/off semi-active damper states is undesirable since it could lead to physical damage of the semi-active damper. Observation of the damping coefficient shown in Figure 7.2 reveals that high frequency switching is present in the test

rig. This is due to the limit cycle in system states and could be compensated for using a specially designed control algorithm but is not studied here.

7.1.2 Fully Active

An active skyhook suspension was experimentally tested with the 0.2-1.6Hz ground input as in Section 6.3.2. The parameters for the active skyhook are the same as for the semi-skyhook given in Table 7.1. The active actuator model is assumed to have instantaneous force capability. Validation of this test result is given in Appendix B2.

The test results in Figure 7.7-7.9 show that the active suspension has nearly identical time responses to the semi-active suspension. The RMS sprung mass acceleration values in Table 7.3 indicate a 63.8% reduction comparing semi-active to passive suspension. Like the semi-active suspension, the active suspension shows a reduction of suspension and tyre displacements when compared to the passive case.

Figure 7.3 shows the command active actuator force compared to the passive damping force. Like the semi-active damper, the active skyhook force is a lot higher than the passive damping forces. This is because of the high skyhook damping coefficient, and the skyhook algorithm performing most of the stabilising action.

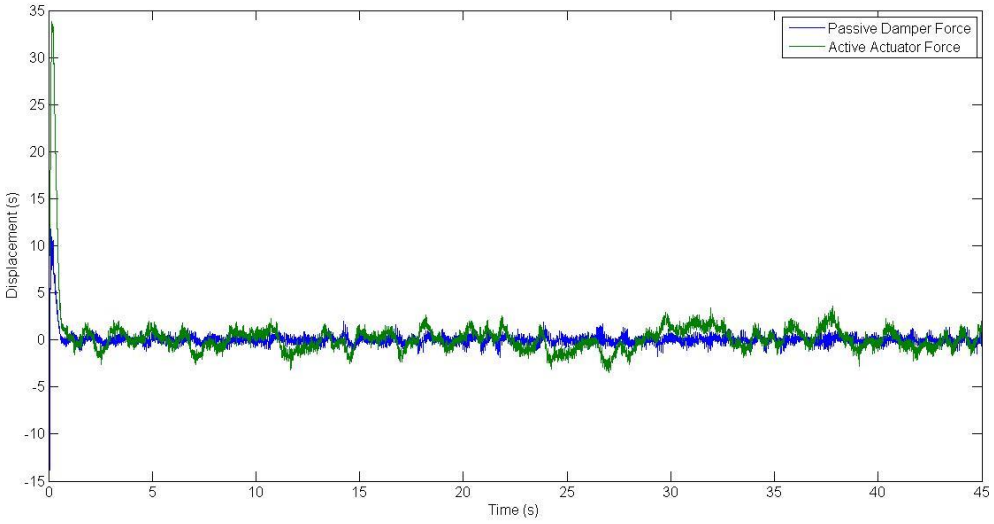

Figure 7.3 – Time response of command active skyhook damping force.

Tests were also conducted comparing different skyhook damping coefficients of 100Ns/m, 200Ns/m and 500Ns/m. The time responses comparing sprung mass position, suspension displacement and tyre displacement are shown in Figure 7.4 – 7.6 respectively. The time responses and Table 7.2 shows that higher skyhook damping leads to greater reduction of sprung mass vibration. However this is traded off in terms of greater suspension and tyre vibration. Although higher skyhook damping reduces suspension vibration during touchdown, it is increaded during taxiing. The tradeoff between sprung mass vibration isolation, suspension usage and tyre displacement is a characteristic of all suspensions due out of phase vibrations for the sprung and unsprung mass outside the body hop natural frequency.

Skyhook Damping Coefficient	RMS Sprung Mass Acceleration
100 Ns/m	0.1039
200 Ns/m	0.0819
500 Ns/m	0.0588

Table 7.2 - Comparison of sprung mass vibration isolation for different skyhook damping coefficients.

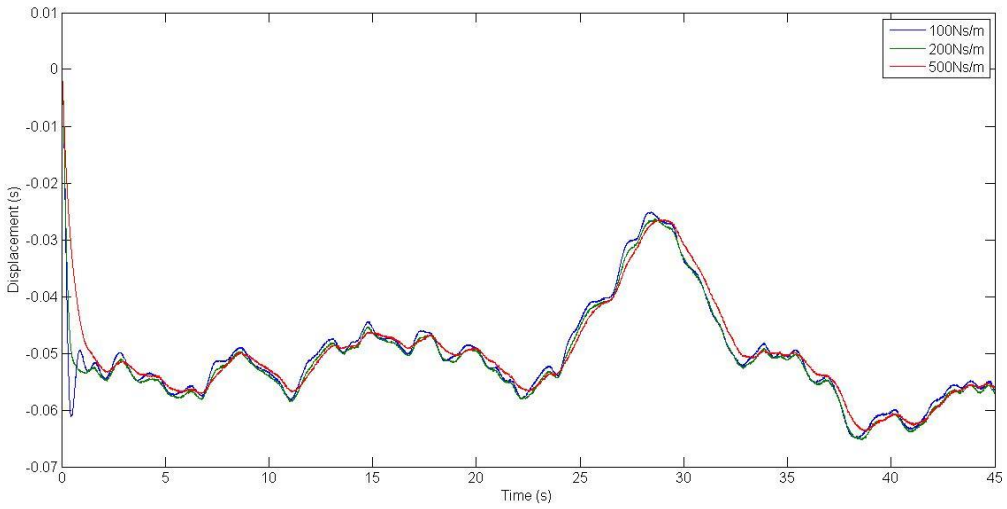

Figure 7.4 – Sprung mass displacement time response comparing different skyhook damping.

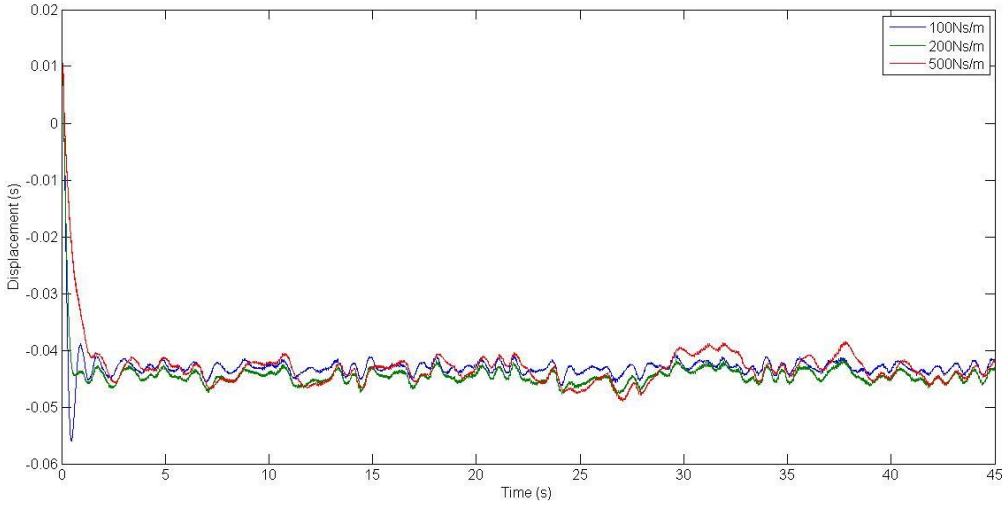

Figure 7.5 - Suspension displacement time response comparing different skyhook damping.

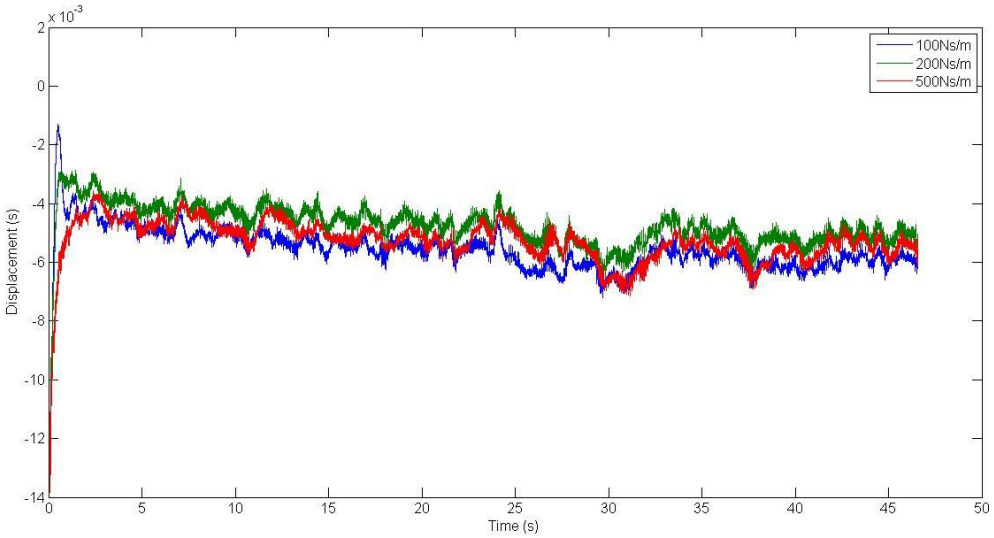

Figure 7.5 - Tyre displacement time response comparing different skyhook damping.

7.1.3 Comparison of Passive, Semi-Active and Active

The experimental results for the passive, semi-active and active suspensions are compared here. Figure 7.7 shows the sprung mass position of the three cases. It is clear that the skyhook algorithm is very effective at sprung mass vibration isolation both for touchdown and taxiing as seen by the lower amplitude vibrations. The RMS sprung mass acceleration in Table 7.3 confirms the reduction of sprung mass vibration. The responses of the active and semi-active cases are nearly identical which is in agreement with findings in literature. The same trend can be seen for suspension displacement shown in Figure 7.8 where the semi-active and active schemes are nearly identical and the suspension deflections much smaller than the passive case. The tyre displacement time response in Figure 7.9 shows that the tyre vibration for the active and semi-active have similar vibration amplitudes and a clear reduction compared to the passive case.

Suspension Type	RMS Sprung Mass Acceleartion
Passive	0.2264
Semi-Active	0.0874
Fully Active	0.0819

Table 7.3 – Comparison of sprung mass vibration isolation for passive, semi-active and active.

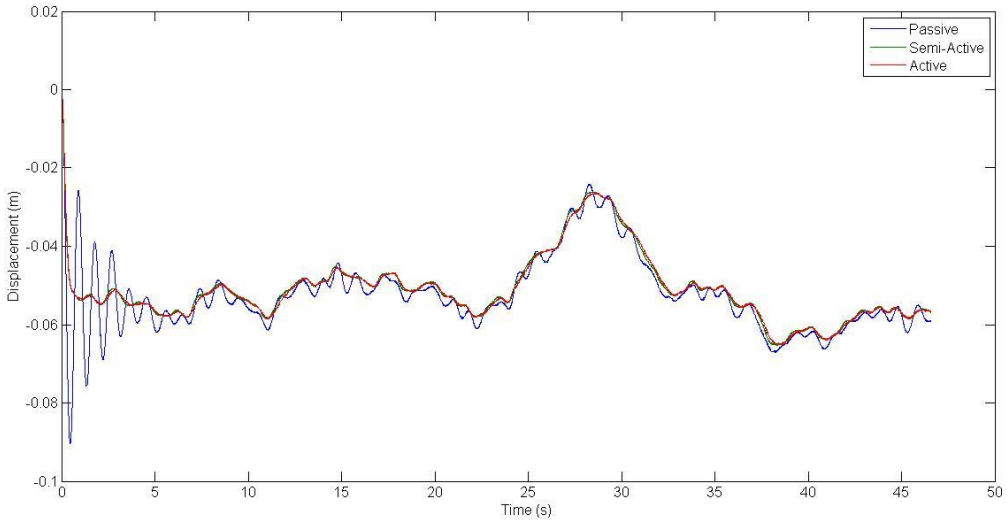

Figure 7.7 – Sprung mass displacement comparison for passive, semi-active and active.

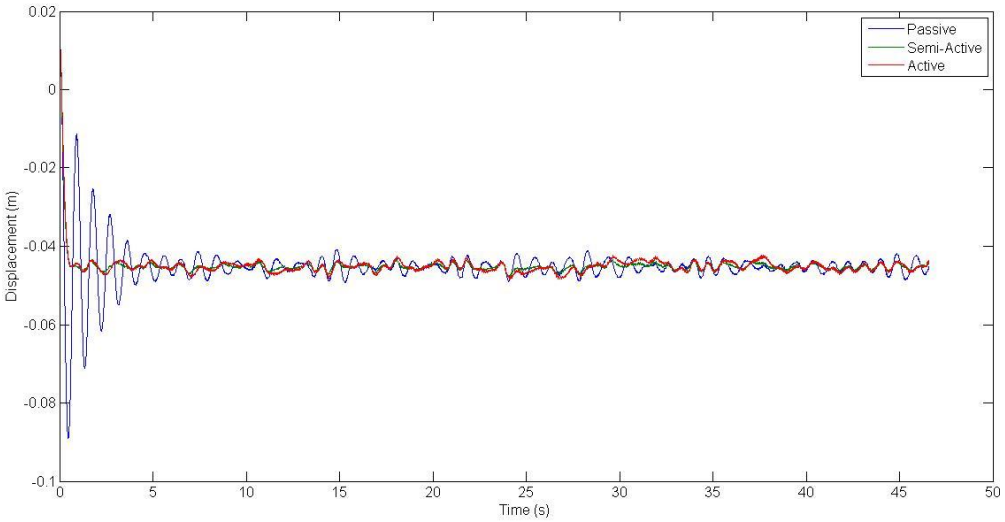

Figure 7.8 – Suspension displacement comparison for passive, semi-active and active.

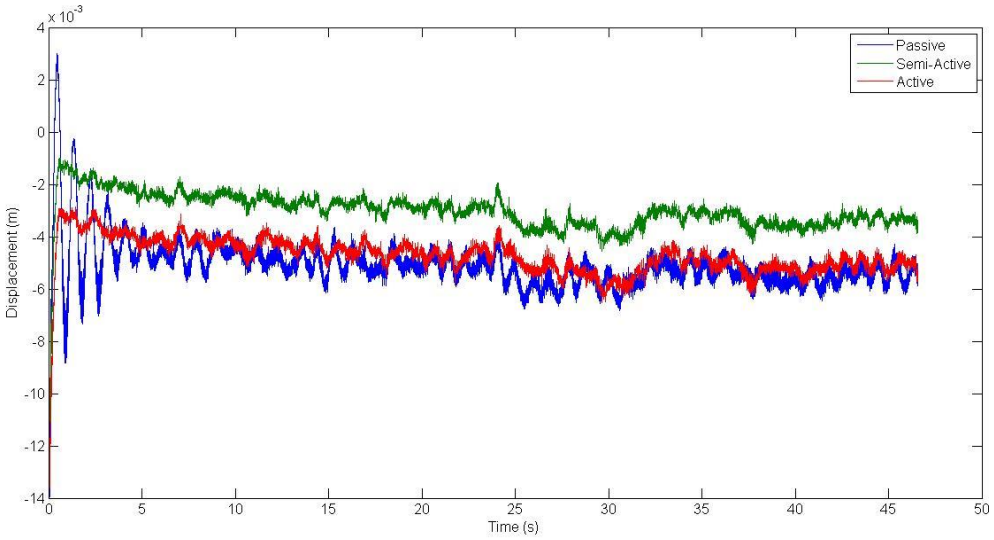

Figure 7.9 – Tyre displacement comparison for passive, semi-active and active.

For the skyhook damping coefficient of 200Ns/m, the semi-active and active suspensions are superior to the passive suspension in all criterias of sprung mass, suspension travel and wheel mass vibration. However as shown in Section 7.1.2 further increases in skyhook damping would lead to tradeoffs in term of suspension displacement and wheel vibration.

From these results it is clear that semi-active suspension represent the best option for both touchdown landing and taxiing of an aircraft. With performance levels comparable to the active system, the semi-active system requires less energy consumption, less weight and has a functional fail safe mechanism.

7.2 Real Time Test - Flexible Structure Sprung Mass Test

7.2.1 Flexible Beam Structure

The aim of this test was to simulate the landing and taxiing of a flexible structure such as an aircraft airframe. A simple flexible 12 beam cross structure shown in Figure 7.10 was modelled in order to introduce structural dynamics that would be excited by the landing gear and road inputs. The structure represents the sprung mass of a quarter car system and the centre of the structure is connected to the suspension displacement (vertical blue line) which is connected to the tyre displacement (vertical red line).

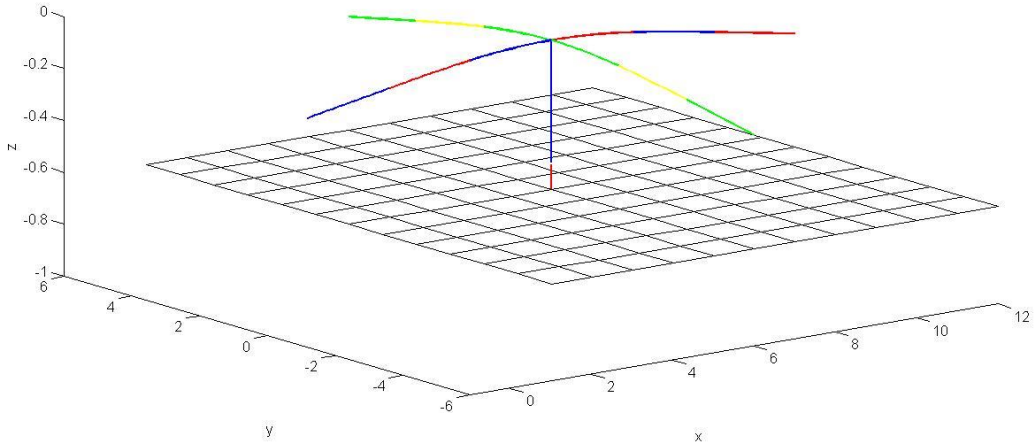

Figure 7.10 – Diagram of 12 beam cross structure where each colour represents a beam. The mid-point of the cross structure is connected to ground via the suspension and wheel and tyre units.

The equations used for the simulation of a cross structure is the Bernoulli beam equation. A single beam is described by 4 equations for 4 modes of vibration. These modes are axial extension/compression, torsion, bending in x-y and bending in x-z. A single beam contains 12 degrees of freedom with 6 nodes at each end comprising of 3 translational and 3 rotational degrees of freedoms as shown in Figure 7.11. The double arrows denote rotational degree of freedoms.

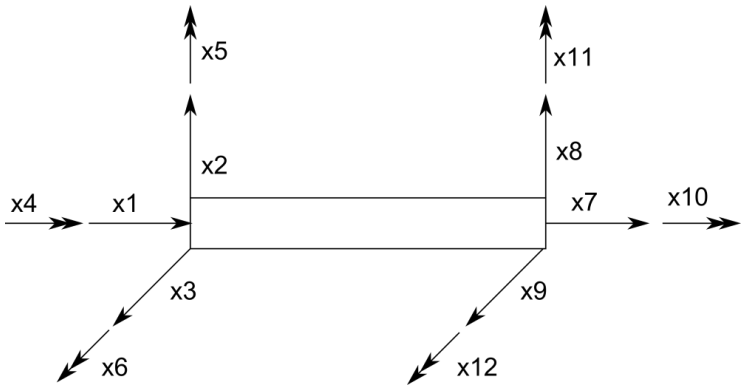

Figure 7.11 – Diagram of beam degree of freedoms.

The Bernoulli beam equations are derived using the stress/strain relationship and the assumption of small angles. Since there are 12 nodes the beam equation can be arranged into a 12x12 matrix for mass and stiffness in the form,

$$\mathbf{m}\ddot{\mathbf{x}} + \mathbf{b}\dot{\mathbf{x}} + \mathbf{k}\mathbf{x} = \mathbf{F} \tag{7.1}$$

Here $\mathbf{m}$, $\mathbf{b}$ and $\mathbf{k}$ are the mass, damping and stiffness matrices and $\mathbf{F}$ is the external force term which comprises of gravity force due to the beam weight and the suspension force acting vertically at the center of the cross structure. The gravity force acts on the vertical degree of freedom and the rotation axis of x_6 and x_{12} of each beam.

The consistent mass matrix for a beam element is given by,

$$m = \frac{\rho \mathrm{AL}}{420}\begin{bmatrix} 140 & 0 & 0 & 0 & 0 & 0 & 70 & 0 & 0 & 0 & 0 & 0 \\ 0 & 156 & 0 & 0 & 0 & 22L & 0 & 54 & 0 & 0 & 0 & -13L \\ 0 & 0 & 156 & 0 & -22L & 0 & 0 & 0 & 54 & 0 & 13L & 0 \\ 0 & 0 & 0 & \frac{140J}{A} & 0 & 0 & 0 & 0 & 0 & \frac{70J}{A} & 0 & 0 \\ 0 & 0 & -22L & 0 & 4L^2 & 0 & 0 & 0 & -13L & 0 & -3L^2 & 0 \\ 0 & 22L & 0 & 0 & 0 & 4L^2 & 0 & 13L & 0 & 0 & 0 & -3L^2 \\ 70 & 0 & 0 & 0 & 0 & 0 & 140 & 0 & 0 & 0 & 0 & 0 \\ 0 & 54 & 0 & 0 & 0 & 13L & 0 & 156 & 0 & 0 & 0 & -22L \\ 0 & 0 & 54 & 0 & -13L & 0 & 0 & 0 & 156 & 0 & 22L & 0 \\ 0 & 0 & 0 & \frac{70J}{A} & 0 & 0 & 0 & 0 & 0 & \frac{140J}{A} & 0 & 0 \\ 0 & 0 & 13L & 0 & -3L^2 & 0 & 0 & 0 & 22L & 0 & 4L^2 & 0 \\ 0 & -13L & 0 & 0 & 0 & -3L^2 & 0 & -22L & 0 & 0 & 0 & -4L^2 \end{bmatrix} \tag{7.2}$$

Where ρ is the density, A the cross-section area, L is the length of the beam and J is the second moment of area. The stiffness matrix of the beam is given by,

$$k = \begin{bmatrix} \frac{\mathrm{EA}}{\mathrm{L}} & 0 & 0 & 0 & 0 & 0 & -\frac{EA}{L} & 0 & 0 & 0 & 0 & 0 \\ 0 & \frac{12EI_z}{L^3} & 0 & 0 & 0 & \frac{6EI_z}{L^2} & 0 & -\frac{12EI_z}{L^3} & 0 & 0 & 0 & \frac{6EI_z}{L^2} \\ 0 & 0 & \frac{12EI_y}{L^3} & 0 & -\frac{6EI_y}{L^2} & 0 & 0 & 0 & -\frac{12EI_y}{L^3} & 0 & -\frac{6EI_y}{L^2} & 0 \\ 0 & 0 & 0 & \frac{GJ}{L} & 0 & 0 & 0 & 0 & 0 & -\frac{GJ}{L} & 0 & 0 \\ 0 & 0 & -\frac{6EI_y}{L^2} & 0 & \frac{4EI_y}{L} & 0 & 0 & 0 & \frac{6EI_y}{L^2} & 0 & \frac{2EI_y}{L} & 0 \\ 0 & \frac{6EI_z}{L^2} & 0 & 0 & 0 & \frac{4EI_z}{L} & 0 & -\frac{6EI_z}{L^2} & 0 & 0 & 0 & \frac{2EI_z}{L} \\ -\frac{EA}{L} & 0 & 0 & 0 & 0 & 0 & \frac{\mathrm{EA}}{\mathrm{L}} & 0 & 0 & 0 & 0 & 0 \\ 0 & -\frac{12EI_z}{L^3} & 0 & 0 & 0 & -\frac{6EI_z}{L^2} & 0 & \frac{12EI_z}{L^3} & 0 & 0 & 0 & -\frac{6EI_z}{L^2} \\ 0 & 0 & -\frac{12EI_y}{L^3} & 0 & \frac{6EI_y}{L^2} & 0 & 0 & 0 & \frac{12EI_y}{L^3} & 0 & \frac{6EI_y}{L^2} & 0 \\ 0 & 0 & 0 & -\frac{GJ}{L} & 0 & 0 & 0 & 0 & 0 & \frac{GJ}{L} & 0 & 0 \\ 0 & 0 & -\frac{6EI_y}{L^2} & 0 & \frac{2EI_y}{L} & 0 & 0 & 0 & \frac{6EI_y}{L^2} & 0 & \frac{4EI_y}{L} & 0 \\ 0 & \frac{6EI_z}{L^2} & 0 & 0 & 0 & \frac{2EI_z}{L} & 0 & -\frac{6EI_z}{L^2} & 0 & 0 & 0 & \frac{4EI_z}{L} \end{bmatrix} \tag{7.3}$$

Where E is the Young's Modulus, G is the shear modulus and I_x and I_y are the moment of inertia for beam bending. The cross structure has 12 beams and 13 nodes, hence the global mass and stiffness matrices will be 78x78. The global matrix is constructed by combining 12x12 matrices for each of the 12 beams. The damping of the structure is chosen to be low and proportional to the structural stiffness as this will allow decomposition of the mass, stiffness and damping matrices into modal form.

In modal form the structural system is decomposed into uncoupled equation of motion described in modal coordinates as opposed to Cartesian coordinates. This is advantageous because computing the equations in modal form allows for modal reduction, by removing any equations of modes with natural frequencies beyond the region of interest. Through modal reduction the computational time required to predict the structural dynamics can be dramatically reduced while the performance in the frequencies of interest is maintained.

For modal transformation into uncoupled equations proportional damping is chosen in the form,

$$\mathbf{b} = \alpha\mathbf{m} + \beta\mathbf{k} \tag{7.4}$$

Here α and β are constants. This assumption is not realistic but yields a form of equation which can be reduced to enhance computational time. Nevertheless it is an adequate assumption and in general structures with higher masses and stiffness will also require higher damping.

The transformation from Cartesian coordinates, $\boldsymbol{x}$, to modal coordinates, $\boldsymbol{\eta}$, is given by,

$$\mathbf{x} = \boldsymbol{\varphi}\boldsymbol{\eta} \tag{7.5}$$

Here φ is the eigenvectors of the undamped system to ensure orthogonality of the modes and is termed the modal transformation matrix. The system equations in modal coordinates become,

$$\boldsymbol{\varphi}^T\mathbf{m}\boldsymbol{\varphi}\ddot{\boldsymbol{\eta}} + \boldsymbol{\varphi}^T\mathbf{b}\boldsymbol{\varphi}\dot{\boldsymbol{\eta}} + \boldsymbol{\varphi}^T\mathbf{k}\boldsymbol{\varphi}\boldsymbol{\eta} = \boldsymbol{\varphi}^T\boldsymbol{F} \tag{7.6}$$

The parameters for the structure are given in Table 6.9. Since the cross structure is symmetric and excited in the vertical direction from the centre point, only bending in the vertical x-z plane is relevant. The structure will not undergo bending in the horizontal x-y plane or torsion and hence I_y, G and J are irrelevant parameters for this system.

Total Structure Weight (kg)	25
Number of Beams	12
E (N/m^2)	1200000
I_z (m^4)	0.01
L (m)	2
A (m^2)	3.828×10^{-4}
P (kg/m^3)	2721
α	0
β	0.01

Table 7.4 – Parameters for cross structure.

7.2.2 Passive Test

In this experimental test, the MIL system mass dynamics were replaced with the flexible structure dynamics. A passive drop test is conducted with the quarter car suspension parameters and a pseudo-random 0.2-1.6Hz ground input as in Section 6.3.2. Validation of this experimental result is given in Appendix B3.

Time responses of the sprung mass displacement, suspension displacement and tyre displacement are shown in Figures 7.12-7.14 respectively. When compared to the passive point mass experiment, the cross structure exhibits greater vibrations during the touchdown and nearly identical results during taxiing. This applies to sprung mass position, suspension deflection and tyre displacement.

It is clear that the greater sprung mass vibration during touchdown landing must be due to the coupling with flexible structure dynamics. Figure 7.15 shows the displacements of different points along the cross structure wing. As expected the vibration of the cross structure are in phase with points further away from the centre exhibiting larger amplitudes. This in phase vibration of the cross structure wings means that it will be positively contributing to the suspension and sprung mass vibration. The result of this coupling is greater vibration of sprung mass, suspension and tyre during touchdown landing. After landing the cross structure displacements settle to their equilibrium positions and therefore there is a smaller contribution of flexible body dynamics to the sprung mass vibration during taxiing. Another reason for the good matching of cross structure and point mass results during taxiing is due to the smaller vibration amplitudes excited due to taxiing compared to touchdown.

The result of the coupling between suspension and flexible structure changes the dynamics of the system. The notable changes apart from higher vibration amplitudes are a decrease in the body hop resonant frequency and an introduction of additional resonant modes. This can be seen from the sprung mass frequency response plot comparing the point mass to the cross structure shown in Figure 7.16. The dynamics of the flexible structure introduces an additional resonant mode occurring at 3 Hz.

This experimental result demonstrates that coupling between a flexible structure and the suspension can introduce substantially different dynamics to the system. For a system with considerable flexibility, a point mass representation will not accurately capture the system dynamics.

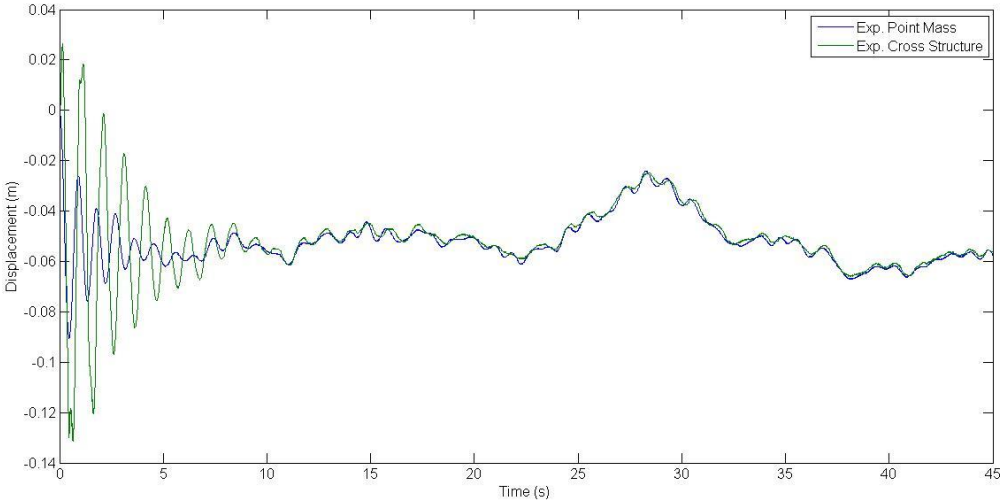

Figure 7.12 – Sprung mass displacement time response.

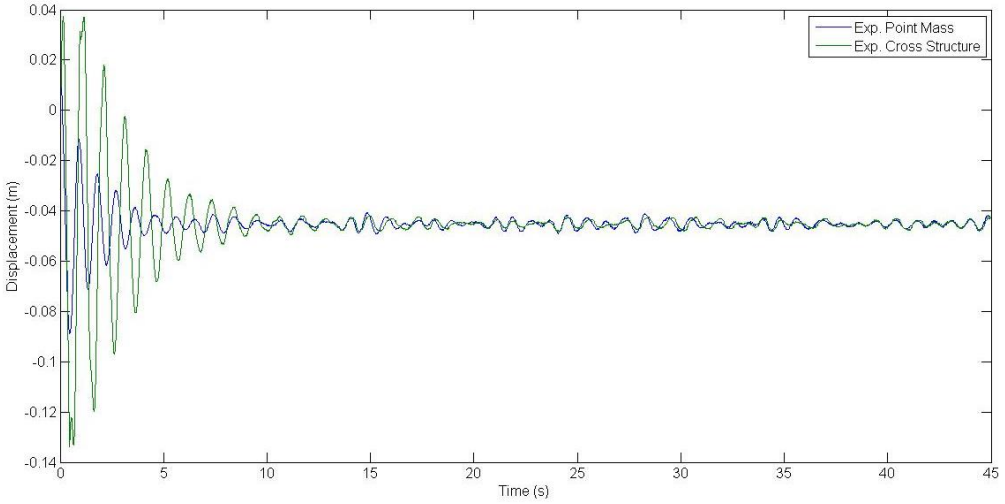

Figure 7.13 – Suspension displacement time response.

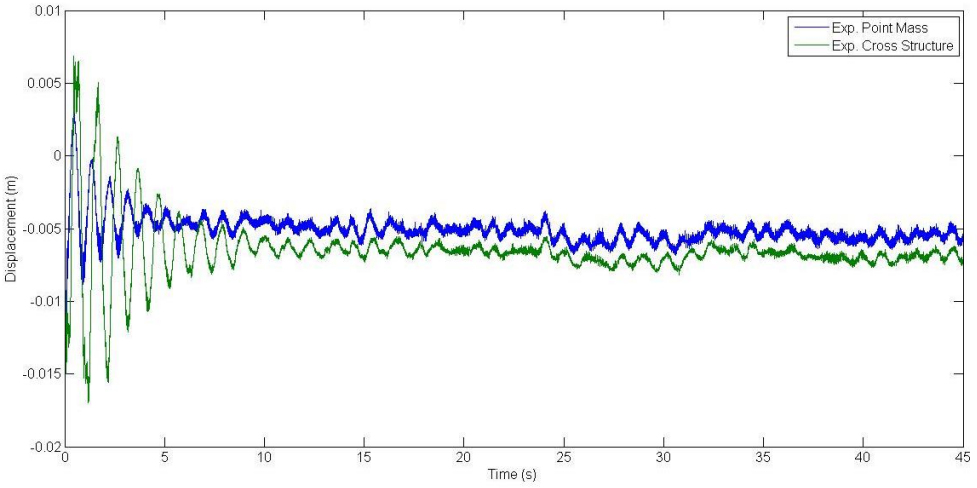

Figure 7.14 – Tyre displacement time response.

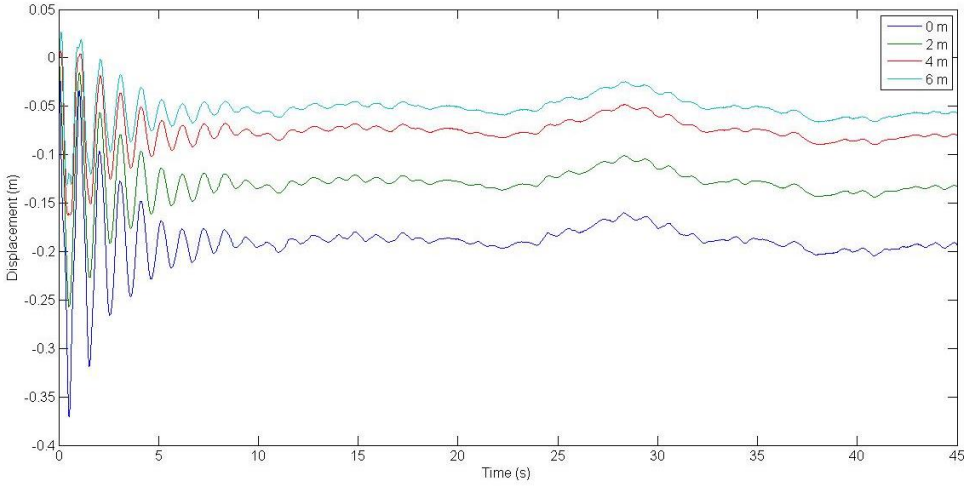

Figure 7.15 – Displacement of points along cross structure wing time response. Legend refers to distance from cross structure centre.

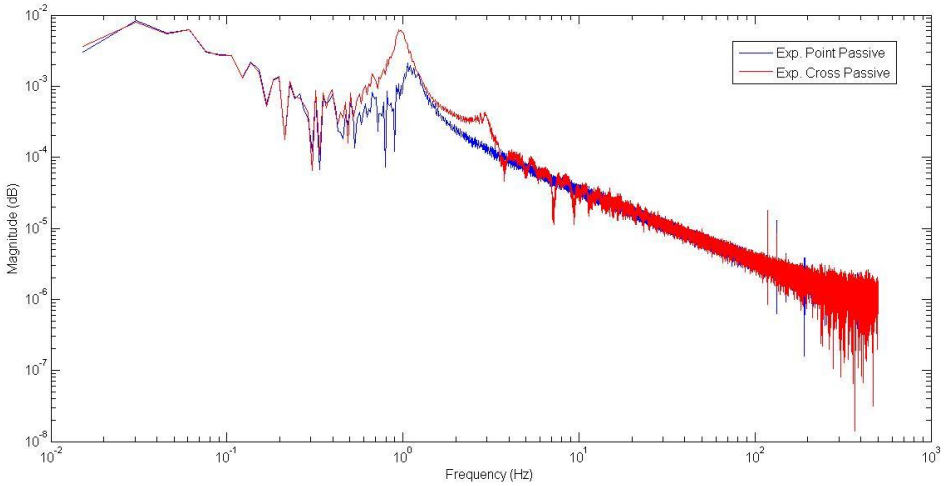

Figure 7.16 – Frequency response of sprung mass position.

7.2.2 Semi-Active Test

A semi-active drop test is conducted with quarter car suspension parameters, except the point mass is replaced with a cross structure of the same weight and a pseudo-random 0.2-1.6Hz ground input as in Section 6.3.2. Validation of this test result is given in Appendix B4.

The time response for sprung mass displacement, suspension displacement and tyre displacement in comparison to semi-active point mass system is shown in Figure 7.17-7.19 respectively. Like the comparison between passive cross structure and passive point mass, here the time responses for semi-active cross structure and semi-active point mass are nearly identical for taxiing while for landing the cross structure shows larger vibration amplitudes. The displacements of different points along the cross structure wing are shown in Figure 7.20. Comparison to the passive cross structure is shown in Figure 7.25 – 7.27. The results in Table 7.5 show that the cross structure reduces RMS sprung mass acceleration by 62.3% compared to the passive case.

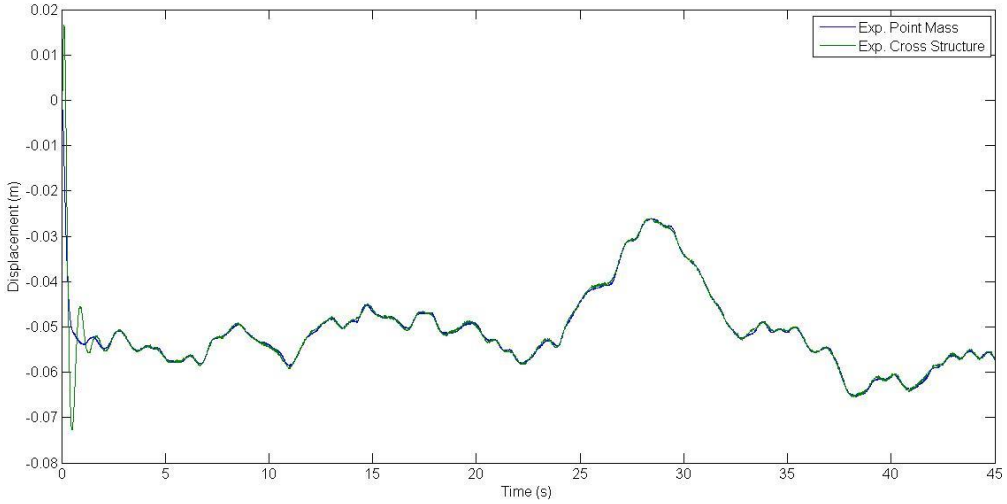

Figure 7.17– Sprung mass displacement time response.

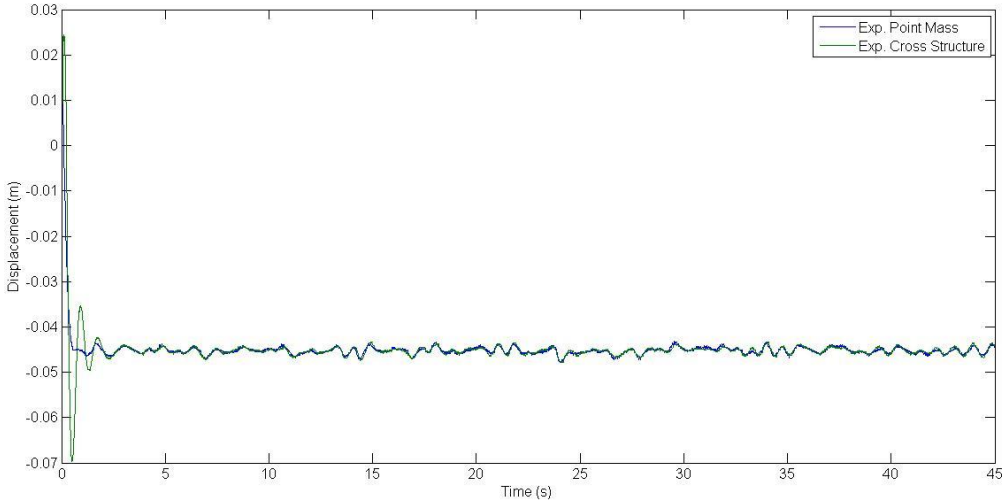

Figure 7.18 – Suspension displacement time response.

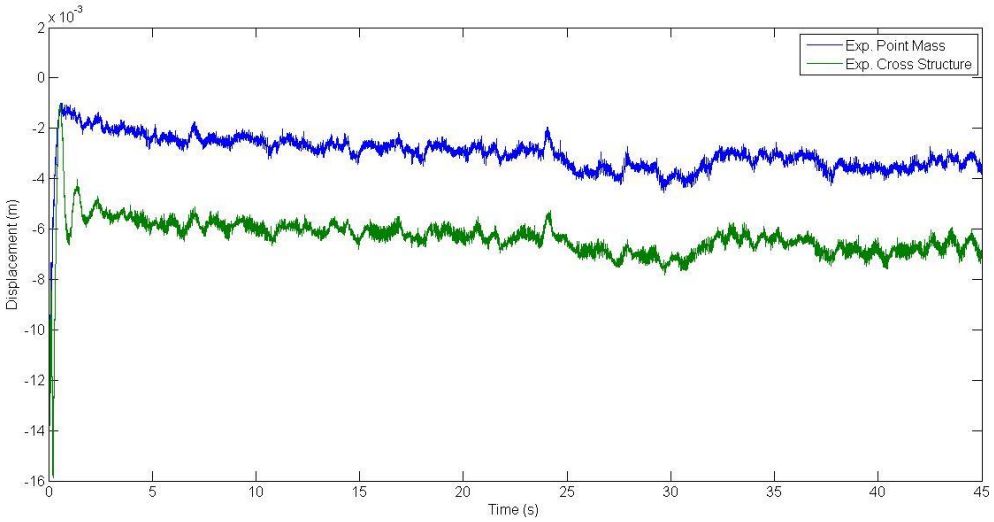

Figure 7.19 – Tyre displacement time response.

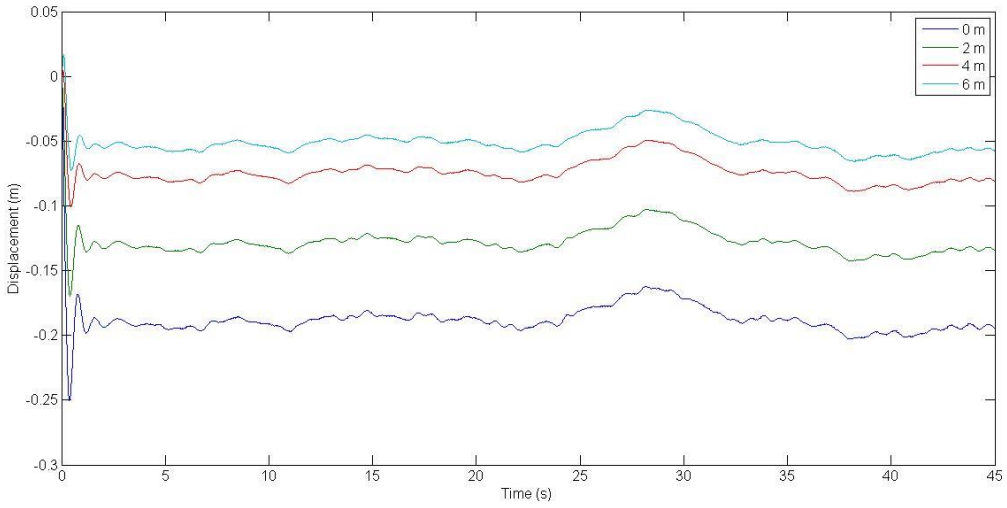

Figure 7.20 – Displacement of points along cross structure wing time response. Legend refers to distance from cross structure centre.

7.2.3 Active Test

An active suspension drop test is conducted with quarter car suspension parameters, except the point mass is replaced with a cross structure of the same weight and a pseudo-random 0.2-1.6Hz ground input as in Section 6.3.5. Validation of this test result is given in Appendix B5.

The time response for sprung mass displacement, suspension displacement and tyre displacement in comparison to active point mass system is shown in Figure 7.21-7.23 respectively. Like the comparison between passive cross structure and passive point mass, here the time responses for active cross structure and active point mass are nearly identical for taxiing while for landing the cross structure shows larger vibration amplitudes. The displacements of different points along the cross structure wing are shown in Figure 7.24. Comparison to the passive cross structure is shown in Figure 7.25 – 7.27. The results in Table 7.5 show that the cross structure reduces RMS sprung mass acceleration by 66.6% compared to the passive case.

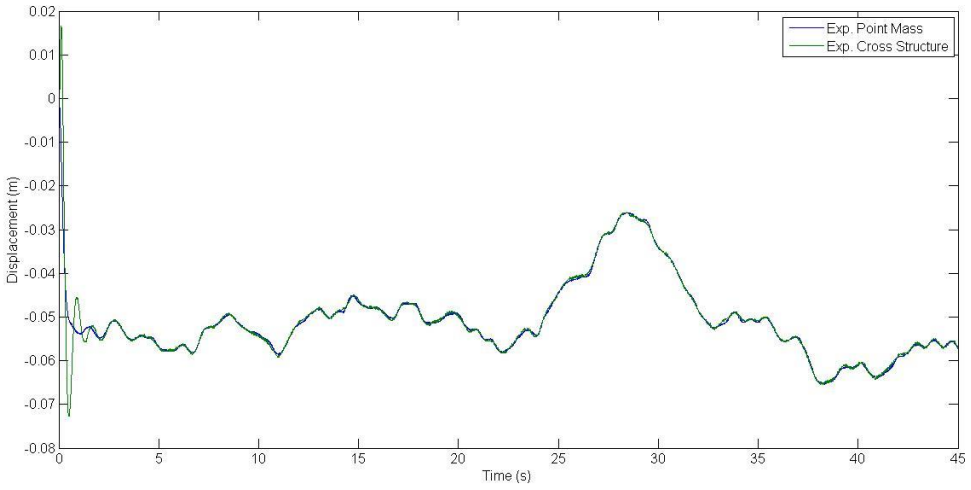

Figure 7.21 – Sprung mass displacement time response.

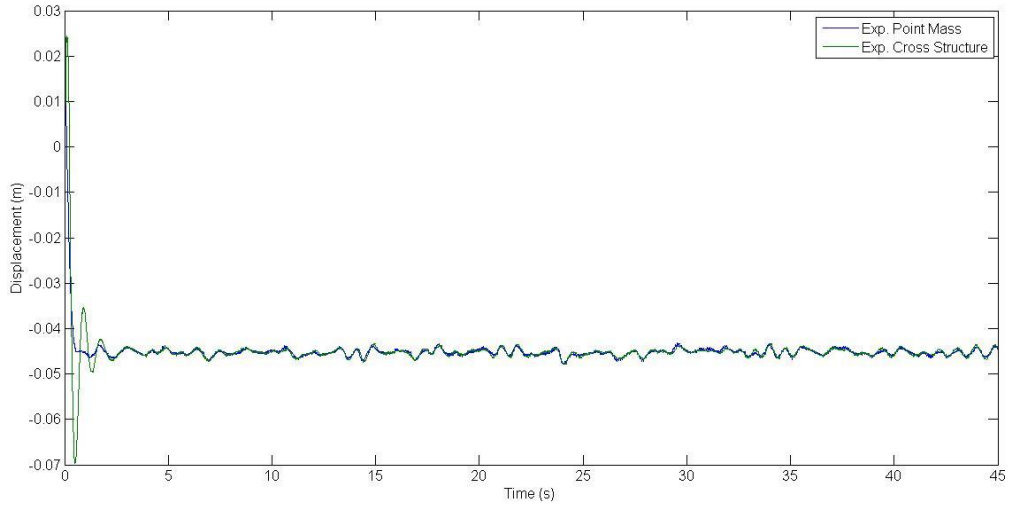

Figure 7.22 – Suspension displacement time response.

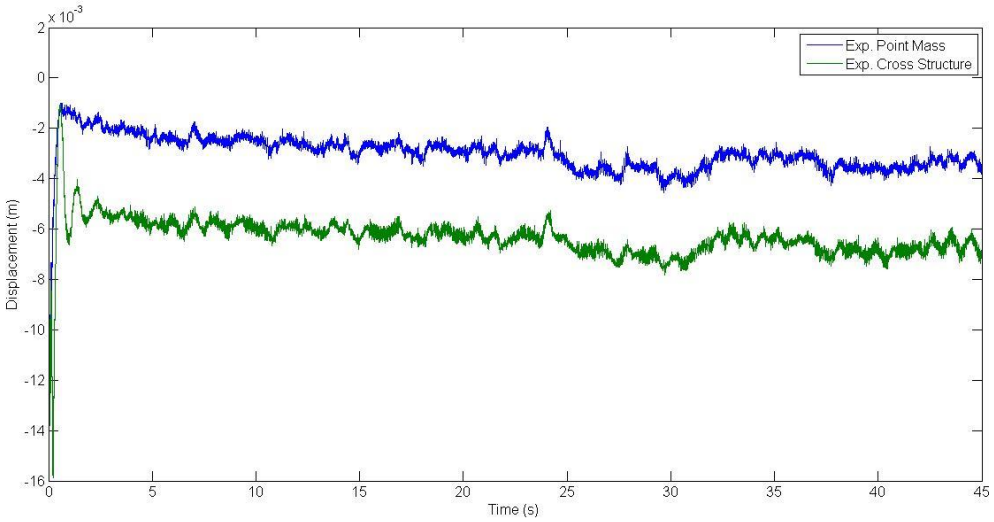

Figure 7.23 – Tyre displacement time response.

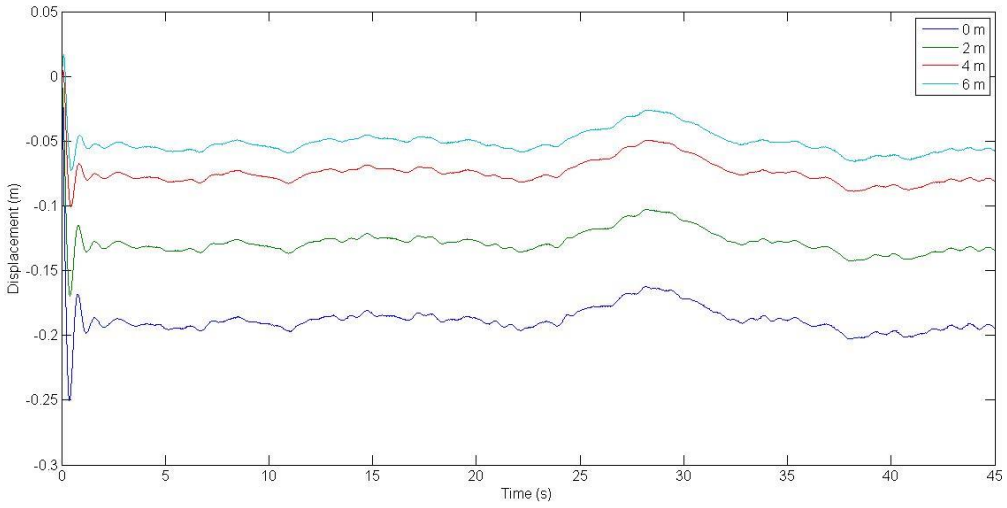

Figure 7.24 – Displacement of points along cross structure wing time response. Legend refers to distance from cross structure centre.

7.2.4 Comparison of Passive and Active Suspension Performance

Figure 7.31 – 7.33 shows the comparison between the time responses of passive, semi-active and active schemes for the cross structure experiments. The plot shows that like the point mass case, the semi-active and active algorithms are nearly identical and they show a dramatic improvement in sprung mass vibration isolation compared to the passive case. The performance improvement in sprung mass vibration isolation is shown in terms of RMS acceleration in Table 7.5. The active and semi-active suspensions also show a reduction in suspension displacement and tyre displacement compared to the passive case.

For the parameters chosen, semi-active and active suspension is shown to be superior to the passive suspension in all areas of vibration isolation, suspension space usage and road holding for both landing and taxiing. Since the semi-active and active suspension have nearly identical responses it would be advantageous to adopt the semi-active suspension due to its lower power consumption, weight and superior fail safe mechanism.

Suspension Type	RMS Sprung Mass Acceleration
Passive	0.679
Semi-Active	0.256
Fully Active	0.227

Table 7.5 - Comparison of sprung mass vibration isolation for passive, semi-active and active.

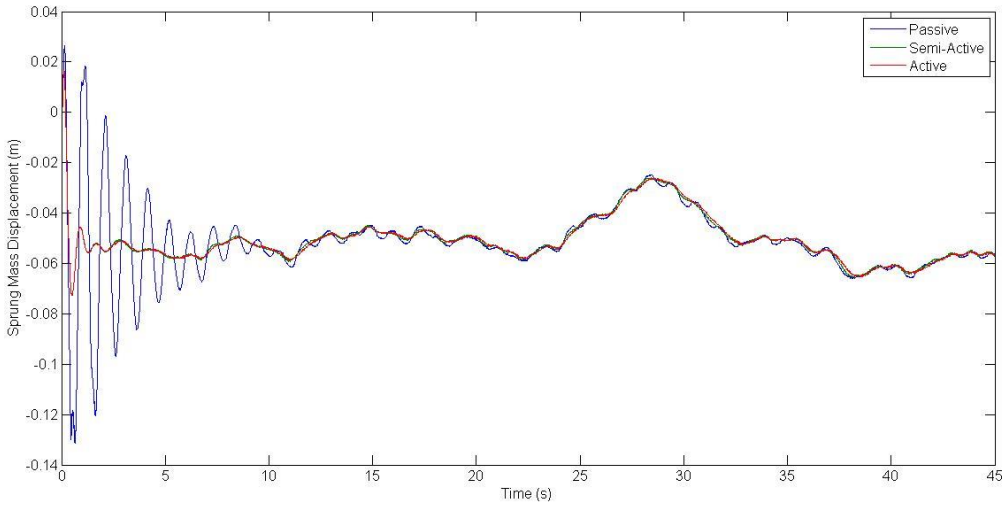

Figure 7.25 – Cross structure passive, semi-active, active schemes sprung mass displacement time response.

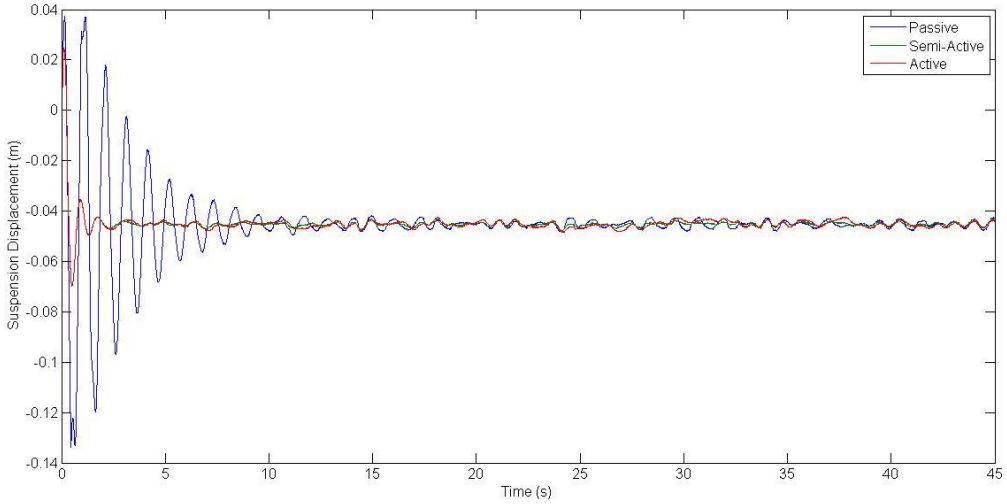

Figure 7.26 – Cross structure passive, semi-active, active schemes suspension displacement time response.

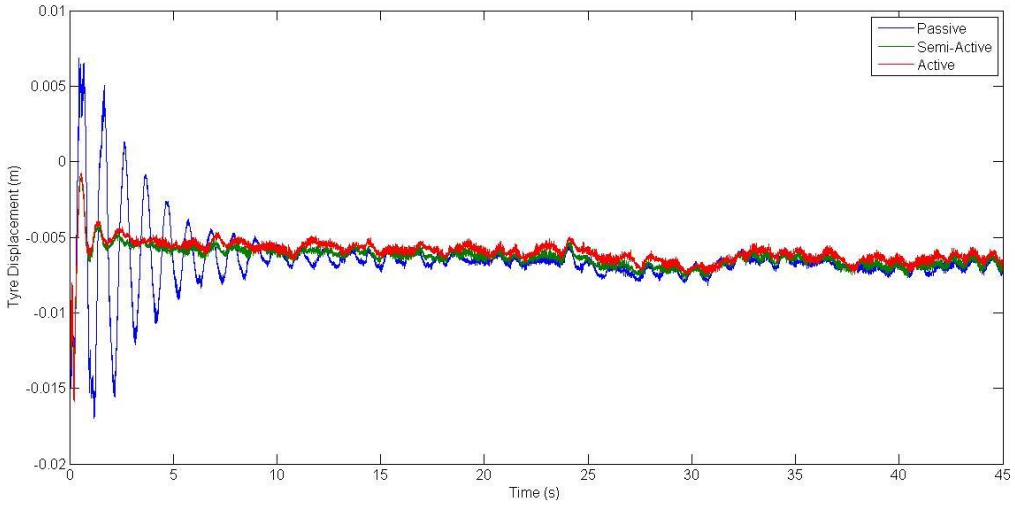

Figure 7.27 – Cross structure passive, semi-active, active schemes tyre displacement time response.

7.3 Conclusion

Vehicle suspension experimental tests were conducted for landing touchdown and response to ground inputs during taxiing. The results in this chapter have demonstrated correctly the expected performance from skyhook algorithms. The skyhook algorithm greatly improved sprung mass vibration isolation compared to the passive case, showing reduction of RMS acceleration by over 60%. Moreover the skyhook also managed reductions in suspension space ultisation and tyre displacements compared to the passive case. This means the skyhook suspension will have better passenger comfort, road handling and a more compact design. Both active and semi-active skyhooks were shown to have comparable performance confirming findings from literature. From these experimental results it is clear that semi-active skyhook systems are superior to active systems for the landing and taxiing of a vehicle since the semi-active system requires less power consumption, weight and has a fail-safe mechanism.

The response of experimental tests conducted with a flexible sprung mass structure was compared to the point mass case. Altered dynamics characterized by higher vibration amplitudes, a shift in body hop frequency and an additional resonance mode introduced by the flexible structure was successfully captured in the experimental results. The test results show that for a structure with considerable flexibility a point mass representation will be unable to accurately represent the system dynamics. This validates the use of a vehicle structure MIL system in hybrid testing of suspensions for large vehicles with flexible structural dynamics since for these type of vehicles prototyping is not so feasible.

8. Conclusion and Future Work

8.1 Conclusion

In this research a numerical-experimental hybrid test rig is developed, studied and experimentally tested for the application of vehicle suspensions. Additionally a vehicle representation with similar characteristics to an aircraft with a flexible structure as the sprung mass, is tested for both touchdown landing and taxiing. The novel contributions of the thesis are:

1. The analysis and experimental testing of a new context for hybrid numerical-experimental test systems. An aspect of the novelty is the use of a MIL suspension and MIL vehicle structure, such that two MIL systems are connected in series. Furthermore another novel feature is the use of a structure with many flexible vibration modes for the MIL vehicle model.
2. Proposal of a novel friction compensation algorithm which was demonstrated experimentally to reduce Coulomb friction significantly.

Chapter 2 provides a comprehensive review of the state of the art of passive, semi-active and active suspension technologies both in terms of hardware and control. The advantages and disadvantages of different suspension systems are discussed. The result of the suspension literature review concludes that an experimental test rig comprising fixed components and active elements would be restricted to a single application and a more flexible rig comprising HIL and MIL elements would widen the sphere of research.

In Chapter 3 a flexible test rig which could test various types of suspension is proposed. Such a test rig is possible by combining an experiment with real components with numerical simulation which interfaces physically through the use of an actuator. This type of testing has, in the past, been termed numerical-experimental hybrid testing, substructuring, hardware in the loop testing and model in the loop testing. A literature review of the benefits and challenges of hybrid testing is conducted. Finally a design of hybrid test rig for vehicle suspensions is presented in detail along with basic experimental validation of the test rig. The quarter car test rig is able to mimic a vehicle with various suspension components and sprung mass structures by representing the suspension force and sprung mass position as numerically modelled, MIL systems. This is achieved by representing the suspension component by a force controlled electric actuator and representing the sprung mass position by a position controlled hydraulic actuator.

The experimental results in Chapter 3 indicate that main obstacle to hybrid testing stems from delays in the control loop and the tracking performance of model in the loop actuators. One of the main sources of error in suspension force tracking is due to friction within the linear actuator. In Chapter 4 a literature review of friction compensation methods is presented. Using the experimental rig the friction characteristics of the linear electric actuator are analysed and a novel compensation method is proposed. The friction compensation method is based upon coulomb friction compensation and a logic algorithm based on feedback force and suspension motion to estimate the time of velocity reversal. The results of the compensation algorithm are presented and a clear

improvement in tracking performance is achieved resulting in improved accuracy of the hybrid test rig by 37% and a reduction of peak force error by approximately 50%.

An analysis of the effect of time delay on the test rig is conducted in Chapter 5. The results of the analysis show that larger time delays lead to degradation of the test rig accuracy and possible instability. The effect of time delays in the suspension force model in the loop system and the sprung mass structure model in the loop system are at first separately evaluated and then in combination using root locus and state space methods. A time delay was found to reduce the apparent damping of the suspension and therefore lead to changes in the frequency and decay rate of the system modes of vibration. Moreover the quarter suspension system parameters are shown to have an effect on system performance and stability for a given time delay.

In Chapter 6 experimental test results are presented and the test rig performance in terms of accuracy and stability is analysed. The control loop is described in detail as well as the model identification of the system actuators and parameters. From this a simulation model of the test rig is used to show that given delays in the test rig, the testing of real vehicle suspensions parameters are unstable. Experimental measurements from the rig confirmed that real time testing of a Boeing 707 scaled suspension is unstable with negative damping. Since the test rig is incapable of testing real suspension parameters, an arbitrary set of stable suspension parameters were chosen and tests conducted. The results of these experimental tests show that overall the test rig is able to capture qualitatively the dynamic response of the emulated system. Challenges in obtaining good wheel hop mode data are discussed in the chapter due to a drawback in the rig design due to high friction in the rail guide which supported the wheel.

Chapter 7 presents experimental results on semi-active and active skyhook suspensions for structures with flexible dynamics. The results show that as expected the skyhook algorithms offer dramatic performance improvement of approximately 60% reduction of sprung mass vibration. The semi-active and active configurations were shown to have comparable performance as suggested by literature. The trade-off between suspension space utilisation and sprung mass vibration was also observed as the skyhook damping is increased to high values. The test conducted using a flexible cross structure as the sprung mass showed substantial coupling between the suspension such that the cross structure had greater sprung mass vibrations compared to the point mass case. The results in Chapter 7 shows that for the stable system parameters chosen, the test rig is capable of testing MIL suspension and MIL vehicle structure systems and capturing the correct trends of the dynamic responses.

Overall the experimental results could be improved by reduction of delays in actuator tracking, reduction of actuator tracking errors in general and by reducing delays in sensor systems and filters which are required to remove signals noise.

8.2 Future Work

The primary method of improving the performance of the test rig is to reduce the friction and the delays within the system control loop. This could be achieved by investing in better sensors and actuators or by improving the control system. The author here feels that the best route for future

work would be to focus on control methods since this is where the most gains can be made with the least cost.

A large body of literature exists for actuator delay compensation with a small number devoted specifically to hybrid test systems. The methods for actuator delay compensation can be categorised in general into three types,

1. Methods focused on devising a new controller structure based upon control engineering techniques.
2. Compensation without altering the controller structure but based upon altering the demand of the controller to compensate for the known time delay.
3. Intelligent control techniques.

All three types of compensation methods provide encouraging avenues for future work. First of all future work could be based upon directly implementing proven techniques on the test rig as this should yield a substantial improvement in performance.

From literature, one of the control engineering methods which has been the most extensively developed for hybrid testing is the linear substructuring controller (LSC). The method is based upon a controller that compensates the delay using a feedforward term and also feedback based upon a model of the rig system including the actuator dynamics. Since the method is dependent on the availability of an accurate linear model, in previous work it was modified to contain an adaptive scheme termed minimal control synthesis with error feedback (MCSEF) [108]. Subsequently the MCSEF controller was extended to the control of hybrid systems with multiple actuators; the application chosen was a full motorcycle real time test rig [113]. Other methods which do not require the model of the test rig are standard control methods such as feedforward of an inverted model of the actuator plant. However this is often difficult to implement practically since many actuator models are not casually invertible. To overcome this Smith predictor has been successfully implemented on a hybrid test system, where an unstable system was stabilised [115]. Other control methods of actuator delay compensation are based upon the type of actuator as they aim to accurately model and compensate for characteristics specific to the actuator type which can also include non-linearities. For the test rig studied here the actuators refers to linear permanent magnet electric motors and large hydraulic actuators.

Methods based on altering the demand signal have been widely studied for the application of hybrid test systems [112]. These are normally implemented in two stages, firstly the time delay and amplitude errors of the actuators has to be determined then secondly a forward prediction scheme is used to extrapolate the demand signal. The forward extrapolation will give a new demand signal whose phase is leading the original demand signal by an amount equal to the time delay. Various methods of time delay estimation, as well as forward prediction schemes are discussed and experimentally compared in [109]. The experimental results are also compared with the MCSmd controller, which is similar and developed by the same authors as MCSEF. The test results showed that both types of method give a dramatic improvement of the test rig and that methods based upon altering controller demand was found to be more effective than the MCSmd controller.

Intelligent methods are methods which are based upon computer algorithms. Neural networks are suited to delay compensation since they can be used with non-linear systems to map the desired

output to the required demand signal. The technique was successfully implemented to compensate the time delay of semi-active MR damper in a HIL test rig and a real vehicle experiment respectively [102, 101].

All the methods discussed here are promising avenues for further research. The work from the literatures presented here may be implemented on the test rig in this thesis. Complications are expected to be encountered and therefore modifications or extensions of the methods are likely to be required.

References

[1] J. K. Hendrick and D. N. Wormley, "Active Suspension for Ground Transport Vehicles - A State of the Art Review," *Mechanics of Transportation Suspension Systems,* vol. 15, pp. 21-39, 1975.

[2] M. J. Crosby and D. C. Karnopp, "The Active Damper - A New Concept for Shock And Vibration Control," in *The Shock and Vibrations Bulletin, Part H*, Washington DC, USA, 1973.

[3] D. Hrovat, "Survey of Advanced Suspension Developments and Related Optimal Control Applications," *Automatica,* vol. 33, no. 10, pp. 1781-1817, 1997.

[4] M. S. Williams and A. Blakeborough, "Laboratory Testing of Structures Under Dynamic Loads: An Introductory Review," *Philosophical Transactions Royal Society London A,* vol. 359, no. 1786, pp. 1651-1669, 2001.

[5] W. E. Misselhorn, N. J. Theron and P. S. Els, "Investigation of Hardware-in-the-Loop for use in Suspension Development," *Vehicle System Dynamics,* vol. 44, no. 1, pp. 65-81, 2006.

[6] A. R. Plummer, "Model-in-the-Loop Testing," *Part I: J. Systems and Control Engineering,* vol. 220, no. 3, pp. 183-199, 2006.

[7] R. S. Sharp and D. A. Crolla, "Road Vehicle Suspension System Design - A Review," *Vehicle System Dynamics,* vol. 16, no. 3, pp. 167-192, 1987.

[8] M. Ahmadian and C. A. Pare, "A Quarter-Car Experimental Analysis of Alternative Semi-Active Control Methods," *Journal of Intelligent Meterial Systems and Structures,* vol. 11, no. 8, pp. 604-612, 2000.

[9] R. M. Chalasani, "Ride Performance Potential of Active Systems - Part I: Simplified Analysis Based on Quarter-Car Model," in *Proceedings of 1986 ASME Winter Annaul Meeting*, Los Angeles, CA, 1986.

[10] M. Nagai, "Recent Researches on Active Suspensions for Ground Vehicles," *JSME International Journal, Series C,* vol. 36, no. 2, pp. 161-170, 1993.

[11] M. Valasek, M. Novak, Z. Sika and O. Vaculin, "Extended Ground-Hook - New Concept of Semi-Active Control of Truck's Suspension," *Vehicle System Dynamics,* vol. 27, no. 5-6, pp. 289-303, 1997.

[12] E. M. Elbeheiry, D. C. Karnopp, M. E. Elaraby and A. M. Abdelraaouf, "Advanced Ground Vehicle Suspension Systems - A Classified Bibliography," *Vehicle System Dynamics,* vol. 24, no. 3, pp. 231-258, 1995.

[13] J. W. Miliken, "Active Suspension," *SAE Technical Paper 880799,* 1988.

[14] L. Den Boer, "Nonlinear Dynamic Behavior of a Conical Spring with Top Mass (Ph.D.)," Eindhoven University of Technology, Eindhoven, Netherlands, 2009.

[15] H. Sugiyama, A. A. Shabana, M. A. Omar and W. Y. Loh, "Development of Nonlinear Elastic Leaf Spring Model for Multibody Vehicle Systems," *Computer Methods in Applied Mechanics and Engineering,* vol. 195, no. 50-51, p. 6925–6941, 2006.

[16] E. Guglielmino and K. A. Edge, "A Controlled Friction Damper for Vehicle Applications," in *UKACC Conference Control*, 2004.

[17] C. Lauwerys, Control of Active and Semi-Active Suspension System for Passenger Cars (Ph.D.), Leuven, Belgium: Katholieke Universiteit Leuven, 2005.

[18] D. Fischer and R. Iserman, "Mechatronic Semi-Active and Active Vehicle Suspensions," *Control Engineering Practice,* vol. 12, no. 11, pp. 1353-1367, 2004.

[19] Y. Liu, T. P. Walters and M. J. Brennan, "A Comparison of Semi-Active Damping Control Strategies for Vibration Isolation of Harmonic Disturbances," *Journal of Sound and Vibration,* vol. 280, pp. 21-39, 2005.

[20] Koni, "www.Koni.com," Koni, 5 April 2014. [Online]. Available: http://www.koni.com/global-content/technology/fsd/.

[21] D. L. Margolis and G. M., "The Chatter of Semi-Active On-Off Suspensions and its Cure," *Vehicle System Dynamics,* vol. 13, no. 3, pp. 129-144, 1984.

[22] S. Nell and J. L. Steyn, "Experimental Evaluation of an Unsophisticated Two-State Semi-Active Damper," *Journal of Terramechanics,* vol. 31, no. 4, p. 227–238, 1994.

[23] D. Cebon, F. H. Besinger and D. J. Cole, "Control Strategies for Semi-Active Lorry Suspensions," *Journal of Automobile Engineering,* vol. 210, no. 2, pp. 161-178, 1996.

[24] E. J. Krasnicki, "The Experimental Performance of an ‘‘On–Off’’ Active Damper," in *Proceedings of the 51st Shock and Vibration Symposium*, San Diego, USA, 1980.

[25] K. J. Kitching, D. J. Cole and D. Cebon, "Performance of a Semi-Active Damper for Heavy Vehicles," *Journal of Dynamic Systems, Measurement, and Control,* vol. 122, no. 3, pp. 498-506, 2000.

[26] G. L. Ghiringhelli, "Testing of Semiactive Landing Gear Control for a General Aviation Aircraft," *Journal of Aircraft,* vol. 37, no. 4, pp. 606-616, 2000.

[27] W. M. Winslow, "Methods and Means of Translating Electrical Impulses into Mechanical Force". US Patent Patent 2147750, 1947.

[28] J. Rabinow, "The Magnetic Fluid Clutch," *American Institute of Electrical Engineers, Transactions of the,* vol. 67, no. 2, pp. 1308-1315, 1948.

[29] R. Stanway, "Smart Fluids: Current and Future Developments," vol. 20, no. 8, pp. 931-939, 2004.

[30] J. D. Carlson and M. R. Jolly, "MR Fluid, Foam and Elastomer Devices," *Mechatronics,* vol. 10, no. 4-5, pp. 555-569, 2000.

[31] A. Muhammad, Y. X. and Z. Deng, "Review of Magnetorheological (MR) Fluids and its Applications in Vibration Control," *Journal of Marine Science and Application,* vol. 5, no. 3, pp. 17-29, 2006.

[32] I. Bica, Y. D. Liu and H. J. Choi, "Physical Characteristics of Magnetorheological Suspensions and their Applications," *Journal of Industrial and Engineering Chemistry,* vol. 19, no. 2, p. 394–406, 2012.

[33] M. R. Jolly, J. W. Bender and J. D. Carlson, "Properties and Applications of Commercial Magnetorhelogical Fluids," *Journal of Intelligent Material Systems and Structures,* vol. 10, no. 5, pp. 5-13, 1999.

[34] J. D. Carlson, "What Makes a Good MR Fluid?," *Journal of Intelligent Material Systems and Structures,* vol. 13, no. 7-8, pp. 431-435, 2002.

[35] X. M. Dong, M. Yu, Z. Li, C. Liao and W. Chen, "A Comparison of Suitable Control Methods for Full Vehicle with Four MR Dampers Part II Controller Synthesis and Road Test Validation," *Journal of Intelligent Material Systems and Structures,* vol. 20, no. 9, pp. 1107-1119, 2009.

[36] B. F. Spencer Jr., S. J. Dyke, M. K. Sain and J. D. Carlson, "Phenomenological Model for Magnetorheological Dampers," *Journal of Engineering Mechanics,* vol. 123, no. 3, p. 230–238, 1997.

[37] G. M. Kamath and N. M. Wereley, "A Nonlinear Viscoelastic-Plastic Model for Electrorheological Fluids," *Smart Material Structures,* vol. 6, no. 3, pp. 351-359, 1997.

[38] W. H. Li, G. Z. Yao, G. Chen, S. H. Yeo and F. F. Yap, "Testing and Steady State Modelling of a Linear MR Damper Under Sinusoidal Loading," *Smart Materials and Structures,* vol. 9, no. 1, pp. 95-102, 2000.

[39] S. B. Choi and S. K. P. Y. P. Lee, "A Hysteresis Model for the Field-Dependent Damping Force of a Magnetorheological Damper," *Journal of Sound and Vibration,* vol. 245, no. 2, p. 375–383, 2001.

[40] "Lord Rheonetic Magnetically Responsive Technology (RD-1005-3)," Product Bulletin, 2003.

[41] LordCorporation, "http://www.lord.com/products-and-solutions/magneto-rheological-

(mr)/automotive-suspensions.xml," LordCorporation, 2014. [Online]. [Accessed 26 4 2014].

[42] J. H. Koo, F. D. Goncalves and M. Ahmadian, "A Comprehensive Analysis of the Response Time of MR Dampers," *Smart Materials and Structures,* vol. 15, no. 2, p. 351–358, 2006.

[43] N. R. Fisco and H. Adeli, "Smart Structures: Part I - Active and Semi-Active Control," *Scientia Iranica, Transactions A: Civil Engineering,* vol. 18, no. 3, p. 275–284, 2011.

[44] F. Casciati, J. Rodellar and U. Yildirim, "Active and Semi-Active Control of Structures - Theory and Applications: A Review of Recent Advances," *Journal of Intelligent Material Systems and Structures,* vol. 23, no. 11, pp. 1181-1195, 2012.

[45] D. C. Batterbee, N. D. Sims, R. Stanway and Z. Wolejsza, "Magnetorheological Landing Gear: 1. A Design Methodology," *Smart Materials and Structures,* vol. 16, no. 6, pp. 2429-2440, 2007.

[46] B. L. Gysen, P. J. J.H., J. L. Janssen and E. A. Lomonova, "Active Electromagnetic Suspension System for Improved Vehicle Dynamics," in *IEEE Vehicle Power and Propulsion Conference (VPPC)*, Harbin, China, 2008.

[47] X. Shen and H. Peng, "Analysis of Active Suspension Systems with Hydraulic Actuators," in *Proceedings of the 2003 IAVSD conference*, Atsugi, Japan, 2003.

[48] I. Martins, J. Esteves, G. D. Marques and F. Pina da Silva, "Permanent-Magnets Linear Actuators Applicability in Automobile Active Suspensions," *Vehicular Technology, IEEE Transactions on,* vol. 55, no. 1, pp. 86-94, 2006.

[49] T. Merker, G. Girres and O. Thriemer, "Active Body Contro (ABC) The Daimler Chrysler Active Suspension and Damping System," *SAE Technical Paper 2002-21-0054,* Vols. 2002-21-0054, 2002.

[50] D. Cao, X. Song and M. Ahmadian, "Editor's Perspectives: Road Vehicle Suspension design, Dynamics and Control," *Vehicle System Dynamics,* vol. 49, pp. 3-28, 2011.

[51] D. E. Williams and W. M. Haddad, "Active Suspension Control to Improve Vehicle Ride and Handling," *Vehicle System Dynamcis,* vol. 28, no. 1, pp. 1-24, 1997.

[52] L. G. Horta, R. H. Daugherty and V. J. Martinson, "Modeling and Validation of a Navy A6-Intruder Actively Controlled Landing Gear System," *National Aeronautics and Space Administration,* Vols. TP-1999-209124, 1999.

[53] W. D. Jones, "Easy Ride: Bose Corp. Uses Speaker Technology to Give Cars Adaptive Suspension," *IEEE Spectrum,* vol. 42, no. 5, pp. 12-14, 2005.

[54] R. J. Hayes, J. H. Beno, D. A. Weeks, A. M. Guenin and J. R. Mock, "Design and Testing of an Active Suspension System for a 2-1/2 Ton Military Truck," *SAE Technical Paper 2005-01-1715,* 2005.

[55] Z. Jin-qiu, P. Zhi-zhao and Z. Y. Z. Lei, "A Review on Energy-Regenerative Suspension Systems for Vehicles," in *Proceedings of the World Congress on Engineering Vol. III, WCE 2013*, London, UK, 2013.

[56] C. Spelta, F. Previdi, S. M. Savaresi, P. Bolzern, M. Cutini, C. Bisaglia and S. A. Bertinotti, "Performance Analysis of Semi-Active Suspensions With Control of Variable Damping and Stiffness," *Vehicle System Dynamics,* vol. 49, no. 1-2, pp. 237-256, 2011.

[57] C. Giliomee and P. Els, "Semi-Active Hydropneumatic Spring and Damper System," *Journal of Terramechanics,* vol. 35, no. 2, pp. 109-117, 1998.

[58] A. Nieto, A. Morales, A. Gonzalez and J. P. P. Chicharro, "An Analytical Model of Pneumatic Suspensions Based on an Experimental Characterization," *Journal of Sound and Vibration,* vol. 313, no. 1-2, pp. 290-307, 2008.

[59] D. Karnopp and D. Margolis, "Adaptive Suspension Concepts for Road Vehicles," *Vehicle System Dynamics,* vol. 13, no. 3, pp. 145-160, 1984.

[60] I. Youn and A. Hac, "Semi-Active Suspensions with Adaptive Capability," *Journal of Sound and Vibration,* vol. 180, no. 3, pp. 475-492, 1995.

[61] Y. Liu, H. Matsuhisa and H. Utsuno, "Semi-active vibration isolation system with variable stiffness and damping control," *Journal of Sound and Vibration,* vol. 313, pp. 16-28, 2008.

[62] O. Altet, X. Moreau, M. Moze, P. Lanusse and A. Oustaloup, "Principles and Synthesis of Hydractive CRONE Suspension," *Nonlinear Dynamics,* vol. 38, pp. 435-459, 2004.

[63] C. Poussot-Vassal, O. Sename, L. Dugard, P. Gaspar, Z. Szabo and J. Bokor, "A LPV Based Semi-Active Suspension Control Strategy," in *3rd IFAC Symposium on System, Structure and Control*, Iguaçu, Brasil, 2007.

[64] A. Kruczek, A. Stříbrský, J. Honců and M. Hlinovský, "Controller Choice for Car Active Suspension," *International Journal of Mechanics,* vol. 4, no. 3, pp. 61-68, 2009.

[65] D. C. Karnopp, M. J. Crosby and R. A. Harwood, "Vibration Control Using Semi-Active Force Generators," *ASME Journal of Engineering for Industry,* vol. 96, no. 2, pp. 619-626, 1974.

[66] S. Savaresi, E. Silani and S. Bittanti, "Acceleration Driven Damper (ADD): An Optimal Control Algorithm for Comfort Oriented Semi-Active Suspensions," *Journal of Dynamic Systems, Measurment and Control,* vol. 127, no. 2, pp. 218-229, 2004.

[67] K. S. Hong, H. C. Sohn and J. C. Hendrick, "Modified Skyhook Control of Semi-Active Suspensions: A New Model, Gain Sceduling, and Hardware-in-the-Loop Tuning," *Journal of Dynamic Systems, Measurement, and Control,* vol. 124, no. 1, pp. 158-167, 2002.

[68] X. Song, M. Ahmadian and S. Southward, "Analysis and Strategy for Superharmonics with Semiactive Suspension Control Systems," *Journal of Dynamic Systems, Measurement, and*

Control, vol. 129, no. 6, pp. 795-803, 2007.

[69] F. D. Goncalves and M. Ahmadian, "A Hybrid Control Policy for Semi-Active Vehicle Suspensions," *Shock and Vibration,* vol. 10, no. 1, pp. 56-69, 2003.

[70] C. Poussot-Vassal, C. Spelta, O. Sename, S. M. Savaresi and L. Dugard, "Survey on Some Automotive Semi-Active Suspension Control Methods: A Comparative Study on a Single-Corner Model," in *18th IFAC World Congress*, Milan, Italy, 2011.

[71] N. H. Amer, R. Ramli, W. N. L. Mahadi and M. A. Z. Abidin, "A Review on Control Strategies for Passenger Car Intelligent Suspension System," in *International Conference on Electrical, Control and Computer Engineering* , Pahang, Malaysia, 2011.

[72] H. Kwakernaak and R. Sivan, Linear Optimal Control Systems, John Wiley & Sons, 1972.

[73] A. G. Thompson, "An Active Suspension with Optimal Linear State Feedback," *Vehicle System Dynamics,* vol. 5, no. 4, pp. 187-203, 1976.

[74] A. Hac, "Suspension Optimization of a 2-DOF Vehicle Model Using a Stochastic Optimal Control Technique," *Journal of Sound and Vibration,* vol. 100, no. 3, p. 343–357, 1985.

[75] P. Gaspar, I. Szaszi and J. Bokor, "Design of Robust Controllers for Active Vehicle Suspension Using the Mixed Mu Synthesis," *Vehicle System Dynamics,* vol. 40, no. 4, pp. 193-228, 2003.

[76] M. Yamashita, K. Fujimori, K. Hayakawa and H. Kimura, "Application of H-infinity Control to Active Suspension," *Automatica ,* vol. 30, no. 11, pp. 1717-1729, 1994.

[77] K. Hayakawa, K. Matsumoto, M. Yamashita, Y. Suzuki and K. K. H. Jujimori, "Robust H-infinity - Output Feedback Control of Decoupled Automobile Active Suspension Systems," *Automatic Control, IEEE Transactions on,* vol. 44, no. 2, pp. 392 - 396, 1999.

[78] A. Zin, O. Sename, P. Gaspar, L. Dugard and J. Bokor, "Robust LPV - H-infinity control for active suspensions with performance adaptation in view of global chassis control," *Vehicle System Dynamics,* vol. 46, no. 10, pp. 889-912, 2008.

[79] R. S. Sharp and H. Peng, "Vehicle Dynamics Applications of Optimal Control Theory," *Vehicle System Dynamics,* vol. 49, no. 7, pp. 1073-1111, 2011.

[80] M. Canale, M. Milanese and C. Novara, "Semi-Active Suspension Control Using "Fast" Model-Predictive Techniques," *IEEE Transactions on Control Systems and Technology,* vol. 14, no. 6, pp. 1034-1046, 2006.

[81] K. Arunachalam, P. M. Jawahar and P. Tamilporai, "Active Suspensions System with Preview Control - A Review," *SAE Technical Paper 2003-28-0037,* 2003.

[82] E. K. Bender, "Optimum Linear Preview Control with Application to Vehicle Suspension,"

Journal of Basic Engineering, vol. 90, no. 2, pp. 213-221 , 1968.

[83] J. Marzbanrad, G. Ahmadi, H. Zohoor and Y. Hojjat, "Stochastic Optimal Preview Control of a Vehicle Suspension," *Journal of Sound and Vibration,* vol. 275, no. 3-5, p. 973–990, 2004.

[84] A. Hac, "Optimal Linear Preview Control of Active Vehicle Suspension," *Vehicle System Dynamics,* vol. 21, no. 1, pp. 167-195, 1992.

[85] A. Vahidi and A. Eskandarian, "Influence of Preview Uncertainties in the Preview Control of Vehicle Suspensions," *Part K: Journal of Multi-body Dynamics,* vol. 216, no. 4, pp. 295-301, 2002.

[86] C. Gohrle, A. Wagner, A. Schindler and O. Sawodny, "Active Suspension Controller Using MPC Based on Full-Car Model with Preview Information," in *American Control Conference (ACC)*, Fairmont Queen Elizabeth, Montréal, Canada, 2012.

[87] J. Cao, H. Liu, P. Li and D. J. Brown, "State of the Art in Vehicle Active Suspension Adaptive Control Systems Based on Intelligent Methodologies," *Intelligent Transportation Systems, IEEE Transactions on,* vol. 9, no. 3, pp. 392 - 405, 2008.

[88] J. S. Lin and I. Kanellakoopoulos, "Nonlinear Design of Active Suspensions," *Control Systems, IEEE,* vol. 17, no. 3, pp. 45-59, 1997.

[89] N. Karlsson, A. Teel and D. Hrovat, "A Backstepping Approach to Control of Active Suspensions," in *Proceedings of the 40th IEEE Conference an Decision and Contml*, Orlando, Florida, USA, 2001.

[90] N. Yagiz and Y. Hacioglu, "Backstepping Control of a Vehicle with Active Suspensions," *Control Engineering Practice,* vol. 16, no. 12, pp. 1457-1467, 2008.

[91] T. Fukao, A. Yamawaki and N. Adachi, "Nonlinear and H-Infinity Control of Active Suspension Systems with Hydraulic Actuators," in *Proceedings of the 38th IEEE conference on Decision and Control*, Pheonix, Arizona, USA, 1999.

[92] C. Kaddissi, J. Kenne and M. Saad, "Drive by Wire Control of an Electro-Hydraulic Active Suspension a Backstepping Approach," in *Proceedings of the 2005 IEEE Conference on Control Applications*, Toronto, Canada, 2005.

[93] A. Alleyne, P. D. Neuhaus and J. K. Hendrick, "Application of Nonlinear Control Theory to Electronically Controlled Suspensions," *Vehicle System Dynamics,* vol. 22, pp. 309-320, 1993.

[94] A. Alleyne and J. K. Hendrick, "Nonlinear Adaptive Control of Active Suspensions," *Control Systems Technology,* vol. 3, no. 1, pp. 94-101, 1995.

[95] T. Yoshimura, A. Kume, M. Kurimoto and J. Hino, "Construction of an active suspension system of a quarter car model using the concept of sliding mode control," *Journal of Sound and*

Vibration, vol. 239, no. 2, 2001.

[96] Y. M. Sam, J. H. Osman, M. Ruddin and A. Ghani, "A Class of Proportional-Integral Sliding Mode Control with Application to Active Suspension System," *System and Control Letters,* vol. 51, pp. 217-223, 2004.

[97] C. Poussot-Vassal, O. Sename, L. Dugard, P. Gaspar, Z. Szabo and J. Bokor, "A New Semi-Active Suspension Control Strategy Through LPV Technique," *Control Engineering Practice,* vol. 16, no. 12, p. 1519–1534, 2008.

[98] I. Fialho and G. J. Balas, "Road Adaptive Active Suspension Design Using Linear Parameter-Varying Gain-Scheduling," *Control Systems Technology, IEEE Transactions on,* vol. 10, no. 1, pp. 43 - 54, 2002.

[99] S.-J. Huang and H.-C. Chao, "Fuzzy Logic Controller for a Vehicle Suspension System," *Part D: Journal of Automobile Engineering,* vol. 214, no. 1, pp. 1-12, 2000.

[100] D. L. Guo, H. Y. Hu and J. Q. Yi, "Neural Network Control for a Semiactive Vehicle Suspension with a Magnetorheological Damper," *Journal of Vibration and Control,* vol. 10, no. 3, pp. 461-471, 2004.

[101] X. M. Dong, M. Yu, Z. Li, C. Liao and W. Chen, "Neural Network Compensation of Semi-Active Control for Magneto-Rheological Suspension with Time Delay Uncertainty," *Smart Materials and Structures,* vol. 18, no. 1, pp. 1-14, 2009.

[102] H. Metered, P. Bonello and S. O. Oyadiji, "An Investigation into the Use of Neural Networks for the Semi-Active Control of a Magnetorheologically Damped Vehicle Suspension," *Part D: Journal of Automobile Engineering,* vol. 224, no. 7, pp. 829-848, 2010.

[103] D. P. Stoten, J. Y. Tu and G. Li, "Synthesis and Control of Generalized Dynamically Substructured Systems," *Part I: Journal of Systems and Control Engineering,* vol. 223, pp. 371-392, 2009.

[104] A. R. Plummer, "Control techniques for structural testing: a review," *Part I: Journal of systems and Control Engineering,* vol. 221, no. Special Issue Paper, pp. 139-169, 2007.

[105] M. J. Hashemi and G. Mosqueda, "Innovative substructuring technique for hybrid simulation of multistory building collapse," *Earthquake Engineering and Structural Dynamics,* vol. 43, pp. 2059-2074, 2014.

[106] M. Nakashima, H. Kato and E. Takaoka, "Development of real-time pseudo dynamic testing," *Earthquake Engineering and Structural Dynamics,* vol. 21, pp. 79-92, 1992.

[107] A. Blakeborough, M. S. Williams, A. P. Darby and D. M. Williams, "The development of real-time substructure testing," *Philosophical Transactions of the Royal Society of London A,* vol. 359, pp. 1869-1891, 2001.

[108] D. P. Stoten and R. A. Hyde, "Adaptive Control of Dynamically Substructured Systems: The Single-Input Single-Output Case," *Part I: Journal of Systems and Control Engineering,* vol. 220, no. 2, pp. 63-79, 2006.

[109] P. A. Bonnet, M. S. Williams and B. A., "Compensation of Actuator Dynamics in Real-Time Hybrid Tests," *Part I: Journal of Systems and Control Engineering,* vol. 220, no. 2, pp. 251-264, 2006.

[110] D. P. Stoten, C. N. Lim and S. A. Neild, "Assesment of Controller Strategies for Real-time Dynamic Substructuring of a Lightly Damped System," *Part I: Journal of Systems and Control Engineering,* vol. 22, no. Special Issue Paper, pp. 235-250, 2007.

[111] M. I. Wallace, J. Sieber, S. A. Neild, D. J. Wagg and B. Wrauskopf, "Stability Analysis of Real-time Dynamic Substructuring using Delay Differential Equation Models," *Earthquake Engineering and Structural Dynamics,* vol. 34, pp. 1817-1832, 2005.

[112] M. I. Wallace, D. J. Wagg and S. A. Nield, "An Adaptive Polynomial Based Forward Prediction Algorithm for Multi-Actuator Real-Time Dynamic Substructuring," *Philosophical Transactions of the Royal Society of London A,* vol. 461, no. 2064, pp. 3807-3826, 2005.

[113] D. P. Stoten and J. Y. L. G. Tu, "Synthesis and Control of Generalized Dynamically Substructured Systems," *Part I: Journal of Systems and Control Engineering,* vol. 223, pp. 371-392, 2009.

[114] P. J. Gawthrop, M. I. Wallace, S. A. Neild and D. J. Wagg, "Robust real-time substructuring techniques for under-damped systems," *Structural Control and Health Monitoring,* vol. 14, pp. 591-608, 2007.

[115] M. Nasiri and M. Montzeri-Gh, "Time-Delay Compensation for Actuator-Based Hardware-in-the-Loop Testing of a Jet Engine Fuel Control Unit," *Part I: Journal of Systems and Control Engineering,* vol. 226, no. 10, pp. 1371-1380, 2012.

[116] T. Horiuchi, M. Nakagawa, M. Sugan and T. Konno, "Development of real-time hybrid experimental system with actuator delay compensation," in *Proceedings of the 11th World Conference on Earthquake engineering*, Acapulco, Mexico, 1996.

[117] T. Horiuchi and T. Konno, "A new method for compensating actuator delay in real-time hybrid experiments," *Philosophical Transactions of the Royal Scoiety of London A,* vol. 359, pp. 1893-1909, 2001.

[118] W. R. Kruger and W. Kortum, "Design of Control Laws for Alleviation of Ground - Induced Vibrations," in *RTO AVT Specialists' Meeting on "Structural Aspects of Flexible Aircraft Control"*, Ottawa, Canada, 1999.

[119] D. Y. Lee, Y. J. Nam, R. Yamane and M. K. Park, "Performance Evaluation on Vibration Control of MR Landing Gear," in *11th Conference on Electrorheological Fluids and Magnetorheological Suspensions*, 2009.

[120] N. S. Currey, Aircraft Landing Gear Design - Principles and Practices, American Institute of Aeronautics and Astronautics, 1988.

[121] P. Eamcharoenying, "Friction compensation for a force controlled electric actuator with unknown sinusoidal disturbance motion," in *UKACC International Conference on Control*, Loughborough, United Kingdom, 2014.

[122] H. Olsson, K. Aastrom, D. C. Canudas, M. Gafvert and P. Lischinsky, "Friction Models and Fiction Compensation," *European Journal of Control,* vol. 4, no. 3, p. 176–195, 1998.

[123] N. Bernstein, D. Lawrence and L. Pao, "Friction Modelling and Compensation for Haptic Interfaces," in *Proceedings of the First Joint Eurohaptics Conference and Symposium on Haptic Interfaces for Virtual Environment and Teleoperator Systems*, 2005.

[124] Y. Wang, Z. Xiong and H. Ding, "Robust Controller Based on Friction Compensation and Disturbace Observer for a Motion Platform Driven by a Linear Motor," *Part I: Journal of Systems and Control Engineering,* vol. 210, no. 1, pp. 33-39, 2006.

[125] G. S. Chen, X. S. Mei and T. Tao, "Friction Compensation Using a Double Pulse Method for a High-Speed High-Precision Table," *Part C: Journal of Mechanical Engineering Science,* vol. 225, no. 5, pp. 1263-1272, 2011.

[126] Y. Zhang, G. Liu and A. A. Goldenberg, "Friction compensation with estimated velocity. Robotics and Automation," in *Proceedings. ICRA '02. IEEE International Conference on* , 2002.

[127] K. Mitsunaga and T. Matsuo, "Adaptive Compensation of Friction Forces with Differential Filter," *International Journal of Computers, Communications & Control,* vol. 3, no. 1, pp. 80-89, 2008.

[128] G. Borghesan and C. Melchiorri, "Model and Modeless Friction Compensation: Application to a Defective Haptic Interface," *Lecture Notes in Computer Science ,* vol. 5024, pp. 94-103, 2008.

[129] J. Yao, Z. Jiao and B. Yao, "Robust Control for Static Loading of Electro-hydraulic Load Simulator with Friction Compensation," *Chinese Journal of Aeronautics,* vol. 25, no. 6, pp. 954-962, 2012.

[130] M. Iwasaki, T. Shibata and N. Matsui, "Disturbance-Observer-Based Nonlinear Friction Compensation in Table Drive System," *Mechatronics, IEEE/ASME Transactions on,* vol. 4, no. 1, pp. 3-8, 1999.

[131] H. S. Ahn, C. Y. Q. and H. Dou, "State-Periodic Adaptive Compensation of Cogging and Coulomb Friction in Permanent Magnet Linear Motors," *Magnetics, IEEE Transactions on,* vol. 41, no. 1, pp. 90-98, 2005.

[132] S. L. Chen, K. K. Tan and S. Huang, "Modeling and Compensation of Ripples and Friction in Permanent-Magnet Linear Motor Using a Hysteretic Relay," *Mechatronics, IEEE/ASME*

Transactions on, vol. 15, no. 4, pp. 586-594, 2010.

[133] K. K. Tan, S. N. Huang and T. H. Lee, "Robust Adaptive Numerical Compensation for Friction and Force Ripple in Permanent-Magnet Linear Motors," *Magnetics, IEEE Transactions on,* vol. 38, no. 1, pp. 221-228, 2002.

[134] E. W. Weisstein, CRC Consise Encyclopedia of Mathematics, Chapman and Hall/CRC, 2003.

[135] K. J. Astrom and T. Hagglund, Advanced PID Control, ISA, 2006.

[136] M. N. Sahinkaya, M. O. Cole and C. R. Burrows, "On the use of Schroeder Phased Haromonic Sequences in multi-frequency vibration control of flexible rotor/magnetic bearing systems," in *8th International Symposium on Magnetic Bearings*, Mito, Japan, 2002.

[137] S. M. Savaresi, E. Silani, S. Bittanti and M. Porciani, "On Performance Evaluation Methods and Control Strategies for Semi-Active Suspension Systems," in *Proceedings of the 42nd IEEE Conference on Decision and Control*, Hawaii, 2003.

[138] L. Wu and W. J. Zhang, "Heirarchical Modelling of Semi-Active Control of a Full Motorcycle Suspension with Six Degrees of Freedom," *International Journal of Automotive Technology,* vol. 11, no. 1, pp. 27-32, 2010.

Appendix A

Appendix A1 – Quarter Car MIL Suspension Parameters Variation Analysis

Appendix A1.1 Variation of Time Constant

The systems parameters are chosen to match the one mass case and is shown in Table A1.1. Two cases are considered with a sprung mass damping ratio of 1 and 0.5.

	Variable Parameter: $\tau = 0.001s \; to \; 1s$	
	Case 1	**Case 2**
Sprung Mass Damping Ratio	1	0.5
$m_s \; (kg)$	50	50
$k_s \; (N/m)$	500	500
$b_s \; (Ns/m)$	316.2	158.1
$m_u \; (kg)$	50	50
$k_t \; (N/m)$	500	500
$b_t \; (Ns/m)$	0	0

Table A1.1 - Parameters for variation of time constant for suspension MIL system.

The root locus for variation of time constant of a two mass MIL system has many similarities with the single mass case. As the time constant increases the system becomes unstable as shown in Figure A1.3 and Figure A1.5. Like in the one mass case, at the stability boundary the two mass system behaves like itself but with no suspension damping. For an ideal two mass system there will always be a pair of conjugate poles representing the body hop mode regardless of damping ratio. Beyond a critical damping ratio the wheel hop mode becomes overdamped and exhibits no frequency component. For comparison purposes with the one mass system, the damping ratio for the sprung mass is kept the same from Section 5.2.

For Case 1 the root locus plot is shown in Figure A1.1 - A1.3. Here the wheel hop mode of the ideal two mass system is overdamped as shown by the two ideal poles which are apart in Figure A1.5. For small delay time constants the MIL system wheel hop mode is critically damped, and all poles closely resemble the ideal system. The additional pole introduced by the delay filter is not dominant and lies on the far left of the root locus. As the time delay increases the additional filter pole and one of the wheel hop poles approach each other until they coincide and then break away. The root locus loop shape of the wheel hop frequency break away curve is similar to that seen for a critically damped one mass MIL system. Eventually both wheel hop and body hop poles move to the right and become unstable with larger delay time constants.

For Case 2 the root locus plot is shown in Figure A1.4 and A1.5 the MIL system resembles the ideal system at small time delays with the additional filter pole being non-dominant. As the time delay increases all system poles move to the right. Eventually both the wheel hop and body hop poles become unstable together with sufficient time delay.

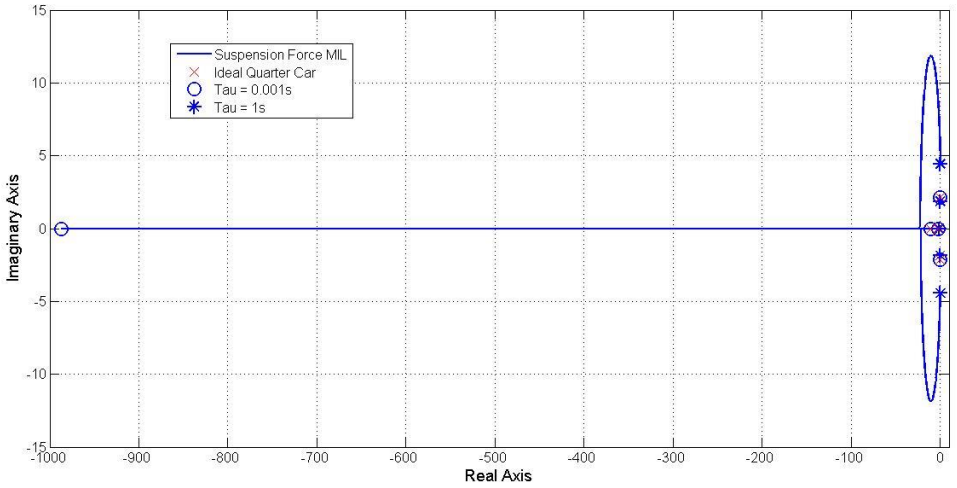

Figure A1.1 – Case 1: Root locus plot for variation of time constant with sprung mass damping ratio of 1.

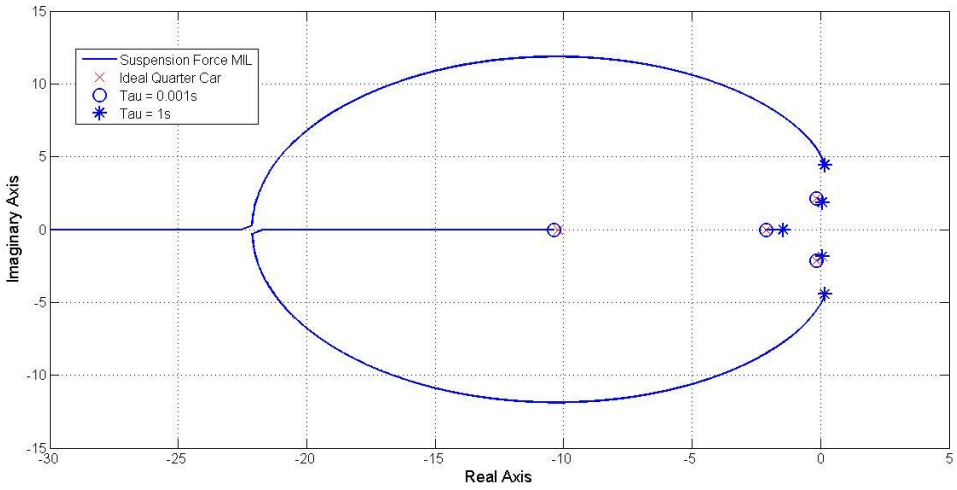

Figure A1.2 – Case 1: Exploded view of root locus plot for variation of time constant with sprung mass damping ratio of 1.

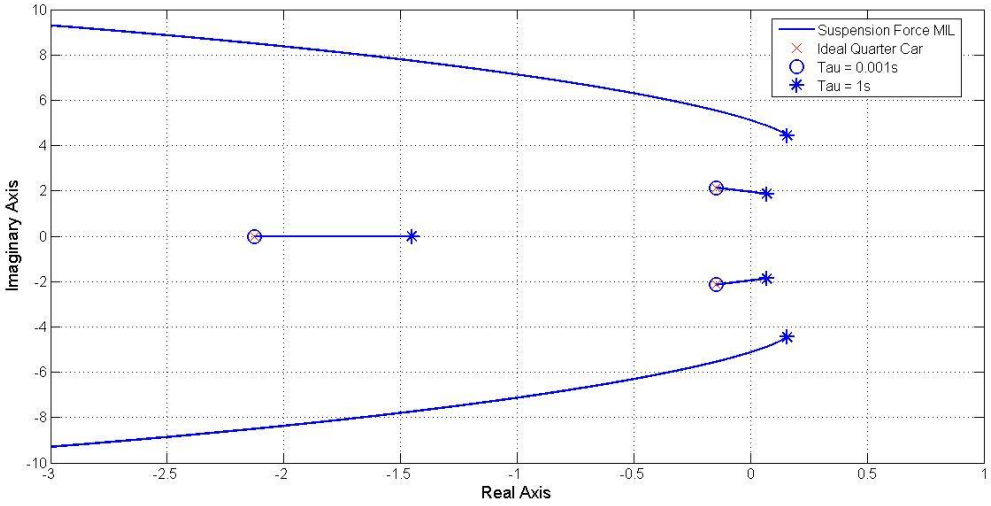

Figure A1.3 – Case 1: Exploded view of root locus plot for variation of time constant with sprung mass damping ratio of 1.

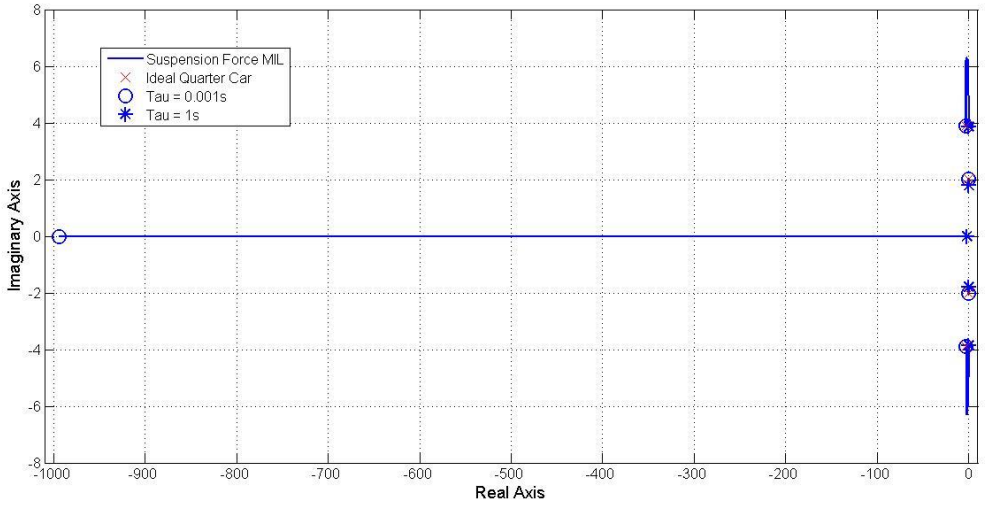

Figure A1.4 – Case 2: Root locus plot for variation of time constant with sprung mass damping ratio of 0.5.

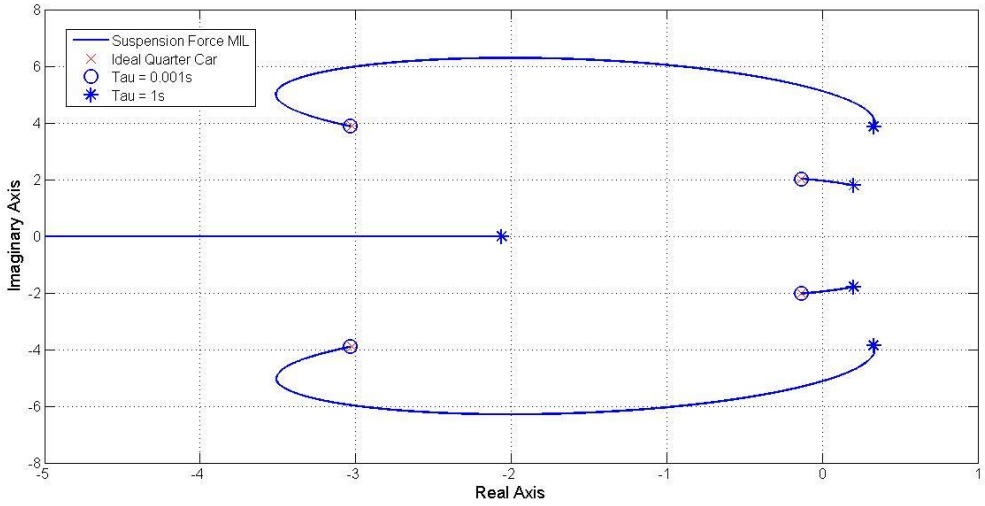

Figure A1.5 – Case 2: Exploded view of root locus plot for variation of time constant with sprung mass damping ratio of 0.5.

Appendix A1.2 Variation of Sprung Mass Natural Frequency

The systems parameters for natural frequency variation are shown below in Table A1.2.

	Variable Parameter: $k_s = 1N/m \ to \ 100000N/m$			**Variable Parameter:** $k_s = 1N/m \ to \ 1000000N/m$		
	Case 1	**Case 2**	**Case 3**	**Case 4**	**Case 5**	**Case 6**
Sprung Mass Damping Ratio	1	1.5	0.5	1	1.5	0.5
$m_s \ (kg)$	50	50	50	50	50	50
$m_u \ (kg)$	50	50	50	50	50	50
$k_t \ (N/m)$	500	500	500	500	500	500
$b_t \ (Ns/m)$	0	0	0	0	0	0
$\tau \ (s)$	0.2	0.2	0.2	0.01	0.01	0.01

Table A1.2 - Parameters for variation of sprung mass natural frequency for suspension MIL system.

The root locus of Case 1, 2 and 3 are shown in Figure A1.6-A1.11. For all three cases the resemblance to the ideal case is greatest when the natural frequency is low, as the natural frequency increases both the wheel hop and body hop modes moves towards the right and becomes unstable. Although it is not so clear from Figure A1.7, A1.9 and A1.11 that the body hop mode is unstable at high frequency, the body hop poles have a positive real part at the natural frequency of 44.72 rad/s. This result is expected and is in agreement with findings from the single mass system.

For the critically and overdamped cases of Case 1 and 2 the ideal wheel hop modes are overdamped and has no frequency component. However in these cases the MIL system wheel hop pole always is underdamped. The increase of natural frequency results a break away point such that a pair of conjugate poles for the body hop mode develops.

The root locus of Case 4, 5 and 6 are shown in Figure A1.12-A1.14 respectively. With a smaller time delay, a higher natural frequency is required to produce instability. When compared to the Case 1

and 2, the smaller time delay in Case 3 and 4 forces the break away point further towards the left of the root locus. This means that with a smaller delay the MIL system can resemble the ideal system at much higher natural frequencies. However at frequencies beyond the break away point the resemblance starts to deteriorate rapidly and the high frequencies introduced from the break away point could cause instability if the controller sampling rate is insufficient. As the natural frequency increases the poles from the break away points move rightwards in a trajectory of increasing frequency. This shows that even at small delays the MIL system could only precisely resemble the ideal system if the natural frequency of the system is not too high. All of these root locus plots also confirm that the cases with higher sprung mass damping ratio are more stable compared to low damping ratios.

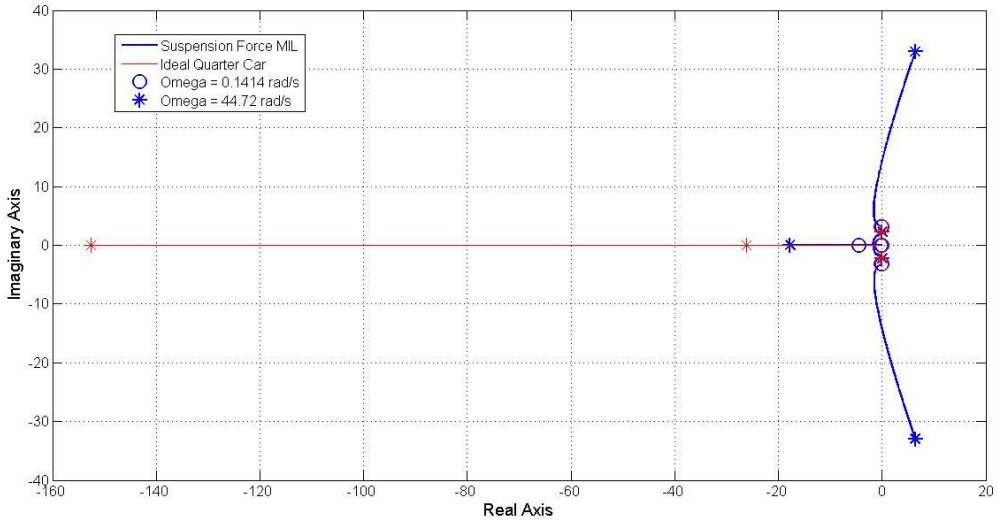

Figure A1.6 – Case 1: Root locus of natural frequency variation for critical damping ratio, $\tau = 0.2s$.

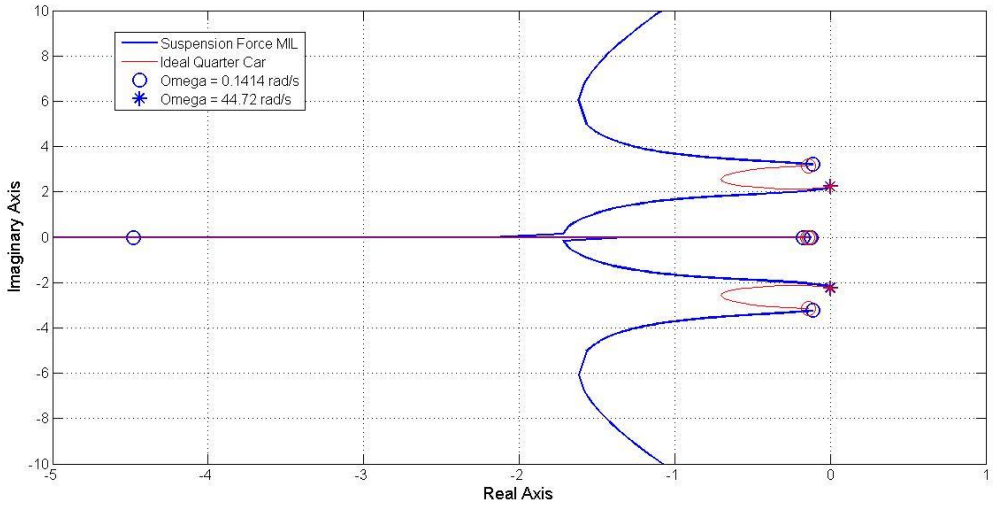

Figure A1.7 – Case 1: Exploded view root locus of natural frequency variation for critical damping ratio, $\tau = 0.2s$.

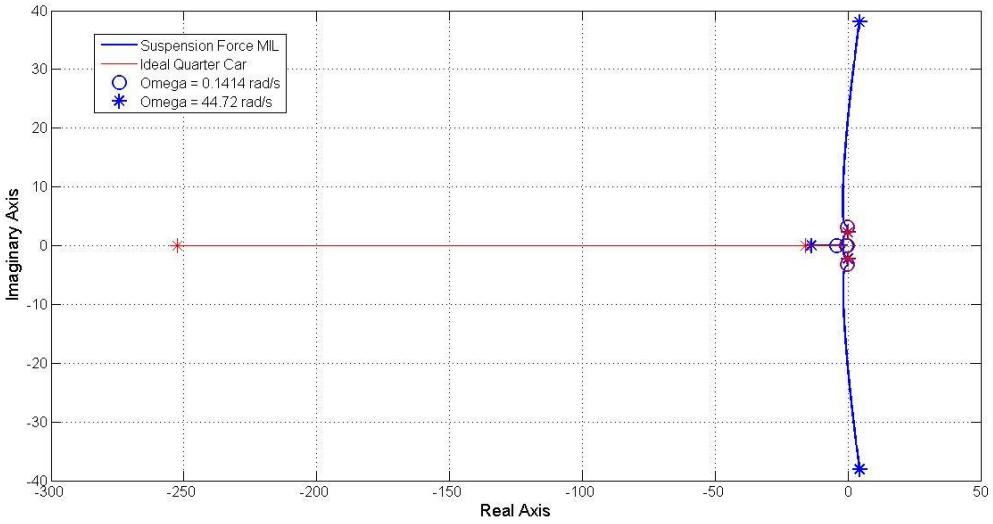

Figure A1.8 – Case 2: Root locus of natural frequency variation for over damped system, $\tau = 0.2s$.

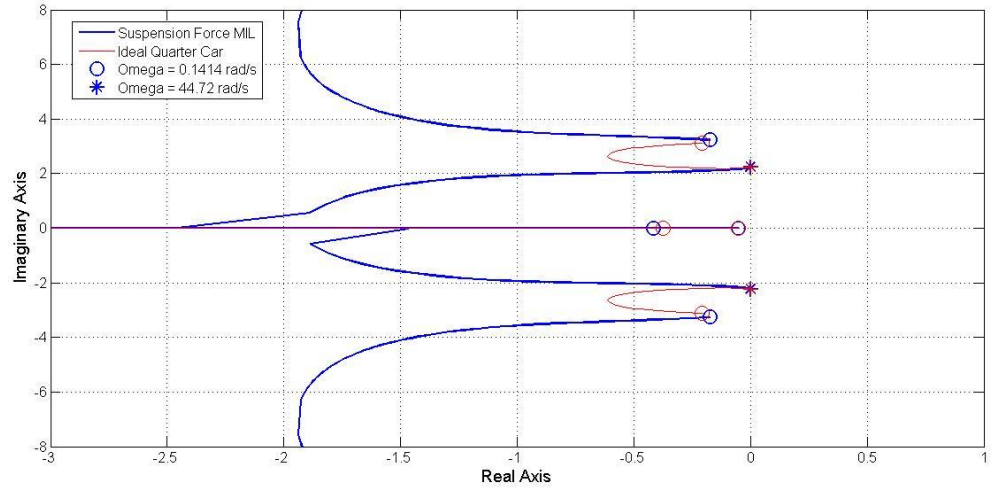

Figure A1.9 – Case 2: Exploded view root locus of natural frequency variation for over damped system, $\tau = 0.2s$.

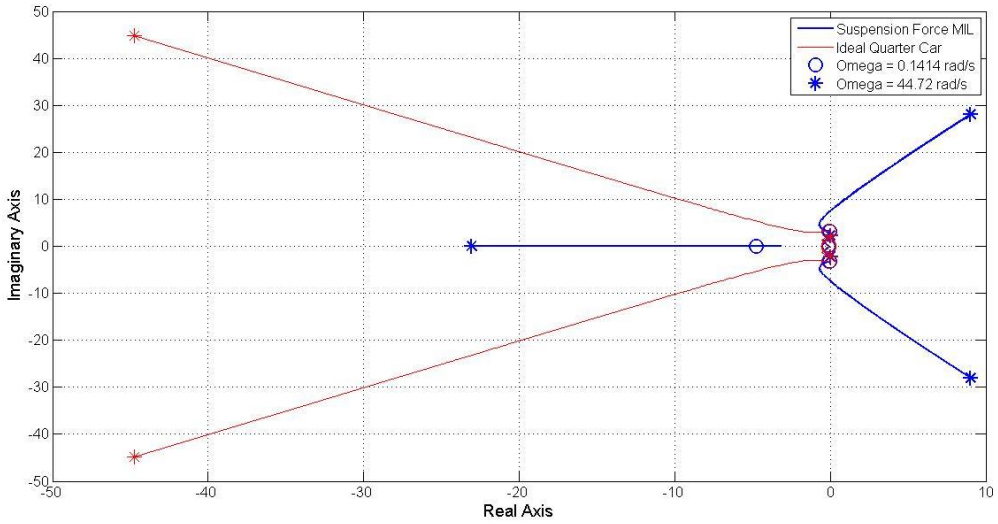

Figure A1.10 – Case 3: Root locus of natural frequency variation for underdamped system, $\tau = 0.2s$.

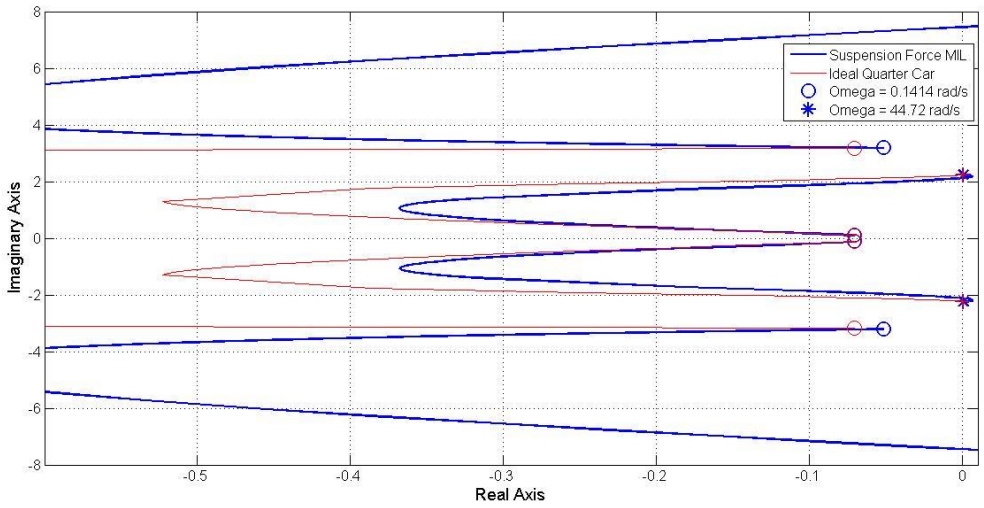

Figure A1.11 – Case 3: Exploded view root locus of natural frequency variation for underdamped system, $\tau = 0.2s$.

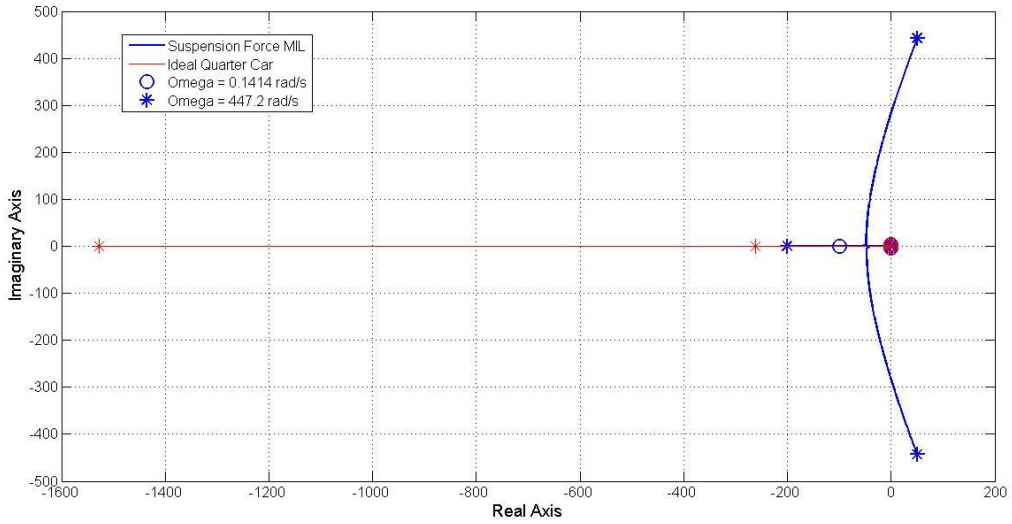

Figure A1.12 – Case 4: Root locus of natural frequency variation for critical damping ratio, $\tau = 0.01s$.

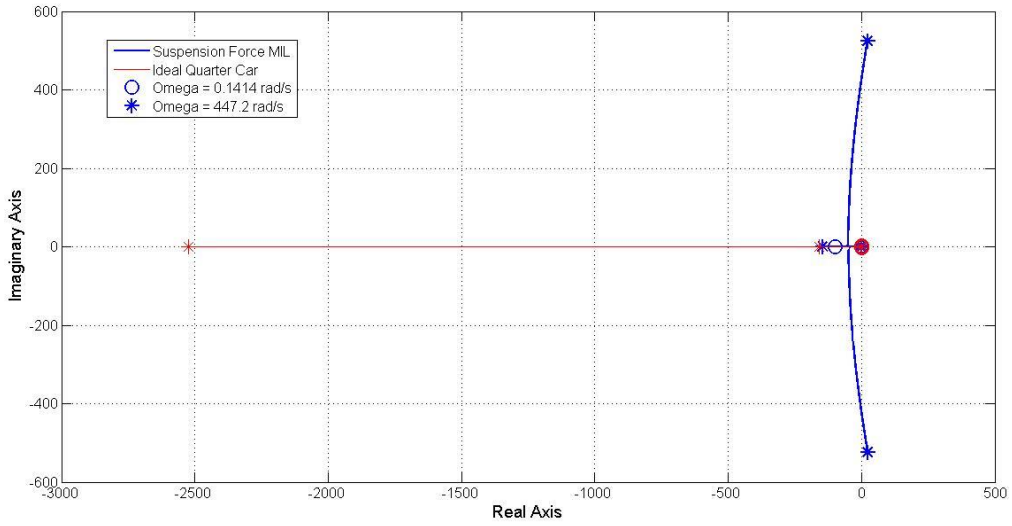

Figure A1.13 – Case 5: Root locus of natural frequency variation for over damped system, $\tau = 0.01s$.

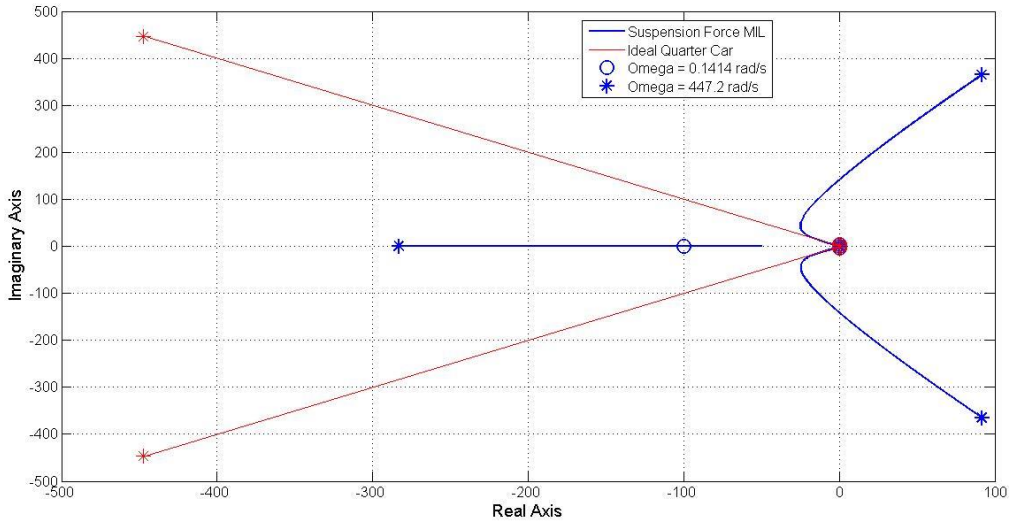

Figure A1.14 – Case 6: Root locus of natural frequency variation for under damped system, $\tau = 0.01s$.

Appendix A1.3 Variation of Sprung Mass Damping Coefficient

The systems parameters for damping coefficient variation are shown below in Table A1.3.

	Variable Parameter: $k_s = m_s = 1 \ \ to \ \ 100000$		
	Case 1	**Case 2**	**Case 3**
$b_s \ (Ns/m)$	100	100	100
$b_u \ (Ns/m)$	0	0	0
$k_t \ (N/m)$	500	500	500
$m_u \ (kg)$	50	50	50
$\tau \ (s)$	0.2	0.01	0.001

Table A1.3 - Parameters for variation of sprung mass damping coefficient for suspension MIL system.

The root locus for Case 1, 2 and 3 are shown in Figure A1.15 – A1.18. The ideal system response seen in Figure A1.16 shows that at high damping ratios the wheel hop mode is overdamped, indicated by the lack of an imaginary component, while the body hop mode is underdamped.

For a large time delay constant of 0.2s the root locus is shown in Figure A1.15 and A1.16. Here for all values of sprung mass damping ratio the MIL system does not represent the ideal system well as the locations of poles differ markedly. At very low values of the sprung mass damping ratio both the wheel and body hop poles become unstable as they eventually move to the right of the root locus. Another interesting observation is that, like the single mass MIL case, there is a vertical asymptote of the wheel hop poles which occurs at high sprung mass damping ratios, this leads to high frequencies which could cause instability if closed loop control sampling rate is insufficient.

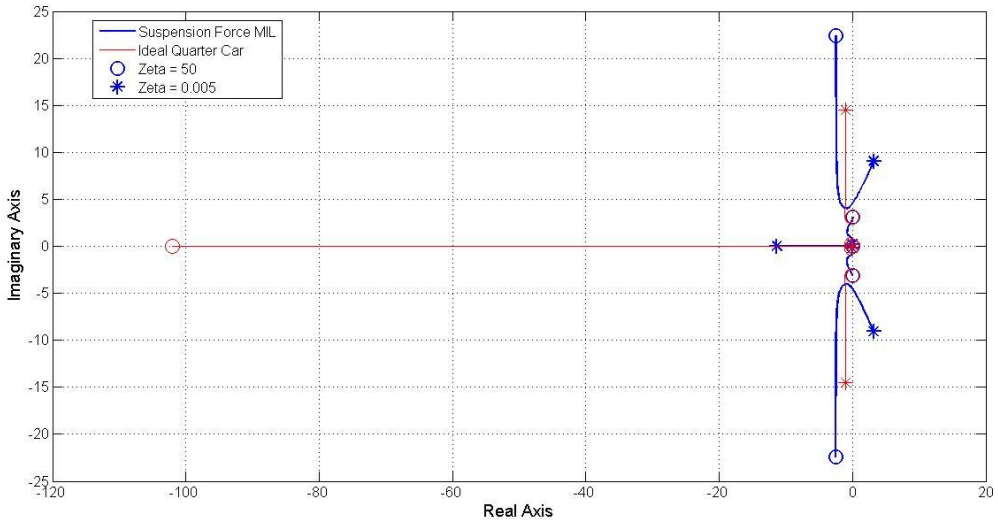

Figure A1.15 – Case 1: Root locus of sprung mass damping ratio variation, $\tau = 0.2s$.

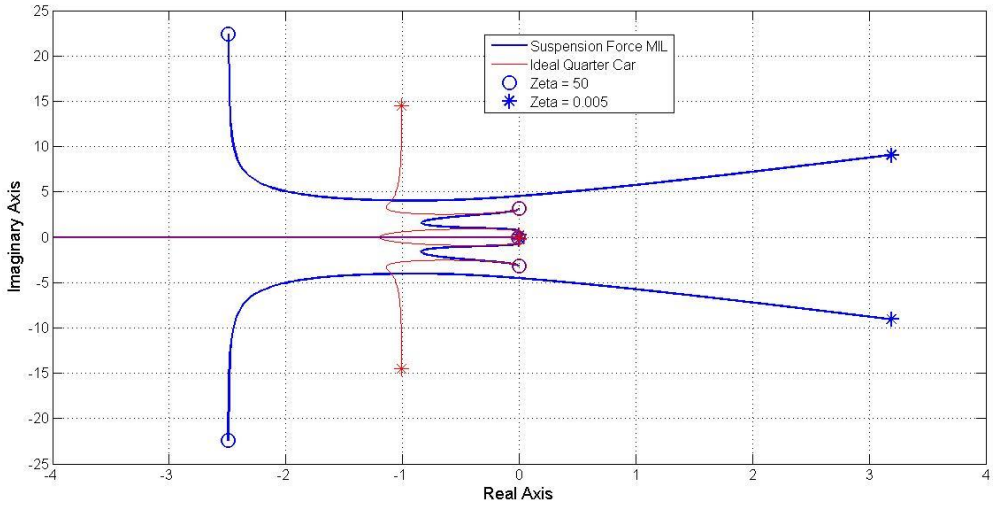

Figure A1.16 – Case 1: Exploded view root locus of sprung mass damping ratio variation, $\tau = 0.2s$.

Figure A1.17 shows the root locus for a smaller time delay of 0.01s. Like in the single mass case, a smaller time delay improves the performance of the MIL substantially and also shifts the vertical asymptote that occurs at high sprung mass damping ratio further to the left of the root locus. At low sprung mass damping ratios both wheel hop and body hope pole approaches instability as both body and wheel hop poles move to the right.

Figure A1.18 shows the root locus for the case of very small time delay of 0.001s. The plot shows all the poles matching up to a higher degree and the additional pole introduced by the filter is not displayed in the plot as it lies much further left on the root locus. In the same manner as the other Cases, the resemblance to the ideal system deteriorates as the sprung mass damping ratio decreases, and this can be seen clearly from the wheel hop poles.

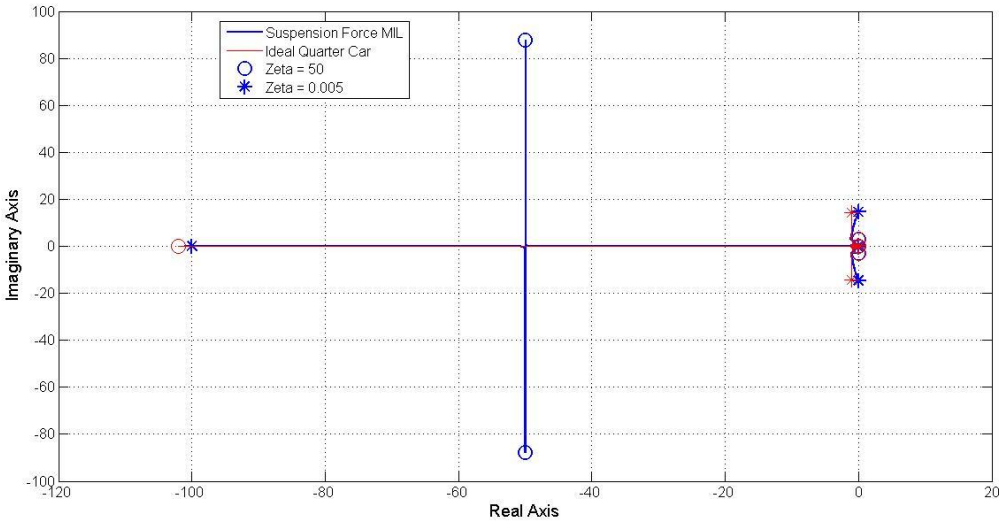

Figure A1.17 – Case 2: Root locus of sprung mass damping ratio variation, $\tau = 0.01s$.

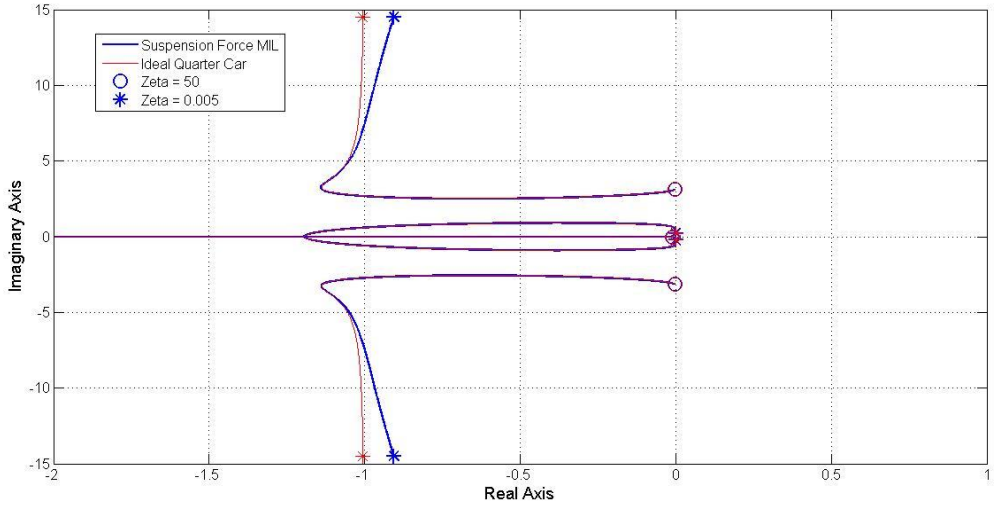

Figure A1.18 – Case 3: Root locus of sprung mass damping ratio variation, $\tau = 0.001s$.

Appendix A1.4 Variation of Tyre Stiffness

The systems parameters for damping coefficient variation are shown below in Table A1.4.

	Variable Parameter: $k_t = 0.01 \ \ to \ \ 100000 \ N/m$	
	Case 1	**Case 2**
$m_s \ (kg)$	50	50
$k_s \ (N/m)$	500	500
$b_s \ (Ns/m)$	100	100
$m_u \ (kg)$	50	50
$b_t \ (Ns/m)$	0	0
$\tau \ (s)$	0.333	0.01

Table A1.4 - Parameters for variation of tyre stiffness for suspension MIL system.

The plots for Case 1 and 2 are shown in Figure A1.19 and A1.20 respectively. The plots show that any magnitude of tyre stiffness cannot cause system instability, if the single mass system is itself stable on its own. The MIL system has greatest resemblance with the ideal system if the tyre stiffness is small. As the tyre stiffness increases the MIL wheel hop mode poles starts to move towards the right and deviate from the ideal wheel mode response, however this would never lead to instability as it is approaching a limit at real part equal to zero. It makes sense that high tyre stiffness would lead to performance deterioration since it is increasing the wheel hop frequency which then requires a smaller MIL time delay for the response to resemble the ideal system.

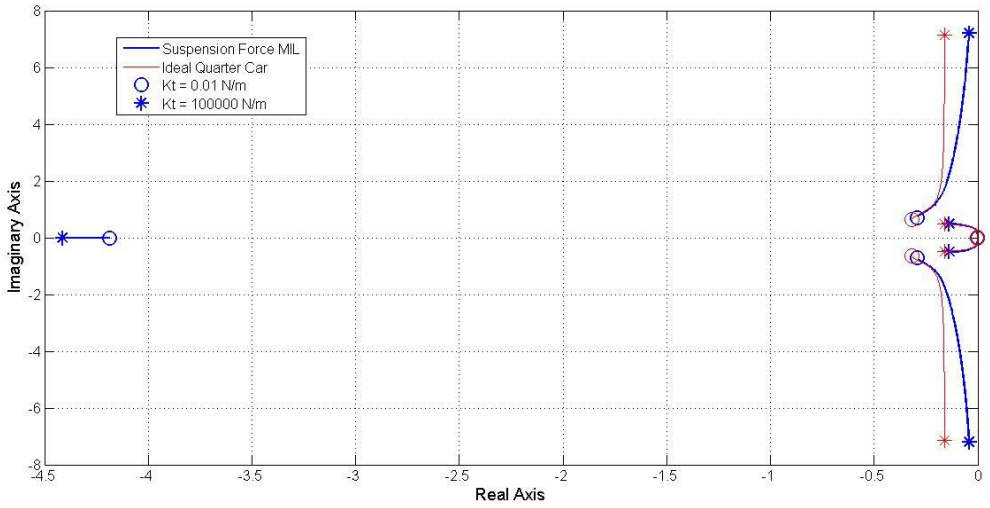

Figure A1.19 – Case 1: Root locus of tyre stiffness variation, $\tau = 0.333s$.

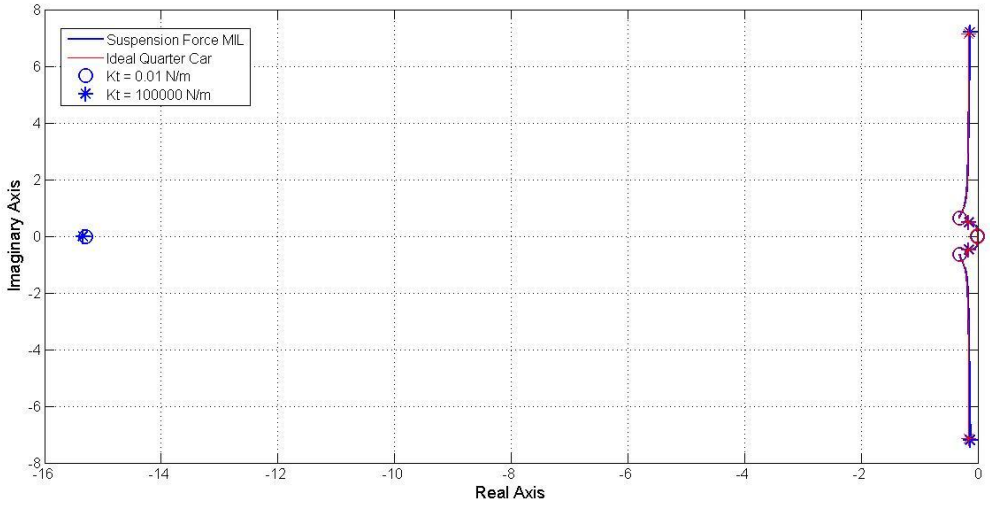

Figure A1.20 – Case 2: Root locus of tyre stiffness variation, $\tau = 0.01s$.

Appendix A1.5 Variation of Wheel Mass

The systems parameters for damping coefficient variation are shown below in Table A1.5.

	Variable Parameter: $m_u = 0.01 \ \ to \ \ 100000 \ \ kg$	
	Case 1	**Case 2**
$m_s \ (kg)$	50	50
$k_s \ (N/m)$	500	500
$b_s \ (Ns/m)$	100	100
$k_t \ (N/m)$	500	500
$b_t \ (Ns/m)$	0	0
$\tau \ (s)$	0.333	0.01

Table A1.5 - Parameters for variation of wheel mass inertia for suspension MIL system.

The plots for Cases 1 and 2 are shown in Figure A1.21 and A1.22 respectively. Both plots show that the system is stable for the range of masses, confirming that the single mass system will remain stable regardless of the unsprung mass. At large value of unsprung mass the MIL system closely resembles the ideal system. An asymptote tending to infinite frequency is present for low values of unsprung mass. For larger time delays the asymptote is occurs further to the left of the root locus and has a higher frequency for the same unsprung mass. It is expected that low values of unsprung mass will deteriorate the MIL performance as it increases the natural frequency of the wheel hop mode and therefore requires a smaller time delay.

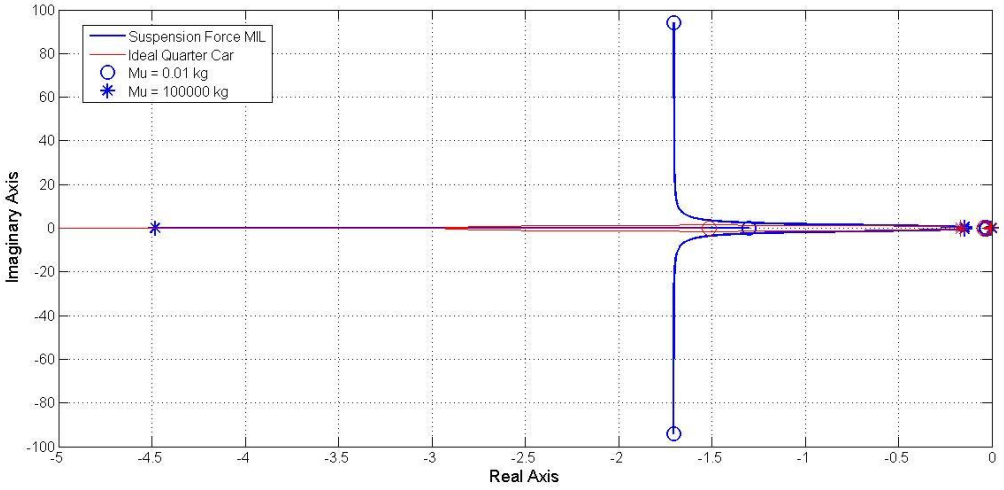

Figure A1.21 – Case 1: Root locus of unsprung mass variation, $\tau = 0.333s$.

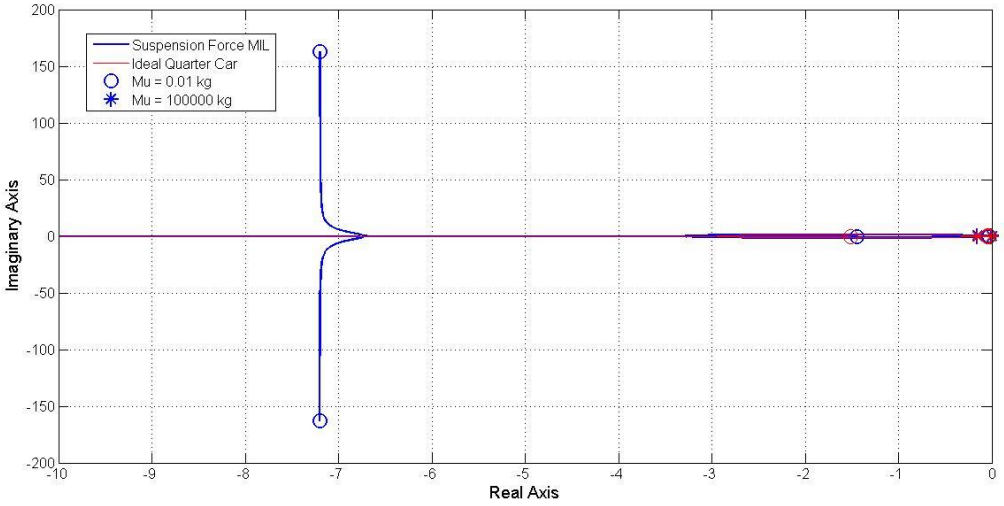

Figure A1.22 – Case 2: Root locus of unsprung mass variation, $\tau = 0.01s$.

Appendix A2 – Quarter Car MIL Vehicle Structure Parameters Variation

Appendix A2.1 Variation of Time Delay

The systems parameter chose are shown below in Table A2.1.

	Variable Parameter: $\tau = 0.001s \; to \; 1s$	
	Case 1	**Case 2**
Sprung Mass Damping Ratio	1	0.5
$m_s \; (kg)$	50	50
$k_s \; (N/m)$	500	500
$b_s \; (Ns/m)$	316.2	158.1
$m_u \; (kg)$	50	50
$k_t \; (N/m)$	500	500
$b_t \; (Ns/m)$	0	0

Table A2.1 - Parameters for variation of delay time constant for vehicle structure MIL system.

The root locus plots for Cases 1 and 2 are shown in Figure A2.1 and A2.2 respectively. Both figures have two real poles starting at time constant of 0.001s on the far left of the root locus which is not shown in the plot. At small time constants the MIL system closely resembles the ideal system for both sprung mass ratios. The breakaway point in Figure A2.1 which occurs as time constant increases is in agreement with previous findings for the suspension MIL case where the effect of increased time constant reduces the apparent damping of the wheel hop mode, such that the system changes from being overdamped to underdamped. As the time constant increases further both wheel and body hop poles move towards the right of the root locus but only the body hop pole becomes unstable. This is unlike the suspension MIL where both wheel and body hop poles become unstable together. A possible reason for this difference is that the vehicle structure MIL only acts on the sprung mass, while the suspension MIL acts on both sprung and unsprung masses, hence for the vehicle structure MIL only the sprung mass mode can become unstable.

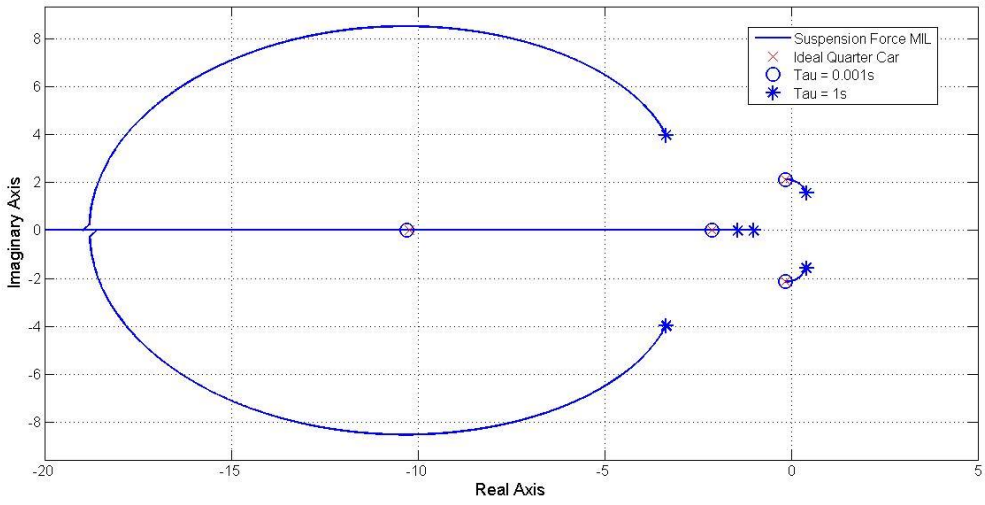

Figure A2.1 – Case 1: Root locus of time constant variation for sprung mass damping ratio of 1.

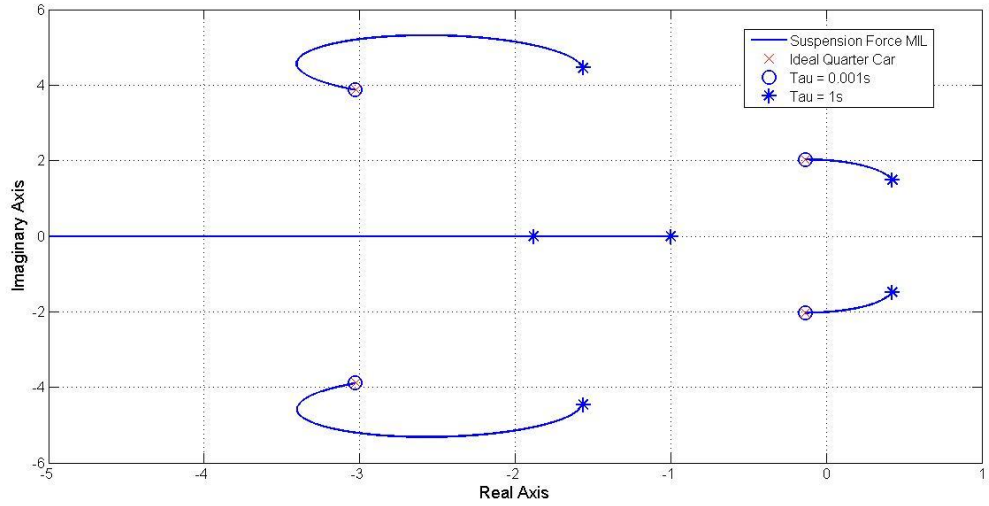

Figure A2.2 – Case 2: Root locus of time constant variation for sprung mass damping ratio of 0.5

Appendix A2.2 Variation of Sprung Mass Natural Frequency

The systems parameters for natural frequency variation are shown below in Table A2.2.

	Variable Parameter: $k_s = 1N/m \; to \; 100000N/m$			**Variable Parameter:** $k_s = 1N/m \; to \; 1000000N/m$		
	Case 1	**Case 2**	**Case 3**	**Case 4**	**Case 5**	**Case 6**
Sprung Mass Damping Ratio	1	1.5	0.5	1	1.5	0.5
$m_s \; (kg)$	50	50	50	50	50	50
$m_u \; (kg)$	50	50	50	50	50	50
$k_t \; (N/m)$	500	500	500	500	500	500
$b_t \; (Ns/m)$	0	0	0	0	0	0
$\tau \; (s)$	0.2	0.2	0.2	0.01	0.01	0.01

Table A2.2 - Parameters for variation of sprung mass natural frequency for vehicle structure MIL system.

Root locus plots for Case 1, 2 and 3 are shown in Figure A2.3, A2.4 and A2.5 respectively. As expected the three plots show that poles of the system resemble the ideal system at low frequencies. At high natural frequencies the body hop pole becomes unstable but the wheel hop pole does not, as shown for MIL vehicle structure system in Section A2.1. For all the critically and over damped sprung mass cases, the MIL body hop poles remains on the ideal body hop root locus trajectory, this is unlike the suspension MIL.

For sprung mass damping ratio of 1 shown in Figure A2.3, as the natural frequency increases the wheel hop poles break away from the real axis, and instead of moving towards the right of the root locus as in the suspension MIL, the wheel hop poles move towards the left and approaches an asymptote.

For sprung mass damping ratio of 1.5 shown in Figure A2.4 the wheel hop pole also breaks away towards the left of the root locus as natural frequency increases. However for this case the break away does not approach an asymptote but forms a loop and the poles break in back on to the real axis.

For sprung mass damping ratio of 0.5 shown in Figure A2.5 the wheel hop poles diverge from the ideal response as frequency increases, but the diveregence is a lot less when compared to the suspension MIL. This is because the wheel hop poles approaches an asymptote that is moving to the left of the root locus, as opposed to moving to the right for the suspension MIL.

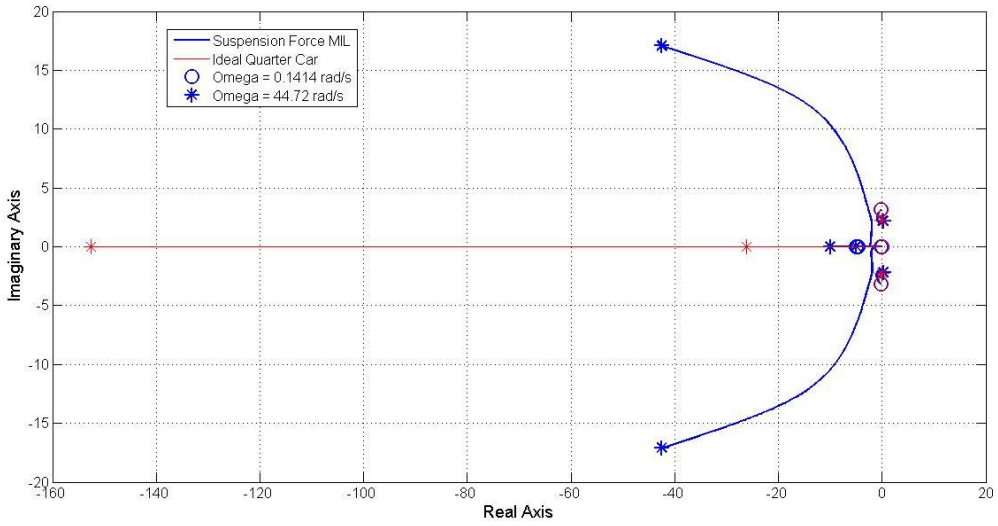

Figure A2.3 – Case 1: Root locus of natural frequency variation for sprung mass damping ratio of 1 and $\tau = 0.2s$.

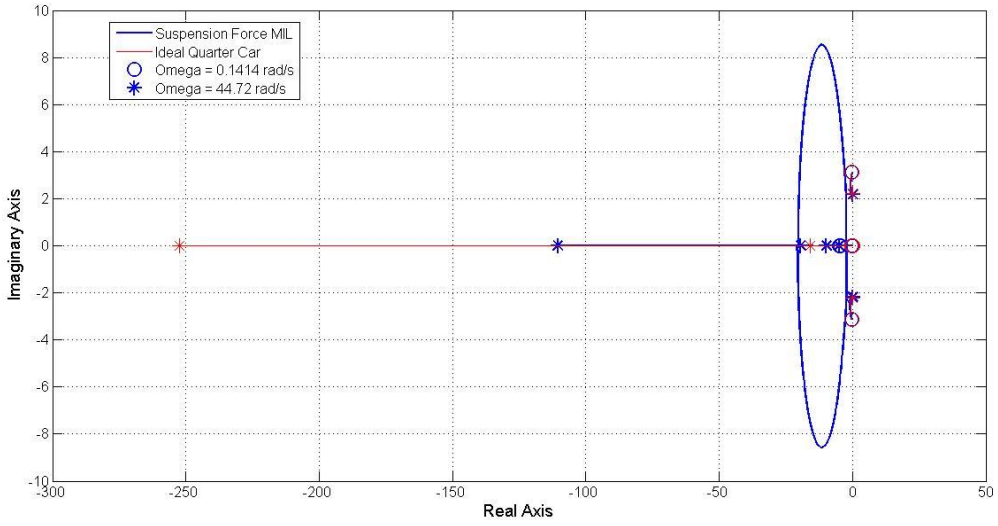

Figure A2.4 – Case 2: Root locus of natural frequency variation for sprung mass damping ratio of 1.5 and $\tau = 0.2s$.

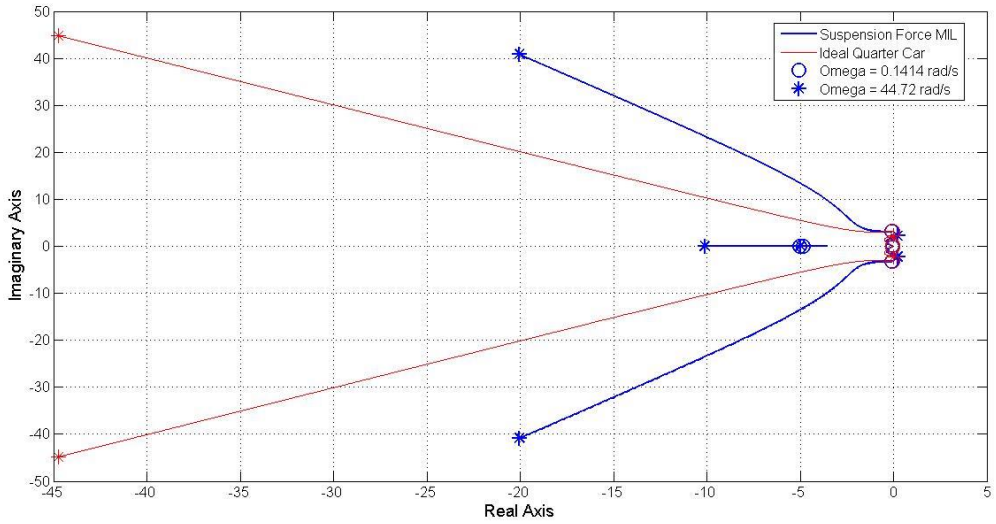

Figure A2.5 – Case 3: Root locus of natural frequency variation for sprung mass damping ratio of 0.5 and $\tau = 0.2s$.

Root locus plots for Case 3, 4 and 5 are shown in Figure A2.6, A2.7 and A2.8 respectively. The root locus plots here show the same shape as Case 1,2 and 3. As in the suspension MIL system, the effect of smaller time delay is that the break away point of the wheel hop mode is shifted towards the left of the root locus.

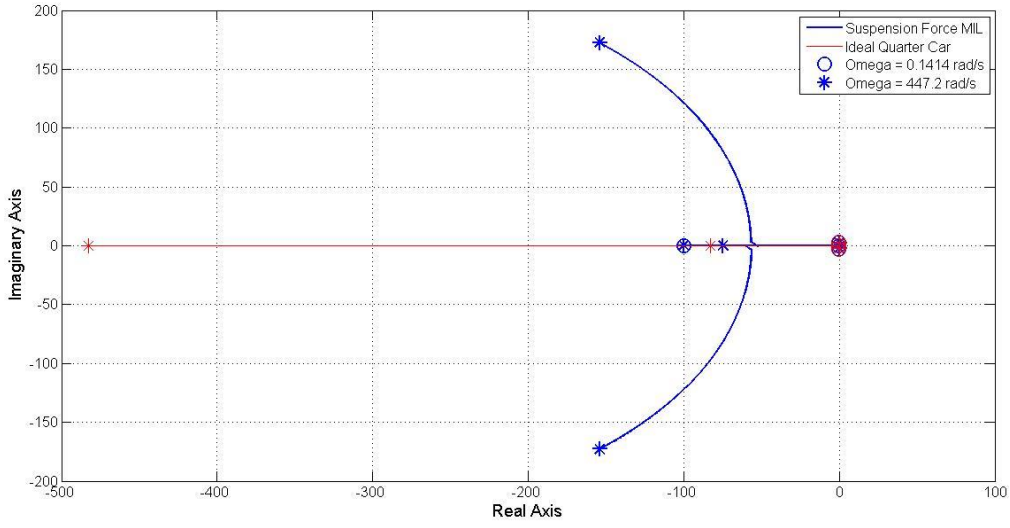

Figure A2.6 – Case 4: Root locus of natural frequency variation for sprung mass damping ratio of 1 and $\tau = 0.01s$.

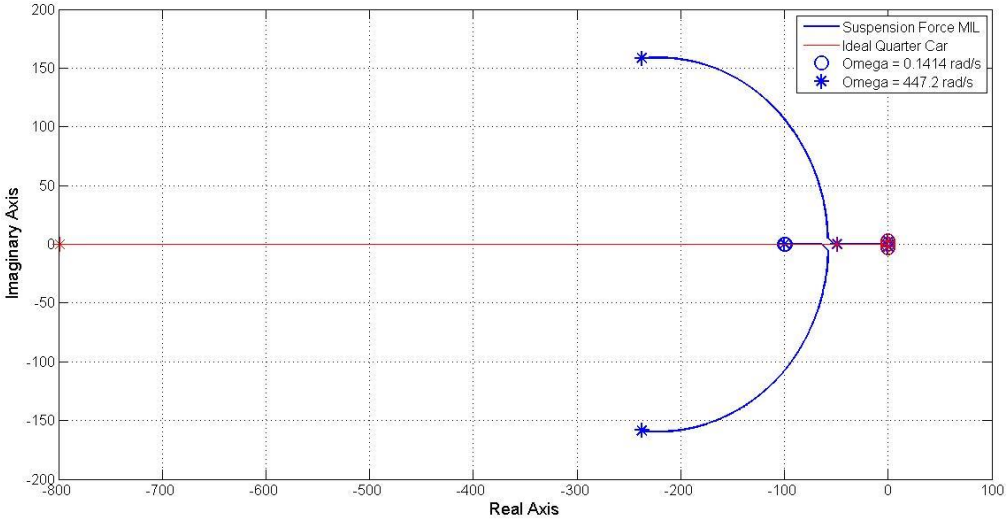

Figure A2.7 – Case 5: Root locus of natural frequency variation for sprung mass damping ratio of 1.5 and $\tau = 0.01s$.

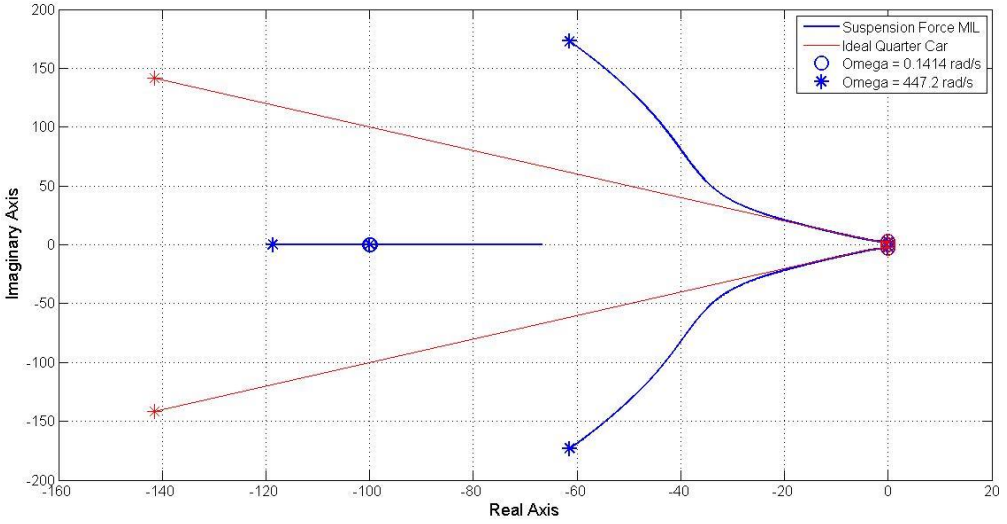

Figure A2.8 – Case 6: Root locus of natural frequency variation for sprung mass damping ratio of 1.5 and $\tau = 0.01s$.

Appendix A2.3 Variation of Sprung Mass Damping Ratio

The systems parameters for damping coefficient variation are shown below in Table A2.3.

	Variable Parameter: $k_s = m_s = 1 \ \ to \ \ 100000$		
	Case 1	**Case 2**	**Case 3**
$b_s \ (Ns/m)$	100	100	100
$m_u \ (kg)$	50	50	50
$b_t \ (Ns/m)$	0	0	0
$k_t \ (N/m)$	500	500	500
$\tau \ (s)$	0.2	0.01	0.001

Table A2.3 - Parameters for variation of sprung mass damping ratio for vehicle structure MIL system.

Root locus of Cases 1, 2 and 3 are shown in Figures A2.9 - A2.12. In all the figures here the body hop poles become unstable at low sprung mass damping ratios and the wheel hop mode is always stable. It was shown in Section 5.3.6 that for vehicle structure MIL systems, high damping can also lead to instability of body hop poles as shown in Figure A2.10. For large time delay of 0.2s shown in Figure A2.9, the MIL system does not resemble the ideal system at any damping ratio. The shape of the body hop poles is similar to that in the suspension MIL case. The wheel hop shape also has similarities, such as the asymptote which occurs for high damping ratios, but there is a difference as when the damping ratio is low the wheel hop poles approach the ideal case instead of becoming unstable.

For smaller time delay constants of 0.01s and 0.001s the root locus is very similar to the trends seen for the suspension MIL system. In Figure A2.11 the wheel hop asymptote at high damping ratios is shifted further towards the left and the poles develop a higher frequency. The only difference from the suspension MIL system is that at low damping ratios the wheel hop poles have very close resemblance to the ideal system. Again this is observed in Figure A2.12 where there is no wheel hop asymptote, and at low damping ratios the wheel hop pole matches the ideal case.

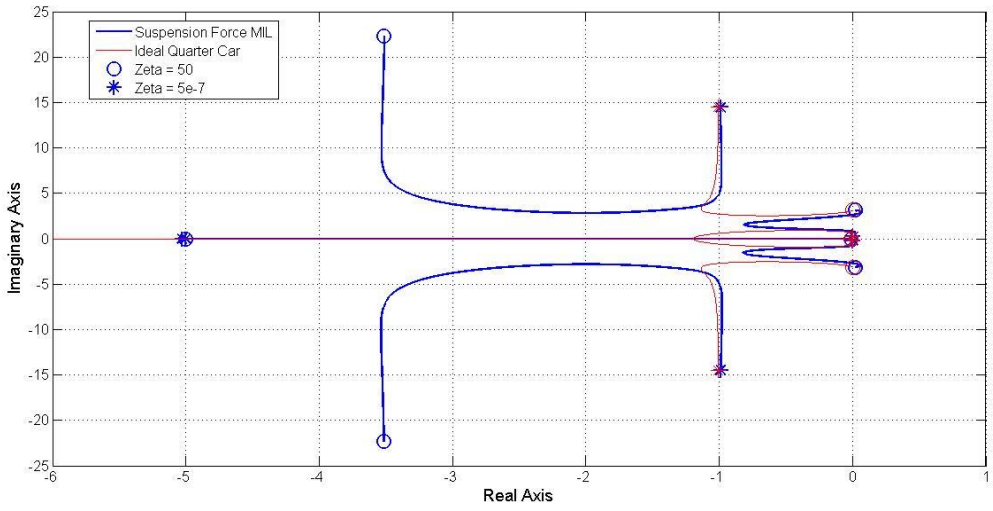

Figure A2.9 – Case 1: Root locus of sprung mass damping ratio variation with $\tau = 0.2s$.

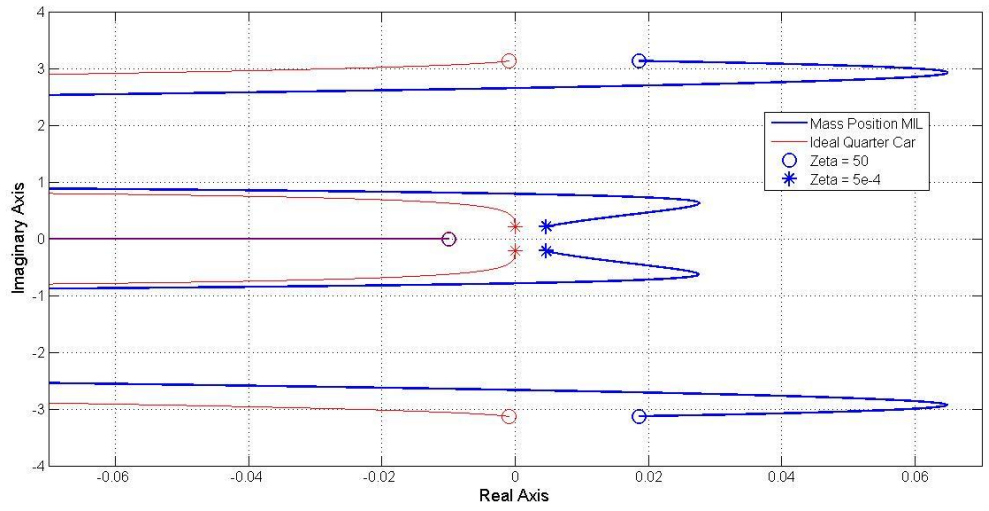

Figure A2.10 – Case 1: Exploded view root locus of sprung mass damping ratio variation with $\tau = 0.2s$.

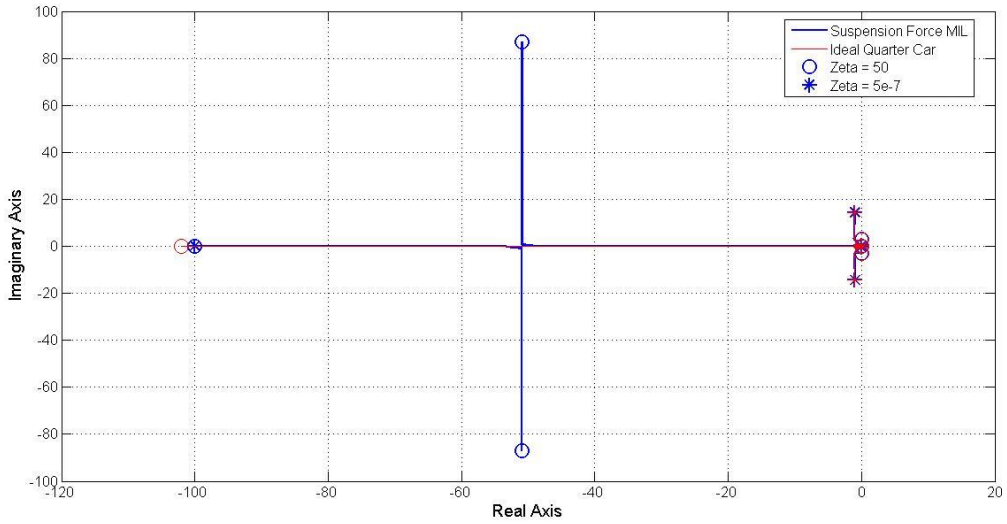

Figure A2.11 – Case 2: Root locus of sprung mass damping ratio variation with $\tau = 0.01s$.

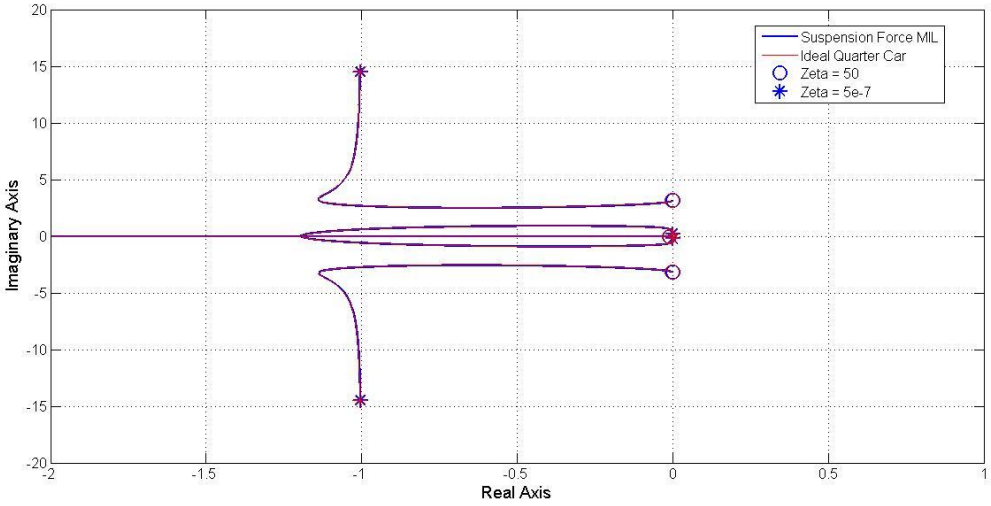

Figure A2.12 – Case 3: Root locus of sprung mass damping ratio variation with $\tau = 0.001s$.

Appendix A2.4 Variation of Tyre Stiffness

The systems parameters for damping coefficient variation are shown below in Table A2.4.

	Variable Parameter: $k_t = 0.01 \ \ to \ \ 100000 \ N/m$	
	Case 1	**Case 2**
$m_s \ (kg)$	50	50
$k_s \ (N/m)$	500	500
$b_s \ (Ns/m)$	100	100
$m_u \ (N/m)$	50	50
$b_t \ (Ns/m)$	0	0
$\tau \ (s)$	0.333	0.01

Table A2.4 - Parameters for variation of tyre stiffness for vehicle structure MIL system.

Root locus plots for Cases 1 and 2 are shown in Figure A2.13 - A2.15. Both plots have two real poles introduced by the MIL filters on the far left of the root locus and not shown in the plot. Comparing Figure A2.13 and A2.15 it is seen that smaller time delays reduces the difference between the MIL and ideal systems. The plots show the error is greatest for the wheel hop mode when tyre stiffness is low, and greatest for the body hop mode when the tyre stiffness is high. This is unlike the suspension MIL where the presence of high tyre stiffness leads to a vertical asymptote at the zero real axis such that the MIL wheel hop poles diverge from the ideal. For the vehicle structure MIL the instability of body hop poles occur at low tyre stiffness as shown in Figure A2.14.

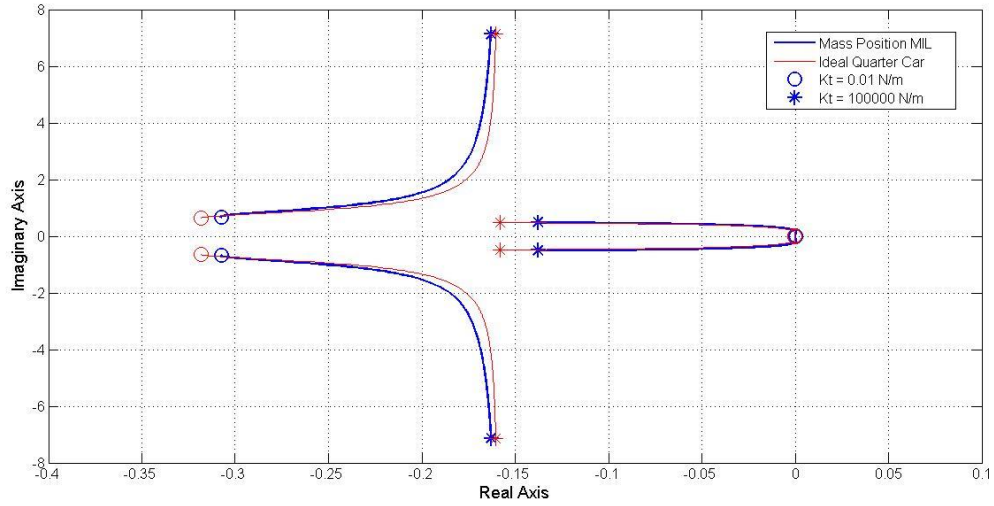

Figure A2.13 – Case 1: Root locus of tyre stiffness variation with $\tau = 0.333s$.

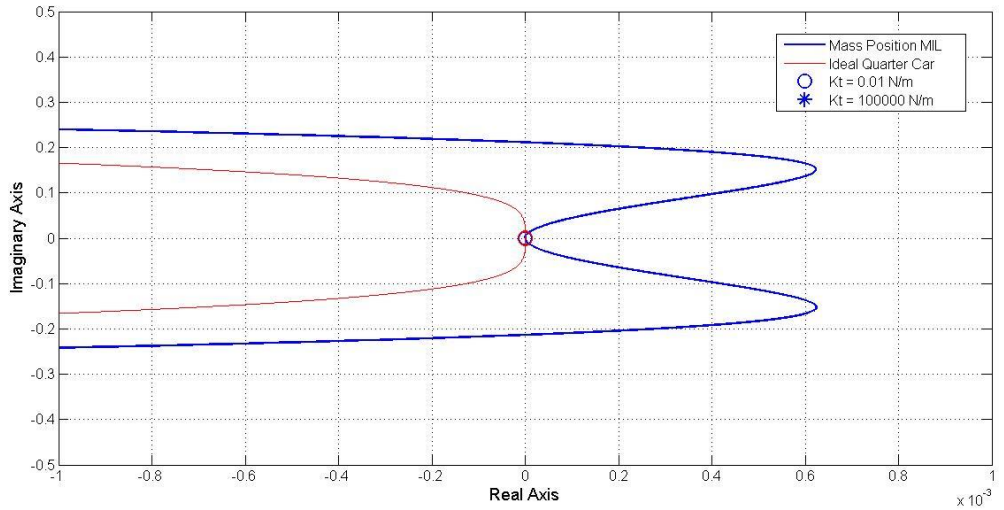

Figure A2.14 – Case 1: Exploded view root locus of tyre stiffness variation with $\tau = 0.333s$.

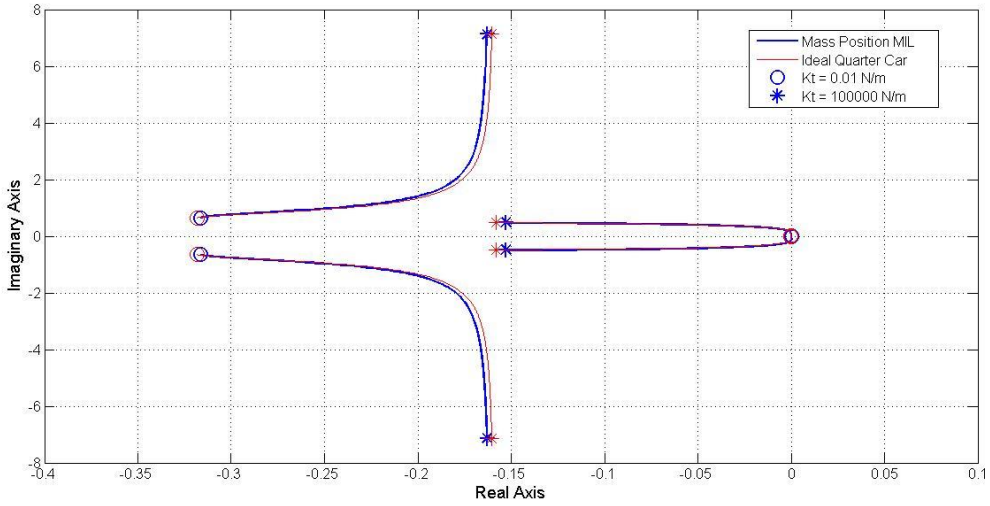

Figure A2.15 - Root locus of tyre stiffness variation with $\tau = 0.001s$.

Appendix A2.5 Variation of Wheel Mass

The systems parameters for damping coefficient variation are shown below in Table A2.5.

	Variable Parameter: $m_u = 0.01 \ \ to \ \ 100000 \ \ kg$	
	Case 1	**Case 2**
$m_s \ (kg)$	50	50
$k_s \ (N/m)$	500	500
$b_s \ (Ns/m)$	100	100
$k_t \ (N/m)$	500	500
$b_t \ (Ns/m)$	0	0
$\tau \ (s)$	0.333	0.01

Table A2.5 - Parameters for variation of wheel mass inertia for vehicle structure MIL system.

Root locus plots for Cases 1 and 2 are shown in Figure A2.16 – A2.18. Both plots have a real pole origin on the far left of the root locus which is not shown on the plot. Like the suspension MIL system, here the root locus trajectory comparison to the ideal case is better for the body hop mode and poorer for the wheel hop mode. Instability for both Cases occurs at high wheel mass as shown in Figure A2.17.

Figure A2.16 shows that at the origin where wheel mass is 0.01kg, there is a close resemblance between the MIL and ideal system. As the wheel mass increases, there is a breakaway point from the real axis, such that the wheel hop modes become underdamped. The breakaway moves to the right and forms a loop, but before breaking back into the real axis it follows the trajectory of the ideal wheel hop poles. A similar shape of root locus is seen in Figure A2.18. The effect of a smaller time delay shifts the breakaway loop of the wheel hop to the left of the root locus. As the breakaway point is sufficiently further from the wheel hop poles, and occurs at smaller wheel mass values, the

loop break back into the real axis and subsequently closely tracking the ideal wheel hop trajectory at higher mass values.

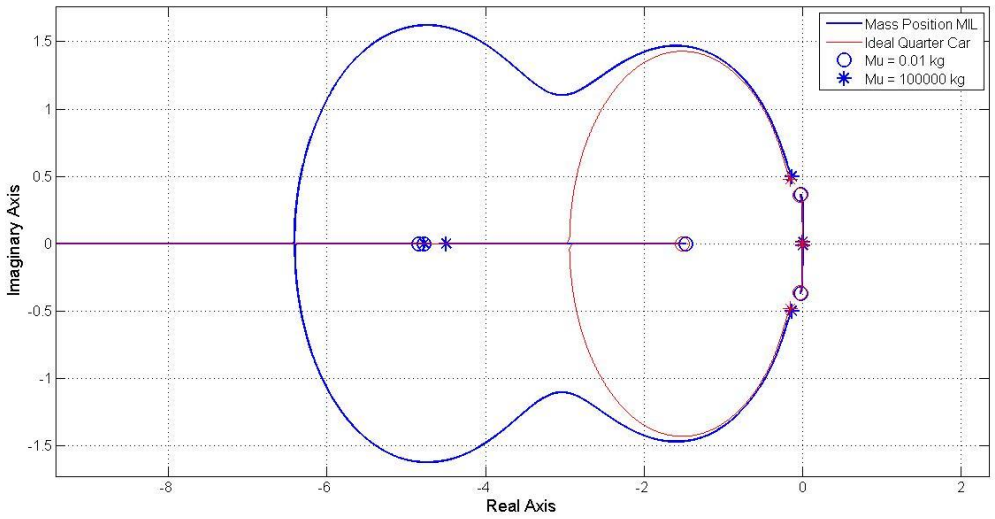

Figure A2.16 – Case 1: Root locus of wheel mass variation with $\tau = 0.333s$.

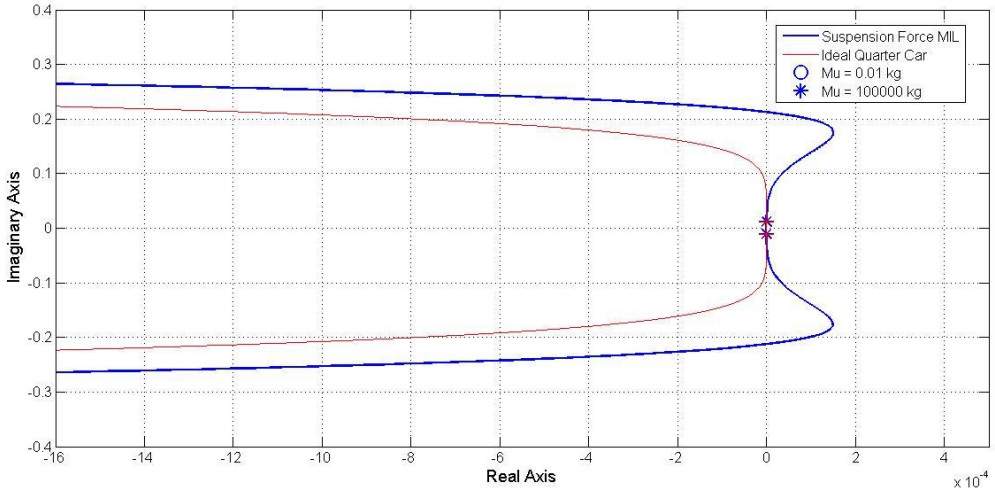

Figure A2.17 – Case 1: Exploded view root locus of wheel mass variation with $\tau = 0.333s$.

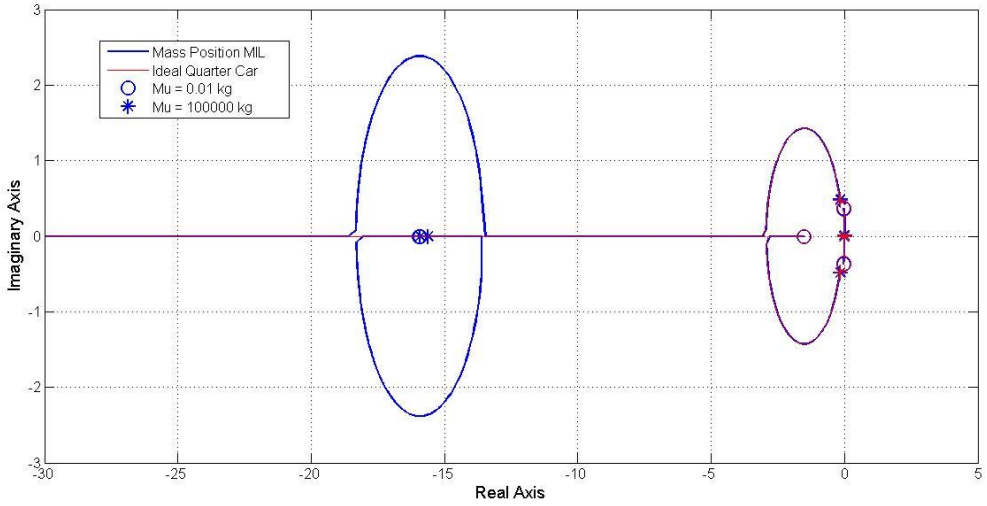

Figure A2.18 – Case 2: Root locus of wheel mass variation with $\tau = 0.01s$.

Appendix A3 – Quarter Car Combined MIL Vehicle Structure and MIL Suspension Parameters Variation

Appendix A3.1 Variation of Time Delay

The systems parameter chose are arbitrary as shown in Table A3.1. For all the analysis here it will be assumed that the suspension MIL system delay (τ_s) and the vehicle structure MIL system delay (τ_m) are equal.

	Variable Parameter: $\tau_s = \tau_m = 0.001s \; to \; 1s$	
	Case 1	**Case 2**
Sprung Mass Damping Ratio	1	0.5
$m_s \; (kg)$	50	50
$k_s \; (N/m)$	500	500
$b_s \; (Ns/m)$	316.2	158.1
$m_u \; (kg)$	50	50
$k_t \; (N/m)$	500	500
$b_t \; (Ns/m)$	0	0

Table A3.1 - Parameters for variation of delay time constant for vehicle structure MIL system.

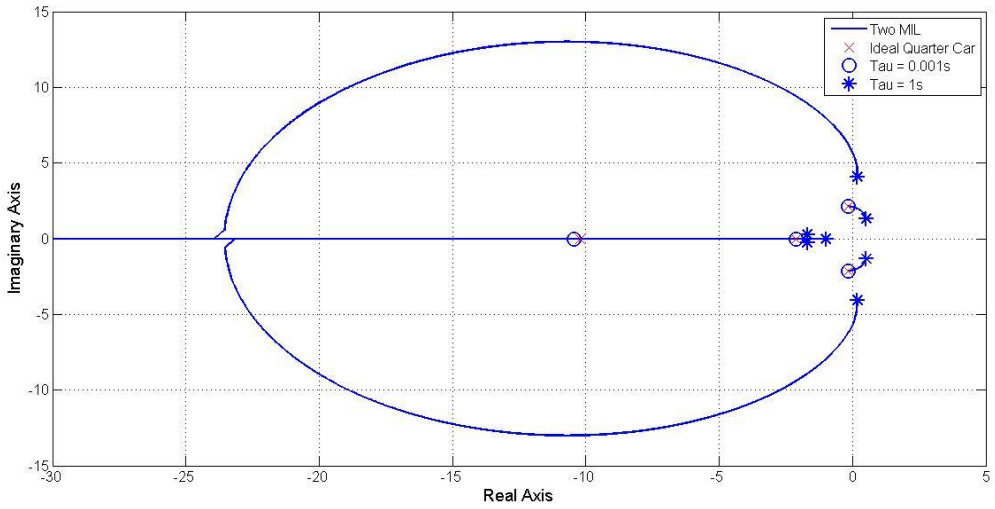

Figure A3.1 – Case 1: Root locus of time constant variation for sprung mass damping ratio of 1.

Root locus plots for Cases 1 and 2 are shown in Figure A3.1 and A3.2 respectively. The root locus of both cases have three poles starting at time constant of 0.001s at the far left of the root locus which are not shown in the plot. Here the root locus plots have a similar shape to both pure suspension MIL system and a pure vehicle structure MIL system. For a suspension MIL system the wheel hop pole and body hop pole become unstable together whilst for the vehicle structure MIL only the body hop pole can become unstable. Following from this a system with suspension MIL and vehicle structure MIL exhibits the combined properties both systems. Figure A3.1 and A3.2 shows that the wheel hop poles become unstable with a large time delay constant, however here the body hop pole reaches instability before the wheel hop pole, due to the contribution of the vehicle structure MIL

system. Figure A3.2 shows that the effect of the two MIL systems introduces additional oscillatory dynamics into the system at large time constants, as a pair of conjugate poles break off from the real axis.

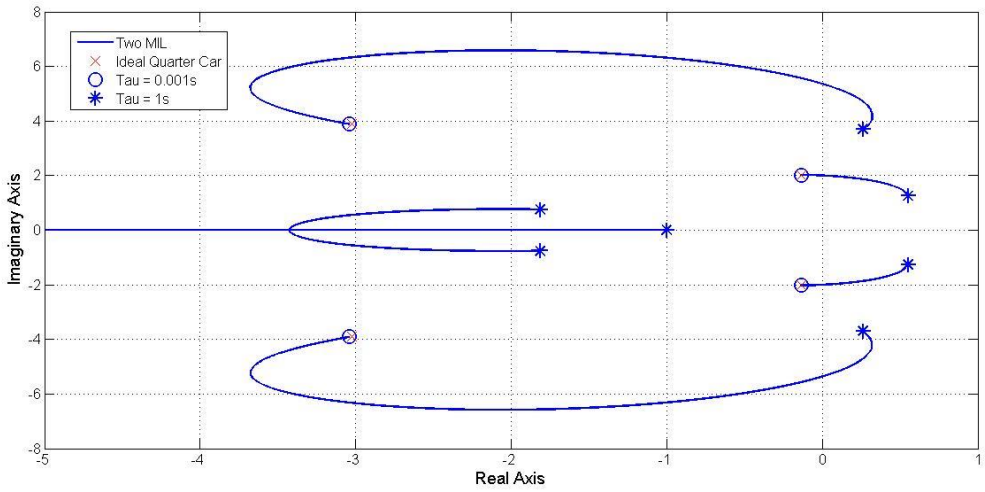

Figure A3.2 – Case 2: Root locus of time constant variation for sprung mass damping ratio of 0.5.

Appendix A3.2 Variation of Sprung Mass Natural Frequency

The system parameters for natural frequency variation are shown in Table A3.2.

	Variable Parameter: $k_s = 1N/m \; to \; 100000N/m$			**Variable Parameter:** $k_s = 1N/m \; to \; 1000000N/m$		
	Case 1	**Case 2**	**Case 3**	**Case 4**	**Case 5**	**Case 6**
Sprung Mass Damping Ratio	1	1.5	0.5	1	1.5	0.5
$m_s \; (kg)$	50	50	50	50	50	50
$m_u \; (kg)$	50	50	50	50	50	50
$b_t \; (Ns/m)$	0	0	0	0	0	0
$k_t \; (N/m)$	500	500	500	500	500	500
$\tau_m \; (s)$	0.2	0.2	0.2	0.01	0.01	0.01
$\tau_s \; (s)$	0.2	0.2	0.2	0.01	0.01	0.01

Table A3.2 - Parameters for variation of sprung mass natural frequency for vehicle structure MIL system.

Root locus plots of Cases 1, 2 and 3 are shown in Figure A3.3, A3.4 and A3.5 respectively. The shape of the root locus for all three cases show the wheel hop and body hop modes similar to that of the single suspension MIL case. The difference is that here the body hop poles are more unstable, and shifted to the right due to the contribution from the vehicle structure MIL system which only destabilises the body hop mode. The additional poles, which are all on the real axis at low natural frequencies, break away at higher frequencies from the real axis and then break in to form a loop. This phenomena is observed for the single vehicle structure MIL system where the breakaway poles

move towards the left of the root locus instead of moving to the right, as in the suspension MIL system.

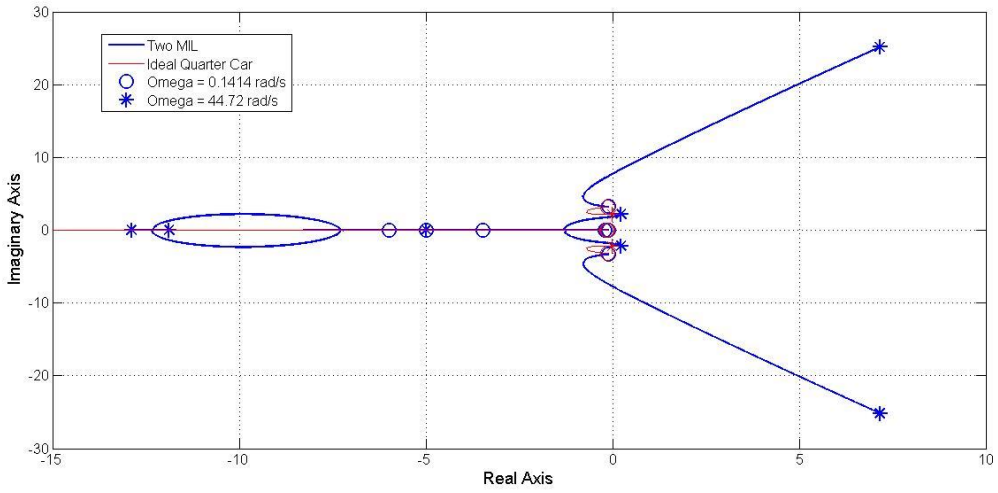

Figure A3.3 – Case 1: Root locus of natural frequency variation for sprung mass damping ratio of 1 and $\tau = 0.2s$.

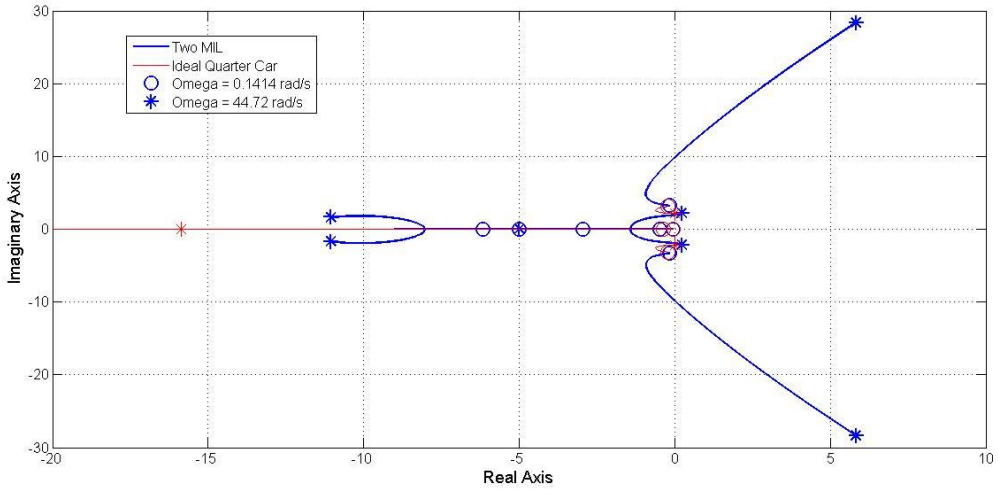

Figure A3.4 – Case 2: Root locus of natural frequency variation for sprung mass damping ratio of 1.5 and $\tau = 0.2s$.

Root locus plots of Case 4, 5 and 6 are shown in Figure A3.6, A3.7 and A3.8 respectively. The general shape of the root locus is the same as the suspension MIL system. As noted the difference is that with combined mass structure and suspension MIL, the body hop poles are more unstable than wheel hop poles and it is the same case here.

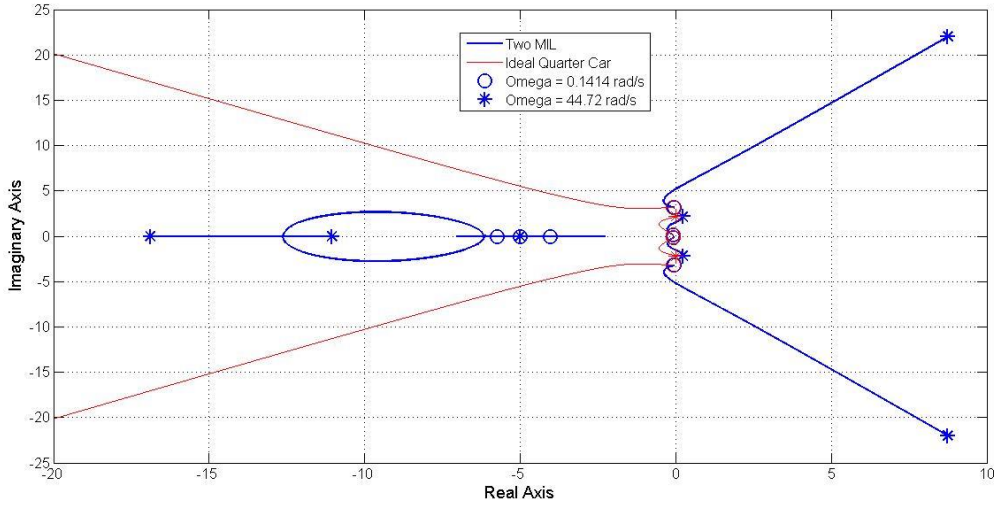

Figure A3.5 – Case 3: Root locus of natural frequency variation for sprung mass damping ratio of 0.5 and $\tau = 0.2s$.

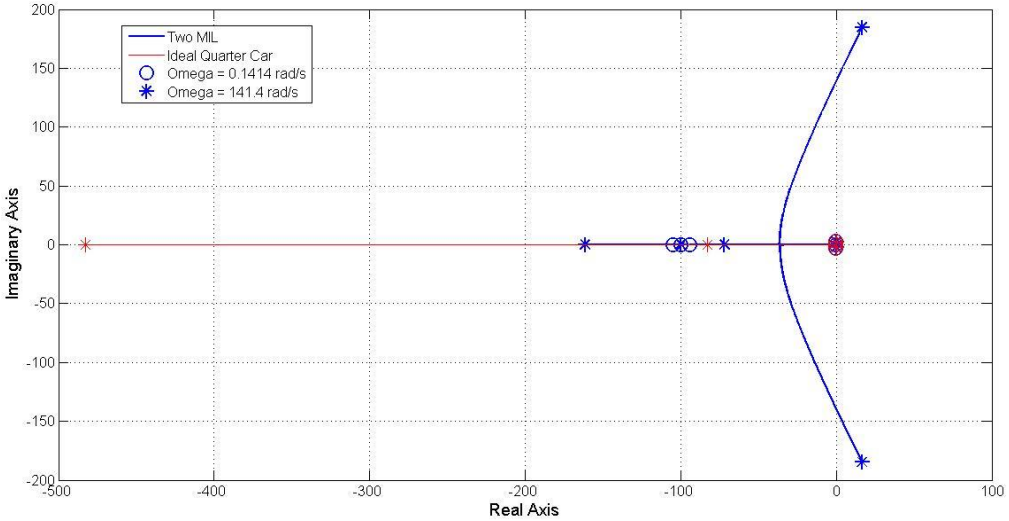

Figure A3.6 – Case 4: Root locus of natural frequency variation for sprung mass damping ratio of 1 and $\tau = 0.01s$.

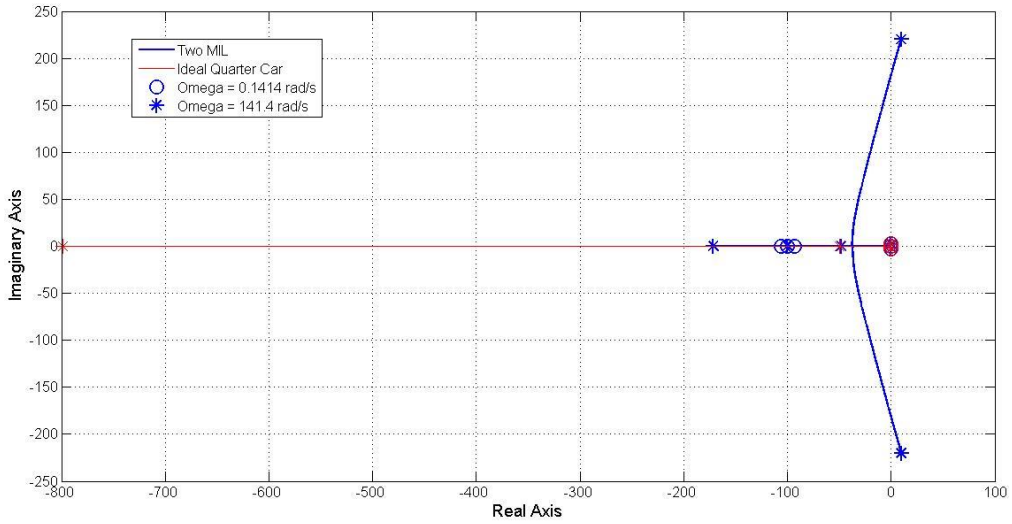

Figure A3.7 – Case 5: Root locus of natural frequency variation for sprung mass damping ratio of 1.5 and $\tau = 0.01s$.

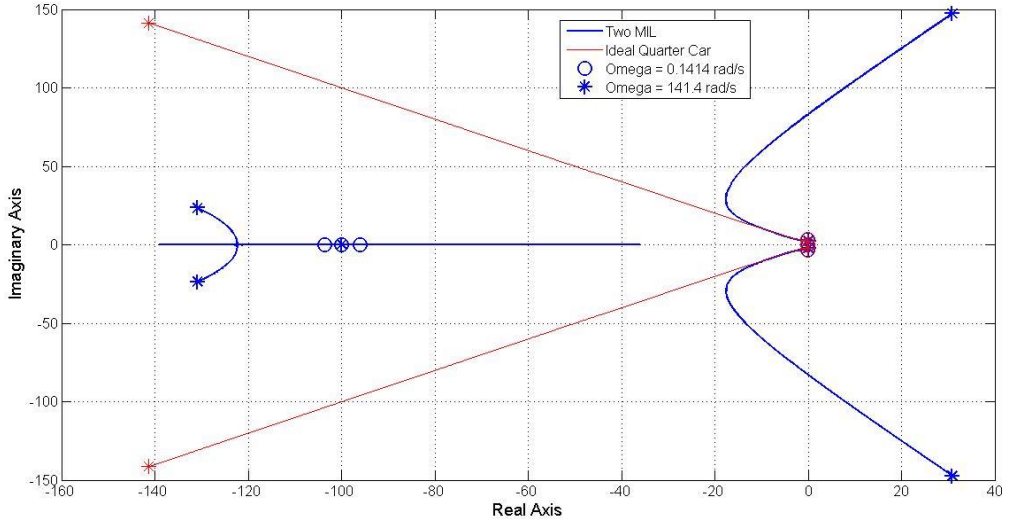

Figure A3.8 – Case 6: Root locus of natural frequency variation for sprung mass damping ratio of 1.5 and $\tau = 0.01s$.

Appendix A3.3 Variation of Sprung Mass Damping Ratio

The systems parameters for damping coefficient variation are shown in Table Figure A3.3.

	Variable Parameter: $k_s = m_s = 1 \ \ to \ \ 100000$		
	Case 1	**Case 2**	**Case 3**
$b_s \ (Ns/m)$	100	100	100
$m_u \ (kg)$	50	50	50
$b_t \ (Ns/m)$	0	0	0
$k_t \ (N/m)$	500	500	500
$\tau_m \ (s)$	0.2	0.01	0.001
$\tau_s \ (s)$	0.2	0.01	0.001

Table Figure A3.3 - Parameters for variation of sprung mass damping ratio for vehicle structure MIL system.

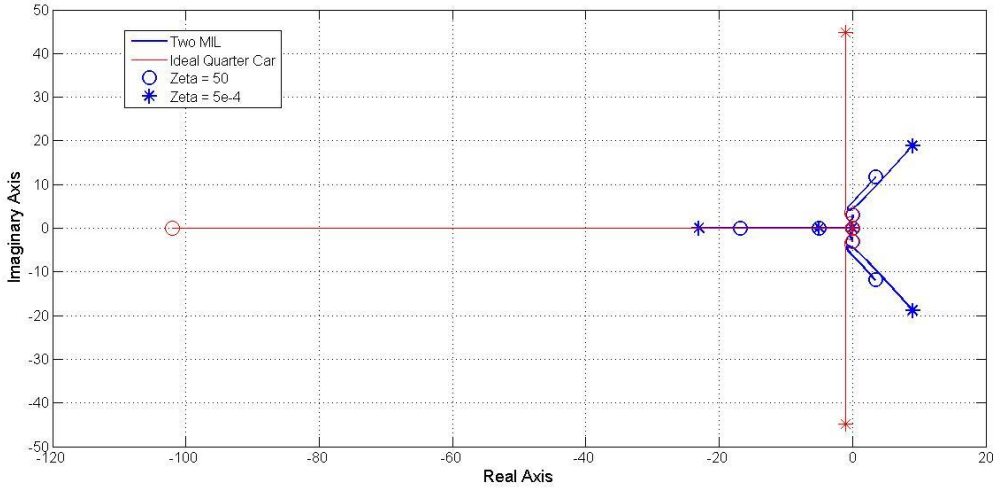

Figure A3.9 – Case 1: Root locus of sprung mass damping ratio variation with $\tau = 0.2s$.

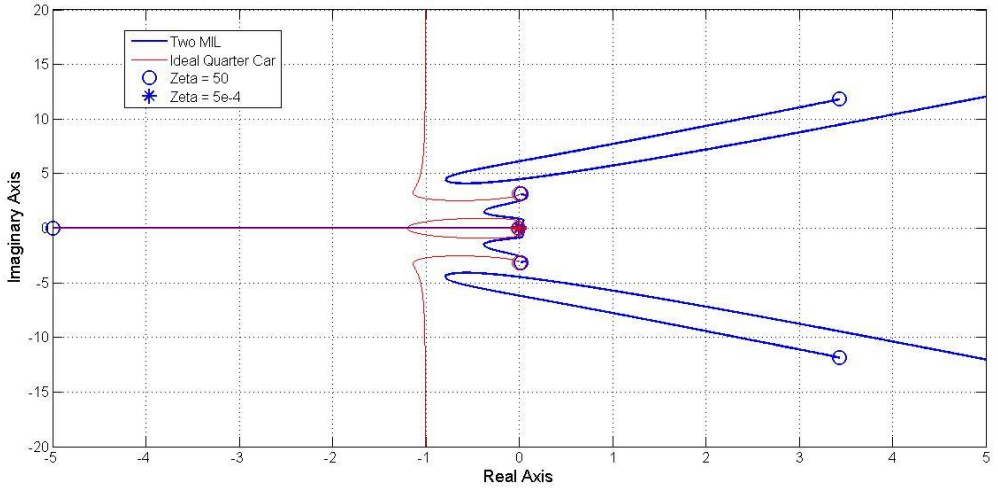

Figure A3.10 – Case 1: Exploded view root locus of sprung mass damping ratio variation with $\tau = 0.2s$.

The root locus plot for Case 1 is shown in Figure A3.9-A3.11. Here the body hop poles follow the same shape as seen for the suspension MIL and the vehicle structure MIL systems. The wheel hop poles become unstable at high damping ratios, similar to the single suspension MIL case. However at low damping ratios, instead of forming a stable vertical asymptote as seen for suspension MIL and vehicle structure MIL cases, the combined system is unstable at low damping ratios as well. Figure A3.11 shows that the body hop poles are unstable both at low and high damping ratios as seen for the vehicle structure MIL system in Section 5.5.3.

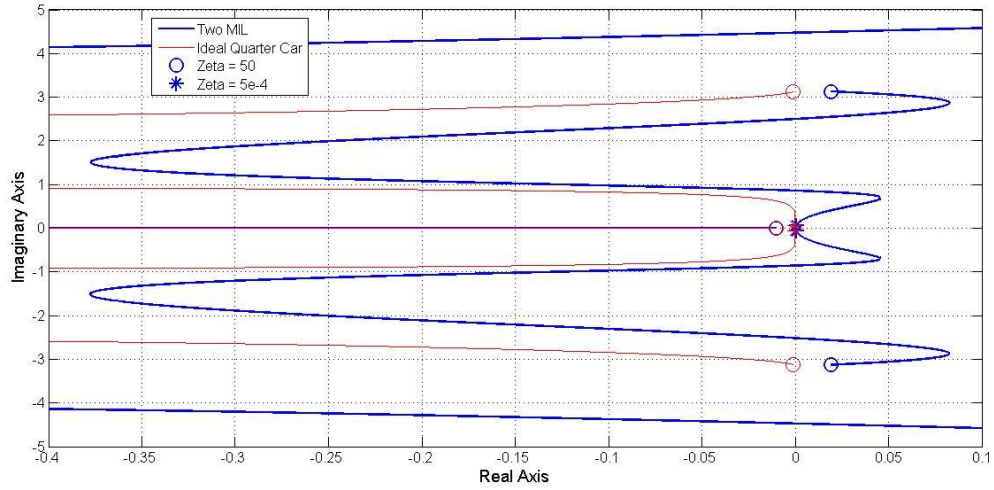

Figure A3.11 – Case 1: Exploded view root locus of sprung mass damping ratio variation with $\tau = 0.2s$.

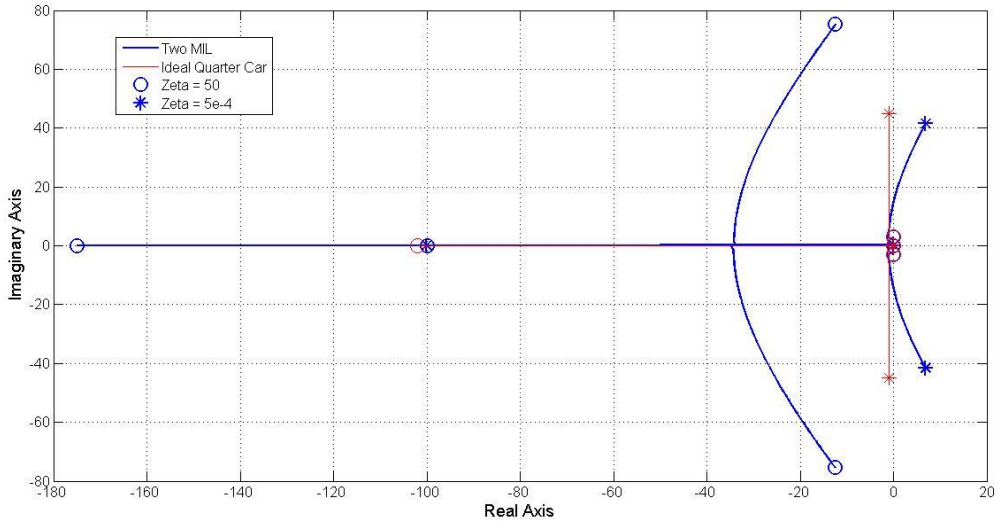

Figure A3.12 – Case 2: Root locus of sprung mass damping ratio variation with $\tau = 0.01s$.

The root locus plot for Case 2 is shown in Figure A3.12. At both low and high damping ratios both wheel hop and body hop poles move towards instability. The trajectory of the body hop poles are

similar to that shown for Case 1 in Figure A3.11. At high damping ratios, there is a breakaway point from the real axis as the wheel hop poles become underdamped. This break away at high damping ratios is seen with both suspension MIL and vehicle structure MIL systems but the breakaway poles approach a vertical asymptote. However in the combined MIL systems the breakaway poles are moving to the right of the root locus, therefore it is possible that instability could occur at high damping ratios as well.

The root locus of Case 3 is shown in Figure A3.13. Here the MIL poles track the ideal trajectory closely for large value of damping and there are no additional dynamics from the additional filter poles. At low values of damping both wheel hop and body hop poles move rightward toward the instability region as seen in the suspension MIL system.

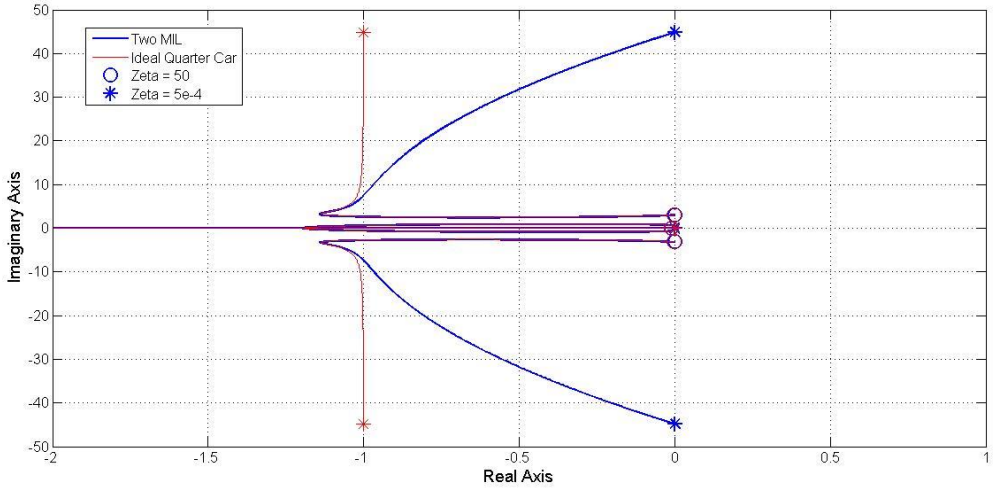

Figure A3.13 – Case 3: Root locus of sprung mass damping ratio variation with $\tau = 0.001s$.

Appendix A3.4 Variation of Tyre Stiffness

The systems parameters for damping coefficient variation are shown in Table A3.4.

	Variable Parameter: $k_t = 0.01 \ \ to \ \ 100000 \ N/m$	
	Case 1	**Case 2**
$m_s \ (kg)$	50	50
$k_s \ (N/m)$	500	500
$b_s \ (Ns/m)$	100	100
$m_u \ (N/m)$	50	50
$b_t \ (Ns/m)$	0	0
$\tau_m \ (s)$	0.333	0.01
$\tau_s \ (s)$	0.333	0.01

Table A1.3 - Parameters for variation of tyre stiffness for vehicle structure MIL system.

The root locus plot of Cases 1 and 2 are shown in Figure A3.14 and A3.15 respectively. The root locus here shows the combined trends of the suspension MIL and the vehicle structure MIL. Although it cannot be seen clearly in the figures, with low tyre stiffness the body hope mode is unstable, similar to the vehicle structure MIL system. With high tyre stiffness the wheel hop pole diverge from the

ideal trajectory and approaches a vertical asymptote at the real axis of zero, this is similar to the MIL suspension system.

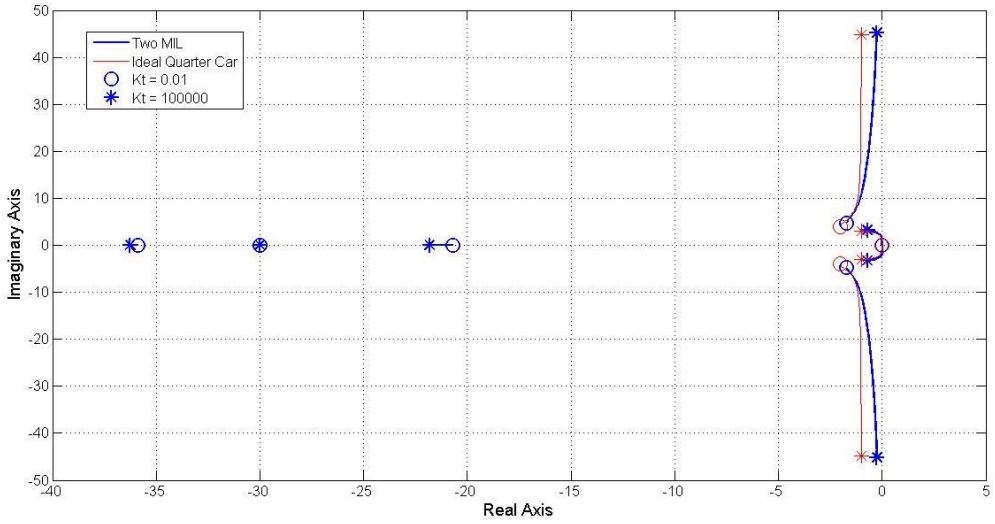

Figure A3.14 – Case 1: Root locus of tyre stiffness variation with $\tau = 0.333s$.

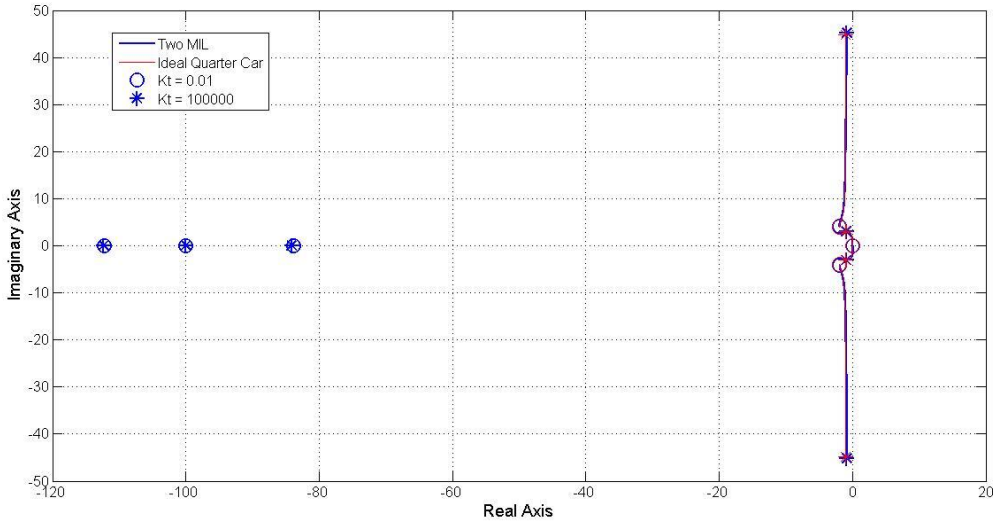

Figure A3.15 – Case 2: Root locus of tyre stiffness variation with $\tau = 0.01s$.

Appendix A3.5 Variation of Wheel Mass

The system parameters for damping coefficient variation are shown in Table A3.5. Root locus plots of Cases 1 and 2 are shown in Figure A3.16 and A3.17 respectively. With low wheel mass the combined MIL system wheel mode resembles the suspension MIL where there is a stable vertical asymptote. Although it is too small to see in the figures, with high wheel mass the body hop poles become unstable in the same manner as the vehicle structure MIL system.

	Variable Parameter: $m_u = 0.01 \;\; to \;\; 100000 \;\; kg$	
	Case 1	**Case 2**
$m_s \; (kg)$	50	50
$k_s \; (N/m)$	500	500
$b_s \; (Ns/m)$	100	100
$k_t \; (N/m)$	500	500
$b_t \; (Ns/m)$	0	0
$\tau_{\,m}(s)$	0.333	0.01
$\tau_{\,s}(s)$	0.333	0.01

Table A3.5 - Parameters for variation of wheel mass inertia for vehicle structure MIL system.

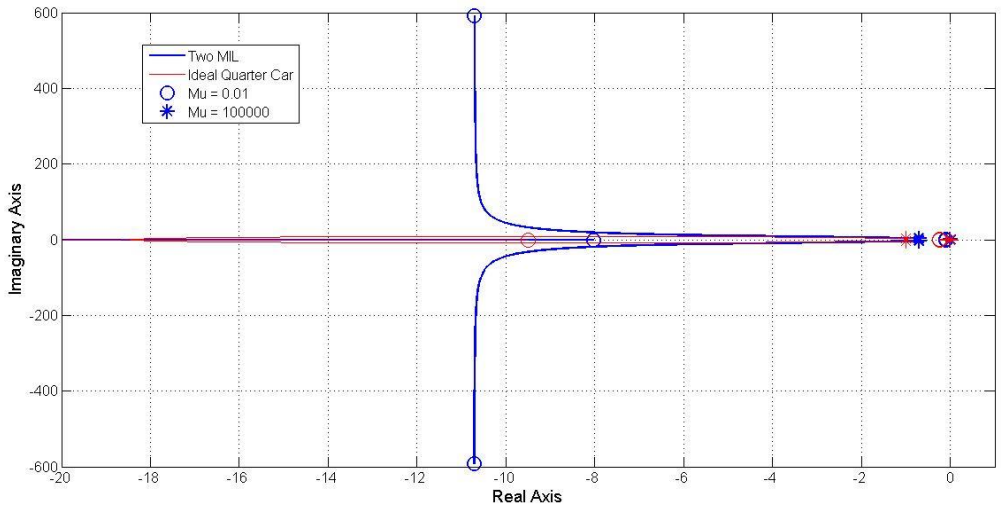

Figure A3.16 – Case 1: Root locus of wheel mass variation with $\tau = 0.333s$.

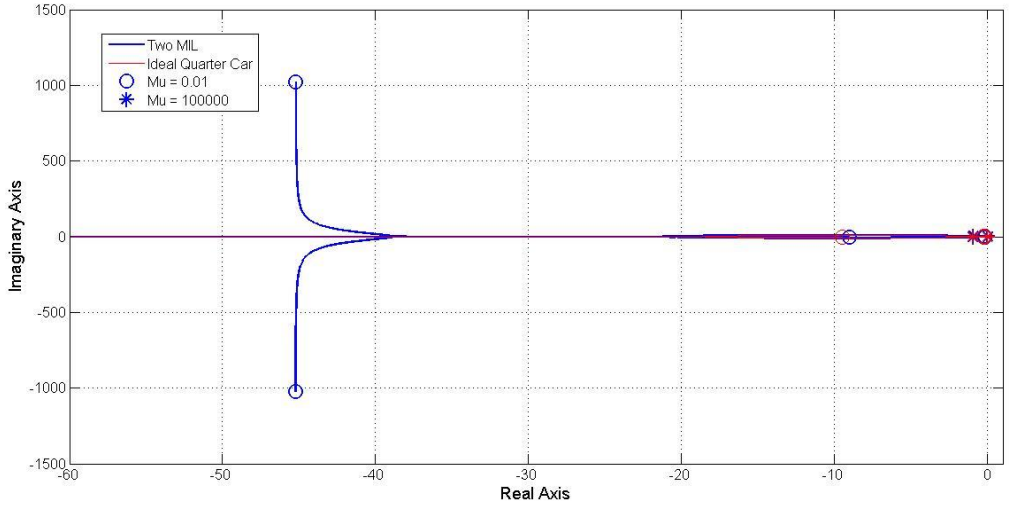

Figure A3.17 – Case 2: Root locus of wheel mass variation with $\tau = 0.001s$.

Appendix B

Appendix B1 – Validation of Semi-Active Skyhook Test

The time response from the experimental test is shown in Figure B1.1 – B1.6. Both sprung mass position, suspension displacement and wheel position shows a good resemblance to the ideal simulated response. Again the wheel hop mode is absent in the wheel vibrations. There is a noticeable drift in the steady state sprung mass and wheel mass position as seen in other tests. The performance in terms of tyre displacement is poor as in previous sections.

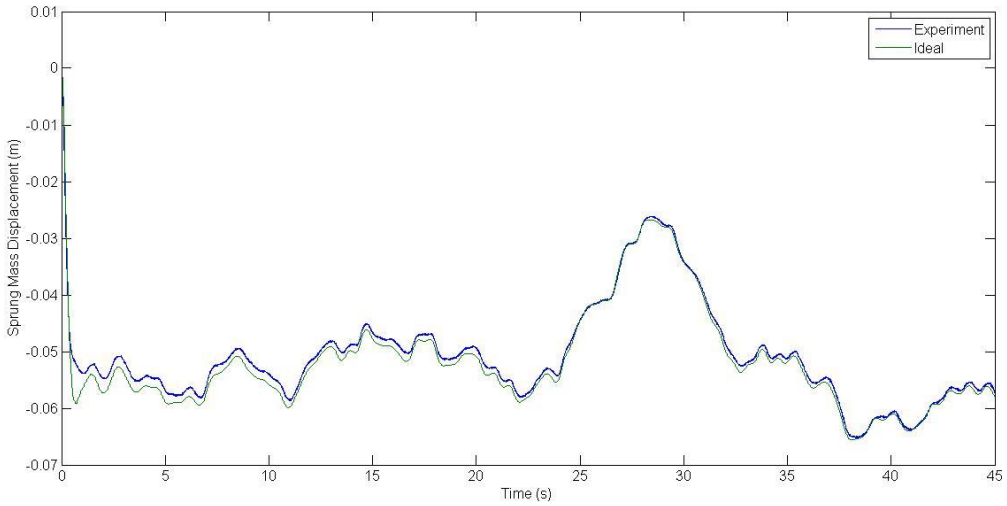

Figure B1.1 – Sprung mass displacement time response.

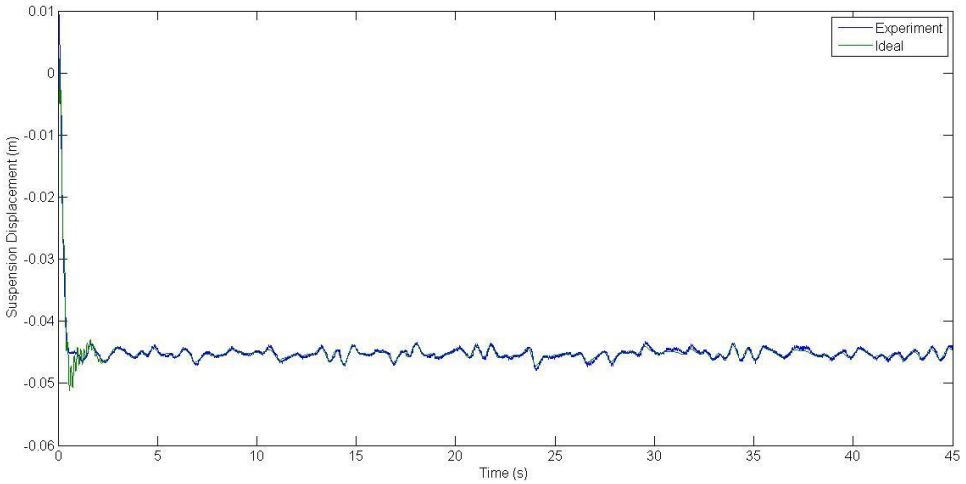

Figure B1.2 – Suspension displacement time response.

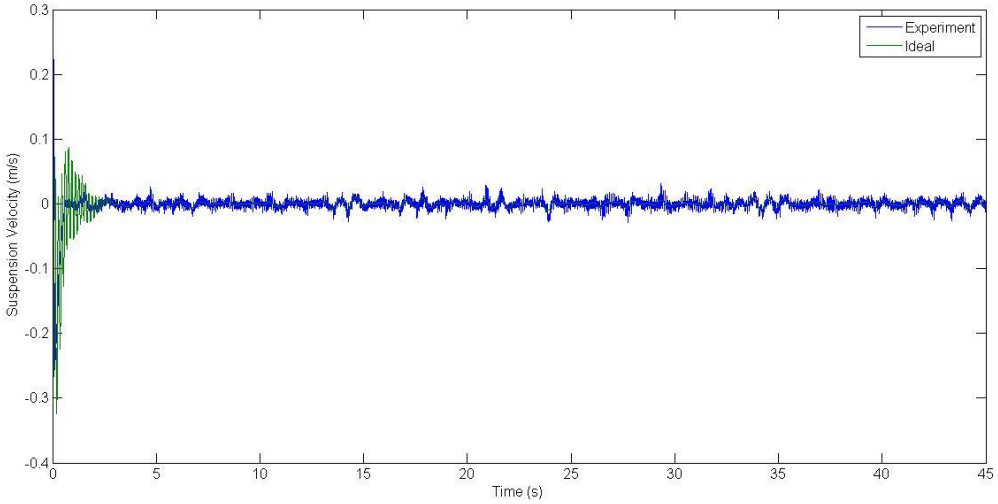

Figure B1.3 – Suspension velocity time response.

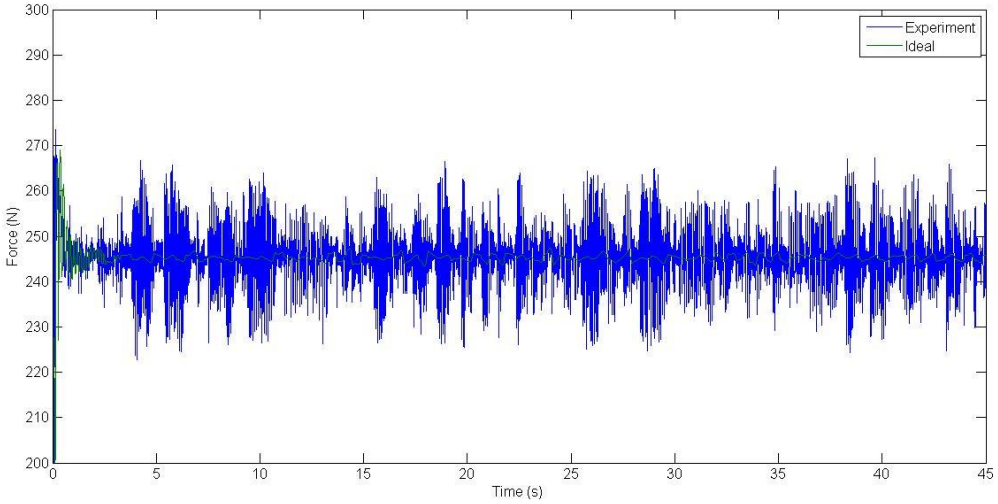

Figure B1.4 – Suspension force time response.

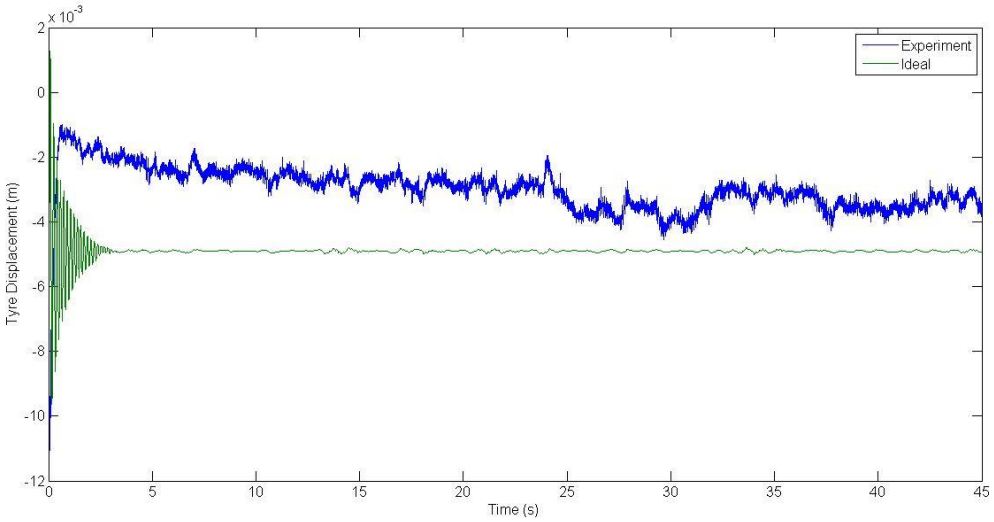

Figure B1.5 – Tyre displacement time response.

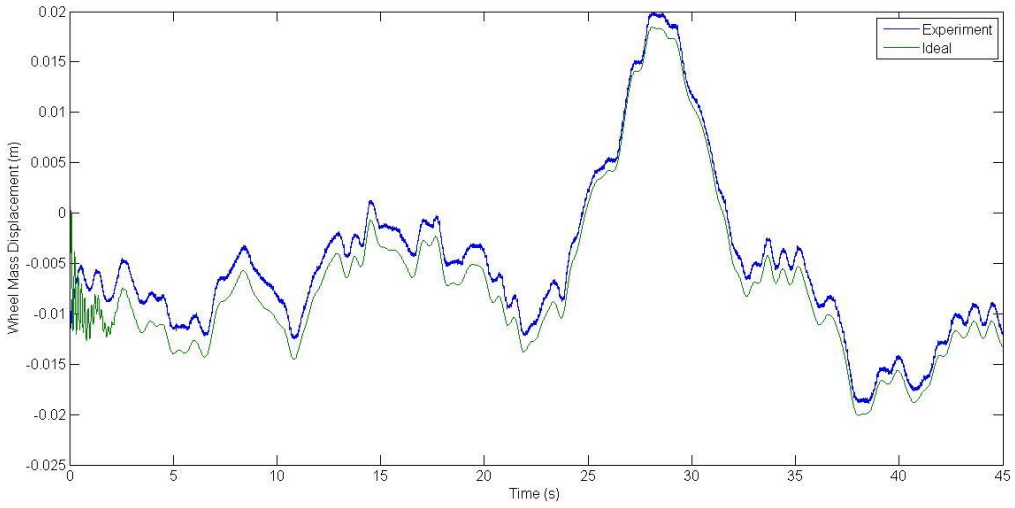

Figure B1.6 – Wheel displacement time response.

The errors of the experimental test is shown in Figure B1.7 and B1.8 and Table B1.1. Here it can be seen that test errors for the semi-active skyhook is less than in the passive test case. This is to be expected because the sprung mass vibrations under the skyhook algorithm is smaller and therefore it is less demanding for the tracking of position and force controllers.

	Suspension MIL	Vehicle structure MIL
Total RMS Error ($e_1 + e_2$)	7.50	0.0593
Percentage Error (%)	286	58

Table B1.1 – Overall test accuracy, the error denotes comparison of emulated to real output.

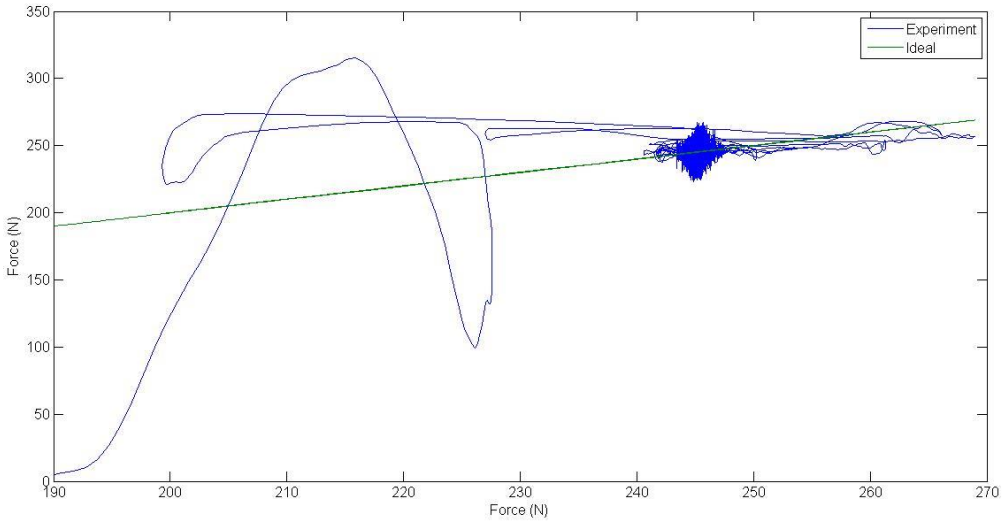

Figure B.7 – Force error subspace plot.

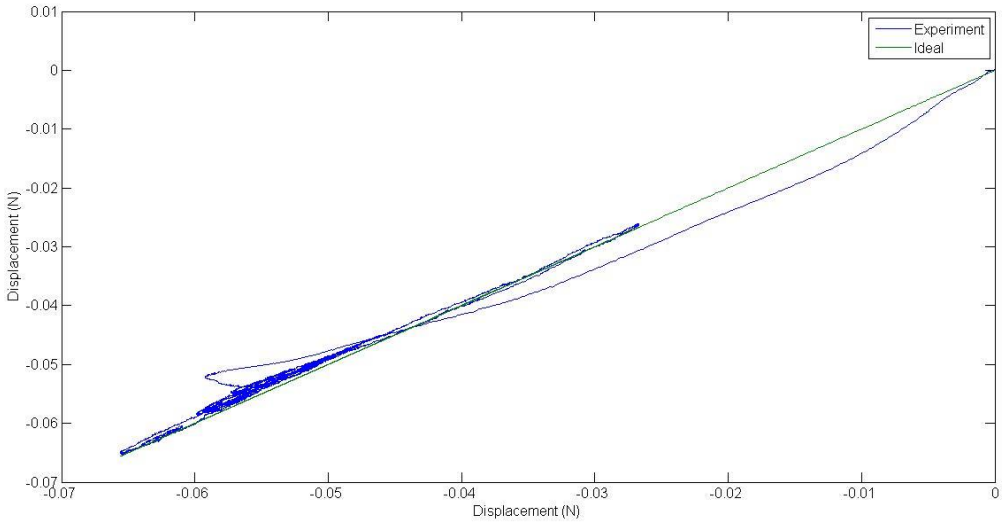

Figure B.8 – Sprung mass displacement error subspace plot.

Appendix B2 – Validation of Active Skyhook Test

The time response from the experimental test is shown in Figure B2.1 – B2.6. Both sprung mass position, suspension displacement and wheel position shows a good resemblance to the ideal simulated response. The performance in terms of tyre displacement is poor and high frequency wheel mode vibrations is absent as in previous sections.

The errors of the experimental test are shown in Figure B2.7 and B2.8 and Table B2.1. Like the semi-active skyhook, it can be seen that test errors for the active skyhook is less than in the passive test case. Overall the responses from active and semi-active skyhook are very similar and confirm the findings in literature that the performance gains from active skyhook are very little compared to the semi-active algorithm.

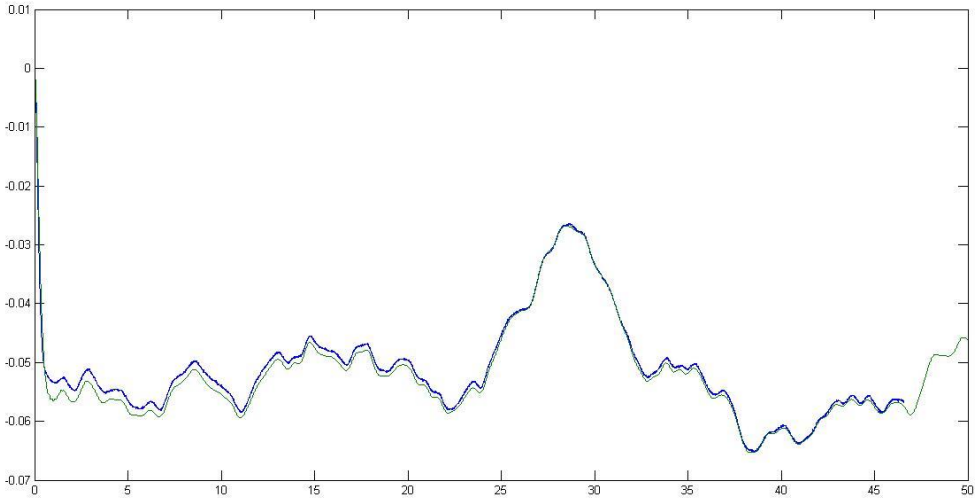

Figure B2.1 – Sprung mass position time response.

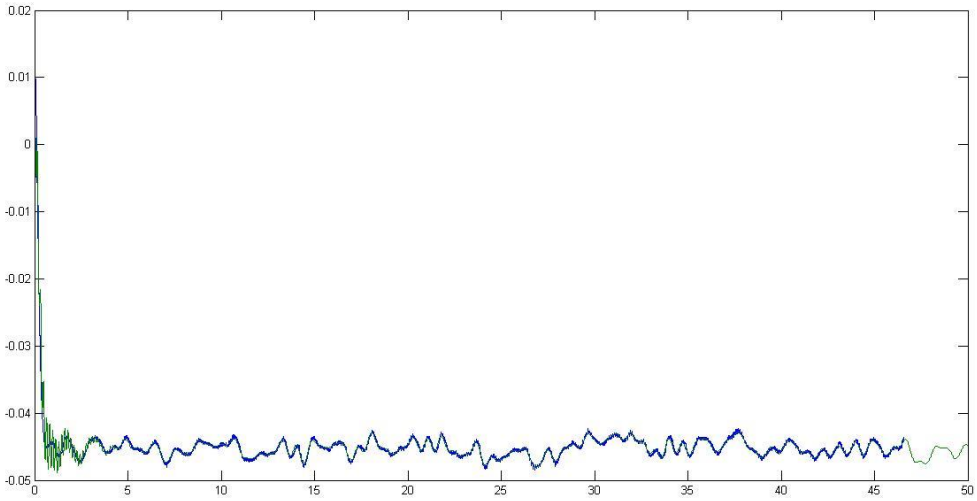

Figure B2.2 – Suspension displacement time response.

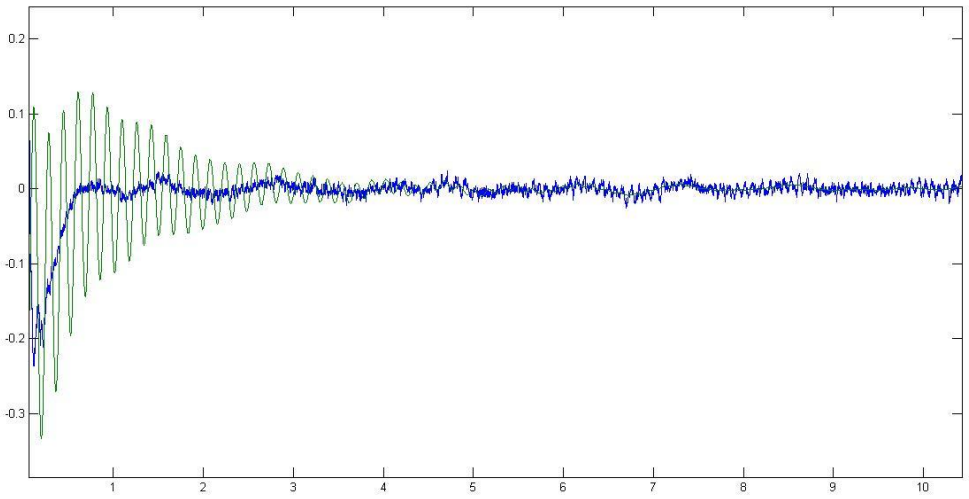

Figure B2.3 – Suspension velocity time trace.

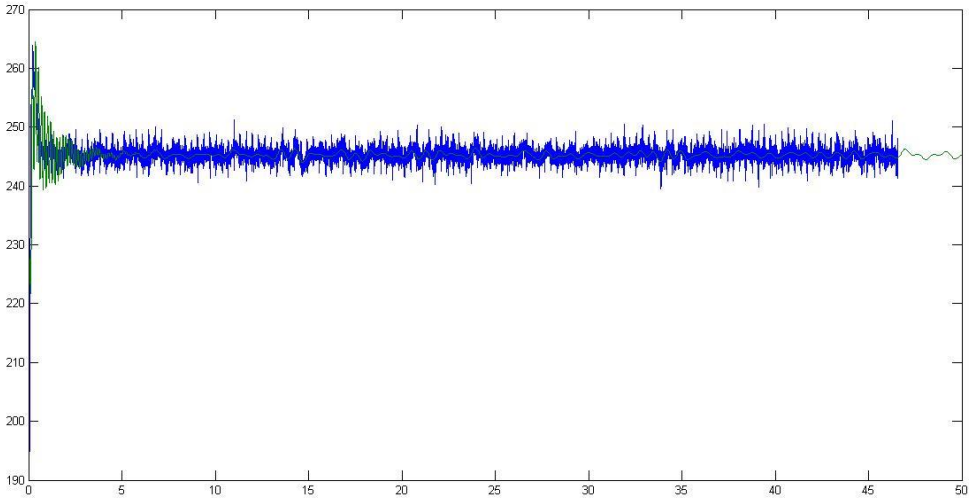

Figure B2.4 – Command force time trace

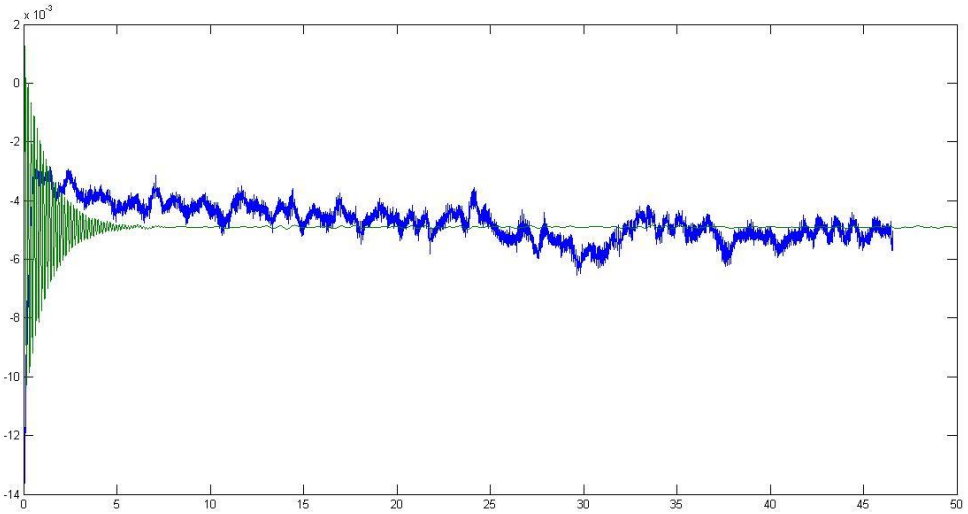

Figure B2.5 – Tyre displacement time trace.

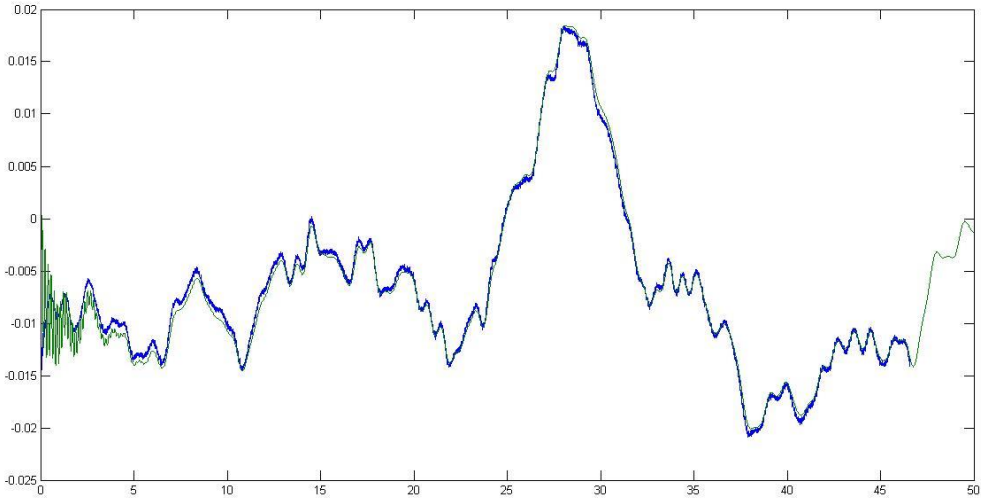

Figure B2.6 Wheel position time trace

	Suspension MIL	Vehicle structure MIL
Total RMS Error ($e_1 + e_2$)	8.47	0.0595
Percentage Error (%)	425	58

Table B2.1 – Overall test accuracy, the error denotes comparison of emulated to real output.

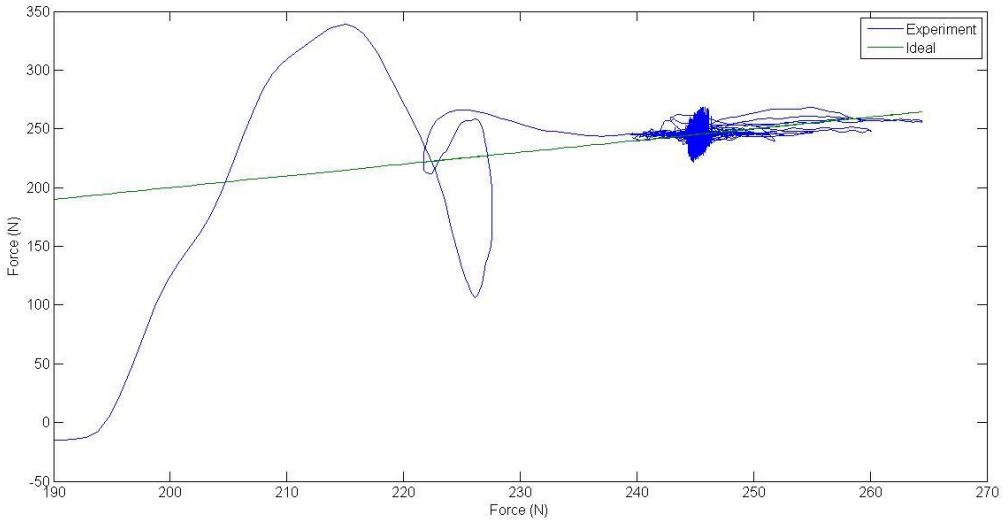

Figure B2.7 – Force error subspace plot.

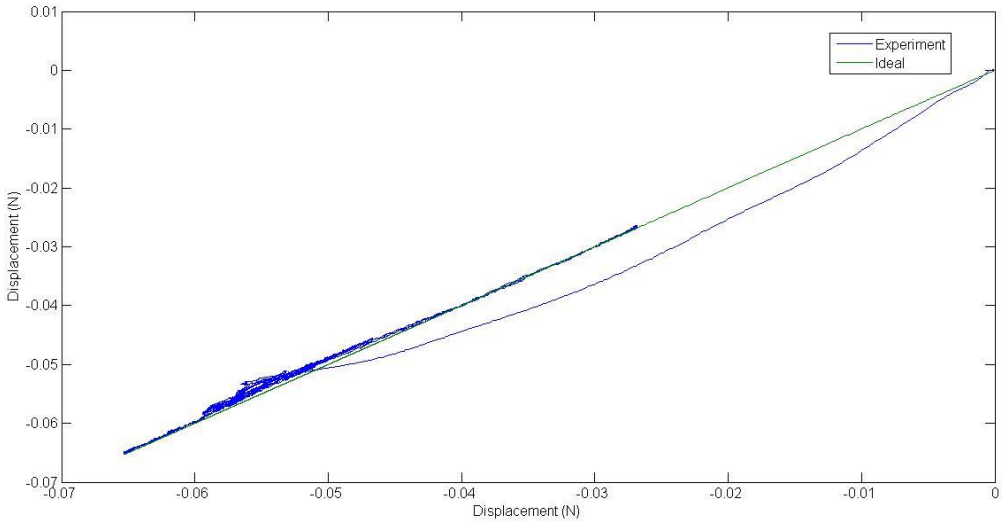

Figure B2.8 – Sprung mass displacement error subspace plot.

Appendix B3 – Validation of Passive Flexible Cross Structure Test

The time response of the experimental test compared to the emulated system is shown in Figure B3.1 – B3.7. The test system has good performance in terms of sprung mass and suspension displacements after transient response from initial conditions have decayed, this is also seen for the point mass tests conducted. The same trend can be seen in the wing tip displacement time response shown in Figure B3.7. The performance in terms of tyre displacement, like in other tests, is poor here as well. The highly damped wheel motion due to friction railings means that for this test there is again no wheel hop m ode seen in the wheel or tyre motion response. There is a steady state error seen for both wheel and tyre displacements.

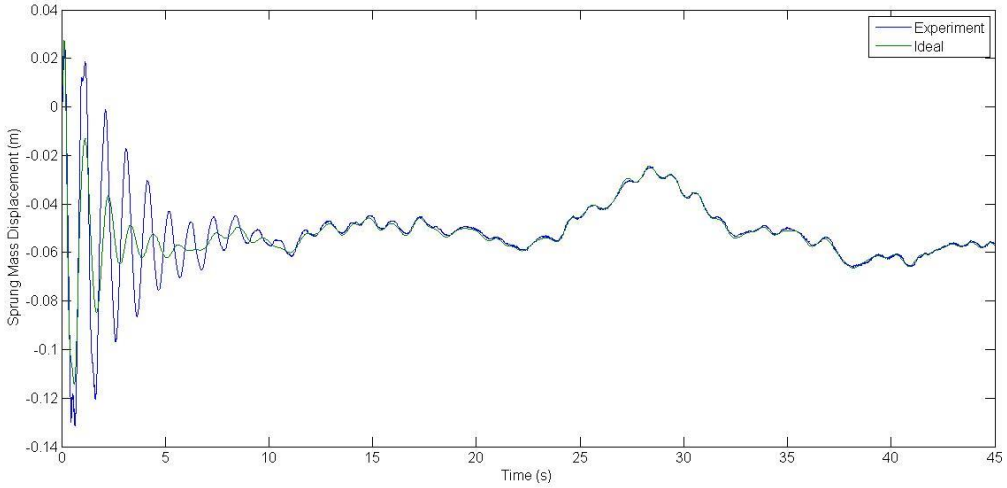

Figure B3.1 – Sprung mass displacement time response.

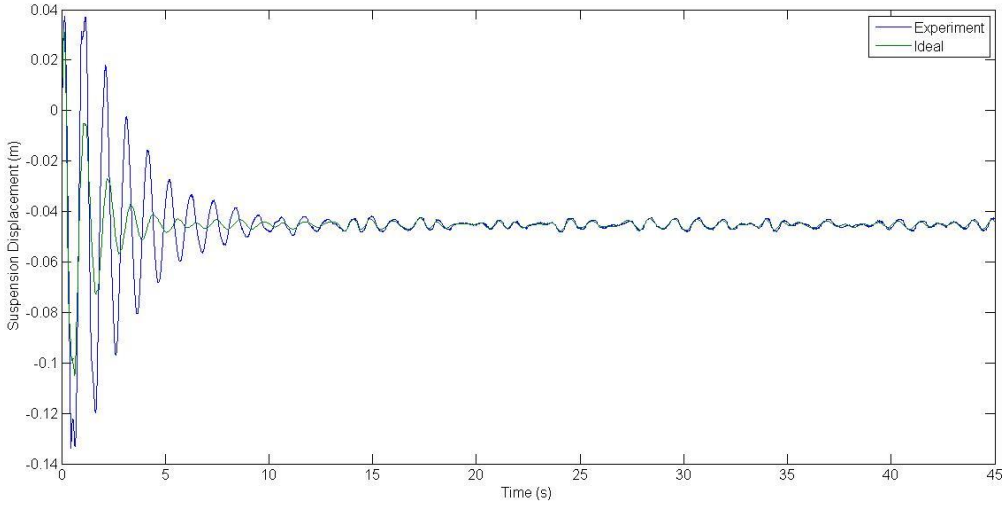

Figure B3.2 – Suspension displacement time response.

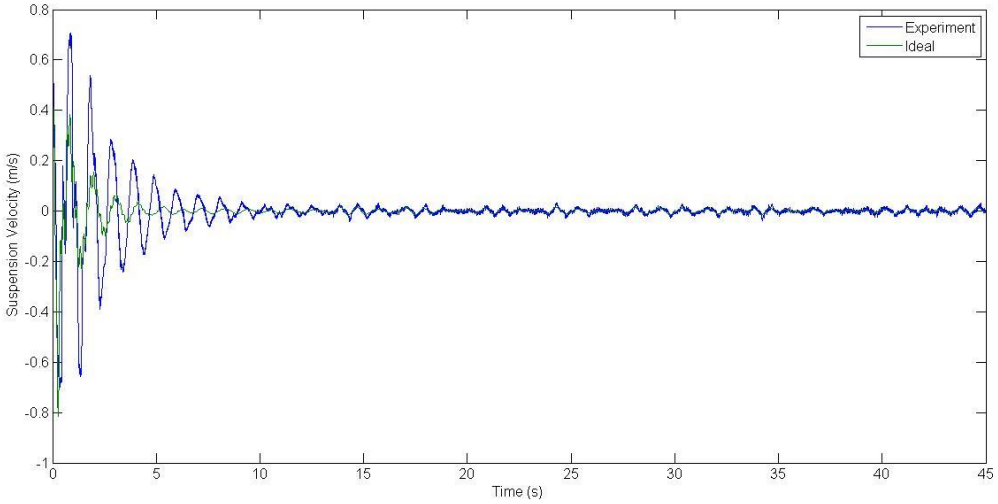

Figure B3.3 – Suspension velocity time response.

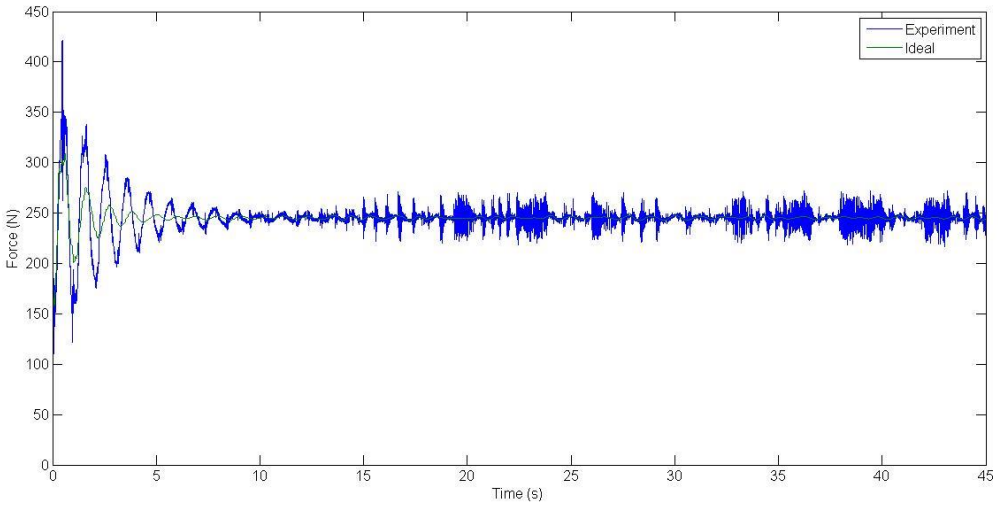

Figure B3.4 – Suspension force time response.

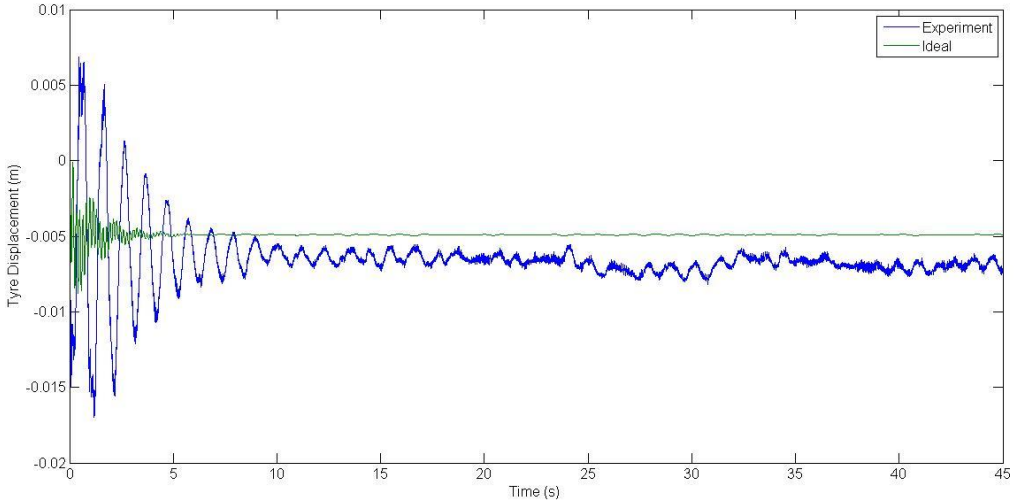

Figure B3.5 – Tyre displacement time response.

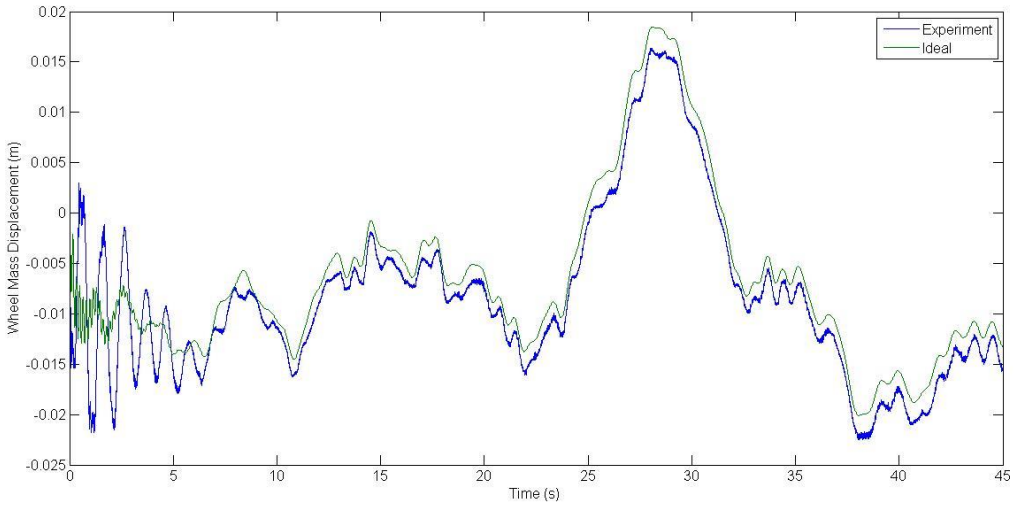

Figure B3.6 – Tyre displacement time response.

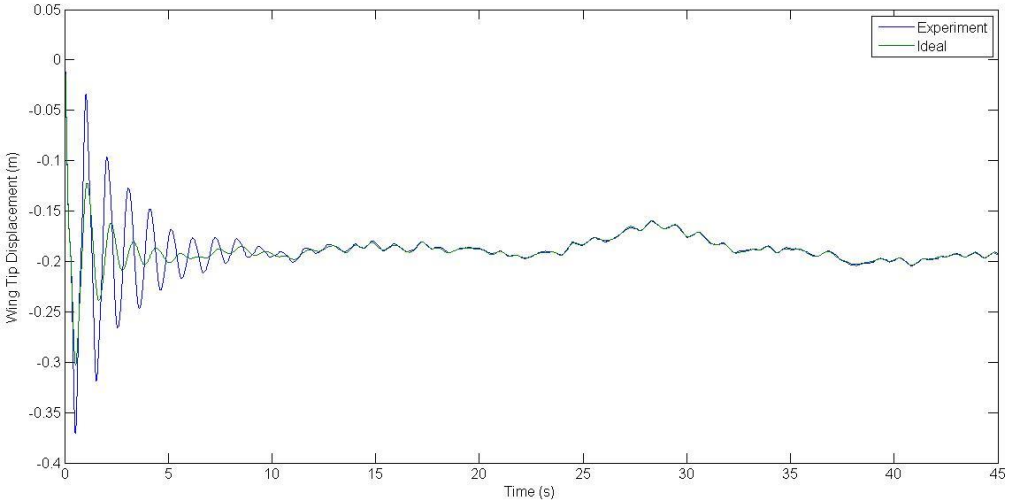

Figure B3.7 – Wing Tip Displacement

Performance evaluation of the test rig is shown in Table B3.1 and Figures B3.8 and B3.9. The RMS errors for force tracking are higher compared to the point mass test in Section 6.3.2 but in terms of percentage error they are roughly the same. For vehicle structure MIL the RMS errors is comparable to the results in Section 6.3.2 in both absolute and percentage terms. The subspace plots in Figure B.38 and B.39 shows that the initial oscillations from the drop test decay slowly, shown by the multiple large oval shaped loops. When compared to the point mass case, with the flexible cross structure vibrations are more severe and decay more slowly since the coupling of vibration modes of the structure add on to the sprung mass vibration.

	Suspension MIL	Vehicle structure MIL
Total RMS Error ($e_1 + e_2$)	13.2	0.0603
Percentage Error (%)	156	59

Table B3.1 - Overall test accuracy, the error denotes comparison of emulated to real output.

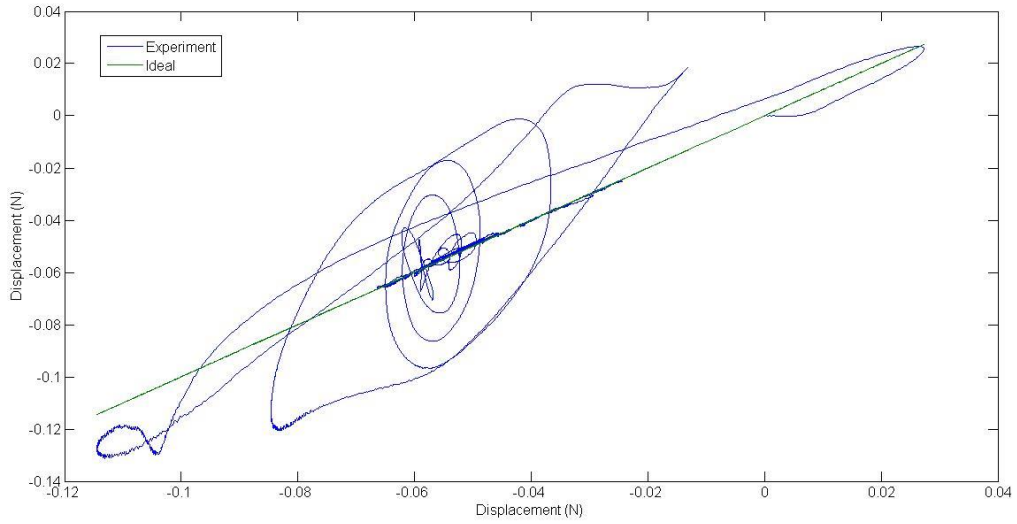

Figure B3.8 – Sprung mass position error subspace plot.

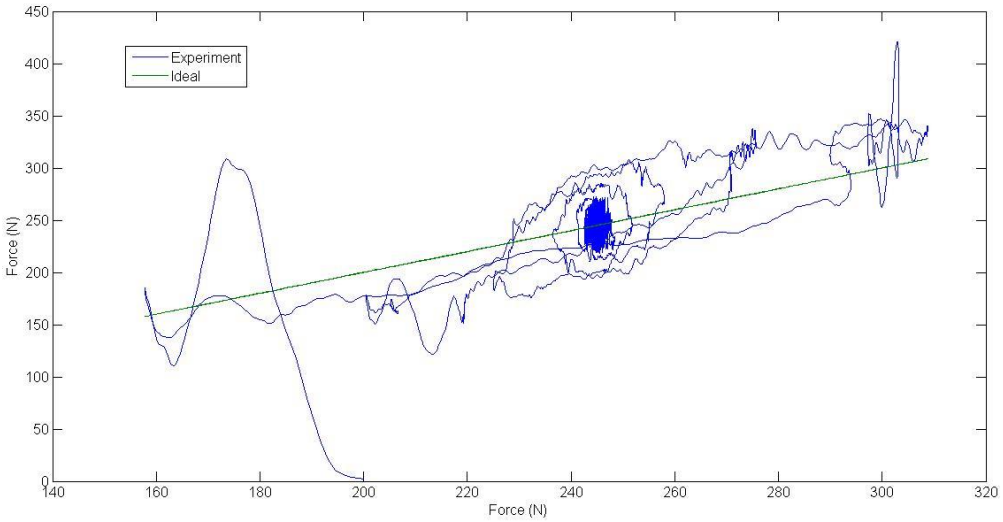

Figure B3.9– Force error subspace plot.

Appendix B4 – Validation of Semi-Active Flexible Cross Structure Test

The time responses from the test are shown in Figure B4.1 – B4.7. The semi-active skyhook algorithm is shown to be effective at reducing sprung mass and suspension vibrations in Figure B4.1 and B4.2. Smaller command amplitudes leads to smaller tracking error and better rig accuracy compared to the passive case. The improvement of the rig accuracy is shown in Table B4.1 and Figures B4.8 and B4.9.The wheel mass position and tyre position as usual do not contain the higher frequency wheel hop mode vibrations and there is also a steady state error.

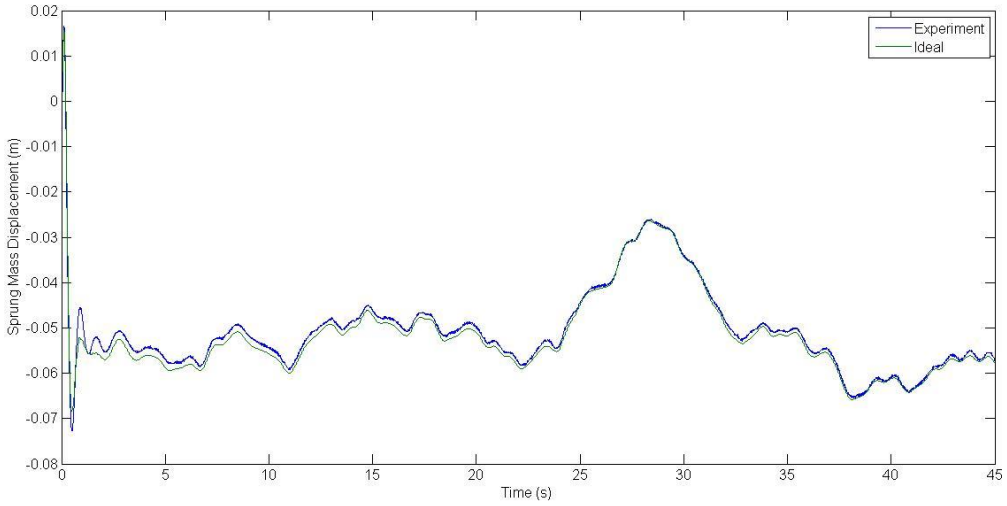

Figure B4.1 – Sprung mass displacement time response.

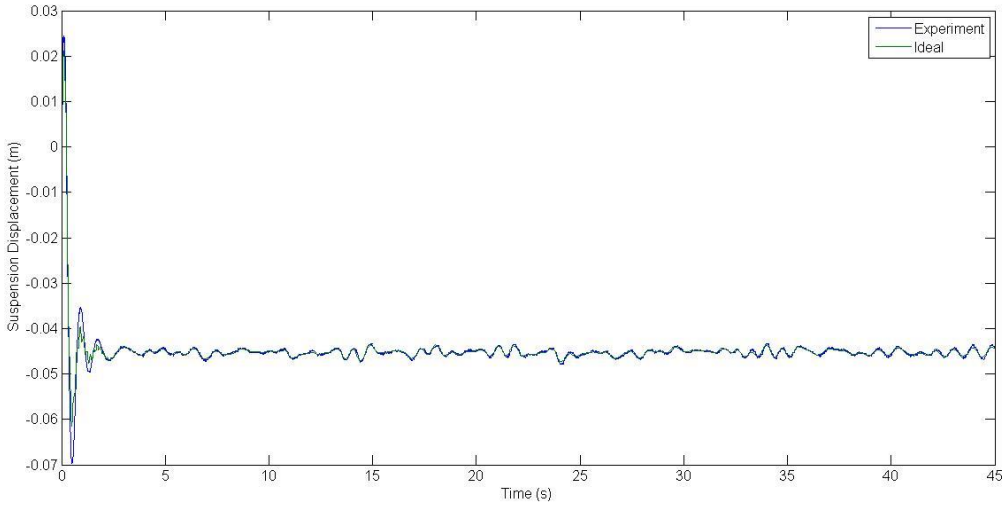

Figure B4.2 – Suspension displacement time response.

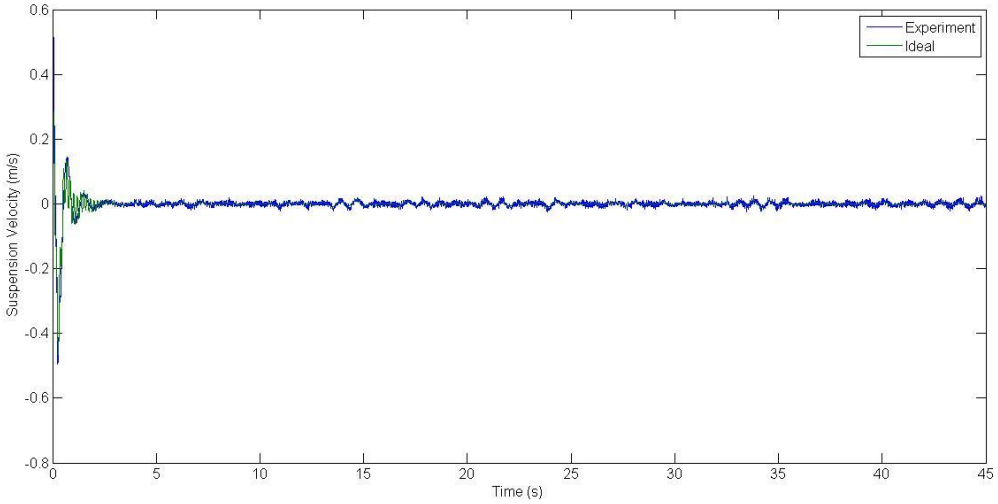

Figure B4.3 – Suspension velocity time response.

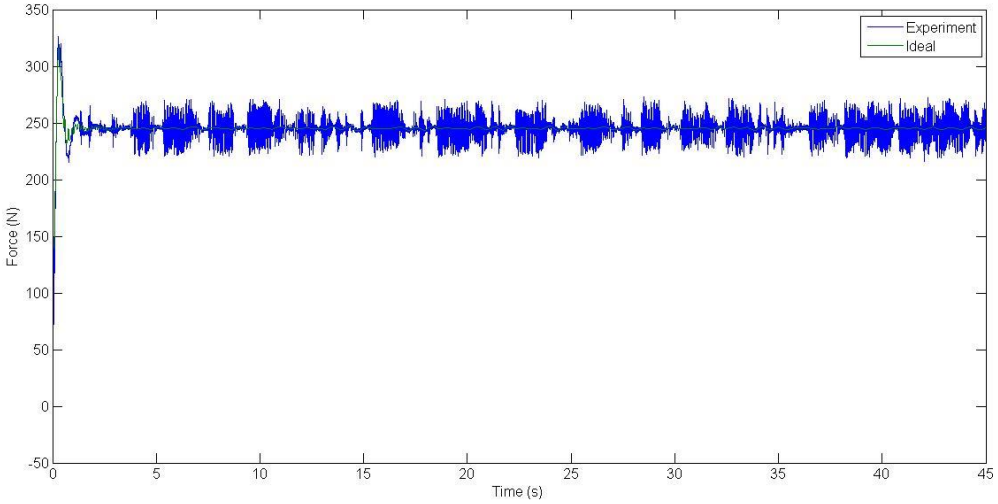

Figure B4.4– Suspension force time response.

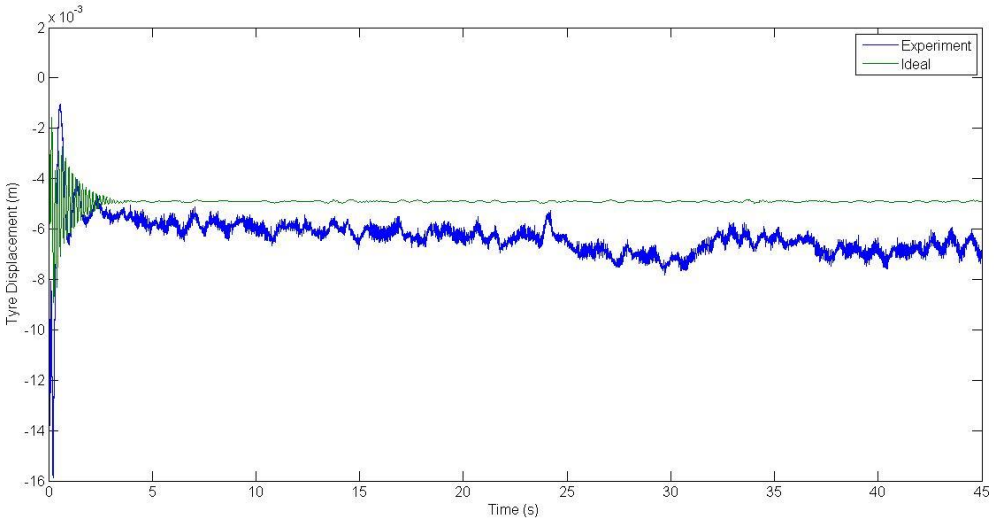

Figure B4.5 – Tyre displacement time response.

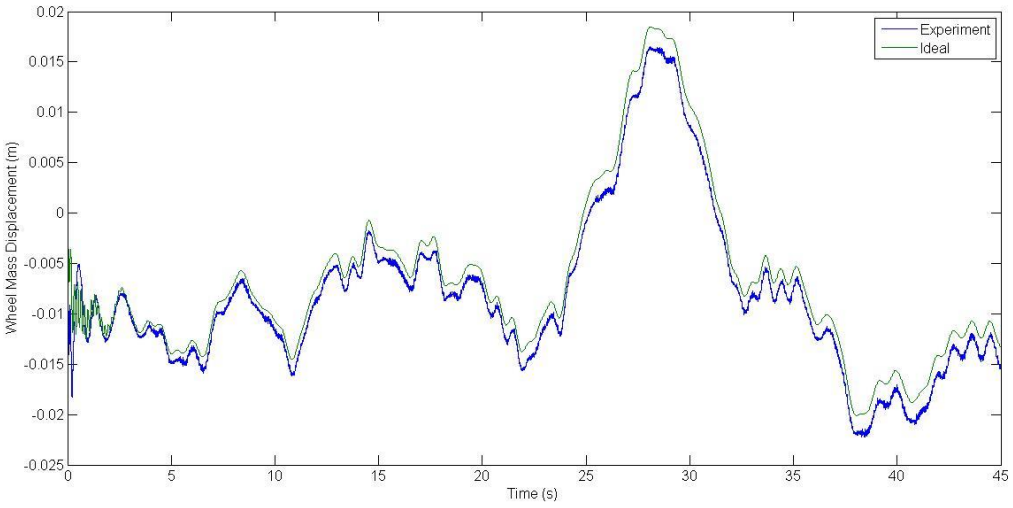

Figure B4.6 – Wheel mass displacement time response.

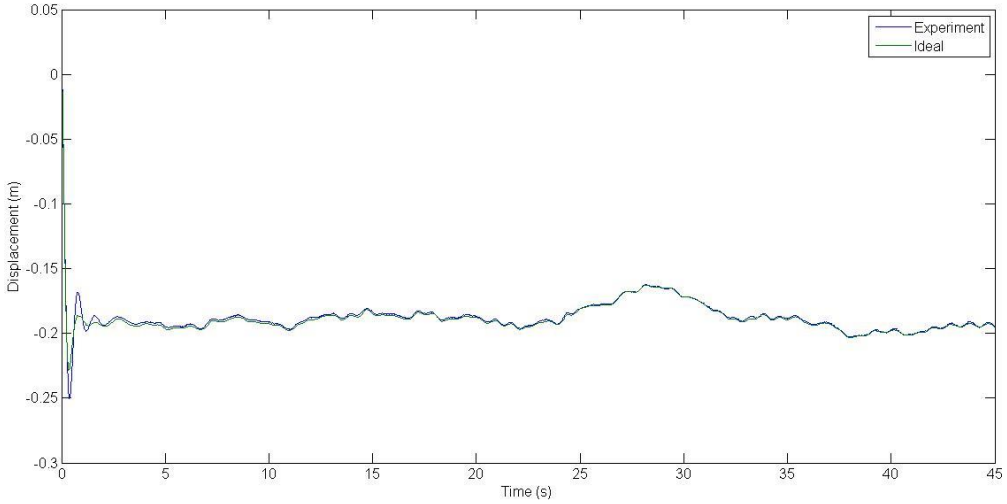

Figure B4.7 – Wing tip displacement time response.

	Suspension MIL	Vehicle structure MIL
Total RMS Error ($e_1 + e_2$)	10.1	0.0593
Percentage Error (%)	154	58

Table B4.1 - Overall test accuracy, the error denotes comparison of emulated to real output.

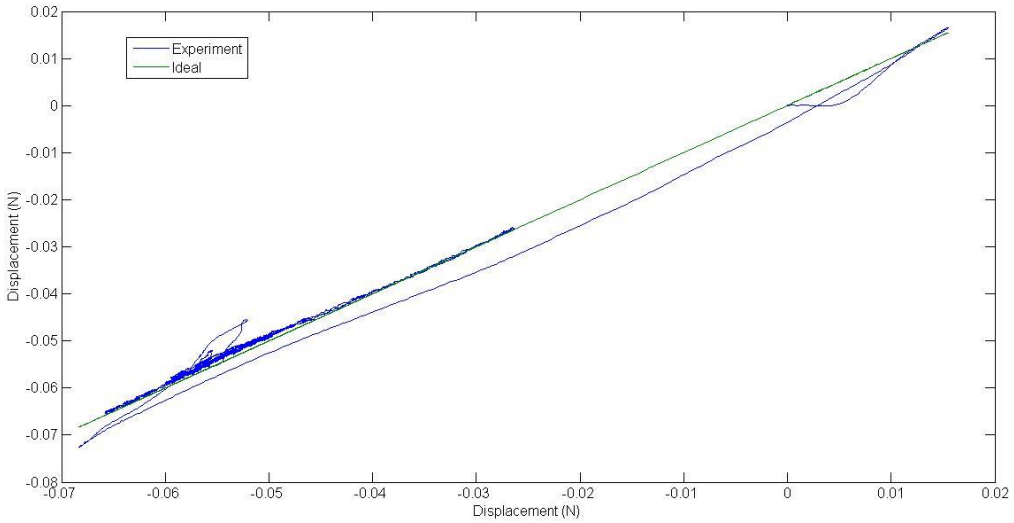

Figure B4.8 – Sprung mass position error subspace plot.

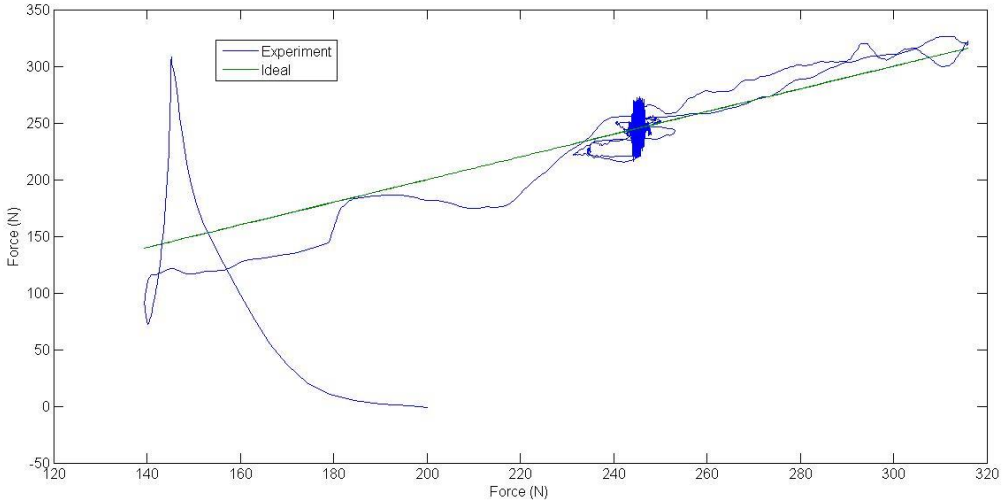

Figure B4.9 – Force error subspace plot.

Appendix B5 – Validation of Active Flexible Cross Structure Test

The time responses of the experimental test are shown in Figure B5.1 – B5.7. The results in Section 7.2.3 demonstrated that semi-active and active skyhook suspensions have nearly identical performance. The accuracy of the test rig is shown in Table B5.1 and Figure B5.8 and B5.9.

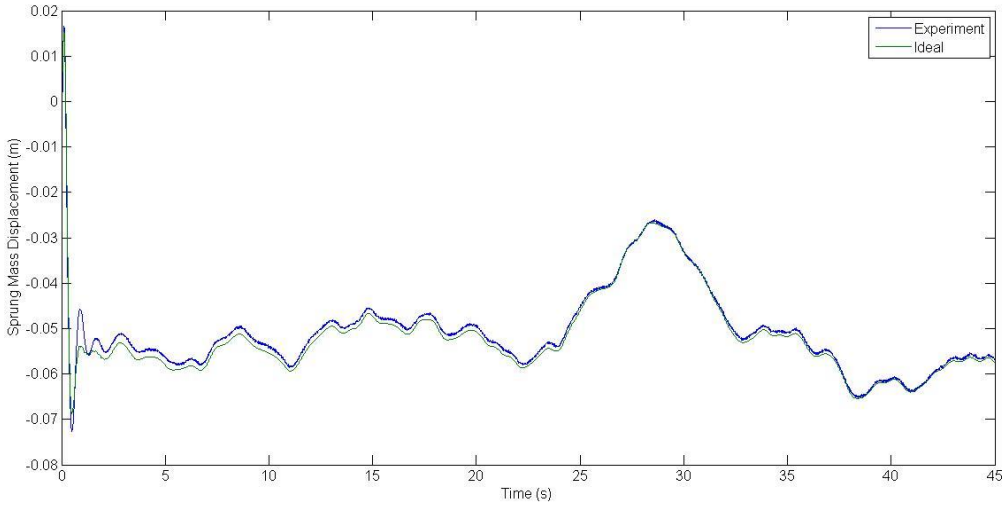

Figure B5.1 – Sprung mass displacement time response.

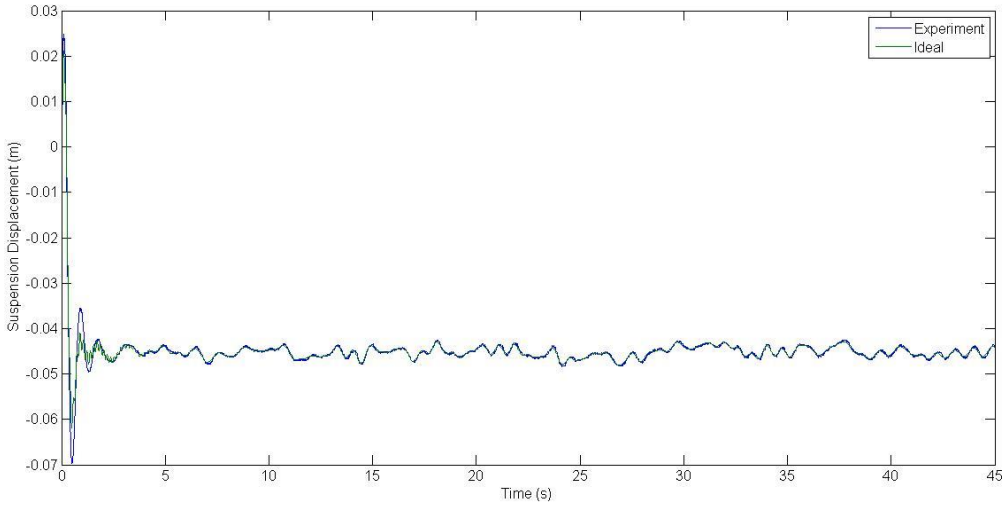

Figure B5.2– Suspension displacement time response.

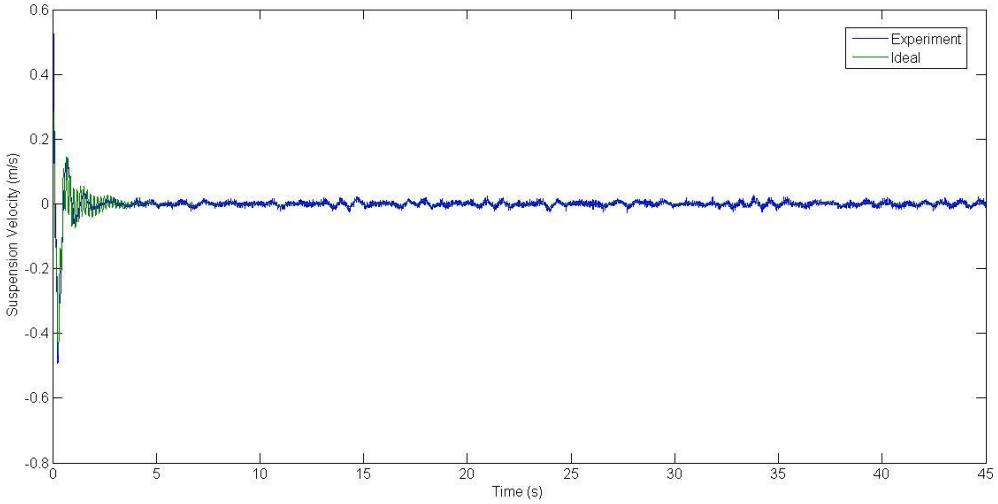

Figure B5.3 – Suspension velocity time response.

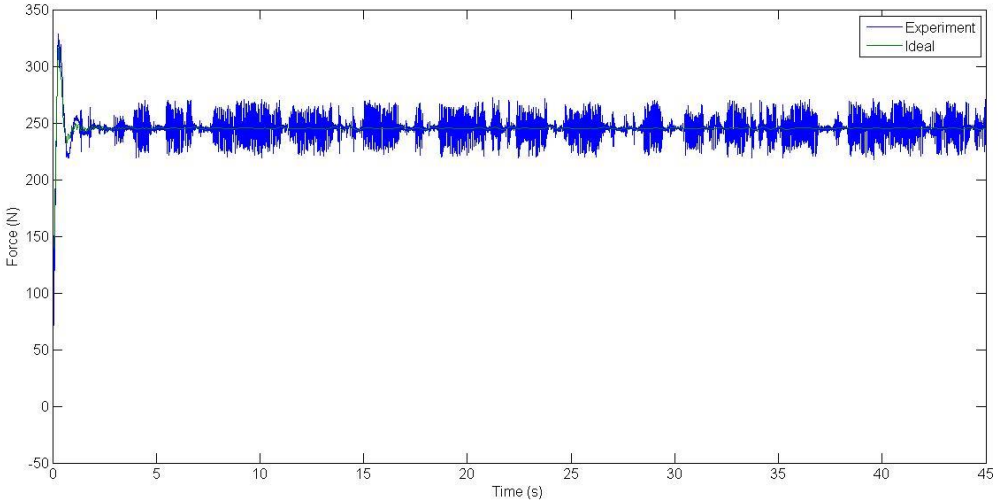

Figure B5.4 – Suspension force time response.

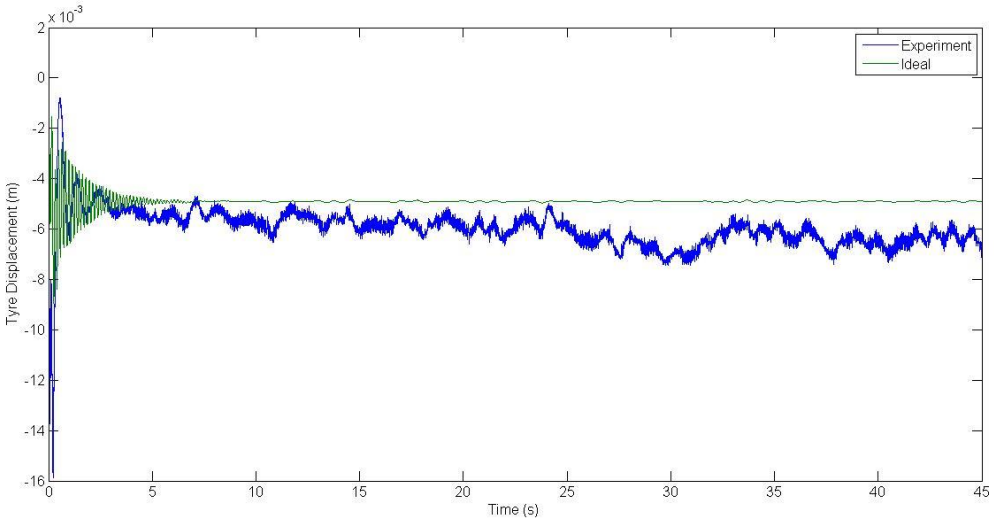

Figure B5.5 – Tyre displacement time response.

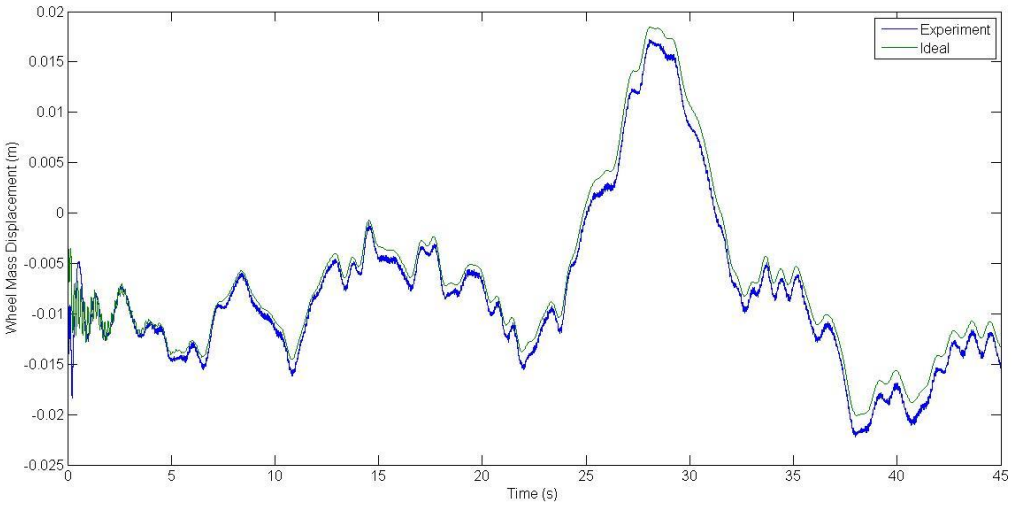

Figure B5.6 – Wheel mass displacement time response.

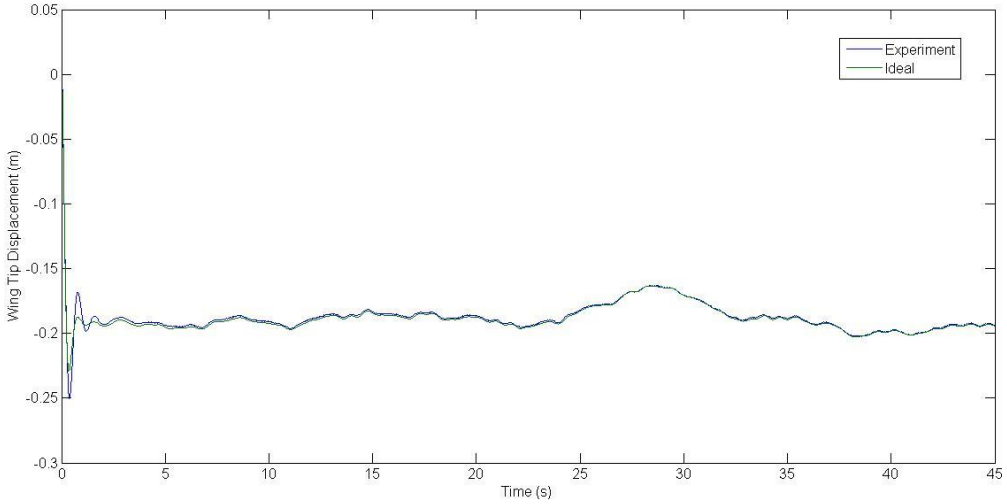

Figure B5.7– Wing tip displacement time response.

	Suspension MIL	Vehicle structure MIL
Total RMS Error ($e_1 + e_2$)	10.4	0.0593
Percentage Error (%)	159	58

Table B5.1 - Overall test accuracy, the error denotes comparison of emulated to real output.

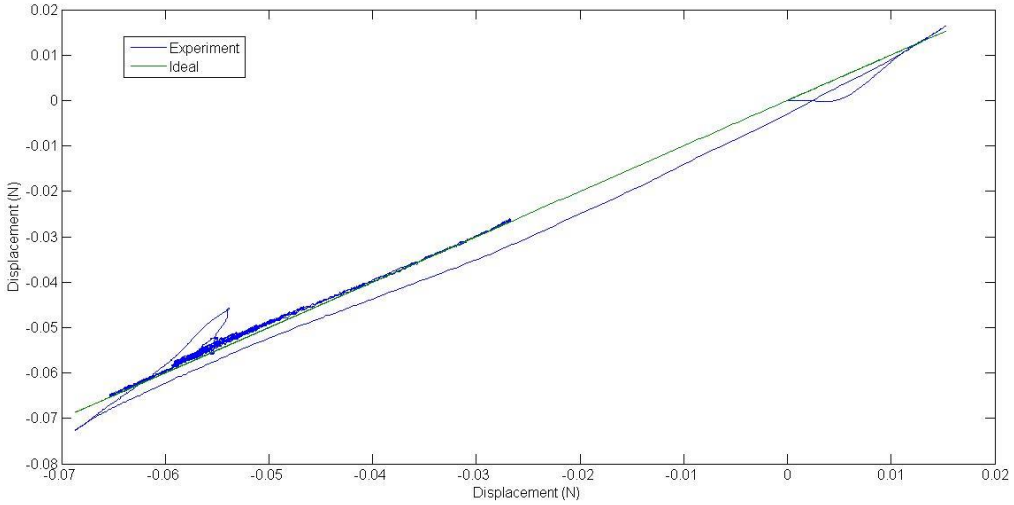

Figure B5.8 – Sprung mass position error subspace plot.

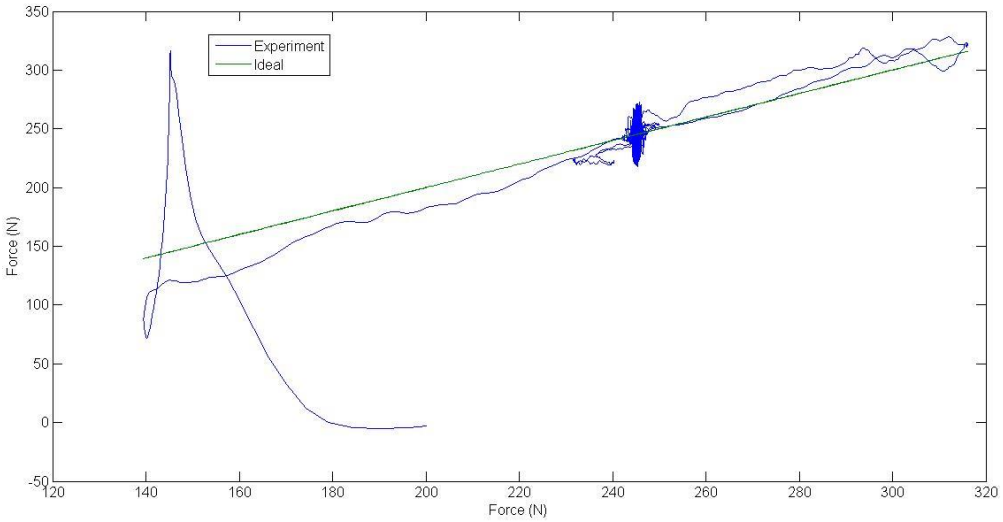

Figure B5.9 – Suspension force error subspace plot.